Laser Welding of 9Cr-1Mo(V, Nb) Ferritic/Martensitic Steel (FMS): Process Optimization and Modelling

Santosh Kumar
(Enrolment No.: ENGG01200804008)
Engineering Sciences
Bhabha Atomic Research Centre
Homi Bhabha National Institute
Mumbai, India – 400094

A thesis submitted to the Board of Studies in Engineering Sciences
under the guidance of
Dr. K. Bhanumurthy (Guide) and Dr. G. K. Dey (Co-Guide)
In partial fulfilment of the requirements
for the degree of
DOCTOR OF PHILOSOPHY
of
Homi Bhabha National Institute, Mumbai

DECLARATION OF THE SCHOLAR

I, hereby declare that the investigations presented in this thesis have been performed by me. The work is original and has not been submitted earlier as a whole or in part for a degree / diploma at this or any other institution / university.

Santosh Kumar
30.12.2014

Santosh Kumar

DECLARATION OF THE GUIDES

We, hereby declare that the investigation presented in the thesis has been carried out by the scholar under our guidance. The work is original and has not been submitted earlier as a whole or in part for a degree / diploma at this or any other institution / University.

K Bhanumurthy
30.12.2014

(Guide: Prof. K. Bhanumurthy)

Outstanding Scientist

and Head, SIRD, BARC

Senior Professor, HBNI, Mumbai

Gautam Kumar Dey
30/12/2014

(Co-Guide: Prof. G. K. Dey)

Distinguished Scientist

and Associate Director,

Material Group, BARC

Senior Professor, HBNI, Mumbai

Recommendations of the Viva Voce Board

1. **Date of Viva Voce Examination: 26th October 2015**
2. **Recommendations for the award of the Ph.D. degree: Recommended / ~~Not Recommended~~**

   (If Recommended, give summary of main findings and overall quality of thesis)

   (If Not Recommended, give reasons for not recommending and guidelines to be communicated by)

Viva voce of ShriSantosh Kumar (Enrolment no. ENGG01200804008) ofMaterials Science Division, Materials Group, BARC was conducted on 26th March 2015 by the viva voce board members comprising the Doctoral Committee Members and the External Examiner Prof. Satish V. Kailas from Indian Institute of Science, Bangalore. ShriSantosh Kumar made a presentation on his PhD work "Laser Welding of 9Cr-1Mo(V, Nb) Ferritic/Martensitic Steel (FMS): Process Optimization and Modelling" which was followed by questions and discussions. He gave satisfactory answers to the questions raised by the examiners as well as members of the doctoral committee.

In his PhD work, he has performed laser welding of 9Cr-1Mo(V, Nb) Ferritic/Martensitic Steel using high power CO_2 laser and has studied the weld joints for microstructure and mechanical properties. He has demonstrated that laser welded joints in this steel are sound, stronger than the parent metal and exhibit no softening in the inter-critical heat affected zone. He has made detailed measurements on residual stresses in the weld joints by neutron diffraction to deduce effect of martensitic transformation and depth to width aspect ratio of the fusion zone on the three orthogonal components of the residual stress. He has carried out studies on phase transformation behaviour of this steel and has demonstrated that for lower austenitization temperatures experienced in the HAZ region; this steel can undergo diffusional transformation. He has performed elevated temperature tensile tests to generate phase-dependent tensile properties of this steel, for the first time, which is very useful input for modelling and simulation studies of welding of ferritic/martensitic steels. He has carried out modelling and simulation studies of laser welding of this steel to compute evolution of the resulting temperature- and stress-field. He could establish a reasonably good agreement between experimentally measured and computed residual stresses. In addition, he has demonstrated that the austenite phase undergoes substantial deformation before its transformation into the martensite, in the fusion zone. He has also demonstrated that even though the final or the residual stresses resulting from laser welding are limited to a very narrow region around the weld, the stress-field during the welding process is much wider. His PhD thesis contains high quality of work.

Based on the performance of Shri Santosh Kumar, the examiner (Prof. Satish V. Kailas) and the doctoral committee is recommending acceptance of the thesis in its present form for the award of the PhD degree. The viva voce committee ascertained that the suggested minor changes by one of the examiners have been incorporated in the revised thesis.

Date: 26th October 2015

Name and Signature of the Viva Voce Board (Doctoral Committee and External Examiner):

Prof. S. Banerjee (Chairman)…… Srikumar Banerjee 26 Oct 2015……

Prof. K. Bhanumurthy (Guide)…… K Bhanu 26.10.2015……

Prof. G. K. Dey (Member and Co-Guide)…… Gautam Kr Dey 26/10/15……

Prof. Satish V. Kailas (External Examiner)…… Satish Kailas 26/10/15……

Prof. S. B. Roy (Member)…… 26.10.15……

Prof. N. K. Maheshwari (Member)…… Naresh Kr. Mahesh 26/10/15……

Homi Bhabha National Institute

Recommendation of the Viva Voce Board

As members of the Viva Voce Board, we certify that we have read the dissertation prepared by ShriSantosh Kumar entitled “Laser Welding of (Cr-1Mo(V, Nb) Ferritic/Martensitic Steel (FMS): Process Optimization and Modelling” and recommended that it may be accepted as fulfilling the dissertation requirement for the Degree of Doctor of Philosophy,

____________________ Date: 26 Oct 2015
Chairman- Prof. S. Banerjee

____________________ Date: 26.10.2015
Guide-Prof. K. Bhanumurthy

____________________ Date: 26/10/15
Co-Guide and Member-Prof. G. K. Dey

____________________ Date:
Technical Adviser: Prof. G. K. Dey

____________________ Date: 26/10/15
External Examiner-Prof. Satish V. Kailas

____________________ Date: 26.10.15
Member: Prof. S. B. Roy

____________________ Date: 26/10/15
Member: Prof. N. K. Maheshwari

Final approval and acceptance of this dissertation is contingent upon the candidate's submission of the final copies of the dissertation to HBNI.

We hereby certify that we have read this dissertation prepared under our direction and recommend that it may be accepted as fulfilling the dissertation requirement.

Date: 26th October, 2015
Place: Mumbai

Co-guide **Guide**

ACKNOWLEDGEMENT

I take this opportunity to express my sincere gratitude to my research adviser Prof. K. Bhanumurthy, Head, Scientific Information and Resources Division, BARC for his continuous encouragement, guidance and support during the course of this thesis. Invaluable suggestions emanating from several discussions and his able guidance have brought this research work to the current stage.

I would like to thank Prof. G. K. Dey, Associate Director, Materials Group, BARC for permitting me to purse this research work and supervising it along with Prof. K. Bhanumurthy. He ensured that all the experimental facilities, irrespective of its geographical location, required for the research work are made accessible to me and arranged all the necessary collaborations and approvals for it. He also encouraged and facilitated presentation of the results of this research work at different national and international conferences for its critical peer review and subsequently its publication in the journals of high impact. Without his continuous persuasion, support and guidance it would not have been possible to make any substantial progress in the present research work.

I would like to thank Dr. J. K. Chakravartty, Director, Materials Group, BARC and Dr. R. N. Singh, Head, Fracture Mechancs Section of Mechanical Metallurgy Division for their help in tensile property evaluation of the laser welded joints. I would like to thank Dr. Madangopal Krishanan, Head, Glass and Advanced Materials Division and Dr. Bikas C. Maji of the same division for their help in evaluation of phase-dependent tensile properties of 9Cr FMS. I would like to thank Shri S. Bhattacharya, Head Research Reactor Design and Projects Division for his help in laser welding of the 9Cr FMS plates. I would like to thank all the seniors and colleagues in Laser Materials Processing Section of Materials Science Division namely S/Shri C. S. Viswanadham, A. Chatterjee, B. P. Badgujar, Jagdish Sharma, R. P. Kushwaha, N. K. Chakraborty and P. C. Bhatt, and Ms. Reena Awasthi for their friendly and informal help for conducting the experiments related to the present research work. Thanks are also due to S/Shri Suman Neogy and Nachiket Keskar of Materials Science Division, BARC for carrying out electron microscopy and to Dr. A. K. Sahu and Dr. A. Ghosh of Glass and Advanced Materials Division, BARC for carrying out dilatometry for me. Contributions of my friend Dr. Arijit Laik, Materials Science Division, BARC deserves special acknowledgement, as he was always available for discussing almost everything – work plan; progress, results etc., related to this research work and has provided invaluable help in appreciating the results in the right perspective. Acknowledgements are also due to many colleagues from different divisions in BARC like S/Shri M. N. Jha of L&PTD, Kaushal Jha of ED&DD, Suman and Arun of FRD and B. K. Jha of INRPRD, NRB extended their valuable help in conducting different experiments and for providing their perspective on the experiments and the results, which improved quality of the research work.

Neutron diffraction for residual stress measurements formed an important part of the present work. I would like to thank our collaborators namely Prof. J. Bouchard of The Open University, UK, Dr. Anna Paradowska, Instrument Engineer at ISIS, UK (presently with ANSTO, Australia) and Dr. S. Paddea of The Open University, UK for introducing neutron diffraction for residual stress measurement to me and extending all the help for these measurements and analysis. Special thanks are due to Dr. Evans Alexander, Instrument Engineer, SALSA at Intitut Laue-Langevin, Grenoble, France, who carried out the neutron diffraction work that forms a part of the present work.

I gratefully acknowledge the contributions of my doctoral committee chairman Prof. S. Banerjee and members Prof. S. B. Roy and Prof. N. K. Maheswari who spared their valuable time for periodical critical assessment of my work. Incorporation of their constructive suggestions has greatly enhanced the technical level of my research work.

Direct and indirect support received from BARC is gratefully acknowledged. The neutron diffraction work that forms parts of the present research was carried out under Indo-UK collaboration and the support received from EPSRC, UK is gratefully acknowledged. Neutron diffraction measurements were performed at Intitut Laue-Langevin, Grenoble, France and I would like to acknowledge all the support received from the institute in connection with these measurements.

I am sure many contributors to this research work must have escaped my attention and therefore their name could not be mentioned here. With an apology, I thank them all for their contributions.

Words will not be enough to express my thanks to my wife Ms. Amrita Priyam and my kids Master Satvik Singh and Ms. Sanskriti Singh who had to suffer neglect, on account of the attention required by this research work, and also, on many occasions, had to cancel at their planned holidays at the last hour, due to the work related to this research. Thanks are due to my parents and elders for their blessings, which provides the inner strength to excel ahead, undeterred by the uncertainties invariably associated with any research work and the adversities present in the real life.

Santosh Kumar

ABSTRACT

Ferritic/martensitic steels are structural and functional materials of interest for ultra supercritical thermal power plants and next generation nuclear reactors because of their excellent elevated temperature strength, good formability, high void swelling resistance and high thermal conductivity. Because of martensitic transformation during cool down of the weld joint, these steels are difficult to weld by conventional arc welding processes and require special care like preheating and interpass heating to produce a sound weld joint. However, high heat input associated with these welding processes induces undesirable microstructural changes in the heat affected zone, which is considerably wide. In addition, joint distortion and residual stresses induced by the conventional arc welding processes are also considerably high. These limitations of conventional welding processes in joining ferritic/martensitic steels provide the rationale for application of high power density or beam welding processes like laser welding and electron beam welding for joining of these steels. Laser and electron beam welding of these steels have is being seriously explored for fabrication of test blanket modules for The International Thermonuclear Experimental Reactor (ITER). However, there is only limited literature available on laser welding of these steels. This prompted a comprehensive experimental and computational study of laser welding of ferritic/martensitic steel covering the process optimization, detailed microstructural characterization, evaluation of weld joint properties and residual stresses in laser welded joints.

In this work laser welding of ASTM A387 Gr91 steel, an important and representative grade of ferritic/martensitic steels, has been studied using a high power (up to 10 kW)CO_2 laser. A large number (22) weld beads were produced on a 30mm thick plate of

ASTM A387 Gr91 steel over a wide range of laser power (2 kW – 8 kW) and welding speed (0.5 m/min – 5.0 m/min) combinations. Subsequently, laser welding of 5 mm and 9 mm thick plates, in square butt configuration, was carried out using optimized process parameters to produce sound weld joints for detailed characterization of the microstructure and evaluation of the mechanical properties (microhardness and tensile properties) and residual stresses. Detailed microstructural characterization of different regions across the weld joint – the parent metal (PM), the heat affected zone (HAZ) and the fusion zone (FZ), was performed at different length scales, using optical and electron microscopy, in as-welded and also in post weld heat treated conditions. Cross-weld microhardness profiles were also measured to understand the effect of welding process parameters on the microstructure and properties of different regions across the weld joint. Cross-weld tensile tests were performed to evaluation the tensile properties of the laser welded joints, in as-welded and also in post-weld heat treated conditions.

Residual stress measurements were made for the 9 mm thick welded joints, produced at a fixed laser power (8 kW) but two welding speeds (0.75 m/min and 1.5 m/min). These measurements were made using neutron diffraction at Institut Laue Langevin at Grenoble, France. These measurements were made using a fine gauge volume (1x1x1 mm^3) across the weld joints at different depths from the top surface to generate a cross-weld residual stress map.

Modelling and simulation studies were performed to compute temporal evolution and spatial distribution of temperature and stresses resulting from laser welding of 9 mm thick plates. These studies were performed using finite element based weld modeling and simulation software, SYSWELD. This software is from ESI, France and is commercially available. Temperature and phase dependent physical and mechanical properties of this steel were used in these computations. However, temperature and phase dependent tensile properties of this steel is not available in literature, therefore, elevated temperature tensile tests were performed to deduce these properties.

Macrograph of the weld cross-section showed a nail shape with a long body and a small nail head. A narrow fusion zone and HAZ, a characteristic of the weld joint made by high power density welding processes were observed in all the weld joints made in this study. Effect of laser power and welding speed could be described as variation in the joining efficiency with welding speed. Joining efficiency of laser welding, for this material, increased with welding speedfrom 15 mm^2/kJ at 0.5 m/min to 55 mm^2/kJ at 5.0 m/min. However, rate of increase was very steep up to 2.0 m/min and moderated considerably beyond that. On the other hand depth of penetration continued to decrease with increasing welding speed. Therefore, welding speed of 2.0 m/min can be taken as a trade-off between depth of penetration and joining efficiency.

Microstructural studied showed that unlike conventional arc welded joint there was no coarsening of the prior austenite grains in the HAZ. The HAZ showed attributes of the fine grained HAZ. This can be attributed to low heat input associated with laser welded, which did not allow time for complete dissolution of the carbide precipitates and appreciable coarsening of the prior austenite grains even near the fusion line. The fusion zone showed as-transformed martensitic structure within coarse and columnar prior austenite grains. The fusion zone microstructure was homogeneous, unlike that in arc welded multi pass joints where multiple passes introduce heterogeneity in the fusion zone microstructure as well.

Cross-weld microhardness profiles showed significant hardening in the fusion zone (~ 500 HVN) and the HAZ, in as-welded condition, because of martensitic transformation. However, post weld heat treatment, at a temperature in 750 ^{o}C – 770 ^{o}C range for 30 minutes, could bring the hardness of the fusion zone (~ 280 HVN) and the HAZ (~ 230 HVN, same as that of the parent metal) to the levels (< 300 HVN) acceptable for levels. The weld joints always fractured in the parent metal, in as-welded and also in post weld heat treated conditions, and thus it can be concluded that the these joints are sound and stronger than the parent metal. However, a minor reduction in elongation of the welded joints was observed in as-welded condition. This loss in elongation of the weld joints could be recovered nearly completely by post weld heat treatment of the weld joint at 770 ^{o}C for 30 minutes, which is the standard heat treatment for this steel.

Residual stress measurements of the laser welded joints showed a low tensile / compressive state of stress in the fusion zone and a high tensile state of residual stresses in the parent metal bordering the HAZ on both sides of the joint. This could be explained on the basis of martensitic transformation that occurs during cool down of the weld joint. The three orthogonal components showed a clear ranking: Longitudinal > Normal > Transverse and the normal component showed similar cross-weld profile as that shown by the transverse component. This could be explained by high depth to width aspect ratio of the region (fusion zone plus HAZ) that experienced martensitic transformation during cool down of the joint.

Modelling and simulation studies showed steep temperature gradient across the weld joint and very rapid heating and cooling of the material in the fusion zone and the HAZ. This explained columnar solidification microstructure in the fusion zone and martensitic transformation in the fusion zone and the HAZ. This also explained absence of any appreciable coarsening of prior austenite grains in the HAZ. The residual stress profiles predicted by these computations showed a reasonably good agreement with those measured by neutron diffraction experiments. An interesting result showed by these computations was significant plastic deformation and work hardening of supercooled prior austenite during cool down of the weld joint. As the prior austenite grains transforms into martensite at a temperature (Ms ~ 375 ^{o}C), significantly higher than the room temperature, it is not possible to observe this by experimental means. Therefore, modeling and simulation studies were useful in revealing deeper insight of the laser welding process of ferritic/martensitic steels that could have been obtained by only the experimental studies.

It can be concluded that this work could produce new and meaningful knowledge about laser welding of ferritic/martensitic steels through experimental and computational studies and has raised new questions for further studies. These experimental and computational studies and the results are presented and discussed in detail in this thesis.

Contents

Chapter 1: Introduction

Ferritic/Martensitic Steels (FMS) with 8-12Cr, 1-2Mo/W, 0.1-0.2C and micro-alloying additions of V (~ 0.24) and Nb/Ta (~0.08), where numbers are wt. % of the respective elements, are high temperature materials for structural as well as functional applications in ultra-supercritical thermal power plants and advanced nuclear reactor systems including fusion reactors [1-4]. 9Cr-1Mo(V, Nb) FMS is a prominent member of this group of steels. Its nominal composition is Fe-9Cr-1Mo-0.1C-0.24V-0.08Nb (where numbers are wt. % of the respective elements). Because of high solute content, this steel exhibits very high hardenability and transforms completely into martensite upon cooling from the austenitic phase-field, even at a very slow cooling rate of ~5^{o}C/minute [5]. It transforms into lath martensite due to low carbon content. As-transformed microstructure shows a hierarchical structure within prior austenite grains, with laths, the smallest structural units, arranging into lath blocks, which arrange into lath packets [6]. As-transformed martensitic structure exhibits high strength but low ductility. Also, martensite, phase being a supersaturated solution of carbon in ferritic structure, is not stable at significantly high service temperatures of about 600^{o}C. Therefore, this steel is used in normalized and tempered (N&T) condition. Tempering causes rearrangement and reduction of dislocations, leading to sub-grain formation. Excess carbon in the supersaturated matrix precipitates out in the form of $M_{23}C_6$ (M being primarily Cr with some Fe and Mo) type carbides on the prior austenite grain boundaries and subgrain boundaries and in the form of MX (M is V or Nb) type carbonitrides within the subgrain. These carbide and carbonitride precipitates contribute to the strength and microstructural stability by pinning down various interfaces. Coarsening of $M_{23}C_6$ type carbide precipitates, during service, leads to loss of creep strength of the material [7]. Other deleterious phases like laves phase and Z-phase also form during service and contribute to loss of fracture toughness and creep resistance of the material [8-10]. These microstructural changes during service are responsible for determining life of the component made of this material.

This steel is welded to fabricate different components and assemblies [11]. Welding is carried out using different conventional welding processes like Manual Metal Arc Welding (MMAW), Gas Tungsten Arc Welding (GTAW), Gas Metal Arc Welding (GMAW), Submerged Arc Welding (SAW), etc. and their advanced versions like Activated Tungsten Inert Gas (A-TIG) welding and Narrow Gap Tungsten Inert Gas (NG-TIG) welding [12 - 16]. Joining of this steel using conventional welding processes, requires preparation of suitable joint design – V, J, U-groove etc. and filling the groove with weld metal by melting the filler wire/rod using the heat from the arc in multiple passes. Often two welding processes are also used in sequence, for example, GTAW is used for the root passes and MMAW for the filling passes. Significantly high volume of the weld metal need to be deposited, in multiple passes, for making a weld joint by employing conventional welding processes. Besides, high hardenability of this steel necessitates use of preheating and inter-pass heating (~200 – 300^{o}C) to avoid cracking during welding [16]. These requirements increase process complexity, add to the cost and have adverse implications on the joint quality.

Welding heat source induces significant alteration in the tempered martensitic structure of this material [16]. Multiple passes, associated with conventional arc welding processes, create microstructural heterogeneity in the fusion zone (FZ) because of reheating of the preceding weld passes by the succeeding weld passes [12, 17]. This microstructural heterogeneity is responsible for failure of the weld joints in this material by Type I and Type II cracking. High heat input associated with the conventional arc welding processes lead to a wide heat affected zone (HAZ) with significant intercritical softening in the HAZ region bordering the parent metal. This intercritical softening is responsible for failure of the weld joints by Type IV cracking [18]. High heat input associated with the conventional arc welding processes cause large distortions and this limits application of these welding processes for fabrication of the components with low distortion allowance.

These limitations can be overcome to a great extent if the weld joints in this material are made in single pass with low heat input and without using any filler material. This is possible by using laser or electron beam welding processes. Laser welding can produce up to 20 mm thick weld joints in steel with low heat input and without using any filler metal. Weld joints are made in keyhole mode and therefore, fusion zone exhibits high depth to width aspect ratio. Because of low heat input, the metallurgical HAZ as well as the residual stress affected zones are also much narrower than those in case of the weld joints made by the conventional arc welding processes. Besides, laser welding being non-contact and automatic, is a versatile welding process. Because of these benefits laser welding of 9Cr FMS has recently attracted attention of material scientists and engineers for fabrication of challenging components.

Test Blanket Module (TBM) for the International Thermonuclear Experimental Reactor (ITER) is one such component, which is challenging to fabricate even by employing the advanced fabrication technologies. This component is made of Reduced Activation

Ferritic Martensitic Steel (RAFMS), which has very similar chemistry, physical metallurgy and welding characteristics as those of 9Cr-1Mo(V, Nb) FMS. Fabrication of this component requires making a large number of weld joints in various challenging configurations having stringent distortion allowance. Most of these joints can be made by using laser welding. This is the reason for the recent interest in laser welding of ferritic martensitic steels. However, literature on laser welding of ferritic martensitic steels is rather limited [19 - 27].

Lee et al. [19] have reported microstructural characterization, notch tensile strength, notch toughness and fatigue crack growth of full penetration laser weld beads produced on 5 mm thick plates of 9Cr-1Mo(V, Nb) using 5 kW continuous wave CO_2 laser (Rofin-Sinar 850). They observed δ-ferrite, retained austenite as well as twinned martensite in the fusion zone microstructure, which was predominantly auto-tempered martensite within coarse prior austenite grains. They have reported much lower impact energy of the fusion zone than that of the parent metal, which increased significantly when the welds were tempered at 750^{o}C. Both the parent metal as well as the welds, tempered at lower temperatures, exhibited significant susceptibility to hydrogen embrittlement. However, this susceptibility was significantly higher for the welds, except for those tempered at 750^{o}C.

Xu [20] has reported laser welding of P91 steel pipe with 3.34 mm wall thickness using a pulsed Nd-YAG laser of 1.6 kW nominal power. He has reported the effect of process parameters on various attributes like depth and lateral spread of the fusion zone and the HAZ. A narrow fusion zone and HAZ with much higher hardness (~420 – 500 VHN) was reported by him. In post weld heat treated (PWHT) condition, cross-weld hardness profile did not show any soft zone, which is always associated with a multipass weld joints in the HAZ-PM interface region and attributed for failure of the weld joint by Type-IV cracking under creep condition.

Shanmugarajan et al. [21] have reported laser welding studies for 6 mm thick plate of P91 steel using continuous wave CO_2 laser of 3.5 kW power. They have studied weld beads and square butt weld joint produced by varying heat input from 168 J/mm to 1500 J/mm and have reported increase in width of the fusion zone and the HAZ with increasing heat input. Further, at low heat input of up to 420 J/mm, they did not observe any δ-ferrite in the fusion zone and any soft inter-critical HAZ; which was observed at heat inputs exceeding 700 J/mm. Besides, they have reported a superior impact toughness of the weld joint than that of the parent metal, which is in contrast to the observation by Lee et al. [19].

Harinath et al. [22] have reported process parameter optimization for laser welding of fuel clad tube – end cap, both made of 9Cr-1Mo(V, Nb) FMS, for potential application in Indian fast breeder reactors. They have reported the presence of δ-ferrite in the fusion zone, which comprised predominantly of as-transformed martensitic microstructure. They have also reported considerable grain refining in the narrow HAZ region adjacent to the fusion zone, and attributed the presence of δ-ferrite to incomplete δ-ferrite to γ (austenite) transformation, during cool down of the weld joint.

Cardella et al. [23] have identified laser welding as one of the prominent joining methods for TBM fabrication. They have presented a macrograph showing cross-section of a weld joint in 9 mm thick EUROFER 97, a RAFMS developed by European

Union, showing a narrow fusion zone and HAZ. However, details regarding the laser welding parameters and weld joint characterization were not reported.

Tanigawa et al. [24] have reported laser welding of F82H, a RAFMS developed by Japan, for fabrication of the membrane panel for Japanese TBM. This requires welding of 1.5 mm thick and 4 mm wide plate with tubes (11 mm diameter and 1 mm wall thickness) on both sides of the plate. In this application laser welding offers advantage of low heat input and negligible distortion. This welding has been done using a fiber laser to produce sound weld joints. However, characterization of the weld joint in terms of microstructure and mechanical properties is not reported. They emphasized the need to characterize the weld joints, involved in TBM fabrication, in terms of residual stresses.

Serizawa et al. [25] have reported welding of 32 mm thick plates of F82H by a combination of laser welding and plasma – MIG hybrid welding. Laser welding was carried out using a 10 kW fiber laser to produce 12 mm thick root pass and plasma-MIG hybrid welding was used for the filling passes. They have performed computational studies to investigate the effect of mechanical restraint on weldability of thick plates of RAFMS. They have used different model sizes and have arrived at a minimum coupon size which should be used for basic test of weldability for 90 mm thick plates of F82H using electron beam welding.

Serizawa et al. [26] have reported dissimilar weld joint between 4 – 5 mm thick plates of F82H and SS316L using 4 kW fiber laser. They produced the dissimilar weld joint by keeping the beam at the seam line and also by shifting the beam by 0.1 mm and 0.2 mm towards SS316L side. Welds were produced at 4 kW of laser power and at different welding speeds in 2 – 4 m/min range. They have reported wider fusion zone and HAZ at lower welding speed and vice-versa. The fusion zone was very hard when the beam was at the seam line and its hardness could not be reduced significantly even after PWHT. However, hardness of the fusion zone could be reduced to that of the parent metal by shifting the laser beam towards SS316L and hardness of the HAZ on the P91 side could be reduced to the parent metal level after PWHT.

Aubert et al. [27] have presented a review of the candidate welding processes of RAFMS for ITER and DEMO TBMs. They have emphasized the importance of high power laser welding and laser/MIG hybrid welding for TBM fabrication. Different research groups in European Union (EU) are actively pursuing laser and laser-MIG welding processes to produce different joint configurations relevant for its TBM. They have reported microstructural variation and microhardness profile across laser welded joints in RAFMS (Eurofer 97).

Based on review of the existing literature, it can be seen that laser welding of 9Cr FMS is of technological importance and there exists considerable interest in laser welding of this steel. However, the existing literature on laser welding of 9Cr FMS covers very limited aspects of the welding process and joint characterization in terms of microstructure and properties. There is no published work on the residual stress measurements in laser welded plates of this steel. Further, literature on the modelling and simulation of laser welding of this steel also does not exist. These studies are required to get a better insight of laser welding of 9Cr FMS in terms of the process parameters, microstructure, residual stresses and properties of the welded joints for effective utilization of laser welding process for fabrication of various challenging components of future generation nuclear reactors, including TBMs for the ITER. The present work is an attempt to expand the understanding of laser welding of 9Cr FMS in terms of microstructure, cross-weld tensile properties and residual stresses, their interplay and their correlation with the welding process parameters.

Simulations of a process allow greater flexibility for variation of process parameters, provide much more information and therefore, deeper insight of the process than the real experiments. Also, simulation is relatively economical to perform. Modelling and simulation of laser welding of 9Cr-1Mo(V, Nb) FMS has been performed to compute temporal evolution and spatial distribution of temperature, metallurgical phase-fraction and stresses resulting from laser welding. The computed and the experimental results have been compared and discussed in the context of physical metallurgy of this steel. Based on these studies, a good correlation has been obtained between the experimentally derived and the computed results.

1.1 Aim and Objectives of the Research Work

Laser welding of 9Cr FMS is of technological importance. However, the existing literature covers very limited aspects of laser welding of 9Cr FMS in terms of microstructure, joint properties and residual stresses and their correlation with process parameters. The objective of the present work is to expand the current understanding of laser welding of 9Cr FMS in terms of microstructure, mechanical properties and residual stresses of the resulting joint and correlation of these attributes of the joint with the process parameters; by performing a detailed experimental and computational study.

Extensive laser welding experiments will be performed on 9Cr FMS plates, using high power CO_2 laser, to study effect of welding process parameters on the joint attributes like depth of penetration and weld defects. Subsequently, full penetration and sound weld joints will be produced, between 9Cr FMS plates, for further characterization. In-depth microstructural characterization of the weld joints will be performed in different regions of the joint – the fusion zone, the heat affected zone and the parent metal and the microstructural attributes will be correlated with the process parameters. Microstructural characterization will be performed at different length scales using optical and electron microscopy. Cross-weld microstructural studies will be complemented with cross-weld microhardness profiling. Cross-weld tensile tests will be performed to evaluate tensile properties of the weld joint in relation to the tensile properties of the parent metal.

Detailed residual stress measurements will be performed for the laser welded plates using neutron diffraction. These measurements will be performed for the laser welded plates, produced at different welding conditions, to understand the effect of martensitic transformation and heat input on residual stresses.

Detailed modelling and simulation studies will be performed to compute temporal evolution and spatial distribution of temperature and stresses resulting from laser welding to get better insight of the process and the resulting phenomena. The computed results will be compared with the experimental results and to comprehend the agreement, or otherwise, between the two and also to comprehend the reasons for differences between the two.

These studies are aimed at producing a comprehensive understanding of laser welding of 9Cr FMS in terms of process parameters and characteristics of the weld joint like microstructure, tensile properties and residual stresses.

1.2 Organization of the Report

The work reported in this thesis has been organized in eight chapters. The structure of the remaining part of this report is as follows:

Chapter 2 describes a detailed literature survey that was conducted to understand basic metallurgy of the material, different welding processes used to join this material, the issues related to welding of this steel, cross-weld microstructural variation resulting from welding of this steel and computations and measurements of residual stresses in the weld joints in this material. This was done to assess the status of laser welding of this material and characterization of the laser welded joints for microstructure, residual stresses and mechanical properties.

Chapter 3 of this thesis describes the material used in this study in terms of its chemistry, starting heat treatment condition and mechanical properties. This chapter also provides a brief description of different experimental methods used in the present work, for processing (welding) and characterization of this material and the weld joints.

Chapter 4 of this thesis describes the results of the characterization of the as-received material for its dilation behaviour, microstructure, microchemistry and phase-dependent (elevated temperature) tensile behaviour.

Chapter 5 of this thesis presents the analysis of the bead on plate experiments in terms of the process parameters, depth of penetration and joining efficiency. This chapter also presents the results of detailed microstructural characterizations of the laser welded joints between 9 mm thick plates of this steel (in square butt configuration), in as-welded and also in post weld heat treated condition. In addition, the results of cross-weld microhardness hardness variation and cross-weld tensile tests are also presented and discussed in this chapter.

Chapter 6 of this thesis presents and discusses the results of residual stress measurements carried out by neutron diffraction across the laser weld joint and also through the thickness of the welded plates in 9Cr-1Mo(V, Nb) FMS.

Chapter 7 of this thesis presents the results of modelling and simulation of laser welding of 9 mm thick plates of 9Cr-1Mo(V, Nb) FMS for computation of thermal field, metallurgical phase field and stress field. Important results obtained from the computation and their implications have been presented and discussed. Comparison with the experimental results are also presented and discussed in this chapter.

In chapter 8, a brief summary of the entire work and the important conclusions drawn from the present investigation are presented. In addition, further possible extension of the present study that may be carried out in future is also discussed.

References

[1] F. Masuyama, “New developments in steels for power generation boilers”, in Advanced Heat Resistant Steels for Power Generation, R. Viswanathan and J.W. Nutting, Eds.; IOM Communications Ltd., London, (1999) 33-48.

[2] F. Masuyama, “History of power plants and progress in heat resistant steels”, ISIJ Intl. 41(6) (2001) 612–625.

[3] R. L. Klueh, “Elevated temperature ferritic and martensitic steels and their application to future nuclear reactors”, Int. Mater. Rev. 50(5) (2005) 287 - 310.

[4] K. H. Mayer and F. Masuyama, “The development of creep-resistant steels” in Creep-Resistant Steels, F. Abe, T U Kern and R. Viswanathan, Eds.; Woodhead Publishing Limited, Cambridge, UK, (2008) 15-77.

[5] B. J. Ganesh, S. Raju, A. K. Rai, E. Mohandas, M. Vijayalakshmi, K. B. S. Rao, and B. Raj, “Differential scanning calorimetry study of diffusional and martensitic phase transformations in some 9 wt% Cr low carbon ferritic steels”, Mater. Sci. and Technol. 27(2) (2011) 500-512.

[6] H. Kitahara, R. Ueji, N. Tsuji and Y. Minamino, “Crystallographic features of lath martensite in low-carbon steel”, Acta Mater. 54 (2006) 1279-1288.

[7] M. Hättestrand and H. -O. Andrén, “Evolution of particle size distribution of precipitates in 9% chromium steel using energy filtered transmission electron microscopy”, Micron, 32 (2001) 789-797.

[8] L. Korcakova, J. Hald and M. A. J. Somers, “Quantification of laves phase particle size particle size in 9CrW steel”, Mater. Charac. 47 (2001) 111-117.

[9] A. Golpayegani, H.-O. Andrén, H. Danielsen, J. Hald, “A study on Z-phase nucleation in martensitic chromium steels”, Mater. Sci. Eng. A489 (2008) 310–318.

[10] A. Aghajani, “Evolution of microstructure during long-term creep of a tempered martensite ferritic steel”, PhD Thesis, Ruhr University, Bochum, Germany (2009).

[11] S. Sulaiman, “Structure of properties of the heat affected zone of P91 creep resistant steel”, PhD Thesis, University of Wollongong, Wollongong, Australia (2007) [http://ro.uow.edu.au/theses/777].

[12] R. Mythili, P. V. Thomas, S. Saroja, M. Vijayalakshmi and V. S. Raghunathan, "Microstructural modification due to reheating in multipass manual metal arc welds of 9Cr-1Mo steel", J. Nucl. Mater. 312 (2003) 199-206.

[13] P. K. Ghosh and U. Singh, "Influence of pre- and post- weld heating on weldability of modified 9Cr-1Mo (V-Nb) steel pipe under shielded metal arc and tungsten inert gas welding process”, Sci. Technol. Weld. Join. 9 (3) (2004) 229 - 236.

[14] P. Mayr, “Weldability of Modern 9%Cr Steels for Application in USC Power Plants”, (2007), PhD Thesis, Graz University of Technology.

[15] S. Paddea, J. A. Francis, A. M. Paradowska, P. J. Bouchard and I. A. Shibli, "Residual stress distribution in a P91 steel-pipe girth weld before and after post weld heat treatment", Mater. Sci. Eng. A534 (2012) 663 - 672.

[16] S. A. David, J. A. Siefert and Z. Feng, “Welding and weldability of candidate ferritic alloys for future advanced ultrasupercritical fossil power plants”, Sci. Technol. Weld. Join. 18(8) (2013) 631 – 651.

[17] R. C. Reed and H. K. D. H. Bhadesia, “A Simple Model for Multipass Steel Welds”, Acta Metall. Mater. 42(11) (1994) 3663 - 3678.

[18] K. Laha, K. S. Chandravathi, P. Parameshwaran, K. B. S. Rao and S. L. Mannan, “Characterization of Microstructures across the Heat-Affected Zone of the Modified 9Cr-1Mo Weld Joint to Understand Its Role in Promoting Type IV Cracking", Metall. Mater. Trans. 38A (2007) 58 - 68.

[19] W. H. Lee, R. K. Shiue and C. Chen, “Mechanical properties of modified 9Cr-1Mo steel welds with notches”, Mater. Sci. Eng. A356 (2003) 153 - 161.

[20] Z. Xu, “Laser welding and post weld heat treatment of modified 9Cr-1VNb steel”, Report No. ANL/NE-12/12, Argonne National Laboratory, Chicago, Illinois (2008).

[21] B. Shanmugarajan, G. Padmanabham, H. Kumar, S. K. Albert and A. K. Bhaduri, “Autogenous laser welding investigations on modified 9Cr-1Mo (P91) steel”, Sci. Technol. Weld. Join. 16(6) (2011) 528 - 534.

[22] Y. V. Harinath, K. A. Gopal, S. Murugan and S. K. Albert, “Study on laser welding of fuel clad tubes and end plugs made of modified 9Cr-1Mo steel for metallic fuel of Fast Breeder Reactors”, J. Nucl. Mater. 435 (2013) 32 - 40.

[23] A. Cardella, E. Rigal, L. Bedel, Ph. Bucci, J. Fiek, L. Forest, L.V. Boccaccini, E. Diegele, L. Giancarli, S. Hermsmeyer, G. Janeschitz, R. Lässer, A. Li Puma, J. D. Lulewicz, A. Möslang, Y. Poitevin, E. Rabaglino, “The manufacturing technologies of the European breeding blankets”, J. Nucl. Mater. 329 - 333 (2004) 133 - 140.

[24] H. Tanigawa, T. Hirose, K. Shiba, R. Kasada, E. Wakai, H. Serizawa, Y. Kawahito, S. Jitsukawa, A. Kimura, Y. Kohno, A. Kohyama, S. Katayama, H. Mori, K. Nishimoto, R.L. Klueh, M.A. Sokolov , R.E. Stoller , S.J. Zinkle, “Technical issues of reduced activation ferritic/martensitic steels for fabrication of ITER test blanket modules”, Fus. Eng. Des. 83 (2008) 1471–1476.

[25] H. Serizawa, S. Nakamura, M. Tanaka, Y. Kawahito, H. Tanigawa, S. Katayama, "Effect of mechanical restraint on weldability of reduced activation ferritic/martensitic steel thick plates", J. Nucl. Mater. 417 (2011) 55 - 58.

[26] H. Serizawa, D. Mori, Y. Shirai, H. Ogiwara, H. Mori, "Weldability of dissimilar joint between F82H and SUS316L under fiber laser welding", Fus. Eng. Des. 88 (2013) 2466 - 2470.

[27] P. Aubert, F. Tavassoli, M. Reith, E. Diegele and Y. Poitevin, "Review of candidate welding processes of RAFM steels for ITER test blanket modules and DEMO", J. Nucl. Mater. 417 (2011) 43 - 50.

[28] ESI Group, SYSWELD, Theory Manuals, ESI France, 2012.

[29] M. Igarshi, S. Muneki and F. Abe, "Microstructure control of martensite phase matrix in advanced ferritic steels for USC boilers to achieve long term stability", in Materials for advanced power engineering – 6th Liege Conference (1998) 637-646.

[30] R. W. Hertzberg: Deformation and Fracture Mechanics of Engineering Materials, 4th ed., John Wiley and Sons Inc., 1995, pp. 62-64.

[31] A. F. Mark, J. A. Francis, H. Dai, M. Turski, P. R. Hurrell, S. K. Bate, J. R. Kornmeier, P. J. Withers, "On the evolution of local material properties and residual stress in a three-pass SA508 steel weld", Acta Mater. 60 (2012) 3268–3278.

[32] A. H. Yaghi, T. H. Hyde, A. A. Becker, J. A. Williams and W. Sun, "Residual stress simulation in welded sections of P91 pipes", J. Mater. Process. Technol. 167 (2005) 480 - 487.

[33] S. K. Bate, R. Charles and A. Warren, "Finite element analysis of a single bead-on-plate specimen using SYSWELD", Int. J. Press. Vessel. Pip. 86 (2009) 73 - 78.

[34] J. J. Xu, P. Gilles, Y. G. Duan and C. Yu, "Temperature and residual stress simulations of the NeT single-bead-on-plate specimen using SYSWELD", Int. J. Press. Vessel. Pip. 99 - 100 (2012) 51 - 60.

[35] G. A. Moraitis and G. N. Labeas, "Prediction of residual stresses and distortions due to laser beam welding of butt joints in pressure vessels", Int. J. Press. Vessel. Pip. 86 (2009) 133 - 142.

[36] N. S. Shanmugam, G. Buvanashekaran, K. Sankaranarayanasamy and S. R. Kumar, "A transient finite element simulation of the temperature and bead profiles of T-joint laser welds", Mater. Des. 31 (2010) 4528 - 4542.

[37] S. H. Kim, J. B. Kim and W. J. Lee, "Numerical prediction and neutron diffraction measurement of residual stresses for a modified 9Cr-1Mo steel weld", J. Mater. Process. Technol. 209 (2009) 3905 - 3913.

Chapter 2: Literature Review

2.1 Ferritic/martensitic Steel (FMS)

2.1.1 Historical Evolution of FMS

Electricity generation on large scale, using thermal power plants, stands as a major milestone of modern industrial civilization. This involves conversion of thermal energy into electrical energy by driving a turbine using hot and compressed steam. Efficiency of thermal to electrical conversion is very important from the considerations of energy conservation, economy of operation and environmental protection. This efficiency increases with increasing temperature and pressure of the steam driving the turbine. This provides the primary incentive for development of high temperature materials. Historically there has been significant increase in the steam temperature and pressure and associated increase in the thermal to electrical conversion efficiency in different parts of the world [1-4].

By 1920s, thermal power plants had reached the upper limits on the steam temperature (370^{o}C) and pressure (4 MPa) imposed by the available materials for construction (carbon steels) [2]. Further developments on the materials front, became essential to construct thermal power plants operating at higher steam temperatures and pressures to achieve higher thermal to electrical conversion efficiency. Different alloying additions in carbon steels like Cr, Mo, Ni, V etc. were explored, individually as well as in combinations [5]. This led to development of different low alloy Cr-Mo and Cr-Mo-V steels for thermal power plants [5]. One of the prominent Cr-Mo steels from this generation is 2.25Cr-1Mo. This is a very popular bainitic steel and is extensively used in the power plant industry even today. As a result of these developments, Mo was identified as an important alloying addition for the elevated temperature strength [5].

During the 1950s, construction of large thermal power plants for public supply, operating at temperatures in 538^{o}C to 566^{o}C called for a new set of heat resistant steels [5]. This led to the development of different grades of 9-12%Cr ferritic / martensitic steels in USA, Europe and Japan. Energy crisis of 1970s and increased concerns regarding emission of pollutants and greenhouse gases provided further thrust for development of power plants operating at still higher efficiency to minimize ecological damage. This called for targeting higher steam temperatures (600 – 650^{o}C) and pressures (up to 35 MPa). This requirement of high temperature materials and the experience with 9-12% Cr steels developed in 1950s led to further developments on materials front. These developments were undertaken under different international programmes in Europe, Japan and USA. Fig. 2.1 shows the prominent international programmes undertaken for the development of creep-resistant steels for advanced power plants [5, 6]. The developments focused on optimization in the chemistry of 9-12% Cr steels developed in 1950s for better creep rupture strength and creep life. Evolution of Cr-Mo ferritic steels through these international programmes is presented in Fig. 2.2 and chemistry and creep-rupture strength of some of the important steel grades produced under different international programmes are presented in Table 2.1 [5, 7].

Besides fossil-fuel fired power plants, developments in the nuclear energy also contributed to the development of heat resistant steels. Fast breeder reactors operate at higher temperatures and use liquid metal as coolant. In late 1970s, USA developed P91 (or mod. 9Cr1Mo steel) under its national programme for fabrication of pipes and vessel for its Liquid Metal Fast Breeder Reactor (LMFBR) [5]. This steel was developed by modifying an existing 9Cr1Mo steel (Grade P9) being used in petrochemical plants since 1950s. The modification was mainly micro-alloying with V (~0.24%) and Nb (~0.08%) and control of impurity and trace elements. This steel is tough, weldable and has high creep rupture strength (94 MPa) at 600^{o}C and 100000 hr. [5]. Since then this steel has found extensive application world over for manufacturing of pipes and forgings for new supercritical and ultra-supercritical power stations. This steel requires special precaution in welding and experience of this material in service has shown that the weld joints are susceptible to premature failure by cracking in outer HAZ region (Type IV cracking) [5, 7].

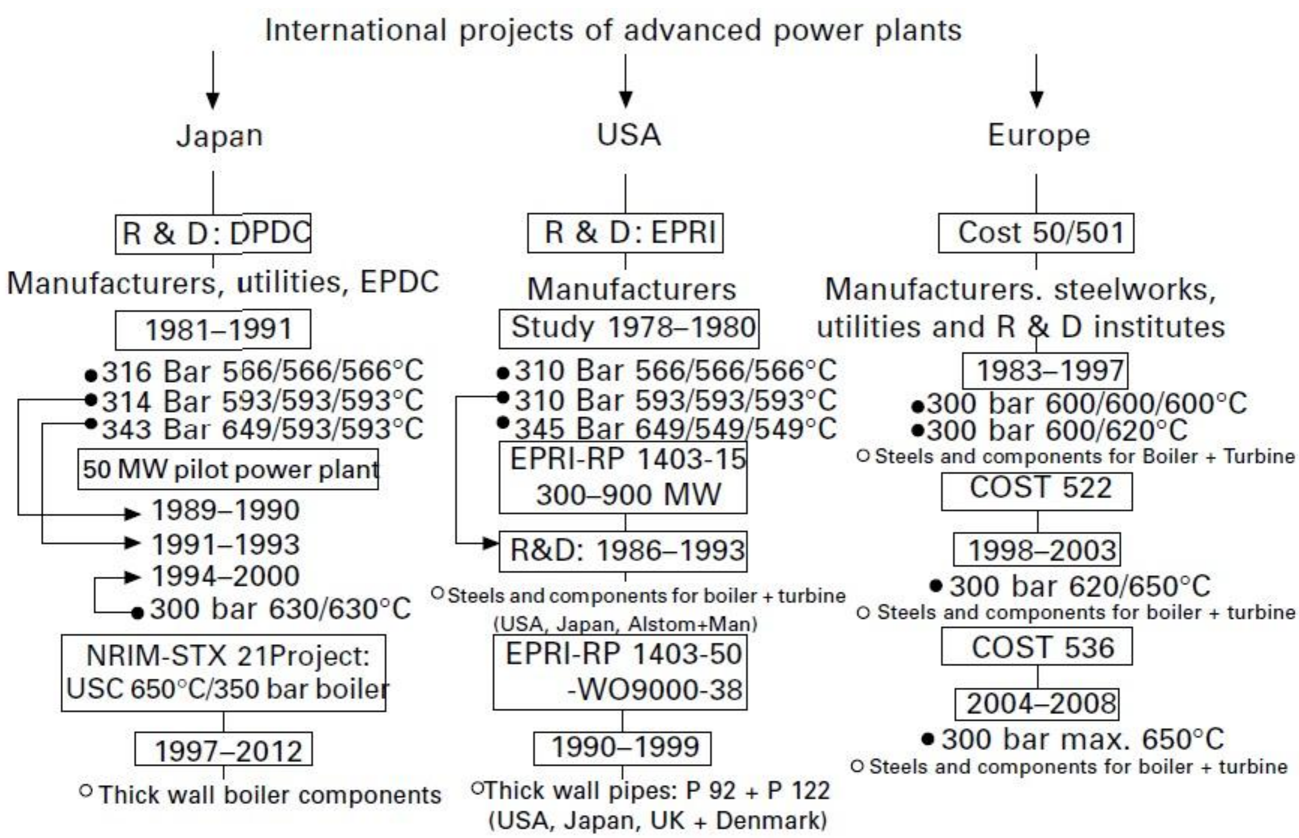

Fig. 2.1: International programmes for development of heat-resistant steels for advanced thermal power plants [5, 6].

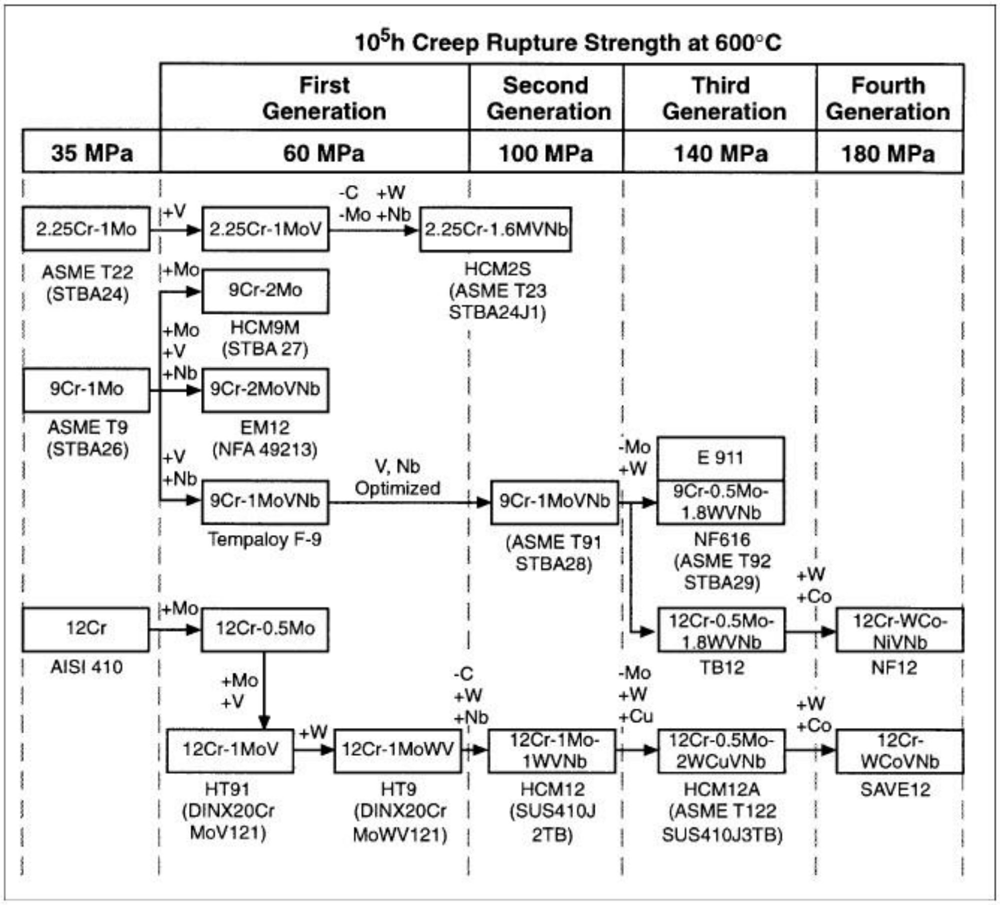

Fig. 2.2: Evolution of Cr-Mo ferritic/martensitic steels [7].

Table 2.1: Various 9-12% Cr steels developed for under different international programmes for high temperature applications [5].

Country		Steel	Chemical composition (weight%)									Rupture strength at 600°C (MPa)	
		Basic steels	C	Cr	Mo	Ni	W	V	Nb	N	B	10^4 h	10^5 h
Germany	1.	X22CrMoV 12 1	0.22	12.0	1.0	0.50	–	0.30	–	–	–	103	59
UK	2.	H46	0.16	11.5	0.65	0.70	–	0.30	0.30	0.05	–	118	62
		FV448	0.13	10.5	0.75	0.70	–	0.15	0.45	0.05	–	139	64
France	3.	56T5	0.19	11.0	0.80	0.40	–	0.20	0.45	0.05	–	144	64
Japan	4.	TAF	0.18	10.5	1.5	0.05	–	0.20	0.15	0.01	0.035	216	(150)
USA	5.	11%CrMoVNbN	0.18	10.5	1.0	0.70	–	0.20	0.08	0.06	–	165	(85)
		Advanced steels											
USA	6.	P 91	0.10	9.0	1.0	<0.40	–	0.22	0.08	0.05		124	94
Japan	7.	HCM 12	0.10	12.0	1.0		1.0	0.25	0.05	0.03			75
Japan	8.	TMK 1	0.14	10.3	1.5	0.60	–	0.17	0.05	0.04		170	90
		TMK 2	0.14	10.5	0.5	0.50	1.8	0.17	0.05	0.04		185	90
Europe	9.	X18CrMoVNbB 91	0.18	9.5	1.5	0.05	–	0.25	0.05	0.01	0.01	170	122
Europe	10.	X12CrMoWVNbN	0.12	10.3	1.0	0.80	0.80	0.18	0.05	0.06	–	165	90
		E911	0.11	9.0	0.95	0.20	1.0	0.20	0.08	0.06	–	139	98
Japan	11.	P92	0.07	9.0	0.50	0.06	1.8	0.20	0.05	0.06	0.003	153	113
Japan	12.	P122	0.10	11.0	0.40	<0.40	2.0	0.22	0.06	0.06	0.003	156	101

Endeavours to harness energy from nuclear fusion provided a fresh opportunity for developing ferritic/martensitic steels for high temperature application under high flux of high energy (14.1 MeV) neutrons with low or reduced post irradiation activity. Based on the experience with existing 9-12% Cr ferritic/martensitic steels, it was realized that these steels with suitably modified chemistry for reduced activation will serve the purpose. Mo and Nb were identified as the main alloying elements contributing to the post irradiation activity. These alloying additions were replaced with W (for Mo) and Ta (for Nb) to ensure that physical metallurgy and mechanical behaviour remained largely unaltered as a result of these changes [8]. Besides, concentration of other alloying elements like Al, Co, Cu, Mo, Ni, Nb, Ni, Sn were reduced to the highest extent possible, to minimize post irradiation activity. Concentration of non-metallic and metalloid impurities was also controlled to minimize post irradiation activity and to improve fracture toughness of the steel. Many grades of the reduced activation ferritic/martensitic steel (RAFMS) like Eurofer 97 (Europe, USA), F82H (Japan, USA), CLAM (China), In-RAFMS (India), Rusfer-EK181 (Russia) etc. were developed by modifying chemistry of 9Cr-1Mo(V, Nb) FMS [8 - 26].

2.1.2 Metallurgy of 9Cr-1Mo(V, Nb) FMS

9Cr-1Mo(V, Nb) belongs to 9-12% Cr ferritic/martensitic steel family. This is known as mod. 9Cr-1Mo steel, where mod. refers to the modifications in the chemistry of 9Cr-1Mo steel by micro alloying addition of V (~0.24%) and Nb (~0.08%). This steel is also known by different designations like P91, T91, F91 and Gr91 corresponding to its product forms pipe, tube, forging and plate respectively. It is a martensitic steel and transforms completely into martensite when cooled from austenitic phase field even at a very slow cooling rates of ~5^{o}C/min. The Ms temperature is ~400^{o}C and the martensite has lath morphology due to low carbon content. Because martensite has very high strength and very low ductility, therefore, this steel is always used in normalized and tempered (N&T) condition [2, 5]. Different metallurgical aspects like phase diagram, continuous cooling transformation curves, microstructural features and role of the alloying elements etc. are briefly discussed in the subsequent sections.

2.1.2.1 Phase Diagram

Computed phase diagram by Mayr et al. [27] and Igarshi et al. [28] for 9-12%Cr ferritic/martensitic steel are presented in Fig. 2.3 and Fig. 2.4 respectively. These diagrams can be used to understand equilibrium phase-fields and phase-transformations in 9Cr-1Mo(V, Nb) FMS. Upon heating, this steel transforms from ferrite to austenite, austenite to δ-ferrite and then δ-ferrite to liquid. The computed equilibrium transformation temperatures for 8.85% Cr are 840^{o}C (Ae_1 i. e. onset of ferrite to austenite transformation), 895^{o}C (Ae_3 i. e. completion of ferrite to austenite transformation) and 1224^{o}C (Ae_4 i. e. onset of austenite to δ-ferrite transformation) [27]. These temperatures are dependent on chemistry of the steel. Austenite stabilizers expand austenite phase field by lowering Ae_1 and Ae_3 and increasing Ae_4.

However, it is very important to realize that most of the engineering processes are far from equilibrium and therefore, kinetics of phase transformation becomes important and dictates the phase-transformation temperatures as well as the final microstructure. This is of particular importance for 9-12% Cr FMS, which shows very sluggish carbide dissolution kinetics while heating and transforms from austenite to martensite even at very slow cooling rates because of very high hardenability on account of high concentration of alloying elements [29]. Therefore, continuous heating and cooling transformation behaviour of these steels becomes important and the same is briefly discussed in the subsequent section.

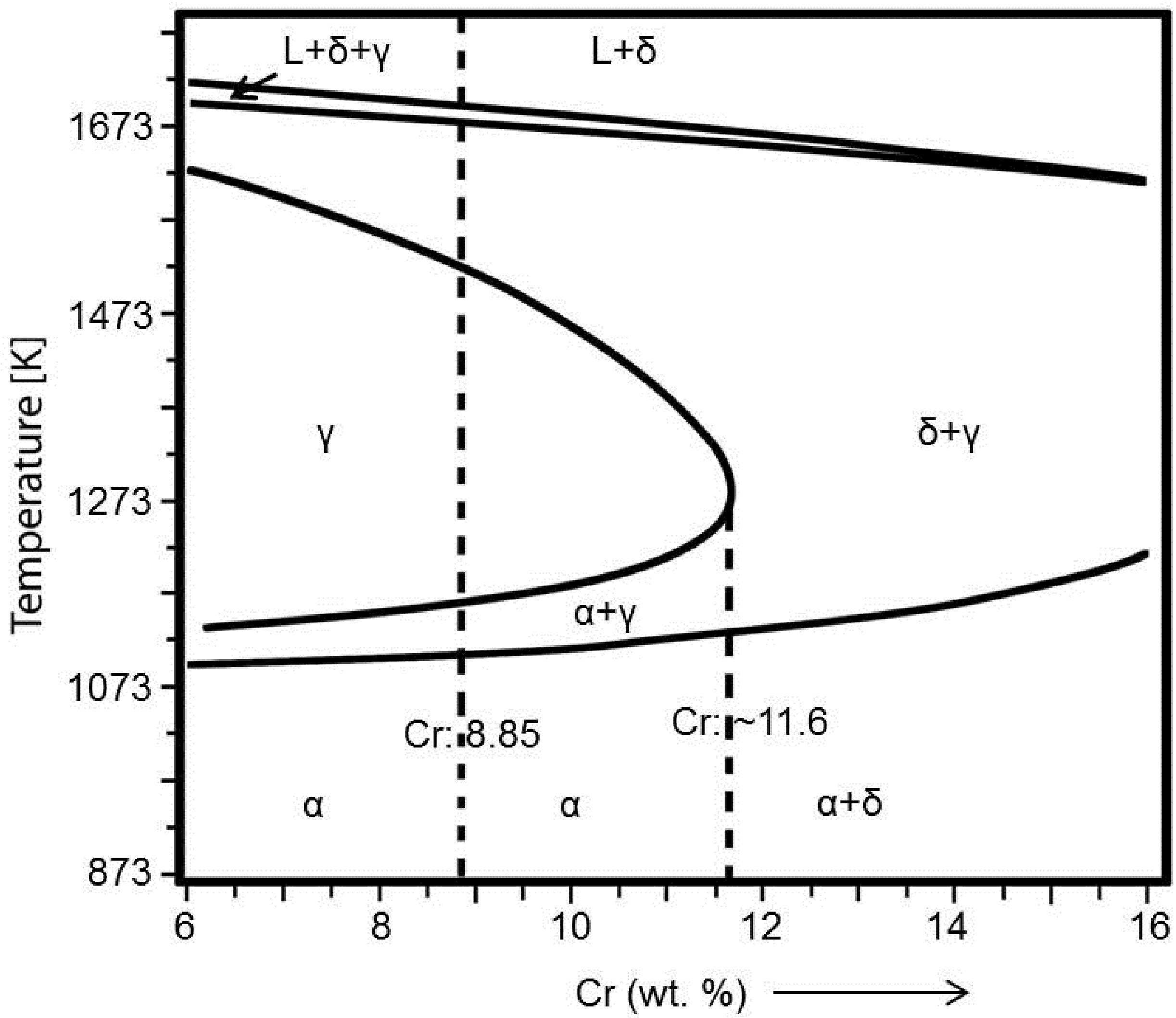

Fig. 2.3: Calculated isopleth for Cr-Mo FMS [27].

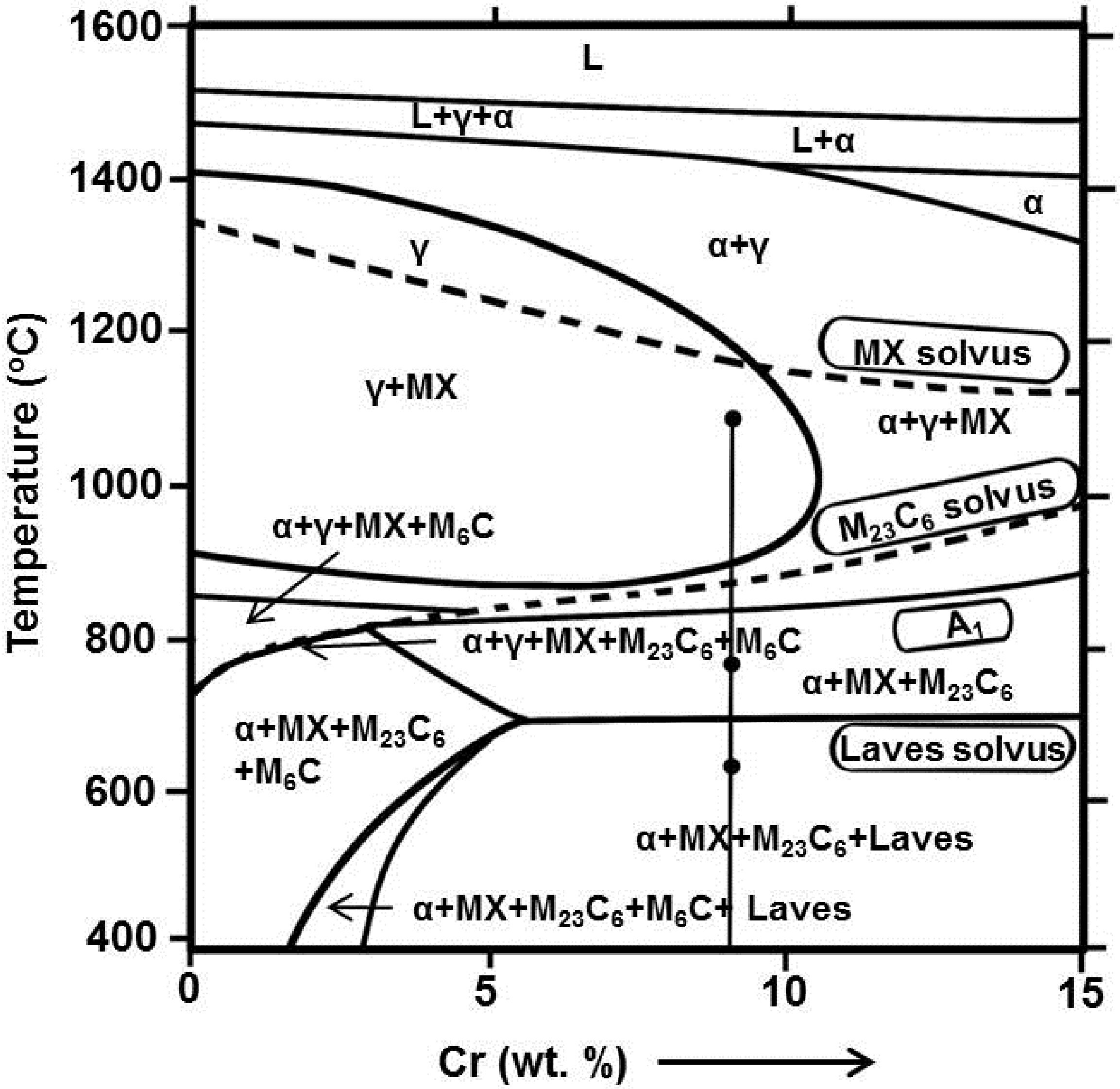

Fig. 2.4: Calculated isopleth for Cr-Mo FMS showing solvus of carbides [28].

2.1.2.2 Continuous Heating Transformation (CHT) and Continuous Cooling Transformation (CCT) Diagram

Ferrite to austenite transformation temperatures - A_1 (temperature of initiation of transformation) and A_3 (temperature of completion of transformation) can be measured experimentally while heating and cooling. Experimentally measured values differ from equilibrium transformation temperatures (Ae) due to kinetic reasons. Experimentally measured values are referred as Ac, if measured during heating and Ar, if measured during cooling. Ac is higher than Ae, which is higher than Ar as some superheating and undercooling is required to drive phase transformations during heating and cooling. Experimentally measured values of Ac_1 and Ac_3 for 9Cr-1Mo(V, Nb) FMS, measured by dilatometry, X-ray radiography and differential scanning calorimetry (DSC) have been reported in the literature [27, 29]. It has been reported that both Ac_1 as well as Ac_3 increase with increasing heating rates, however increase in Ac_3 is relatively more, as shown in Fig. 2.5, which shows a typical continuous heating transformation (CHT) diagram of P91 steel [29]. This leads to broadening of the intercritical region and has very important consequence for microstructure of the heat affected zone (HAZ) resulting from welding.

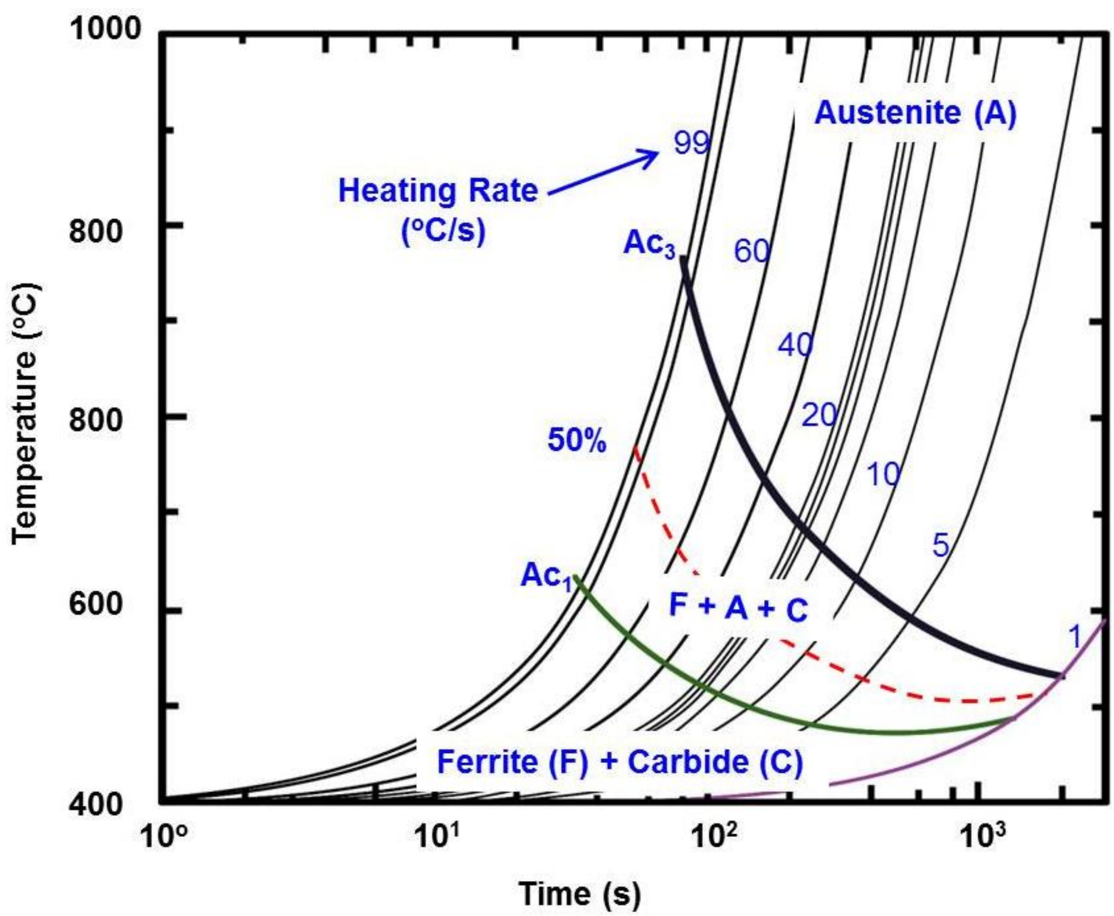

Fig. 2.5: Continuous Heating Transformation (CHT) diagram of P91 Steel [29].

The temperatures Ar_1 and Ar_3 do not have any significance for 9Cr-1Mo(V, Nb) FMS, because its austenite phase does not transform into equilibrium ferrite, rather it transforms into martensite even at very low cooling rates (~ 5^oC/min) [29]. Therefore, martensitic start and finish temperatures – M_s and M_f, are important. Continuous cooling transformation (CCT) diagram of P91 steel is presented in Fig. 2.6 [30]. From this diagram, it can be seen that austenite to equilibrium ferrite transformation curve is shifted towards far right on time axis. Even the nose of the C-curve is at more than 2 hrs. and the critical cooling rate is of the order of ~3 – 5^oC/min. This implies that for the practical cooling rates the austenite does not undergo any diffusional transformation. Besides, there is no bainitic transformation region and this means, the austenite transforms completely into martensite upon cooling. The martensite start temperature (M_s) is ~400^oC. Because of high hardenability, it is very easy to produce completely martensitic microstructure even in thick sections, without inducing distortions. This steel is normalized to produce completely martensitic structure within prior austenite grains. Normalizing is carried out by solutionizing at a temperature in the range of 1050 – 1080^oC for a time duration that depends on the section thickness. Lower normalizing temperatures and / or time results in incomplete dissolution of carbides and inhomogeneous prior austenite grain size and higher normalizing temperature leads to abnormal coarsening of prior austenite grains.

P91 steel in the normalized condition has a 3-level hierarchical microstructure within prior austenite grains, size of which depends on normalizing temperature and time. Prior austenite grains are divided into packets comprising of lath blocks, which in turn are comprised of martensite laths, the smallest microstructural entity in normalized ferritic/martensitic steel (Fig. 2.7) [31 - 34]. The martensitic transformation effectively divides a prior austenite grain in a large number of tiny crystallographic units (laths) and their aggregations (lath blocks and packets) and creates many interfaces - lath boundary, block boundary and packet boundary within it. Besides the as-transformed martensitic structure has very high density of dislocations. Martensite has high strength but poor ductility and toughness. Therefore, the normalized microstructure is tempered to improve ductility and toughness.

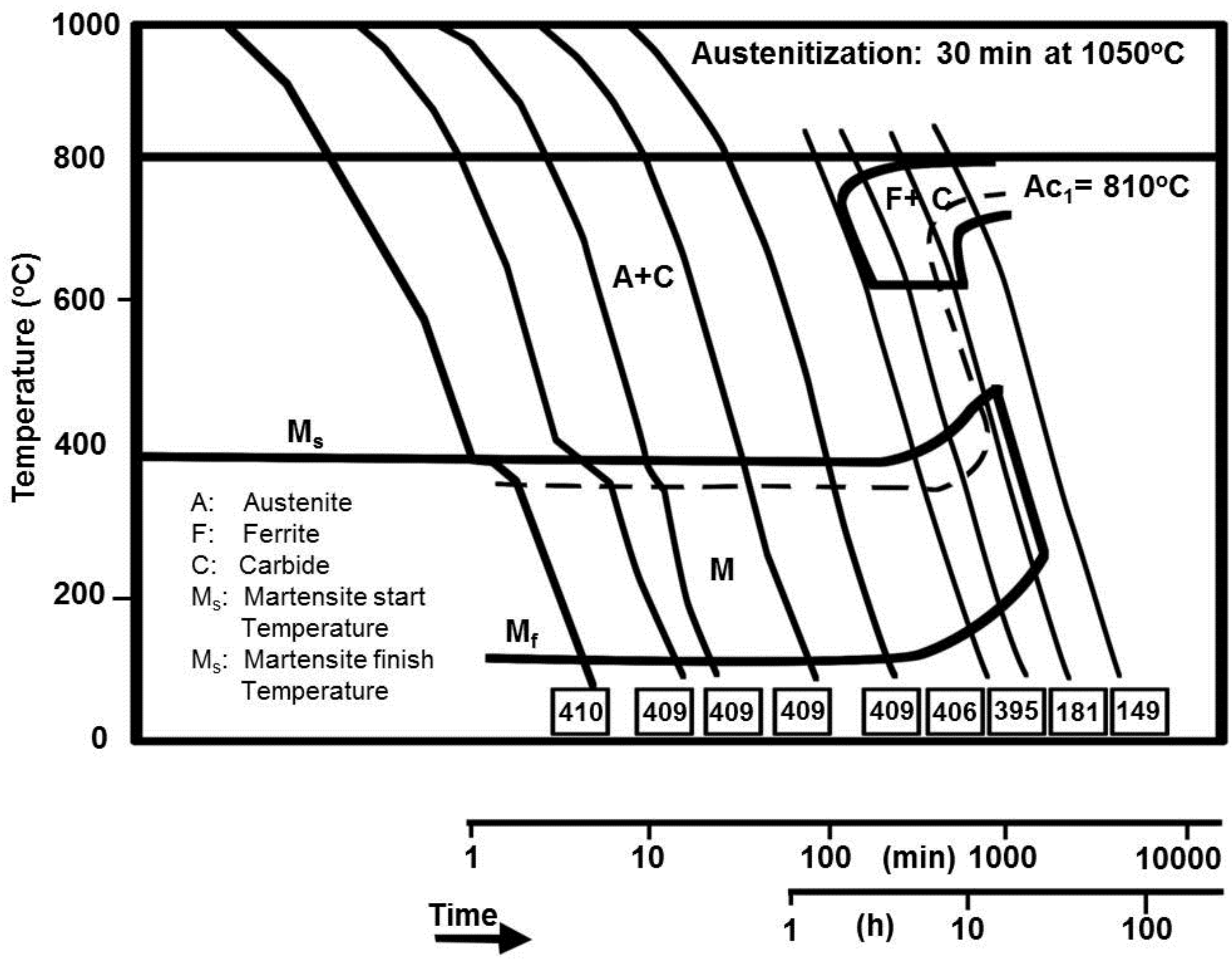

Fig. 2.6: Continuous Cooling Transformation (CCT) diagram of P91 Steel [30].

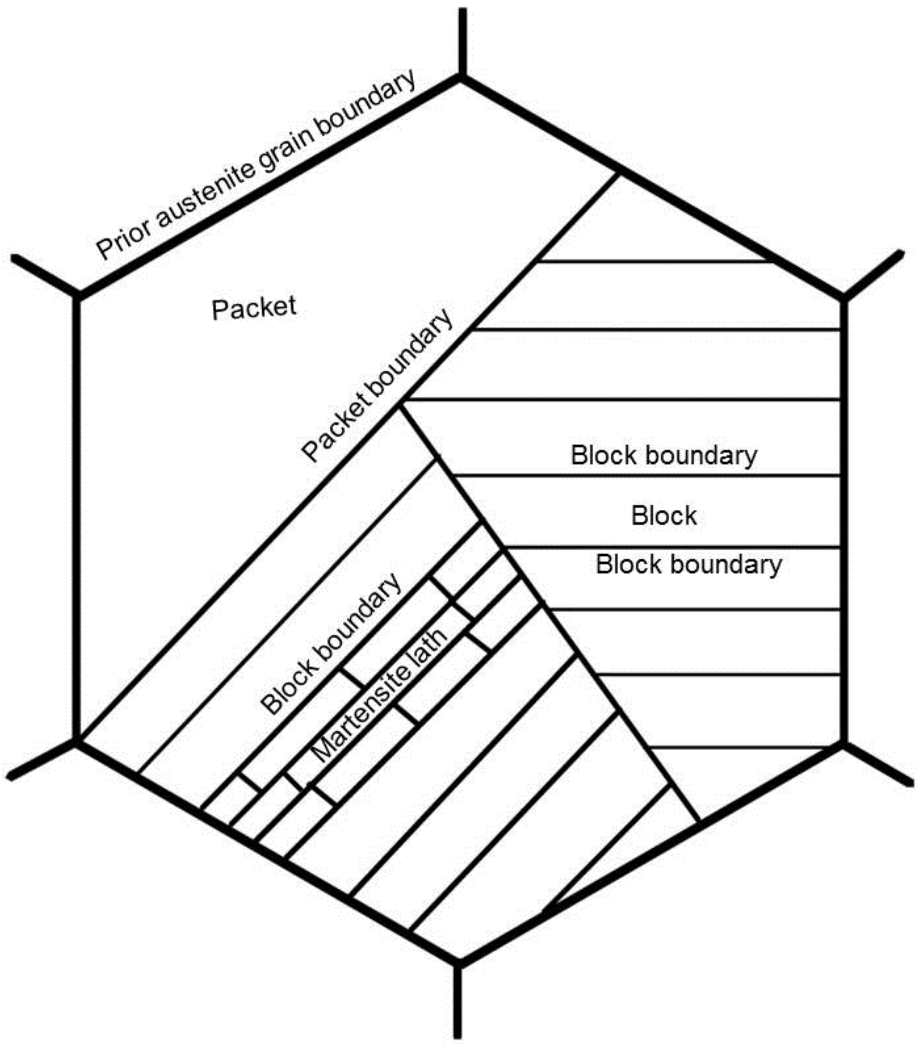

Fig. 2.7: Schematic diagram showing 3-level hierarchical microstructure in P91 steel in normalized condition [31].

2.1.2.3 Tempering of 9Cr-1Mo(V, Nb) FMS

Tempering is carried out in a temperature range of 740 – 780^{o}C for a time duration that depends on the section thickness. Lower tempering temperature is used if high strength is required and higher tempering temperature is used if higher ductility is required in the end use. If welding of the component is involved then higher tempering temperature is used. Tempering of martensitic microstructure in alloy steel proceeds in four stages and leads to important microstructural changes like decomposition of retained austenite, precipitation of different carbides, reduction and rearrangement of dislocations etc. [35]. Tempering of P91 steel in normalized condition leads to reduction in dislocation density and rearrangement of dislocations resulting in formation of elongated subgrains. Besides, there is precipitation of carbides ($M_{23}C_6$) and carbonitrides (MX) at different interfaces like prior austenite grain boundaries, packet boundaries, block boundaries and subgrain boundaries and within the subgrains, as shown in schematic microstructure of P91 steel in tempered condition (Fig. 2.8) [3, 36]. These carbides play very important role in stabilizing the microstructure at elevated temperature and contribute to high temperature strength.

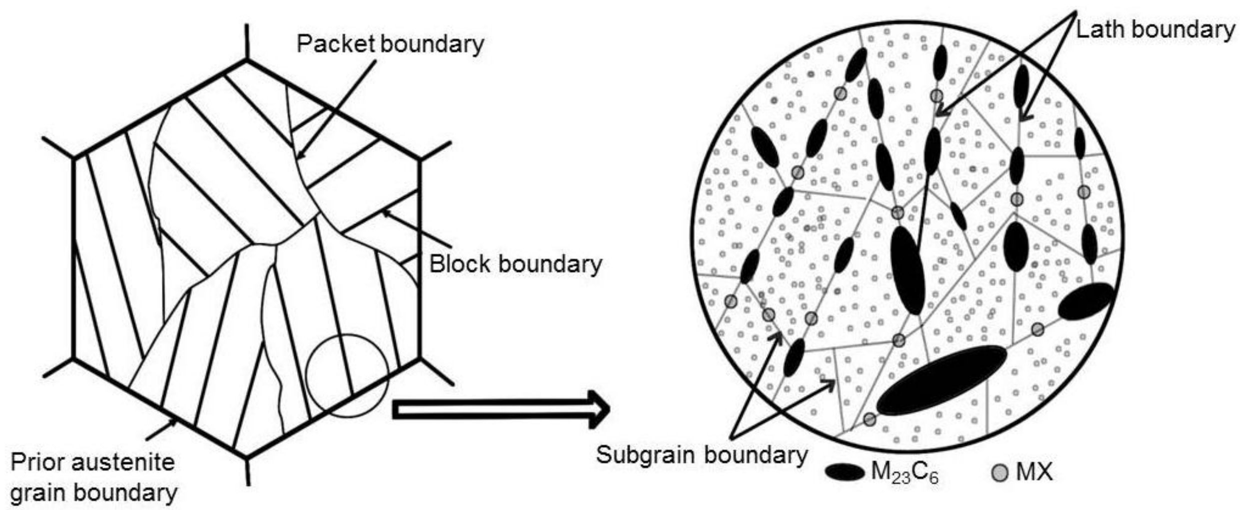

Fig. 2.8: Schematic diagram showing microstructure of tempered P91 steel [3].

2.1.2.4 Role of the Alloying Elements

Alloying elements play multiple roles in steel and many times their roles also depend on the other alloying element. Therefore, it is not very easy to describe, however some general observations can be made about the major roles played by the important alloying elements in this steel. Roles played by important alloying elements in P91 steel is briefly summarized below.

Chromium (Cr)

This is the main alloying element of P91 steel. This is a ferrite stabilizer and therefore, limits austenitic phase field. In P91 steel it improves hardenability, which is very important to obtain complete martensitic microstructure. This is a strong carbide former and forms $M_{23}C_6$ carbides, which contributes to the strength of tempered martensitic steel. These carbides also stabilize the microstructure by preventing coarsening of the subgrains. Therefore, chromium contributes to creep resistance. However at elevated temperatures these carbides coarsen, particularly in the intercritical and fine grain heat affected zones of a weld joint, and facilitate premature failure of the welded components in service [3, 4]. In addition, chromium also contributes to general corrosion resistance.

Molybdenum (Mo), Tungsten (W) and Rhenium (Re)

Mo is the 2nd most alloying addition after Cr. This is also a ferrite stabilizer. This improves hardenability and contributes to high temperature strength of P91 steel. However, it cannot be added in larger concentration as it leads to formation of δ-ferrite and laves phases. δ-ferrite reduces strength and creep-rupture strength while laves phase reduce toughness of P91. W and Re are two other alloying additions in creep resistant steels with 9-12% Cr, with similar effects on metallurgy of these steels.

Vanadium (V) and Niobium (Nb)

These are micro alloying additions in P91 steel. They are strong carbide formers and form MX type carbides and carbonitrides at the subgrain boundaries and within. These carbides are resistant to coarsening in creep condition encountered in service and contribute to high temperature strength of P91 steel. Ta and Ti also have similar characteristics as micro alloying addition in steel.

Carbon (C) and Nitrogen (N)

These are interstitial alloying additions and austenite stabilizers. They improve strength and hardenability of steel. They combine with carbide and carbonitride formers leading to formation of $M_{23}C_6$ and MX, which is critical for high temperature strength of this steel. A high N to Al ratio is also beneficial for controlling type IV cracking in the soft inter-critical HAZ (ICHAZ) of weld joints in P91 steel [37]. However, higher carbon content has adverse effect on weldability of steel.

Boron (B)

Boron improves strength and hardenability of steel. In 9-12% Cr FMS, B gets absorbed on $M_{23}C_6$ type carbides and thus retards it's coarsening under in-service creep conditions [17]. Thus type IV cracking resistance in the FGHAZ and ICHAZ region of weld joints is improved. However, B causes hot shortness and reduces fracture toughness of steel.

Manganese (Mn), Nickel (Ni), Copper (Cu) and Cobalt (Co):

These are austenite stabilizers and therefore inhibit formation of δ-ferrite. These alloying additions thus contribute to the toughness of P91 steel. However, these alloying additions also lower Ac_1 temperature. This is very important for P91 steel as tempering temperature of this steel is very close to Ac_1 temperature and one has to be careful that tempering temperature does not exceed this temperature. Besides, Mn counters deleterious effect of S by forming MnS.

Sulphur (S) and Phosphorus (P):

These are impurities and therefore, undesired. Therefore, concentration of these elements is kept as low as possible.

2.1.2.5 Microstructural Features

P91steel is used in the tempered martensitic condition. Its microstructure consists of subgrains (within prior austenite grain) formed during tempering, by rearrangement of dislocations in normalized or as-transformed lath martensitic microstructure. Besides, there are various carbides, carbonitrides and other precipitates at different interfaces like prior austenite grain boundaries, lath block and lath packet boundaries, subgrain boundaries and within the subgrains. While carbides and carbonitrides form during tempering, laves phase and Z-phase form during service. Crystallography and chemical composition of these precipitates is briefly discussed below.

$M_{23}C_6$ Precipitates

This is $Cr_{23}C_6$ with some Cr being replaced with other elements like Fe, Ni, Mo, Mn etc. This is the main precipitate in 9-12% Cr ferritic martensitic steels. These carbides form in the early stages of tempering and mainly on the various interfaces available in the microstructure. High temperature strength and creep behaviour of these steels is strongly influenced by the size, volume fraction and distribution of these carbides. This has a face centred cubic (fcc) structure with lattice parameter in 1.057 nm to 1.068 nm. Schematic crystal structure of this carbide is presented in Fig. 2.9 [4].

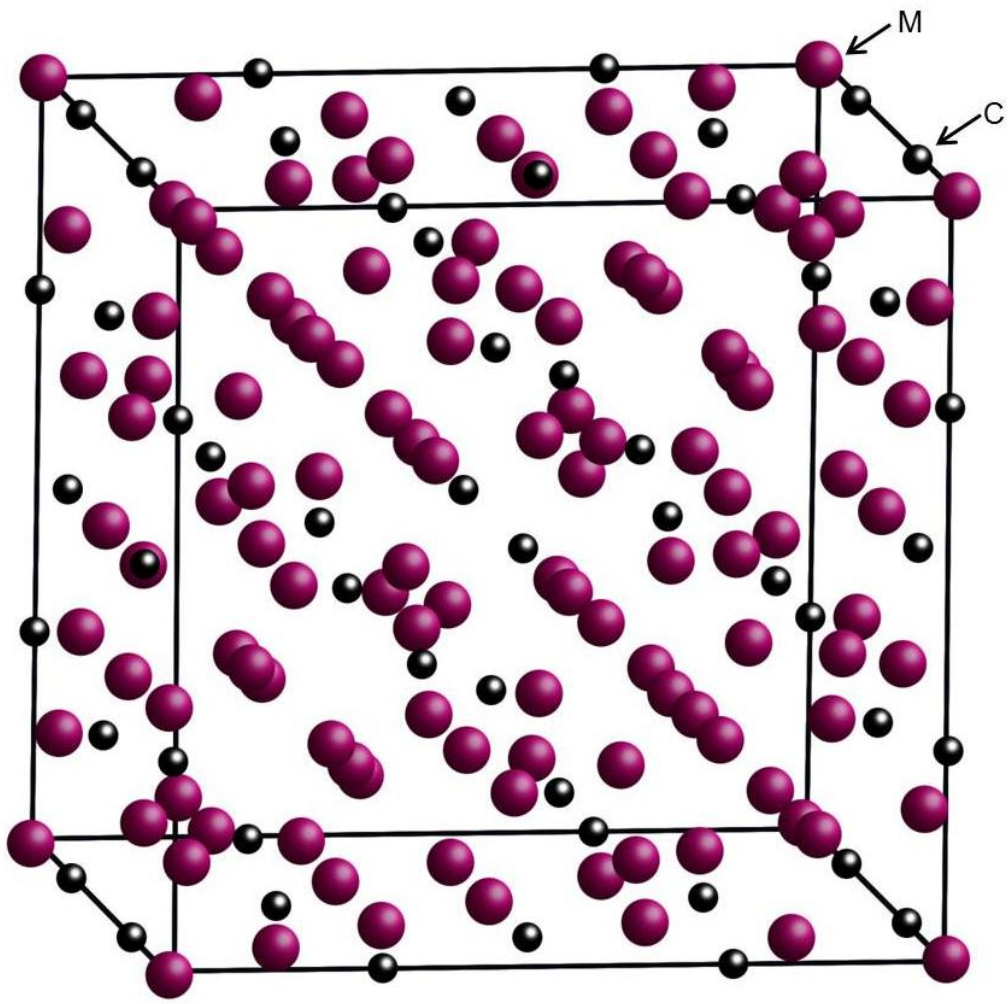

Fig. 2.9: Schematic crystal structure of $M_{23}C_6$ carbide, M is Cr (Fe, Ni, Mo, Mn) [4].

These carbides ($M_{23}C_6$) coarsen during service under creep condition. Larger particles grow in size while the smaller ones dissolve, leading to reduction in number of carbide particles. Coarsening of these particles gets accelerated under creep condition at 600^oC [38 - 40]. Coarsening of $M_{23}C_6$ carbides is the life limiting factor for P91 steel and leads to premature failure through type IV cracking in the ICHAZ and FGHAZ region of weld joint. Boron in very small quantity is beneficial in controlling coarsening rate of these carbide particles [41 - 44]. Boron replaces some of the carbon in $M_{23}C_6$ making it $M_{23}(CB)_6$.

MX Precipitates

MX is a generic term representing carbonitrides of strong carbide/nitride formers like Ti, V, Nb, Zr, Ta etc. present in steel as micro-alloying additions. In P91 steel, mainly carbonitrides of V and Nb form on tempering. MX carbonitrides have NaCl type fcc structure (Fig. 2.10) [4]. Normally solid solution of the carbonitrides is observed and not the pure carbide or nitride and therefore, the experimentally measured lattice parameters differ slightly from that of the pure carbide/nitride. MX carbonitrides normally form on dislocations, staking faults, lath block and packet boundaries and prior austenite grain boundaries. These particles coarsen at very negligible rate and increase creep resistance by pinning down the dislocations [45 - 50].

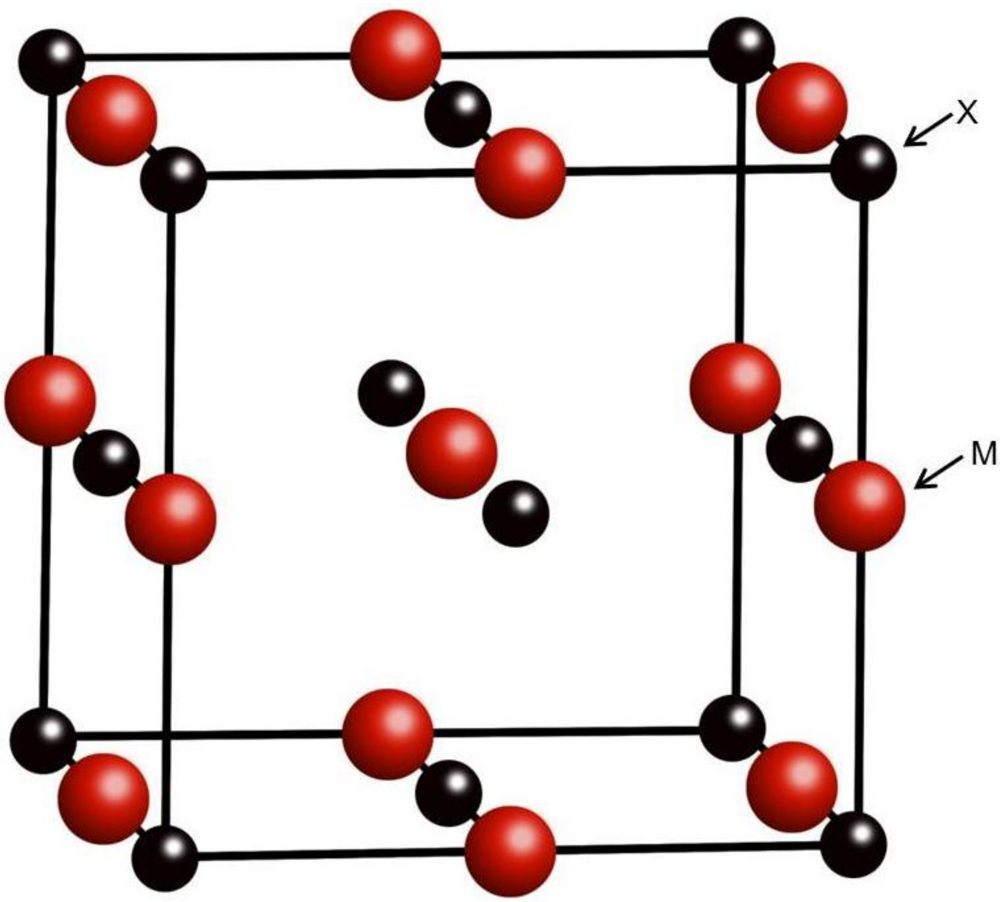

Fig. 2.10: Schematic crystal structure of MX carbonitride, M is Nb, Ta, Ti, Zr, V [4]

Laves Phase

It has a generic formula (Fe, Cr)$_2$(Mo, W). It has hexagonal structure (Fig. 2.11). These can be made to form during tempering by increasing Mo or W content. Presence of Si and Cu accelerates formation of Laves phase [51]. It forms along prior austenite grain boundaries during long term exposure to high temperatures (550^{o}C or higher) after ~10,000 hrs. and decreases fracture toughness of P91 steel [52 - 55].

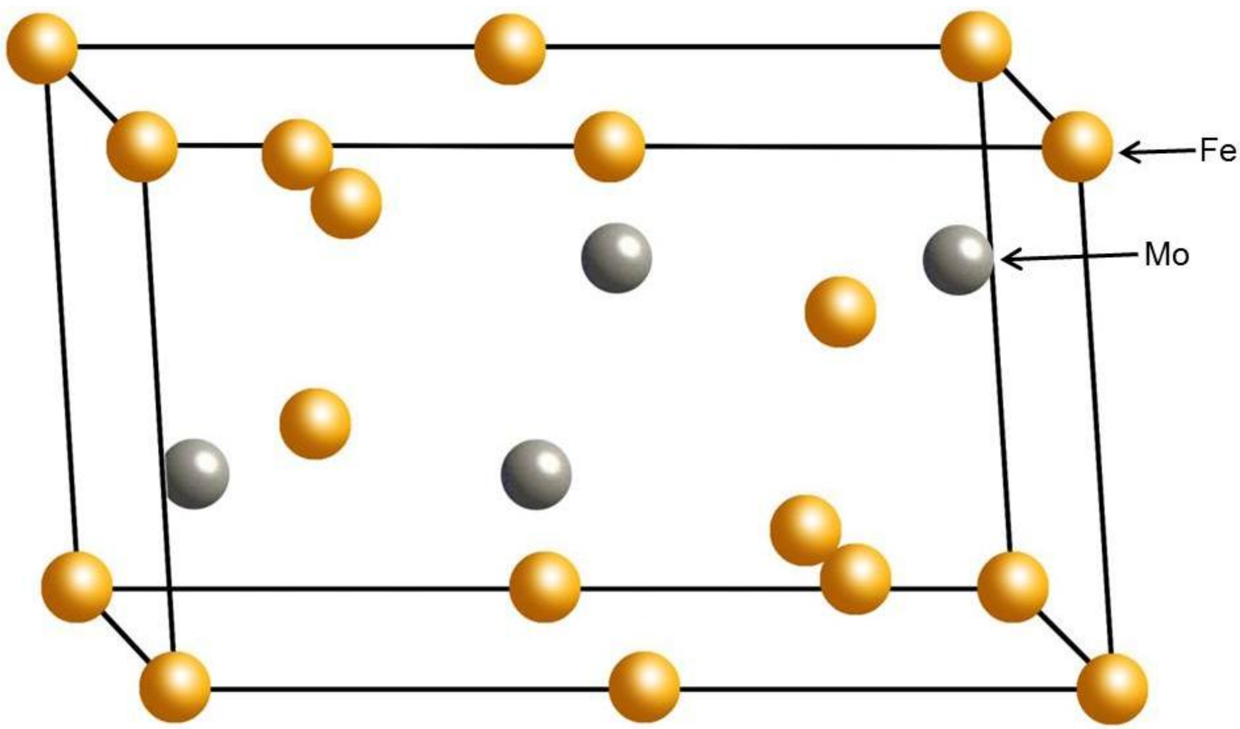

Fig. 2.11: Schematic crystal structure of laves phase (Fe_2Mo) [4].

Z-Phase

It is the equilibrium nitride in 9-12 Cr ferritic/martensitic steels. It is a complex nitride of Cr(V, Nb)N form and has tetragonal lattice (Fig. 2.12) [56, 57]. It forms during service at the expense of beneficial MX type carbonitride and leads to reduction in the creep rupture strength of 9-12 Cr ferritic/martensitic steels [58, 59].

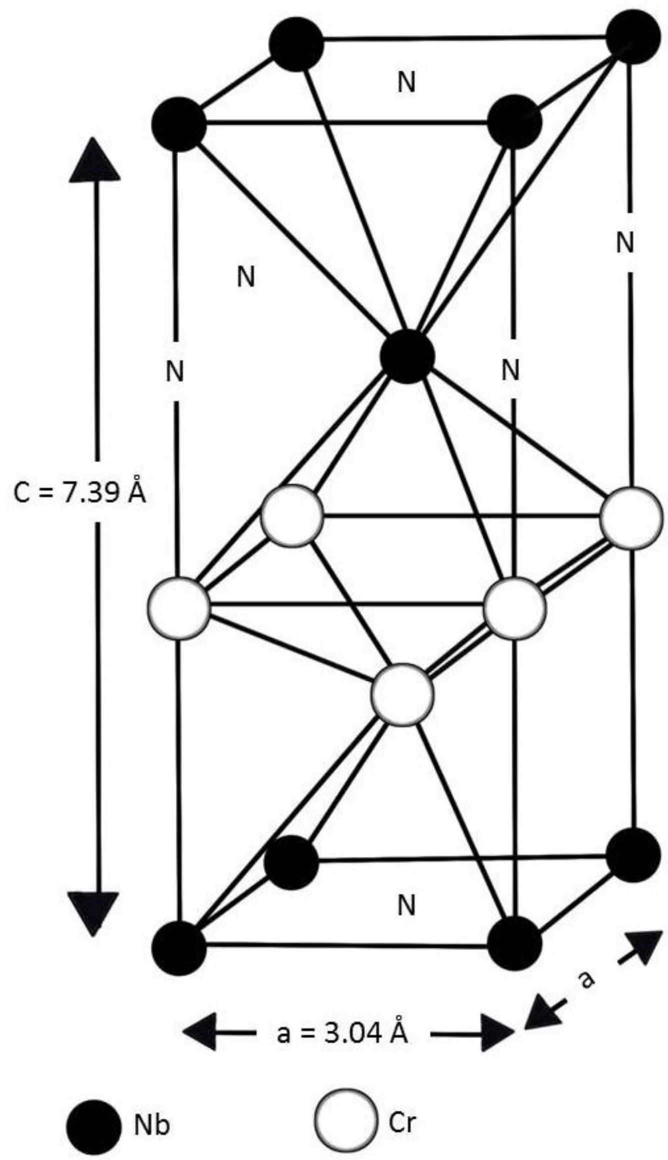

Fig. 2.12: Schematic crystal structure of Z-phase [56].

2.2 Welding Processes for Joining 9Cr-1Mo(V, Nb) FMS

Ferritic/martensitic steels are joined by different welding processes for making components and assemblies for a variety of engineering applications in thermal power plants as well as well as in nuclear reactors. Welding of 9Cr-1Mo(V, Nb) FMS requires special care because of its high hardenability. Different conventional arc welding processes like Manual Metal Arc Welding (MMAW), Gas Tungsten Arc Welding (GTAW) etc. are widely used for joining of 9Cr-1Mo(V, Nb) FMS [37, 60 - 77]. Advance welding processes like uniaxial diffusion welding and hot isostatic pressing (HIPing), electron beam welding, laser welding, laser-arc hybrid welding etc. are also being actively explored for joining of this steel and RAFMS for fabrication of different components of the TBM for ITER [78 - 94]. A brief description of the different joining processes used for joining this steel is presented in the subsequent sections and the detailed description of these welding processes can be found in the standard textbooks on welding [60 - 61].

2.2.1 Conventional Welding Processes

Conventional arc welding refer to a group of welding processes, in which thermal energy required for fusing the work piece and / or the weld metal is produced by striking an electrical arc between the work piece and an electrode. The electrode can be either consumable, forming the weld metal by itself or non-consumable, requiring a separate filler wire to form the weld metal. The power density of the arc is of the order of 1 kW/cm^2 and therefore, this can deposit energy on the surface of the work piece and cannot penetrate deep inside. Therefore, making a suitable joint (U-groove, V-groove etc.) and filling it with weld metal becomes necessary for joining of thick components using conventional arc welding processes. Some prominent arc welding processes used for joining of 9Cr-1Mo(V, Nb) FMS are Manual or Shielded Metal Arc Welding (MMAW/SMAW), Gas Tungsten Arc Welding (GTAW), Gas Metal Arc Welding (GMAW), Flux Cored Arc Welding (FCAW), Submerged Arc Welding (SAW) etc. Different conventional welding processes used for joining of this steel is briefly discussed below.

2.2.1.1 Manual Metal Arc Welding (MMAW)

Manual Metal Arc Welding (MMAW), also known as Shielded Metal Arc Welding (SMAW) is the most common welding method employed for joining of different metals across a wide spectrum of applications [60 - 61]. Substantial literature exists on welding of 9Cr-1Mo(V, Nb) by MMAW [62 – 67]. In this method a consumable electrode, covered with flux and other desirable additives, is used to strike arc between itself and the parts to be welded. The electrode melts with the heat generated by the arc and gets deposited in the joint (U-, V-, J- groove) and solidifies with slag cover over it, protecting the weld metal from getting oxidized. The entire joint is filled with the weld metal in multiple passes. This is a simple welding process and is used extensively on the shop floor as well as in the fields for fabrication as well as repair. However, this is a slow and high heat input welding process. Being a manual welding process, joint quality depends on the welder, who must be skilled and qualified as per the suitable code in force. Slag inclusions leading to loss of fracture toughness is an important issue with the weld joints made by using this process.

2.2.1.2 Gas Tungsten Arc Welding (GTAW)

This is also a simple welding process like MMAW. In this process, a non-consumable electrode made of tungsten is used to strike arc between itself and the parts to be welded. Heat produced by the arc, melts the parts to be joined and the filler rod, which fuse together to form the weld joint. A shielding gas (Ar, He etc.) is used to protect the hot and molten metal from oxidizing. Sometimes, active gases like CO_2, O_2 etc. are also mixed, in very small quantity, in the shielding gas to modify melt pool convection from diverging to converging. Thin components can be welded without using any filler metal.

The welding process can be manual as well as semi-automatic. The resulting weld joint is clean as there is no slag inclusion. However, sometimes W particle inclusions are observed. This process is extensively used for welding of 9Cr-1Mo(V, Nb) FMS [67 – 72]. Weld joints produced by GTAW are very clean as no slag is involved. Therefore, GTAW process is generally used to make high quality weld joints and for the root passes of a thick weld joint [66, 70].

There have been many improvisations in GTAW process aimed at controlling the heat input to the weld joints leading to many variants of this process. One important variant of this process is 'Activated Tungsten Inert Gas' (A-TIG) process [72]. In this process, a thin coating is applied on the work piece to be joined. This thin coating confines the arc in the vicinity of the weld seam, leading to very high energy density and also promotes converging flow of the melt in the fusion zone. The net result is deeper penetration and joints up to 6 mm thickness can be made without the need of any filler metal. However, inclusions resulting from the thin flux layer may have an adverse impact on the fracture toughness of the weld joint.

Another important variant of this process is Narrow Gap TIG or NG-TIG [70 - 71]. When very thick plates are to be welded, then conventional joint designs call for huge amount of weld metal deposition. This will require huge amount of costly filler metal, very slow welding process, very high heat input, unacceptable level of distortion etc. Therefore, narrow gap concept was developed. This concept is not exclusive to only GTAW process; rather it is utilized with other welding processes like GMAW, SAW and Laser-Arc hybrid welding processes as well. The groove angle is kept small (~ 2^{o} – 5^{o}) leading to a very high aspect ratio of the fusion zone. Welding is carried out in automatic mode with welding machine, welding torch and the welding process designed to ensure proper access in the narrow groove. Welding is carried out in multiple passes. Further variation in NG-TIG has been Hot Wire NG-TIG, in which the filler wire is heated by ‘joule heating’ before it is melted by the arc produced by the electrode [70 - 71].

2.2.1.3 Gas Metal Arc Welding (GMAW)

This is an automatic welding process. In this process, an arc is struck between a consumable filler wire, which is continuously fed through a spool, and the parts being welded. A shielding gas (Ar or He) is used to protect the hot and molten metal. In case of ferrous metal welding, active gases like CO_2 or O_2 in small quantities, is mixed with Ar to avoid under cutting. GMAW is carried out in reverse polarity i.e. Direct Current Electrode Positive (DCEP) to ensure higher deposition rate of weld metal and smooth metal transfer. Like GTAW process, GMAW also gives a very clean weld. However, weld metal deposition rate is much higher in GMAW process and therefore, thick joints can be produced at much higher welding speed. The skill to maintain a short and stable arc, as in case of GTAW process, is not required in case of GMAW process. However, the GMAW gun is bulky and therefore, joint accessibility can be an issue in many situations. GMAW process is also used in Narrow Gap mode for joining of thick plates.

A similar welding process is FCAW process, in which flux forms the core of the consumable wire electrode, being continuously fed into the weld pool. The flux forms slag and protects the molten metal in the fusion zone. FCAW process has been reported for welding of 9Cr-1Mo(V, Nb) FMS [73 – 74].

2.2.1.4 Submerged Arc Welding (SAW)

This welding process is used for joining of very thick sections. Arc is struck between a consumable electrode and the sections to be welded. The arc is covered within the granular flux, which is fed continuously through a hopper, and the slag. Very high current is used and the melt deposition rate is very high. However, there is no melt splatter, as the arc is submerged within the flux. The resulting weld metal is clean, as the melt is protected and refined by the flux and the slag. SAW process is also used in Narrow Gap mode for joining of thick plates. This method is used for joining of thick section of 9Cr-1Mo(V, Nb) FMS [75].

2.2.2 Advance Welding Processes

Advance welding processes for 9Cr-1Mo(V, Nb) FMS include Uniaxial Diffusion Welding (UDW), Electron Beam Welding (EBW), Laser Welding and Laser-Arc Hybrid Welding. These advanced welding processes for this steel has drawn considerable interest in recent times for fabrication of the challenging components for fusion reactor applications. In diffusion welding and HIPing welding is performed in the solid state; while a beam of high power density is used to fuse a very narrow zone of the material along the weld seam in case of beam welding processes. A brief description of these welding processes is presented in the following sections.

2.2.2.1 Diffusion Welding and Hot Isostatic Pressing (HIPing)

This is a solid state joining process, which employs a combination of temperature and pressure to form a weld joint across a clean interface. When clean surfaces are brought into intimate contact (by application of pressure), atomic bonds form and the interface gets annihilated by diffusion of atoms. Minimization of the surface energy and/or chemical potential energy is the main driving force for diffusion bonding. Application of temperature helps the bonding process by enhancing the rate of diffusion. This method is employed to produce weld joints between the materials, which are difficult to weld by fusion welding processes. Hot Isostatic Pressing (HIPing) is a three dimensional variant of diffusion bonding, which is used for densification of powder metallurgy products, cast products and fabrication of components with intricate design. Diffusion bonding and HIPing of RAFMS has evinced considerable interest for fabrication of components with intricate cooling channels like the first wall and cooling plates of the Test Blanket Module (TBM) for ITER [78 – 82].

Extensive work has been done by different countries participating in ITER for process parameter optimization (surface finish, temperature and pressure) for diffusion bonding and HIPing of RAFMS [78 – 82]. Diffusion bonding takes place in austenitic phase-field with growth of the austenite grains across the interface being the underlying mechanism. Because appreciable grain growth in this steel occurs at ~ 1100^{o}C, therefore diffusion bonding or HIPing is carried out at 1100/1150^{o}C. In addition a pressure of 150 MPa is also applied to ensure intimate contact at the interface [78 – 82]. An elaborate procedure is required for preparing the assembly for HIPing. It has to be ensured that the interfaces have been sufficiently degassed before closing the assembly for formation of a good joint. The advantage of diffusion bonding or HIPing is uniform microstructure and therefore, properties, across the joint, unlike the fusion welded components which have graded microstructure across the joint. However, the joint is planer and therefore, the discontinuities are arranged in a plane forming a wall and this leads to significant drop in the Charpy impact energy of the joint [80]. Besides, this joining process requires a huge and costly dedicated facility, a HIPing machine. Also, this method is not amenable for making many joints configurations while fabricating a component.

2.2.2.2 Electron Beam Welding (EBW)

In this process a focused beam of electrons (beam current ~ 50 – 1000 mA) accelerated to very high voltage (~ 30 – 175 kV) is used as the heat source [60]. Diameter of the focussed beam on the work piece is ~ 0.5 mm; leading to very high power density (a few MW/cm^2) of the incident beam. This power density is sufficient to instantly vaporize the material in the line of sight of the beam. A metal vapour filled hole (termed as keyhole) surrounded by the melt, is thus created in the work piece. Electron beam propagates through this keyhole and melts and vaporizes the metal deep inside [60]. The keyhole is moved along the welding seam by translating / rotating the parts being welded. As the keyhole moves ahead, melt from its front wall is pushed towards its rear wall and fills the hole.

Due to very high beam power and power density very thick weld joints – up to 200 mm in steel and even more in aluminium, can be made using EBW process, in single pass, without using any filler rod. High quality weld joints with very high depth to width aspect ratio of the fusion zone are produced and the joint distortion is negligible due to low heat input associated with this process. Due to these reasons, EBW finds extensive application in fabricating critical and strategic components. However, this welding can be carried out in vacuum only and therefore, size of the component that can be welded and manoeuvrability of the component during welding is restricted by the size of the vacuum chamber. Vacuum less EBW processes have also been developed, which extend the range of applications of this process. Harmful radiations like X-rays are also produced during welding, due to high kV electron beam and therefore, necessary protection for the operator is essential. While joining magnetic materials like ferritic steel, the material must be demagnetized to avoid uncontrolled and unpredictable deflection of the beam. As the beam diameter is very small, the joint fit up should be very good and sufficient care is required to ensure that the beam does not miss the joint line during welding process. Recently, there has been considerable interest in EB welding of 9Cr FMS, driven mainly by the TBM fabrication activities [83, 90 - 92]. This is because, fabrication of TBM requires welding of very thick back and or side plates (thickness in 45 – 90 mm range) with the first wall and distortion allowance in very strict so conventional welding processes cannot be used.

2.2.2.3 Laser Welding

In this process, a focused laser beam is used as the heat source to weld metallic materials. Laser welding has been extensively discussed by Steen el al [84]. Laser beam is a beam of monochromatic and coherent photons, produced in a lasing media by stimulated emission and conditioned in a suitably designed design cavity. Due to its coherent and monochromatic characteristics, a laser beam can be focused to very fine diameters. While lasers are used for a wide range of applications, a laser used for welding applications has typically a few kW of beam power and the focused beam diameter is typically ~ 0.5 mm, leading to very high power density (a few MW/cm^2), comparable to that achieved in case of electron beam welding. Therefore, welding is generally performed in keyhole mode. However, for thin sections, lower power density can be achieved by decreasing the beam power and / or increasing the beam diameter and welding can be performed in conduction mode, as well.

Different lasers used for welding are – CO_2 Laser, Nd-YAG Laser, Disk Laser, Fiber Laser and High Power Diode Laser (HPDL). Besides CO_2 laser, which is a gas laser and lases at 10.6 μm; all the other lasers are solid state lasers and lase at a wavelength ~ 1 μm. CO_2 laser was the first laser to provide multi kW laser beams and has been the main workhorse of laser welding for many decades. There have been significant developments in high power solid state lasers during past 10 – 15 years in terms of beam power and beam quality. Nd-YAG laser was the most important solid laser, however, its beam power is limited to ~ 4 – 5 kW and this laser is getting obsolete now. High power diode lasers offer laser beam in 8 – 10 kW power range, however, beam quality is not very good and therefore, these lasers are not suitable for producing a deep and narrow fusion zone. Disk laser offers beam power more than 16 kW and fiber laser in excess of 20 kW. Beam quality of these lasers is excellent and these lasers are capable of producing a deep and narrow fusion zone. However, these lasers are relatively new and significant amount of research is required before, they can compete with CO_2 laser in terms of welding applications. However, due to lower wavelength, solid state lasers have a clear advantage over CO_2 laser for welding of metals with high reflectivity like Cu, Mo, and Nb – alloys.

Compared to electron beam welding, laser welding can be carried out in open air with shielding gas and the welding head itself can be maneuverered using a CNC / robot. These features make laser welding very flexible and versatile and therefore, weld joints can be made in different configurations and positions, with ease. Due to these benefits, industrial application of laser welding is expanding rapidly. Recently, the interest in laser welding of 9Cr FMS has increased considerably due to its suitability for making challenging joints required for TBM fabrication [85 – 94].

2.2.2.4 Laser-Arc Hybrid Welding

Laser-Arc welding combines laser welding with arc welding (TIG or GMAW). This combination harnesses synergy of the two heat sources. A narrow laser beam serves to achieve deep penetration, while a wide arc ensures that the joint gap is bridged, without fail. Further, preheating of the work piece by the arc, improves coupling of the laser beam energy and the metallic vapours produced by the laser beam provide a conducting path, thus restricting spread of the arc. Due to these benefits laser-arc hybrid welding is finding increasing application, particularly in joining of thick sections. The benefit is that high quality weld joints can be produced in thick sections with very narrow gap, and therefore less weld metal and heat input are required. In these joints, a deep root pass is produced by high power laser beam, followed by weld metal deposition in a narrow V-joint with Laser-GMAW hybrid welding process. Laser-Arc hybrid welding of 9Cr RAFMS has been identified as a potential joining method for TBM fabrication [89].

2.2.3 Welding of 9Cr-1Mo(V, Nb) FMS

Ferritic/Martensitic steels including 9Cr-1Mo(V, Nb) steels are welded by different welding processes like SMAW, GTAW, Flux Cored Arc Welding (FCAW), GMAW and SAW or a combination of these processes [62 - 77]. Laha et al. [63] have reported a detailed microstructural and creep study on weld joints in modified 9Cr-1Mo steel and also on simulated HAZ specimens. These weld joints were made between 12 mm thick plates of modified 9Cr-1Mo steel by SMAW process. The study focussed on the microstructural variation across the HAZ and its role on intercritical softening and loss of creep rupture strength by Type – IV cracking. It was reported that the soft region in the weld joint correspond to the intercritical HAZ. The soft intercritical region sandwiched between hard regions (parent and the weldment) creates stress triaxiality, which in-turn facilitates localization of the creep deformation in this region and failure of the weld joint by Type – IV cracking. Reduction in the strength in the intercritical region was attributed to the combined effects of coarsening of dislocation substructures and precipitates. However, they have not suspected and interrogated the effect of low austenitization temperature, which is present in the intercritical HAZ, on transformation behaviour of austenite while cooling and its role in intercritical softening.

Mythili et al. [64] have reported microstructural modification due to reheating in multipass manual metal arc welds of 9Cr–1Mo steel. Presence of a repetitive microstructure consisting of columnar grain, coarse grained austenite, fine grained austenite and unaffected structure within the weld zone was reported in this study, confirming a significant modification of microstructure due to multiple passes. Significant coarsening of laths, decrease in defect density and extensive precipitation with Cr enrichment in the carbides along the weld centre line from top to root was also reported in this study. The microstructural variations caused by the multiple passes showed a good correlation with the variation in the lattice strain indicated by FWHM of the X-ray diffraction peaks. They have also reported extensive tempering of the primary solidification structure as the root is approached. Therefore, it can be concluded that multiple passes associated with arc welding introduces considerable heterogeneity in the fusion zone microstructure.

Shiue et al. [65] have reported effect of tempering temperature on fracture toughness and stability of retained austenite in the weld joints in modified 9Cr-1Mo FMS. The welds were made by multipass arc welding (GTAW for root pass and MMAW for filling passes) between 6.4 mm thick plates. The fusion zone produced by MMAW showed showed profound slag inclusions. Significant drop in the fracture toughness and increase in the hardness for the weld joints tempered in 450 – 610 ^{o}C temperature range with lowest fracture toughness for the welds tempered at 540 ^{o}C was reported in this study. However, there was significant improvement in the fracture toughness for the tempering temperatures higher than 680 ^{o}C. It was also reported that for tempering temperatures in 450 – 610 ^{o}C range, the retained austenite in the welds, transformed into untempered martensite and this could be the reason for loss of toughness of the welds tempered in this temperature range. However, acceptable fracture toughness and hardness was obtained for the welds tempered at 750 ^{o}C for 1 hour and these welds fractured in ductile manner with dimpled fracture surface.

Arivazhagan et al. [66] have reported the effect of surface remelting using TIG arc on the toughness of MMAW welds in P91 steel. MMAW process was reported to introduce profound micro inclusions in the weld metal which has adverse effect on fracture toughness of these weld joints. It was reported that surface remelting of the MMAW welds by TIG arc resulted in refinement of the coarse (> 5 μm) inclusions and improvements in the fracture toughness of the weld joints from 40 J for MMAW welds to 72 J for the TIG arc remelted MMAW welds.

Ghosh et al. [67] have reported influence of pre- and post-weld heat treatment temperatures on weldability of modified 9Cr-1Mo(V-Nb) steel pipe, produced using SMAW and TIG welding. In this study, the preheating temperatures and PWHT temperatures were respectively varied in 200 – 300 ^oC and 650 – 850 ^oC range. They have not explained the use of a PWHT temperature of 850 ^oC, much higher than the code specified values (730 – 780 ^oC range) and also, where this PWHT temperature stands in relation to the Ac_1 temperature of the material, they have used. No appreciable reduction in the hardness of the weldment was reported as a result of PWHT at any temperature, they have used. The results reported in this study does not confirm to the existing and well accepted knowledge about characteristics of the welds in this steel. The reason for such a result could be insufficient time for PWHT, which is not reported in this paper.

Watanabe et al. [68] have reported evaluation of creep damage of 9Cr-Mo-V-Nb steel welded joints by conducting experiments over a temperature range of 550 – 650 ^oC and stress range of 40 – 230 MPa range. A shift in the rupture location from weldment region at high stress – low temperature condition to the FGHAZ region at low stress – high temperature condition was reported in this study. The fracture in the FGHAZ at high temperature – low stress condition is known as Type IV cracking. It was reported that before creep tests, the FGHAZ region did not show any lath martensitic structure and the dislocation density in the subgrains in this region was also much lower than that in the weldment. They observed accelerated coarsening of carbides and recovery of the dislocation structure in the FGHAZ region, which led to preferential accumulation of creep damage in this region causing creep void formation and Type IV cracking. Hongo et al. [69] have also reported similar results for weld joints, in 25 mm thick Grade 91 steel plates.

Kumar [70] has reported welding of P91 steel by autogenous and cold- and hot wire TIG welding processes for fabrication of steam generators of the 500 MWe Prototype Fast Breeder Reactor. The steam generators are designed to operate at high steam outlet temperature and pressure of 493 ^{o}C and 172 bar respectively. A preheating temperature in 200 – 250 ^{o}C range and PWHT at 760$\pm$10 ^{o}C was used in these weldings. It was reported that hot wire TIG not only increases the weld deposition rate, there is also associated lower heat input, lower distortion and a significant reduction in the porosity as joule heating removes any volatile matter from the filler wire. Barthoux [71] has also reported similar benefits for welding of heavy wall thickness materials by narrow gap welding for nuclear application.

Arivazhagan et al. [72] have reported effect of variation in heat input on the microstructure of reduced activation ferritic martensitic steel weld metal produced by GTAW process. In the weld metal, δ-ferrite was observed, volume fraction of which increased with increasing heat input. They inferred that slower cooling rate associated with high heat input was the facilitating factor for formation of δ-ferrite in the weldment.

A detailed study on structure and properties of the actual as well as Gleeble simulated heat affected zone of P91 steel has been subject of doctoral study of Sulaiman [73]. He reported very good agreement between the actual and the Gleeble simulated HAZ in terms of structure and properties. It was reported that except for prior austenite grain size variation there is no microstructural marker to distinguish the different sub regions of the HAZ. The cross-weld hardness profile showed softening in the FGHAZ and

ICHAZ. Dilatometric studies showed that simulated normalizing did not result in complete dissolution of the carbides affecting hardness and transformation temperatures of the resulting austenite and the Ms temperature. It was reported that in spite of high hardenability of the P91 steel which resulted in complete martensitic transformation, the Ms temperature and the hardness of the resultant martensite varied substantially with the associated thermal cycle. The Ms varied in 370 – 420 ^{o}C range and the hardness in 365 – 480 HV range. However, no explanation was provided for this variation.

Arivazhagan et al. [74] have reported influence of shielding gas composition and TIG arc remelting on toughness of flux-cored arc weld of P91 steel. They found that Ar+5%CO_2 mixture resulted in minimal slag inclusion and superior toughness of the weld metal. Increasing the proportion of CO_2 led to inclusion of coarse slag particles and associated deterioration in the weld toughness. This deterioration in the toughness of the weld due to slag inclusions could be rectified by TIG arc remelting of the welds, which led to formation of fine inclusion particles at the expense of coarse particles. However, the researchers have not provided any rationale for this study on variation of the shielding gas composition and also why this variation affected the inclusion content of the welds.

Paddea et al. [75] have reported residual stress distributions in a P91 steel-pipe girth weld before and after PWHT. They produced a weld joint between two pipes (325 mm outer diameter and 25.4 mm wall thickness) made of P91 steel by employing GTAW for root passes and SAW for the filling passes and studied residual stress distribution across the joint as well as through the thickness of the joint by neutron diffraction. It was reported that highest residual stress was found towards the outer HAZ region and the root region in as-welded and also in PWHT condition. This work hints at a possible role of the weld residual stresses on the Type IV cracking encountered in the welded components in this steel, but that cannot be confirmed without a comprehensive study. It was also reported that a compressive state of the residual stresses in the weldment corresponding to the final pass, confirming the compressive effect of the martensitic transformation on the weld residual stresses.

Parker [77] has reported his investigation on the factors affecting Type IV creep damage in Grade 91 steel welds. Through microstructural and creep studies on welds made in P91 steel pipes and Grade 91 steel plates by MMAW process, he concluded that in the outer HAZ region, which forms FGHAZ and ICHAZ, martensitic transformation is not likely to occur because for the fine grained austenite the ability to undergo martensitic transformation may be limited. This region is susceptible for accelerated softening of the matrix and accelerated coarsening of the precipitates leading to localization of the creep damage, creep cavitation and Type IV cracking.

Welding and weldability of these steels have been extensively reviewed by David et al. [62]. Tempered martensitic microstructure of these steels is completely altered by the weld thermal cycle. This material undergoes melting in the fusion zone and solidifies as δ (ferrite), which then transforms into γ (austenite), which finally transforms into α’ (martensite). In the heat affected zone, ferritic to austenitic transformation and dissolution of the carbide particles takes place during heating cycle. This material is highly hardenable and therefore, all the austenite produced in the fusion zone and HAZ undergoes complete martensitic transformation during cooling leg of the weld thermal cycle. Martensite is a hard and brittle phase and this necessitates preheating of the parts to be joined, particularly, when multiple passes are required to produce a weld joint. Therefore, a preheating and inter-pass temperature is maintained during welding of 9Cr-1Mo(V, Nb) FMS (Fig. 2.13) [62]. Preheating temperature depends on many factors like composition of the material and constraint imposed on the parts being joined. Lower end of the preheating temperature is guided by the ductility required to avoid cracks in the weld and the upper end is guided by the necessity to ensure complete martensitic transformation of the austenite during cooling cycle. Typically the upper end of the preheating and the inter-pass temperature is kept ~ 100^{o}C below Ms of the weld metal. The preheating temperature generally kept for an extended time after completion of welding, also termed as post heating or bake-out of the weld, particularly for thick sections. This is preferred if the joint is not going for post weld heat treatment (PWHT), soon after welding. This serves to keep the joint dry, facilitates hydrogen diffusion and avoids any unwarranted contamination.

In as-welded condition, microstructure in the fusion zone and HAZ is as-transformed martensite within prior austenite grains of varying shapes and sizes. In this condition, the fusion zone and the HAZ have much higher strength and hardness; but much lower ductility and toughness and therefore, the component cannot be put into the service in as-welded condition. Post weld heat treatment (PWHT) of the weld joint is carried out to improve ductility and toughness of the joint. Range of PWHT temperatures allowed by ASME for P/T91 steel weld joints is 730-800^{o}C [62]. Lower tempering temperature leads to higher joint strength and higher tempering temperature leads to higher ductility. However, upper end of tempering temperature is capped by A_1 temperature, which can vary considerably (770 – 850^{o}C), depending on composition of the weld metal [77]. Care should be taken to ensure that tempering temperature does not exceed A_1 temperature of the weld metal, else some part of it gets reaustenitized and transforms into martensite, leading to degradation of fracture toughness of the weld joint.

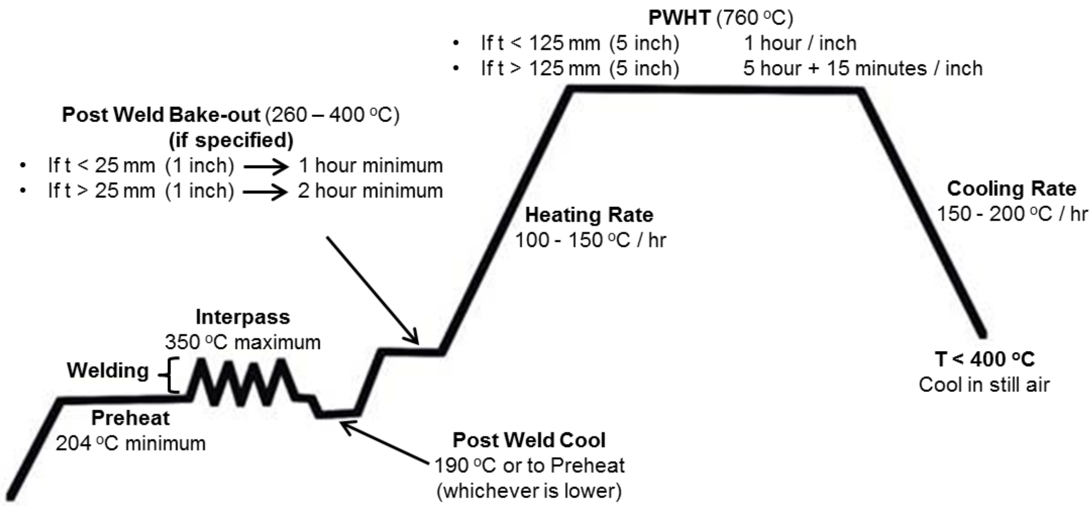

Fig. 2.13: A typical preheating/inter-pass heating/post weld bake-out and post weld heat treatment (PWHT) used for welding of 9Cr-1Mo(V, Nb) FMS [62].

Cross-weld microstructural variation in this steel has been subject of the extensive studies [64, 76]. Thermal cycle imposed on the material, by the welding heat source induces different metallurgical changes. This leads to a gradually varying microstructure across the weld joint (Fig. 2.14) [76].

In the fusion zone, the material melts and then solidifies in columnar morphology. Adjacent to it lies a narrow partially melted zone (PMZ) in which the peak temperature was between solidus and liquidus of the steel. Beyond PMZ lies the HAZ, which can be broadly divided into following four sub-regions depending on the strength of the thermal cycle and the resultant metallurgical changes experienced by the material.

Coarse Grained HAZ (CGHAZ): The peak temperature in this region is between ~ 1100°C and solidus temperature. In this region complete austenitization of the tempered martensitic structure, dissolution of the carbide precipitates and coarsening of the prior austenitic grains take place. This zone includes two phase δ+γ region, in which a fraction of austenite transforms into δ-ferrite, which at times gets retained right up to room temperature [76].

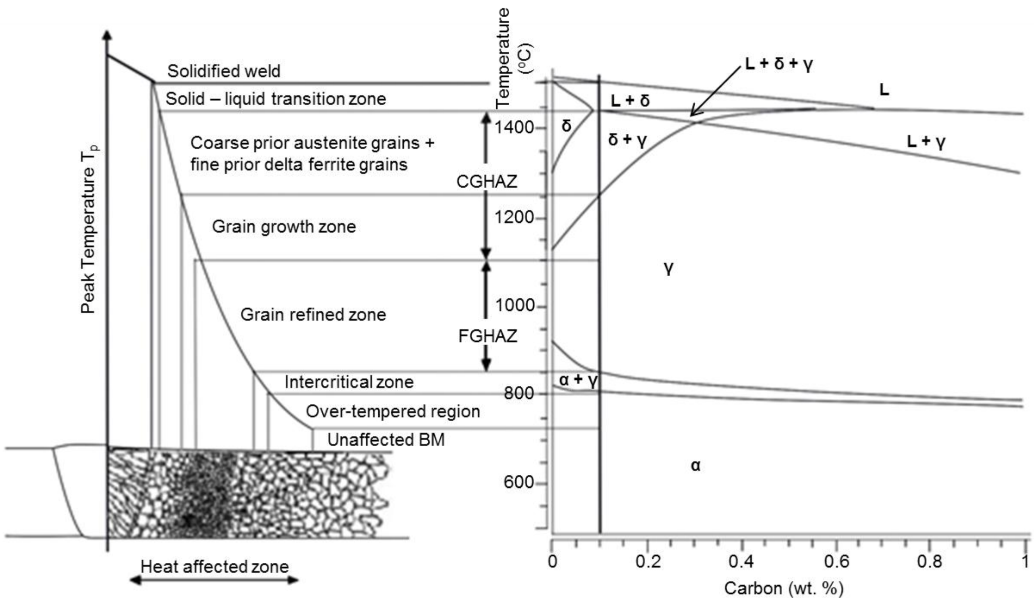

Fig. 2.14: Schematic diagram showing microstructural variation across weld joint in P(T)91 steel and corresponding regions in the calculated phase diagram [76].

Fine Grained HAZ (FGHAZ): In this region, the peak temperature is between A_3 and ~ 1100°C. Tempered martensitic structure undergoes complete austenitization, however, complete dissolution of carbide precipitates does not takes place. As a result of relatively weak thermal cycle, the original prior austenite grains get divided into multiple new austenite grains. This results in fine prior austenite grains.

Intercritical HAZ (ICHAZ): The peak temperature in this zone lies between A_1 and A_3 and the tempered martensite undergoes partial austenitization. This zone consists of as transformed martensitic structure within fine prior austenite grains and over tempered ferritic subgrains.

Subcritical HAZ: In this zone the peak temperature is less than A_1 temperature and therefore, this zone undergoes some additional tempering.

Multipass welding processes introduce non-uniformity in the fusion zone microstructure as the heat from the succeeding passes leads to formation of a graded HAZ, consisting of various microstructural zones, in the weld metal deposited by the preceding passes and also cause tempering of the same. Thus fusion zone of a multipass weld joint in ferritic steels is essentially a mixture of fusion zone, HAZ and tempered fusion zone [64, 76, 95]. Reed et al. [95] have presented a model for multipass weld joints in steels. Different metallurgical regions in fusion zone and HAZ resulting from a typical multipass welding process in a ferritic steel are shown in Fig. 2.15. In this figure, it can be seen that the fusion zone and the HAZ consists of a mixtures of different metallurgical regions, resulting from the heat input of multiple passes. This kind of microstructural heterogeneity is always present in the fusion zone and HAZ of a multipass weld joints in 9Cr FMS [64, 76]. This microstructural heterogeneity is one of the prominent contributing factors for the weld joint failure by Type I and Type II cracking [76].

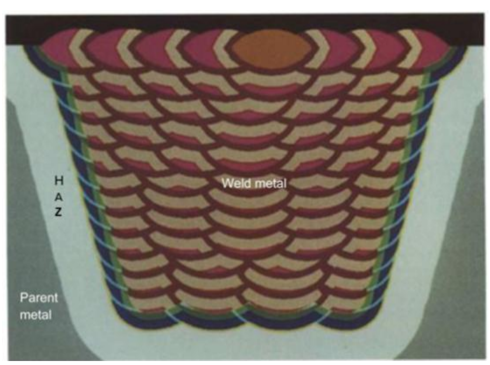

Fig. 2.15: Schematic diagram showing heterogeneous microstructure in the fusion zone and the HAZ of a typical multipass weld joint in a ferritic steel [95].

2.2.4 Rationale for Laser Welding of 9Cr-1Mo(V, Nb) FMS

Conventional arc welding processes are being used for decades to join a large number of components and assemblies made of 9Cr-1Mo(V, Nb) steel, for power plants, petrochemical industries and nuclear reactors. There have been considerable improvements in the area of arc welding process, which resulted in cleaner and tougher weld metal. However, there are certain limitations like high heat input and heterogeneous microstructure in the fusion zone and HAZ, which are inherent to the process and therefore, cannot be avoided. These limitations lead to failure of the joint by different modes of cracking like – Type I, Type II, Type III and Type IV (Fig. 2.16) [76]. Type I cracks originate and culminate in the weldment. Type II cracks originate in the weldment but may extend into the HAZ or even the parent metal. Type III cracks originate in the coarse-grained HAZ and can propagate in this zone as well as into the parent metal. Type IV cracks originate and propagate into the fine-grained or inter-critical HAZ. Laser welding being a low heat input and single pass process, produces uniform fusion zone and HAZ and therefore, a better alternative joining process to overcome these problems.

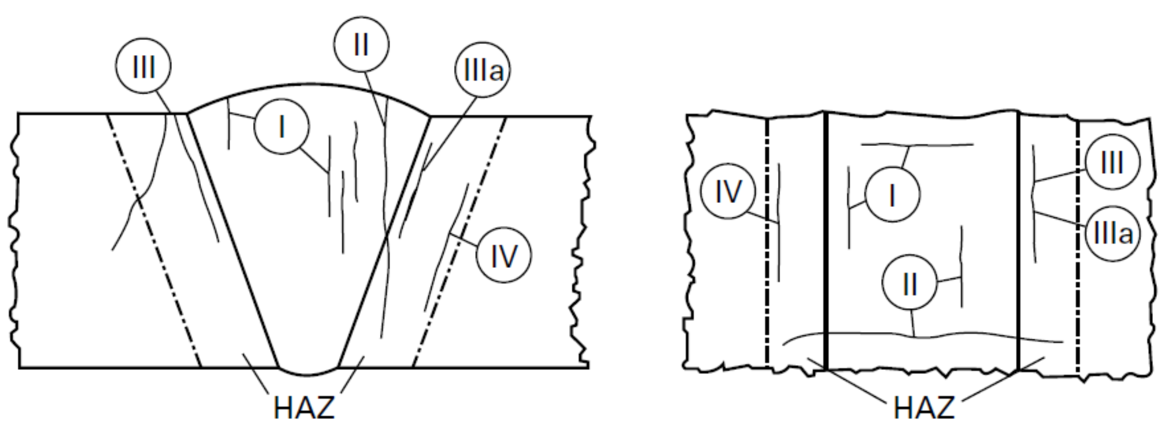

Fig. 2.16: Different modes of cracking associated with weld joints in 9Cr-1Mo(V, Nb) FMS [76].

Besides, many joint configurations do not allow for making grooves and filling it with weld metal due to design considerations and also have minimal distortion allowance. These kind of very demanding joint configurations are present in the Test Blanket Modules (TBMs) to be used at International Thermonuclear Experimental Reactor (ITER). These TBMs are to be made of RAFMS, a material with very similar chemistry, physical metallurgy and weldability as that of 9Cr-1Mo(V, Nb) FMS. Therefore, making of these joints calls for single pass, low heat input welding processes or a combination of low heat input welding processes (laser welding) and arc welding process. While EBW can be used to make single pass, low distortion weld joints with low heat input and narrow FZ and HAZ; the process does not offer sufficient flexibility (beam manoeuvrability) to be used for many joint configurations. Therefore, laser welding remains potentially the only option to make those weld joints. Due to these reasons, laser welding has emerged as the welding process of choice for many joints (up to 10 mm thick) in TBM fabrication [89 - 94]. Because of very similar chemistry, metallurgy and weldability characteristics, the results of laser welding of 9Cr-1Mo(V, Nb) FMS can be utilized for laser welding of RAFMS. However, the literature on laser welding of 9Cr-1Mo(V, Nb) FMS and RAFMS is rather limited [85 - 94]. This provides rationale for a detailed study on laser welding of 9Cr-1Mo(V, Nb) FMS.

2.2.5 Laser Welding of 9Cr-Mo(V, Nb) FMS and RAFMS

Rather limited literature on laser welding of 9Cr-1Mo(V, Nb) is primarily because this material is being welded by multipass arc welding processes for over last three decades [85 - 94]. Lee et al. [85] produced and characterized full penetration weld beads on 5 mm thick plates of 9Cr-1Mo(V, Nb) FMS in normalized condition (1040^{o}C, 30 minutes), using 5 kW continuous wave CO_2 laser (Rofin-Sinar 850). They produced two weld beads, overlapping 6% at the root, on each plate to produce wide enough fusion zone for further characterization. The welds were tempered at 250^{o}C, 540^{o}C and 750^{o}C for 1 hour. They have characterized the welds and the parent material for the microstructure, impact toughness and notch tensile strength and fatigue crack growth, in air as well in hydrogen atmosphere. They have reported presence of δ-ferrite, retained austenite as well as twinned martensite in the fusion zone microstructure, which was predominantly auto-tempered martensite within coarse prior austenite grains. They have reported considerable drop in the impact energy for the parent metal tempered at a temperature in the vicinity of 540^{o}C. They have reported much lower impact energy of the fusion zone than that of the parent metal. However, the impact energy for welds increased significantly when tempered at 750^{o}C. Both the parent metal as well as the welds, tempered at lower temperatures, exhibited significant susceptibility to hydrogen embrittlement; however, this susceptibility was significantly higher for the welds. Susceptibility towards hydrogen embrittlement became negligible for the parent metal as well as the welds tempered at 750^{o}C. The specimen with lower impact toughness displayed unstable fatigue crack growth and quasi-cleavage on fracture surface. The welds showed higher fatigue crack growth rate than the parent metal; however, this difference became negligible for the parent metal and the weld tempered at 750^{o}C.

Xu [86] has reported laser welding of pipe with 3.34 mm wall thickness using a pulsed Nd-YAG laser of 1.6 kW nominal power. He has reported the effect of process parameters on the various attributes like depth and lateral spread of fusion zone and the HAZ. A narrow fusion zone and HAZ with much higher hardness (~420 – 500 VHN) was reported by him. In post weld heat treated condition, cross-weld hardness profile did not show any soft zone, which is always associated with a multipass weld joints in the HAZ-PM interface region and attributed for failure by Type-IV cracking under creep condition.

Shanmugarajan et al. [87] have reported laser welding studies for 6 mm thick plate of P91 steel using continuous wave CO_2 laser (Power 3.5 kW). They have studied weld beads and square butt weld joint produced by varying heat input in 168 J/mm to 1500 J/mm. They have reported increase in width of the fusion zone and the HAZ with increasing heat input. Further, at lower heat input up to 420 J/mm, they did not observe any soft inter-critical region; which was observed at heat inputs exceeding 700 J/mm. At lower heat input (up to 420 J/mm) they did not observe any δ-ferrite in the fusion zone, which was present in the fusion zone of the joints made at heat inputs exceeding 700 J/mm. Besides, they have reported superior impact toughness for the weld joints than that of the parent metal, which is in contrast to that reported by Lee et al. [85].

Harinath et al. [88] have reported their work on laser welding of fuel clad tube – end cap, both made of 9Cr-1Mo(V, Nb) FMS, for potential application in Indian fast breeder reactors. They have reported their work on process parameter optimization and preliminary microstructural examination on the weld joint cross-section. They have reported presence of δ-ferrite in the fusion zone, which comprised predominantly of as-transformed martensitic microstructure. They have also reported considerable grain refining in the narrow HAZ region adjacent to the fusion zone. They have attributed the presence of δ-ferrite to incomplete δ-ferrite to γ (austenite) transformation, during cool down of the weld joint.

Fabrication of TBMs has led to renewed interest in laser welding FMS and significant amount of literature exists on laser of RAFMS, which has very similar metallurgy and weldability characteristics as that of 9Cr-1Mo(V, Nb) FMS [89 - 94]. Cardella et al. [89] have mentioned laser welding as one of the prominent joining method for TBM fabrication. They have presented a macrograph showing cross-section of weld joint in 9 mm thick EUROFER 97, a reduced activation ferritic/martensitic steel developed by European Union, showing a narrow fusion zone and HAZ. However, details regarding the laser welding parameters and weld joint characterization were not reported.

Tanigawa et al. [90] have reported laser welding of F82H, a reduced activation ferritic/martensitic steel developed by Japan, for fabrication of the membrane panel for Japanese TBM. This requires welding of a 1.5 mm thick and 4 mm wide plate with tubes (11 mm diameter and 1 mm wall thickness) on both sides of the plate. In this application laser welding offers advantage of low heat input and negligible distortion. This welding has been done using a fiber laser to produce sound weld joints. However, characterization of the weld joint in terms of microstructure and mechanical properties is not reported. They have emphasized the need to characterize the weld joints, involved in TBM fabrication, in terms of residual stresses.

Serizawa et al. [91] have reported welding of 32 mm thick plates of F82H by a combination of laser welding and plasma – MIG hybrid welding. Laser welding was carried out using a 10 kW fiber laser to produce 12 mm thick root pass and plasma-MIG hybrid welding was used for the filling passes. They have performed computational studies to investigate the effect of mechanical restraint on weldability of thick plates of RAFMS. They have used different model sizes and have arrived at a minimum coupon size which should be used for basic test of weldability for 90 mm thick plates of F82H using electron beam welding.

Serizawa et al. [92] have reported dissimilar weld joint between 4 – 5 mm thick plates of F82H and SS316L using a 4 kW fiber laser. They produced the dissimilar weld joint by keeping the beam at the seam line and also by shifting the beam by 0.1 mm and 0.2 mm towards SS316L side. Welds were produced at 4 kW of laser power and welding speed of 2 m/minute – 4 m/minute. They have reported a wider fusion zone and HAZ at the lower welding speed and vice-versa. The fusion zone was very hard when the beam was at the seam line and its hardness could not be reduced significantly even after post weld heat treatment (PWHT). However, hardness of the fusion zone could be reduced to the parent metal level by shifting the laser beam towards SS316L and hardness of the HAZ on P91 side could be reduced to the parent metal level after PWHT.

Aubert et al. [93] have presented a review of candidate welding processes of RAFMS for ITER and DEMO TBMs. They have emphasized the importance of high power laser welding and Laser/MIG hybrid welding for TBM fabrication. Commissariat à l'Energie Atomique et aux Energies Alternatives (CEA), France is using a high power (multi kilowatt) disk laser to produce different joint configurations relevant for European TBM. It has reported microstructural variation and microhardness profile across laser welded joint in 11 mm thick EUROFER 97 plates using 8 kW disk laser at 0.35 m/minute welding speed. They have also produced sound weld joints of same thickness (11 mm) at much higher welding speed (2.5 m/minute) by using still higher laser power (10 kW).

Thus it can be seen that laser welding of FMS and RAFMS is finding increased attention, due to its benefits. However, a detailed study on laser welding of 9Cr-1Mo(V, Nb) FMS in terms of process parameters, microstructure and residual stresses is not reported in the literature. This work presents detailed study on laser welding of 9Cr-1Mo(V, Nb) steel using high power CO_2 laser, in terms of the process parameters, microstructure and residual stresses. Besides, thermo-metallurgical and thermo-mechanical modelling and simulation of laser welding of 9Cr-1Mo(V, Nb) FMS have also been done to get a better insight of the process.

2.3 Modelling and Simulation of Welding

Welding is a complex process comprising of many seamlessly interrelated electrical, physical, chemical, metallurgical and structural phenomena and therefore, modelling and simulation of a welding process is very challenging. The starting point can be interaction of the energy source – flame, arc, beam etc., with the material leading to generation of heat in the solid. This is a very complex problem to model, in itself. The heat source resulting from the interaction of the energy source can be of different spatial (point, line, area, volume with different kind of intensity distributions) and temporal profile (continuous, pulsed, modulated etc.). Computation of the temperature profile and the heating and cooling rates resulting from a heat source requires simultaneous solution of the heat diffusion equation in the solid, in conjugation with cooling of the solid by convection and radiation. If the heat source is strong enough to cause phase changes, modelling of the same becomes necessary, to predict many outcomes of relevance. When melting is involved, which is invariably associated with welding, modelling of solid to liquid transition and convection in the melt, driven by surface tension and density gradients, becomes necessary to accurately predict weld pool morphology and temperature profile in the weld pool. One can go on counting a large number of phenomena that need to be considered simultaneously, for accurate modelling of any welding process. However, it is not possible to include all of these in a single model. Therefore, only the phenomena of interest and relevance for the outcomes of interest are included in a model. The outcomes of interest can be the temperature profiles, the FZ and HAZ profiles, the heating and the cooling rates, distortion of the joint, residual stress profiles etc.

Heat conduction in solid forms the core of all the analytical and numerical models of welding. Analytical solution of the heat conduction equation has been extensively described by Carslaw and Jaeger [96]. Rosenthal [97] presented analytical solution of temperature profiles resulting from the application of a point heat source incident on the surface of an infinite solid and moving along weld line. This solution is applicable for welding in the conduction mode. Rosenthal [97] also proposed analytical solution for an infinite line source extending through the thickness of the joint and moving along the welding direction. This solution can be used for through-thickness as well as partially penetrating, deep weld joints. However, the point and line source models do not account for the finite size of actual welding heat sources and therefore, predict infinite temperature at the source. Solutions from point and line sources can be integrated to obtain analytical solutions resulting from a surface and a volume heat source with different intensity profiles (flat top, Gaussian etc.); however, analytical models cannot incorporate temperature and phase-dependent material properties. To incorporate the variation in material properties with temperature, one has to go for numerical solution of the model. Besides, numerical solutions can incorporate any joint configuration and provide much more results and therefore, much deeper insight, than one can get from the analytical solutions. Due to these reasons, numerical modelling and simulation of welding process have gained considerable interest. Considerable amount of work on finite element modelling and simulation covering different aspects of arc welding has been reported in the literature [98 - 128]. The interest in modelling and simulation of welding can be gauged by the fact that Mackerle [127, 128] has presented a bibliography of over 1300 papers between 1976 – 2001, on finite element modelling and simulation of welding and the number of publications has continued to increase at a rapid pace since then. Different multiphysics software packages like ANSYS, FLUENT, ABAQUS, SYSWELD etc. are available for modelling different aspects of welding [129 - 141]. These software packages along with much stronger computing systems help in modelling and simulating different aspects of the welding process such as thermal, fluid, metallurgical and structural. Modelling and simulation of the conventional arc welding of 9Cr-1Mo(V, Nb) FMS has been extensively reported in the literature [129 - 131]. However, modelling and simulation of laser welding of 9Cr-1Mo(V, Nb) FMS is not reported in the literature.

2.3.1 Modelling and Simulation of Laser Welding

Analytical solution for an infinite line source, extending through depth of the material and moving along the welding line, can be taken as a starting point for analytical solution of laser welding. As line source cannot account for finite size of the heat source, therefore, by integrating the point and the line source solutions over an area, different kinds of heat sources can be constructed. Lax [142] provided solution for steady state temperature distribution resulting from a stationary Gaussian beam incident on a semi-infinite medium. This solution is applicable for laser welding in conduction mode. Nissim [143] presented a 3-D solution for a moving elliptical Gaussian heat source. Miyazaki and Giedt [144] presented solution of the heat conduction equation for a cylindrical molten region with elliptical cross-section. A laser weld joint made in keyhole mode of welding has a nail like shape. This shape was modelled by a combination of point and line source solutions by Steen et al.. [145], which has been extended further by different researchers [146 – 148].

Again analytical solution of laser welding has its own limitations and therefore, numerical modelling and simulation has been used extensively to study different aspects of laser welding. Mazumder et al. [149] presented numerical model for heat transfer resulting from materials processing using a continuous wave laser. They assumed a Gaussian heat source model and 100% coupling of beam energy above boiling point of the material. Besides, conduction, melt pool convection has very significant effect on the temperature distribution within the melt pool and on the morphology of the melt pool itself. Significant amount of modelling and simulation studies have been carried out on melt pool convection during laser welding [150 - 154]. The underlying mechanism for deep penetration laser welding is formation of a 'keyhole', which travels along the welding line. This keyhole is filled with metal vapour, through which laser beam propagates deep inside and gets absorbed on the walls formed of the molten metal. Absorption of the laser beam energy is increased due to lower angle of incidence [155] as well as entrapment of the laser beam within the keyhole leading to multiple reflection and absorption on the keyhole walls. Morphology of the keyhole is determined by the combined effect of melt flow within the keyhole as well as that of the melt surrounding the keyhole. Significant amount of modelling and simulation studies have been reported in the literature on different aspects - formation, stability, morphology etc. [156 - 174]. An extensive review of thermal modelling of laser welding and related processes has been presented by Mackwood and Crafer [175].

Thermo-metallurgical computations provide thermal field and metallurgical phase field, which are then used for thermo-mechanical computations. Thermo-metallurgical computations involve computing phase-fractions due to the weld thermal cycle. Phase-transformations lead to formation of different phases, which differ in thermo-physical properties. Therefore, thermal and metallurgical computations are simultaneously coupled. For this purpose, thermal equations describing heat diffusion in the solid and convective-radiative cooling of the solid and phase transformation equations describing diffusional or martensitic transformations are solved simultaneously. These computations are performed numerically using commercially available software packages like SYSWELD [136] and provide temporal evolution and spatial distribution of different phases resulting due to welding operation.

Results of Thermo-metallurgical computations i.e. thermal and metallurgical phase profiles, along with temperature and phase-dependent mechanical properties form the input for thermo-mechanical computations. As mechanical behaviour of the material does not have significant bearing on the evolution of thermal and metallurgical phase-field, thermo-mechanical computations are sequentially coupled to the thermo-metallurgical computations. Thermo-mechanical computations are made numerically using commercially available software packages like ANSYS, ABAQUS, SYSWELD etc. [129 - 138]. Yaghi et al. [129] have reported residual stress simulation using ABAQUS in multi-pass arc welded section of P91 pipes. They have used an axisymmetric model of the butt joint between P91 steel pipes for this simulation and have computed through thickness residual stress profiles along weld centre line and in the HAZ. They performed the analysis for five joint configurations each for two wall thicknesses – 7.1 mm and 40 mm, by varying the inside radius to wall thickness in 1 to 100 range. It was reported that the peak tensile stresses occurred nearer to the inside surface of the pipe in the thin walled joints and nearer to the outside surface of the pipe in the thick walled joints. The peak compressive stresses, if any, occurred nearer to the outside surface of the thin walled pipe and nearer to the inside surface of the thick walled pipe. A set of material properties generated for this purpose was used in this study. However, material properties of supercooled austenite were not considered in these computations. In addition, solid state phase transformation (SSPT) of the austenite into martensite was also not considered in their model.

Deng et al. [130] have reported computation of welding residual stresses using ABAQUS in multi-pass arc welded modified 9Cr-1Mo steel pipe in butt configuration, considering SSPT effects. They have also used axisymmetric model and considered the effects of volumetric and/or yield strength change arising out of SSPT of austenite into martensite during welding. It was reported that the volume and yield strength changes associated with SSPT of austenite to martensite during welding have significant effects on residual stress and must be considered for computation of stresses arising out of welding of this material. Because of non-availability of mechanical properties of the low temperature austenite, they have used properties of the base metal itself in this regime. However, it was recommended that phase-dependent mechanical properties of the material should be used for further improvements in the computed results.

Kim et al. [131] have reported numerical computation using ABAQUS and experimental measurements using neutron diffraction of residual stresses for a modified 9Cr-1Mo steel weld joints. They have used material property data from Yaghi et al. [129] and have not used phase-dependent material property data. The weld joints were produced in butt and fillet configurations using arc welding methods. They had not implemented SSPT of austenite into martensite; however, based on the experimental results it was recommended that SSPT should be considered for arriving at more reliable results.

Price et al. [132] have reported comparison of the residual stress in welds computed using SYSWELD and that measured experimentally using neutron diffraction. They have used metal inert gas deposited weld beads on low carbon steel. Their results show that longitudinal component of the residual stress is the most significant and the normal and transverse components are much smaller and comparable to each-other. Bate et al. [133] have reported thermo-metallurgical and thermo-mechanical computations using SYSWELD for bead on plate specimen produced by tungsten inert gas welding. They have presented transient temperature evolution and residual stress profiles on the weld bead cross-section. Aloraier et al. [134] have reported computation of residual stresses in flux cored arc welding process in bead on plate specimen for a boiler and pressure vessel steel (Fe-1.35Mn-0.155C) using SYSWELD. They have presented temperature distribution at different instants of time and residual stress field. Xu et al. [135] have reported transient thermo-metallurgical and thermo-mechanical computations using SYSWELD for bead on plate specimen of an austenitic stainless steel (SS316L) produced by automated tungsten inert gas welding. They have presented residual stress profiles as well as temporal evolution of temperature and stress field. This work clearly shows the effect of heating, melting and post-solidification cooling on the evolution of stress field.

Joshi et al. [137] have reported experimental and computational approach for determination of the geometrical parameters of the Goldak heat source (double ellipsoid) used for weld simulation using SYSWELD for two overlapping GMAW beads. They varied the overlap percentages from 40% to 80% in increments of 10%. They used the parameters of Goldak's double ellipsoidal heat source model, determined in this study, for simulation of the overlapping beads on the plate and for computation of the simulated bead geometry, extent of the molten pool and the HAZ. They reported a reasonably good agreement between the computed and the experimentally observed results.

Joshi et al. [138] have reported computation of weld-induced residual stresses in a prototype dragline cluster using SYSWELD and comparison of the computed values with design codes. The welding process was in a single weld pass, with the approach used in two design codes: (i) R6 - Revision 4, Assessment of the Integrity of Structures Containing Defects and (ii) American Petroleum Institute API 579-1/ ASME FFS-1 2007. They reported that the computed values of the residual stresses in the fused area was higher than the yield stress at some points, however, these were generally not capable of inducing cracks on their own.

These solutions provide temporal evolution and spatial distribution of temperature, displacement, strain and residual stresses of the weld joints produced by arc welding and are useful for distortion engineering of welded structures. Significant amount of thermo-metallurgical and thermo-mechanical modelling and simulation studies pertaining to laser welding of different materials is also reported in the literature for different steels [139 – 141]. Tsirkas et al. [139] have reported thermo-mechanical computation of laser welding in 4 mm thick plate of AH36 ship building steel using SYSWELD. However, the results are limited to the temperature contours and displacement contours. Moraitis et al. [140] have reported thermo-mechanical computation of laser welding in high strength steel and an aluminium alloy using ANSYS. They have reported transient temperature field and residual stress profiles across the weld joint and through thickness of the weld joint. However, details of the steel in terms of composition and properties and also if any SSPT has been considered is not reported in this paper. Shanmugam et al. [141] have reported transient thermal computation using SYSWELD for T-joints in austenitic stainless steel (SS304L) made by laser welding. They reported that for proper fusion of base material (horizontal and vertical sheets), and for formation of a good joint between the two, incidence angle of the laser beam should be 60^o, irrespective of beam power and welding speed. Lack of penetration was reported by them for a beam angle of 30^o. For the beam angle of 45^o, they reported that proper fusion of base material was achieved between the horizontal and vertical sheets, however, lack of fusion could not be ruled out. A very good agreement between the computed and the experimentally measured depth of penetration and width of the fusion zone was reported, with standard errors of 2.78% and 1.9%, respectively. However, a very high values of the peak temperatures in the fusion zone was reported, which shows that the latent heat of fusion and vaporization was not considered in their model.

2.3.2 Modelling and Simulation of Laser Welding of 9Cr-1Mo(V, Nb) FMS

While significant volume of literature exists on modelling and simulation of different welding processes on different materials including 9Cr-1Mo(V, Nb); the literature on modelling and simulation on beam welding of 9Cr FMS is rather limited. Serizawa et al. [91] have reported FEM modelling and simulation of EB welding of RAFMS to assess weldability of 90 mm thick plates this steel under restraint. They considered models of different total lengths (150 mm, 200 mm and 400 mm) with weld lengths of 136 mm and 176mm to examine cracking tendency under the restraint. Their results showed that for assessing weldability study of 90 mm thick plates of this steel by EB welding, the minimum coupon size should be 200 mm long, 400 mm wide and 90 mm thick with ~ 180 mm long weld length. However, this work does not provide the details like material properties used in this study and also if SSPT was considered in this study. Their computed residual stress values do not reflect the effect of SSPT and therefore, it appears that SSPT was not considerd by them, in this study. As the literature on modelling and simulation of laser welding of 9Cr FMS is very limited therefore, this was pursued as an important component of the present work.

2.4 Residual Stress Measurements of Weld Joints

Stress is response of solid, constrained against free body motion, to applied force. Residual stresses, on the other hand are self-equilibrating stresses present in a solid without any force applied to it. Instead, different regions of solid exert force on each other leading to a stress-field, which is self-equilibrating over entire volume of the solid. Residual stresses are generated when a solid is subjected to some kind of non-linear change during different shaping processes like casting, machining, rolling, forging, welding, bending etc. Depending on the length scale, on which these self-equilibrating stresses vary within the body of the solid, residual stresses are classified as:

Type I or Macro-stresses: The scale of variation of stress encompasses many (typically more than hundred thousand) grains and the typical length scale is mm. This is of engineering interest.

Type II or Micro-stresses: This varies from grain to grain.

Type III or Micro-stresses: This varies within a grain and is due to defects like dislocations.

Residual stresses are of interest to engineers as they affect the life of a component in service. Many life limiting phenomena like stress corrosion cracking (SCC), creep, and fatigue are accelerated in presence of residual stresses. Welded joints are generally associated with high level of residual stresses. These residual stresses arise from a complex interplay of thermal and / or metallurgical phase-transformation induced dilation of material in a localized region near the weld joint under self- as well as clamp-imposed constraints. Residual stress contributions from different phenomena associated with a welding process are shown in Fig. 2.17 [176].

High residual stresses resulting from welding have significant bearing on the structural integrity and in-service performance of welded components. Therefore, reliable estimation and prediction of residual stresses in a weld joint is of significant interest to engineers. Methods of residual stress measurement are briefly discussed in the subsequent section.

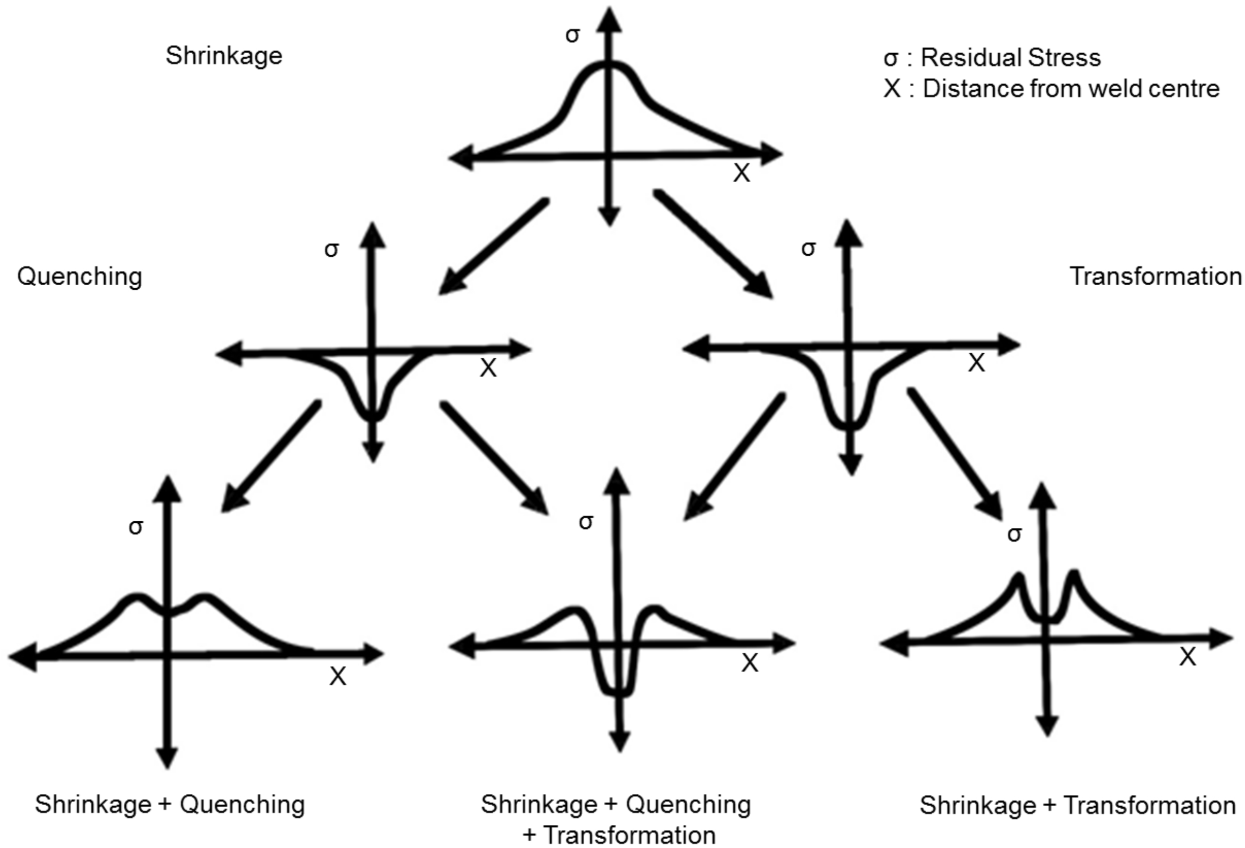

Fig. 2.17: Contribution of different processes associated with welding on variation of residual stresses across weld joint [176].

2.4.1 Methods for Residual Stress Measurements

Residual stresses of type I or macro residual stresses are of interest to engineering community and experimental measurements focus on this stress. Experimental measurement of residual stresses is carried out either by measuring the strain resulting from relieving the residual stress by sectioning, drilling etc. of solid (destructive / semi-destructive methods) or by measuring interaction of a suitable probe with the residual stress field present in the solid (non-destructive). There are many methods for experimental measurement of residual stresses in welded components. Rossini el al have presented an exhaustive review of different methods for residual stress measurement [176]. These methods can be broadly classified under the following three categories:

2.4.1.1 Destructive Methods

These methods are based on measurements of strains resulting from relieving the residual stresses by sectioning of the stressed region in the solid. Sectioning method and contour method are two prominent methods in this category. In sectioning technique an instrumented plate is cut along the line of interest and the resulting strain is measured using electrical or mechanical strain gauges [177]. The measured strain is then converted into residual stress. This method is suitable when longitudinal stress is the most significant. Care should be taken to ensure that the method employed for cutting does not induce plastic deformation or heating of the part.

Another very important destructive method for residual stress measurements is 'contour method', which provides 2D map of a residual stress field on the cross-section of interest [178, 179]. In this method, the solid is cut across the section of interest, employing a technique, usually wire-electro-discharge machining (wire-EDM), which does not introduce plasticity or heat. This results in relieving of the residual stress component normal to the cross-section. The resulting strain field is then measured by a suitable co-ordinate measuring machine (CMM) (contact or non-contact) to generate strain map on the cross-section. This strain map and elastic properties (elastic modulus and Poisson's ratio) form the input from which the residual stress is then computed using suitable finite element based software package like ABAQUS. However, destructive methods cannot be employed on actual components.

2.4.1.2 Semi-Destructive Methods

Semi-destructive methods also rely on measurement of strain resulting from relieving residual stresses present in the solid by removal of the material from the stressed region. However, the extent of material removal is small and therefore, many times functionality of the component is not affected. Therefore, these methods can be employed on actual components as well. Three prominent semi-destructive methods employed for measurement of residual stresses are – hole-drilling method, ring-core method and deep-hole method. In hole-drilling method, a small hole (diameter ~ 1.8 mm and depth ~ 2 mm) is drilled in the region of interest to relieve the stress. The strains around the hole, resulting from the relieving of residual stress are measured by using a strain gauge of appropriate design (Fig. 2.18) [180]. From the strain, thus measured, the residual stress is then calculated by using suitable calibration standard. In ring-core method, an annular slot is cut around the rosette strain gauge, to relieve the residual stress, which is then calculated from the measured strain [181]. Deep-hole drilling method combines the hole-drilling method and ring-core method [182, 183]. In this method, a through-thickness hole is drilled in the region of interest and diameter of this hole is measured. Subsequently, material around this central hole is trepanned out and diameter of the central hole is measured again. Residual stresses are calculated from the change in the diameter of the hole. Hole-drilling methods are relatively simple and are most commonly used in industry. However, destructive and semi-destructive methods interact with the residual stress-field in destructive manner and provide only limited information about the stress field. Therefore, many non-destructive methods for residual stress measurements have been also developed over time. Non-destructive methods for residual stress measurements are discussed in the subsequent section.

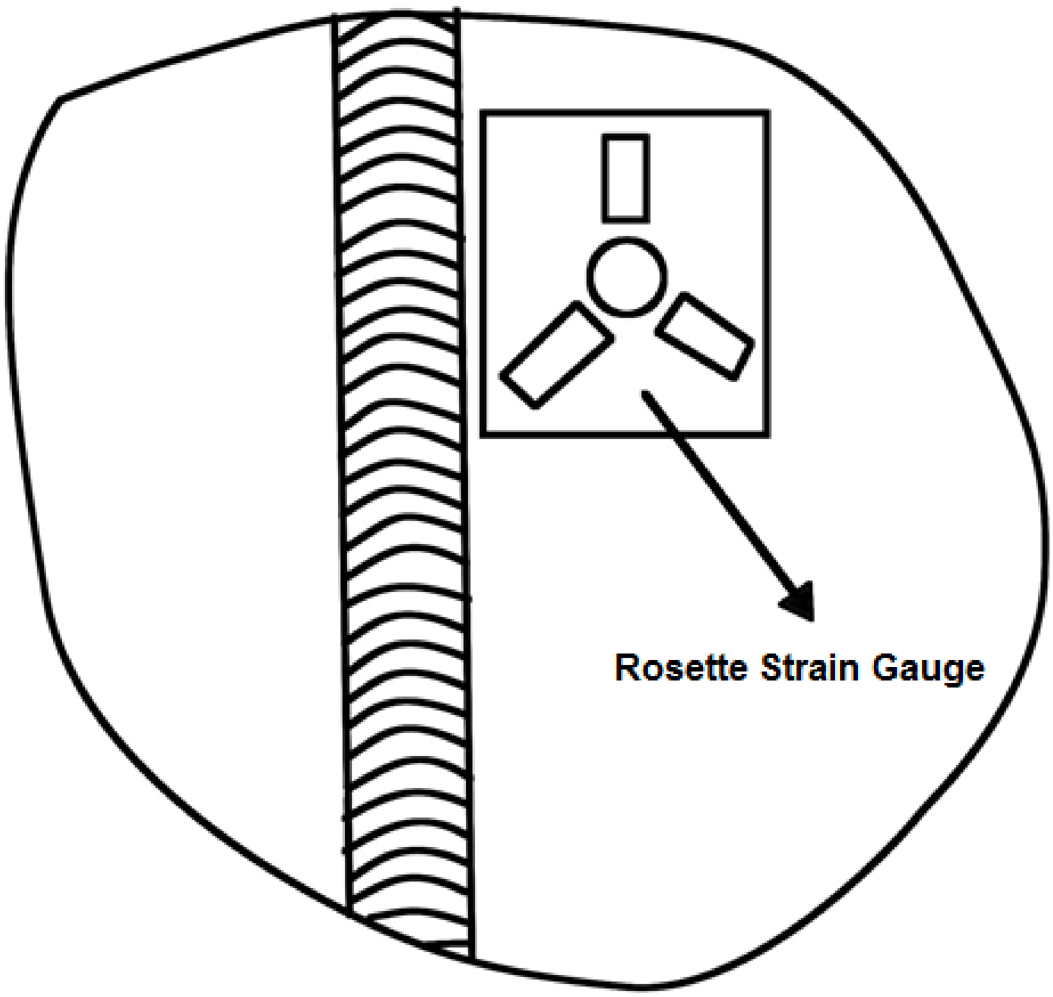

Fig. 2.18: Schematic illustration of residual stress measurement by hole-drilling method [180].

2.4.1.3 Non-Destructive Methods

Non-destructive methods use a probe – magnetic, acoustic, X-ray or neutron beam, which interacts with the residual stress-field present in the solid in non-destructive manner and provides a response. This response depends on the stress-field present in the solid and by comparing the response from region under stress to another free from stress; residual stresses in the stressed region is calculated. Prominent non-destructive methods used for residual stress measurements are ‘Barkhausen noise method’, ‘Ultrasonic method’, ‘X-ray diffraction method’ and ‘Neutron diffraction method’. Magnetic Barkhausen Noise (MBN) method is based on magneto-elastic interaction, and can be used to measure surface stresses in ferromagnetic materials [184, 185]. Tensile stresses increase MBN signal, while compressive stresses reduce it. However, microstructural features like grain boundary, intra-grain interfaces and defects also affect MBN signal and therefore, the effect of microstructural features has to be accounted for. Ultrasonic method is based on acoustic-elasticity effects, wherein velocity of elastic wave propagation in solids is affected by the stress-field [186, 187]. This method is applicable for any metallic material and can be used for measurements in reasonably thick components (~ 10 mm). However, this method has poor spatial resolution. X-ray diffraction method is based on measurements of deviation in the inter-planer spacing in the crystalline material under the influence of stress [188, 189]. From this deviation, strain is computed and then stress is back calculated using elastic constants like modulus (E) and Poisson’s coefficient (ν) of the material. However, due to limited penetration of X-rays into the material, information from only thin surface layer (~ 10 – 100 µm, depending on atomic number of the material) can be obtained and therefore, only biaxial state of stress can be measured. These limitations are overcome if synchrotron radiation is used. In that case, one can measure section thickness in 5 - 10 mm range with greatly improved resolution of ~0.1 mm. Residual stresses in thicker sections can be measured using neutron diffraction, which is discussed in the subsequent section. Section thickness and spatial resolution of different methods for residual stress measurements are presented in Fig. 2.19 [177].

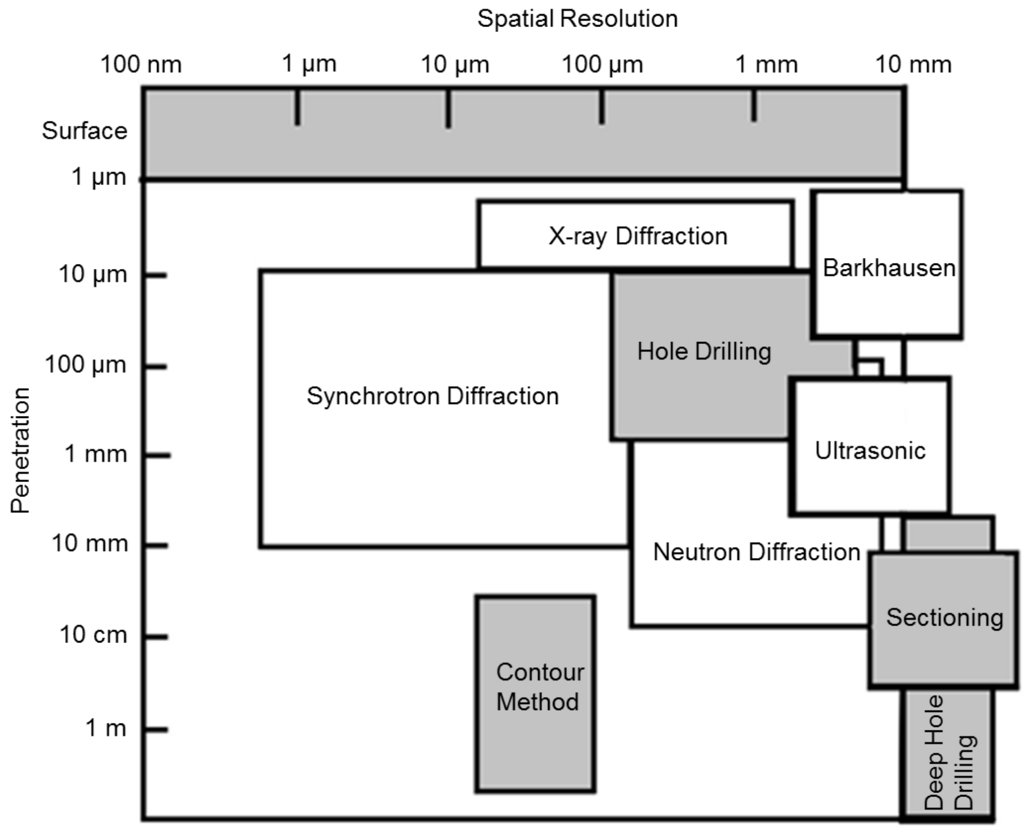

Fig. 2.19: Penetration and spatial resolution of different methods for residual stress measurement [177].

2.4.2 Residual Stress Measurements by Neutron Diffraction

Neutron diffraction is the most versatile, non-invasive method for stress measurements. This method is not limited to the measurements of only the residual stresses, but even the stresses arising from in-service loading can be measured by simulating the service conditions on the actual components. Stress measurements can be done even in thick (up to 100 mm) walled components due to deep penetration capability of neutrons and the individual component of the residual stress along the desired direction can be determined by strain measurements in multiple directions in the gauge volume of interest. Like X-ray and synchrotron diffraction method, this method also, relies on deviation in the inter-planar spacing under the influence of stress.

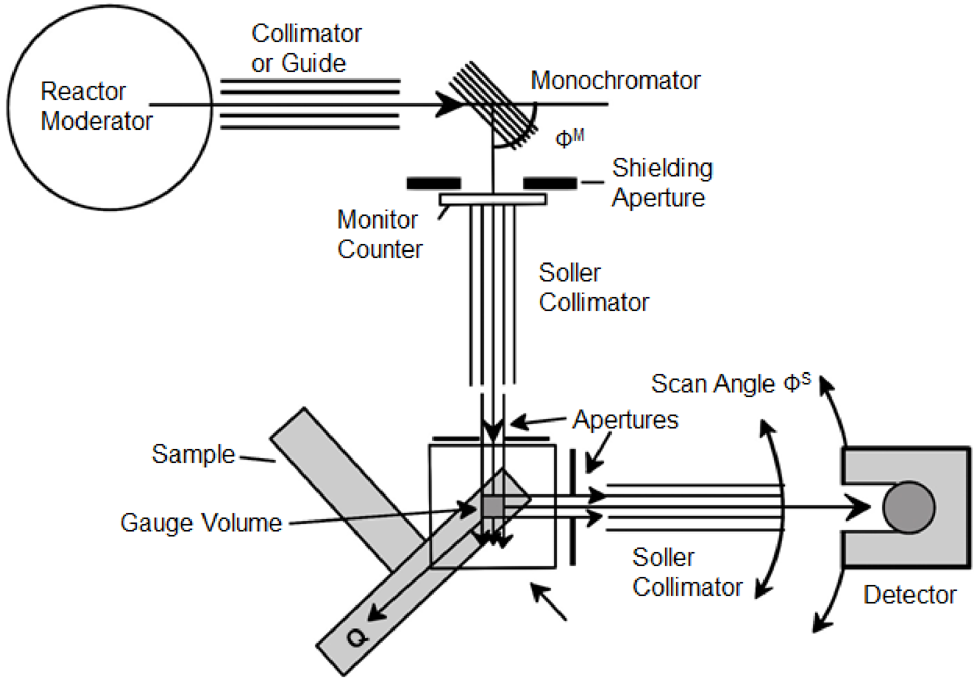

Fig. 2.20: Schematic diagram showing neutron diffraction set up using monochromatic neutron source [190].

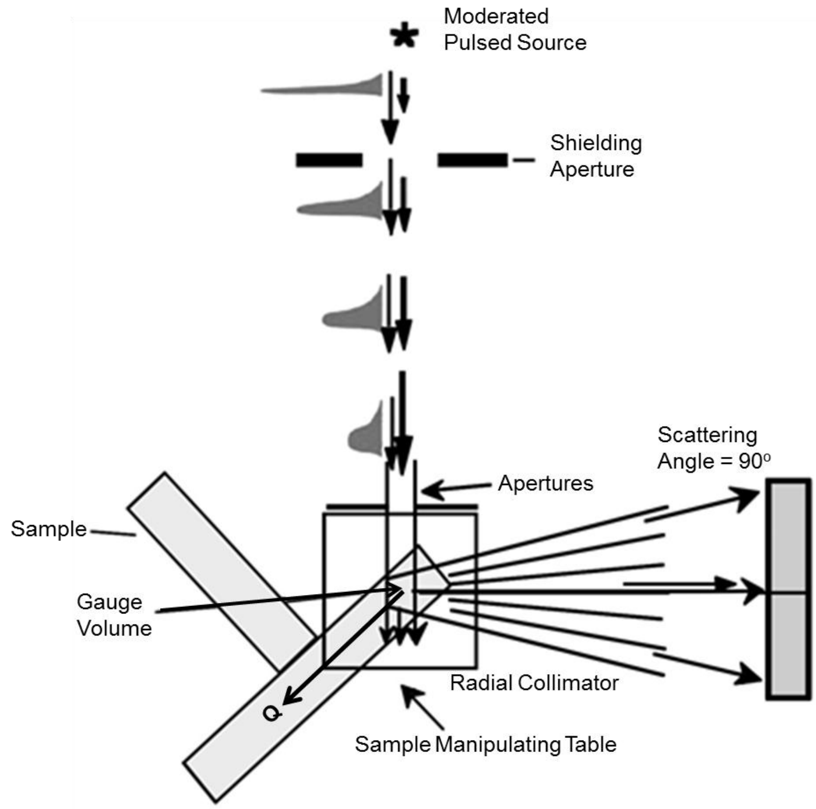

Fig. 2.21: Schematic diagram showing neutron diffraction set up using white neutron source [190].

Neutron diffraction requires a high flux neutron source, which can be obtained either from a nuclear reactor or a spallation source. Nuclear reactors provide continuous neutron beam which is then made monochromatic. Spallation sources on the other hand provide white neutron beam in pulsed mode. Dedicated beam lines and diffractometers, constructed in the vicinity of the neutron sources are used for these diffraction measurements. Schematic of neutron diffraction set up for residual stress measurements using continuous and monochromatic neutron beam from a nuclear reactor, and pulsed and white neutron beam from a spallation source are shown in Figs. 2.20 and 2.21 respectively [190]. Gauge volume or measurement volume is defined by apertures on the incident beam side and on the detector side. The direction of strain measurement is defined by the diffraction vector Q. Direction of measurement of the diffraction vector can be changed by reorienting the sample, without changing the gauge volume. Diffraction peaks are recorded in 2θ domain in case of a monochromatic beam and in time of flight (τ) domain in case of a white neutron beam. There are many neutron diffraction facilities, the world over for residual stress measurements. Some important facilities are listed below.

Reactor based:

ILL, Grenoble, and Saclay, France; Berlin and Munich, Germany; Rˇ ež, Czech Republic; Chalk River, Canada; Petten, Netherlands; Budapest; NIST, MURR and HFIR, Oak Ridge, USA; ANSTO, Australia.

Spallation source based:

ENGIN-X at ISIS, UK, POLDI on SINQ, Switzerland, SMARTS at Los Alamos and VULCAN at SNS, ORNL, USA.

Institut Laue-Langevin (ILL) at Grenoble, France is a reactor based research centre to perform neutron related research. It has a 58 MWth research reactor and a large number of neutron beam lines and instruments to perform a wide variety of experiments using neutrons. Residual stress measurements are performed using a dedicated beam line and the instrument named, SALSA. Neutron diffraction for residual stress measurements reported in present work was performed at ILL, Grenoble.

Neutron diffraction provides peak location (2θ) for a particular plane (h k l) along chosen scattering vector in the gauge volume. From this data lattice spacing (d) of the plane can be calculated using Bragg's law, $\lambda = 2dSin\theta$. By conducting diffraction experiment, in the same setting, stress-free lattice spacing (d_o) for the same plane (hkl) along the same scattering vector can be obtained. By combining these two, one can calculate strain (ϵ) along the scattering vector as, $\epsilon = (d-d_o)/d_o$. By measuring neutron diffraction peaks and therefore, strain along three principal directions x, y and z, one can obtain three orthogonal components σ_x, σ_y and σ_z of the residual stress in the gauge volume, using Equation 1.

$$\sigma_x = \frac{E}{(1+\nu)(1-2\nu)}\left[(1-\nu)\varepsilon_x + \nu(\varepsilon_y + \varepsilon_z)\right] \tag{1}$$

Where σ_x and ε_x are stress and strain components in principal directions x and E and v are respectively the crystallographic elastic modulus for the (h k l) plane and Poisson's ratio of the material.

Location of the measurement can be changed by manipulating (translating, rotating) the sample and thus residual stress distribution can be mapped. Because, fine gauge volumes of size as small as 1x1x1 mm can be employed and therefore, it is possible to map very steep residual stress profiles resulting from high energy welding processes like laser and electron beam welding.

Neutron diffraction is today a well-established method for residual stress measurement. Significant volume of literature exists on residual stress measurements in the weld joints, produced by different welding processes, in different materials [190 - 206]. However, literature on the residual stress measurements, using neutron diffraction, in laser and EB welded joints in 9Cr-1Mo(V, Nb) FMS are rather limited [83, 206]. Narrow fusion zone and HAZ and steep metallurgical and residual stress variation across the laser / EB welded joints in this material, makes it challenging to measure residual stresses even with neutron diffraction. Residual stress measurements, in laser welded 9Cr-1Mo(V, Nb) FMS plates, by neutron diffraction form an important component of this research work.

2.5 Basis of the Present Work

Based on an extensive literature survey of welding of 9Cr-1Mo(V, Nb) FMS, it is important to mention that this material is welded by several conventional processes including SMAW, GTAW, FCAW, SAW etc. and optimum joint characteristics have been achieved. However, the work related to laser welding of this steel is rather limited. In addition, the measurement of residual stress is not well documented in laser welded joints of this steel. In the present work on laser welding of 9Cr-1Mo(V, Nb) FMS, it has been attempted to optimize laser welding process parameters and characterize the weld joints in terms of microstructure, microhardness and cross-weld tensile behaviour. Measurement of residual stress field in laser welded joints in this material by neutron diffraction has been reported for the first time. In addition, thermo-metallurgical and thermo-mechanical modelling and simulation of laser welding of this material has been performed for the first time to compute temporal evolution and spatial distribution of temperature, metallurgical phase-fraction and stress-field distribution resulting from laser welding.

References

[1] R. I. Jaffee, “Metallurgical problems and opportunities in coal-fired steam power plants, Metall. Trans. 10(2) (1979) 139-164.

[2] F. Masuyama, “History of power plants and progress in heat resistant steels”, ISIJ Intl 41(6) (2001) 612–625.

[3] I. Holzer, “Modelling and simulation of strengthening in complex martensitic 9-12%Cr steel and binary Fe-Cu alloy”, PhD. Thesis (2010), Graz University of Technology, Graz

[4] A. Aghajani, “Evolution of microstructure during long-term creep of a tempered martensite ferritic steel”, PhD Thesis (2009), Ruhr University, Bochum, Germany

[5] K. H. Mayer and F. Masuyama, “The development of creep-resistant steels” in Creep-Resistant Steels, F. Abe, T U Kern and R. Viswanathan Eds.; Woodhead Publishing Limited, Cambridge, UK, (2008) 15-77 .

[6] D. V. Thornton and K. H. Mayer, “European high temperature materials development” in Advanced Heat Resistant Steels for Power Generation, R. Viswanathan and J.W. Nutting, Eds.; IOM Communications Ltd., London, (1999) 349-365.

[7] F. Masuyama, “New developments in steels for power generation boilers”, in Advanced Heat Resistant Steels for Power Generation, R. Viswanathan and J.W. Nutting, Eds.; IOM Communications Ltd., London, (1999) 33-48.

[8] G. J. Butterworth and O. N. Jarvis, “Comparison of Transmutation and Activation effects in five ferritic alloys and AISI 316 stainless steel in a fusion reactor spectrum”, J. Nucl. Mater. 122 - 123 (1984) 982 – 988.

[9] M. Tamura, H. Hayakawa, M. Tanimura, A. Hishinuma and T. Kondo, “Development of potential low activation ferritic and austenitic steels, J. Nucl. Mater. 141-143 (1986) 1067 - 1073.

[10] D. G. Doran, A. F. Rowcliffe and F. M. Mann, “Prospects for reduced activation alloys”, J. Nucl. Mater. 141- 143 (1986) 1074 – 1080.

[11] R. L. Klueh, D. S. Giles and T. A. Lechtenberg, “Development of ferritic steels for reduced activation: The US program”, J. Nucl. Mater. 141-143 (1986) 1081-1087.

[12] D. Dulieu, K. W. Topholme and G. J. Butterworth, “Development of low-activation martensitic stainless steels, J. Nucl. Mater. 141-143 (1986) 1097-1101.

[13] T. Noda, F. Abe, H. Araki and M. Okada, “Development of low activation ferritic steels”, J. Nucl. Mater. 141-143 (1986) 1102-1106.

[14] Chen-Yih Hsu and T. A. Lechtenberg, “Microstructure and mechanical properties of unirradiated low activation ferritic steel”, J. Nucl. Mater. 141-143 (1986) 1107-1112.

[15] R. L. Klueh and D. R. Harries, “High-Chromium Ferritic and martensitic steels for nuclear applications”, Retrieved from

http://www.astm.org/BOOKSTORE/PREVIEWM3/Chapter2_Mono3.pdf on March 10, 2014

[16] A. G. Ioltukhovskiy, A. I. Blokhin, N. I. Budylkin, V. M. Chernov, M. V. Leont'eva-Smirnova, E. G. Mironova, E. A. Medvedeva, M. I. Solonin, S. I. Porollo and L. P. Zavyalsky, “Material science and manufacturing of heat-resistant reduced-activation ferritic - martensitic steels for fusion”, J. Nucl. Mater. 283 - 287 (2000) 652 - 656.

[17] R. L. Klueh, “Elevated temperature ferritic and martensitic steels and their application to future nuclear reactors”, Int. Mater. Rev. 50(5) (2005) 287 - 310.

[18] E. Lucon, P. Benoit, P. Jacquet, E. Diegele, R. Lässer, A. Alamo, R. Coppola, F. Gillemot, P. Jung, A. Lind, S. Messoloras, P. Novosad, R. Lindau, D. Preininger, M. Klimiankou, C. Petersen, M. Rieth, E. Materna-Morris, H.-C. Schneider, J.-W. Rensman, B. van der Schaaf, B. K. Singh and P. Spaetig, "The European effort towards the development of a demo structural material: Irradiation behaviour of the European reference RAFM steel EUROFER", Fus. Eng. Des. 81 (2006) 917–923.

[19] Q. Huang, C. Li, Y. Li, M. Chen, M. Zhang, L. Peng, Z. Zhu, Y. Song and S. Gao, "Progress in development of China Low Activation Martensitic steel for fusion application", J. Nucl. Mater. 367–370 (2007) 142–146.

[20] B. Raj and T. Jayakumar, "Development of reduced activation ferritic–martensitic steels and fabrication technologies for Indian test blanket module", J. Nucl. Mater. 417 (2011) 72–76.

[21] Qing-sheng Wu, Shu-hui Zheng, Qun-ying Huang, Shao-jun Liu and Yang-yang Han, "Continuous cooling transformation behaviors of CLAM steel", J. Nucl. Mater. 442 (2013) S67–S70.

[22] T. Jayakumar, M. D. Mathew and K. Laha, "High temperature materials for nuclear fast fission and fusion reactors and advanced fossil power plants", Procedia Engineering 55 (2013) 259 – 270.

[23] D. Stork, P. Agostini, J.-L. Boutard, D. Buckthorpe, E. Diegele, S. L. Dudarev, C. English, G. Federici, M. R. Gilbert, S. Gonzalez, A. Ibarra, C. Linsmeier, A. L. Puma, G. Marbach, L. W. Packer, B. Raj, M. Rieth, M. Q. Tran, D. J. Ward and S. J. Zinkle, "Materials R&D for a timely DEMO: Key findings and recommendations of the EU

Roadmap Materials Assessment Group", Fus. Eng. Des. (2014) http://dx.doi.org/10.1016/j.fusengdes.2013.11.007.

[24] T. Nishitani, T. Yamanishi, H. Tanigawa, M. Nakamichi, T. Nozawa, T. Hoshino and K. Ochiai, "Blanket material and technology developments toward DEMO under the broader approach framework", Fusion Engineering and Design, (2014) http://dx.doi.org/10.1016/j.fusengdes.2014.01.075.

[25] A. V. Panin, V. M. Chernov, M. V. Leontieva-Smirnova and E. A. Melnikova, "Strengthening of the RAFMS RUSFER-EK181 through nanostructuring surface layers", J. Nucl. Mater. 386–388 (2009) 466–470.

[26] A. V. Spitsyn, A. V. Golubeva, N. P. Bobyr, B. I. Khripunov, D. I. Cherkez, V. B. Petrov, M. Mayer, O. V. Ogorodnikova, V. Kh. Alimov, N. S. Klimov, A. Putrik, V. M. Chernov, M. V. Leontieva-Smirnova, Yu. M. Gasparyan and V.S. Efimov, "Retention of deuterium in damaged low-activation steel Rusfer (EK-181) after gas and plasma exposure", J. Nucl. Mater. 455 (2014) 561–567

[27] P. Mayr, T. A. Palmer, J. W. Elmer, E. D. Specht and S. M. Allen, "Formation of delta ferrite in 9 wt pct Cr steel investigated by in-situ X-ray diffraction using synchrotron radiation", Metall. Mater. Trans. A41 (2010) 2462-2465.

[28] M. Igarshi, S. Muneki and F. Abe, "Microstructure control of martensite phase matrix in advanced ferritic steels for USC boilers to achieve long term stability", in Materials for advanced power engineering – 6th Liege Conference (1998) 637-646.

[29] B. J. Ganesh, S. Raju, A. K. Rai, E. Mohandas, M. Vijayalakshmi, K. B. S. Rao, and B. Raj, "Differential scanning calorimetry study of diffusional and martensitic phase

transformations in some 9 wt% Cr low carbon ferritic steels", Mater. Sci. and Technol. 27(2) (2011) 500-512.

[30] K. Haarmann, J. C. Vaillant, W. Bendick and A. Arbab, The T91/P91 Book, Vallourec and Mannessmann Tubes, (1999) 14-29.

[31] H. Kitahara, R. Ueji, N. Tsuji and Y. Minamino, "Crystallographic features of lath martensite in low-carbon steel", Acta Mater 54 (2006) 1279-1288.

[32] S. Morito, H. Tanaka, R. Konishi, T. Furuhara and T. Maki, "The morphology and crystallography of lath martensite in Fe-C alloys", Acta Mater 51 (2003) 1789-1799.

[33] S. Morito, X. Huang, T. Furuhara, T. Maki and N. Hansen, "The morphology and crystallography of lath martensite in alloy steels", Acta Mater 54 (2006) 5323-5331.

[34] S. Nambu, N. Shibuta, M. Ojima, J. Inoue, T. Koseki and H.K.D.H. Bhadeshia, "In situ observations and crystallographic analysis of martensitic transformation in steel", Acta Mater 61 (2013) 4831-4839.

[35] H. K. D. H. Bhadeshia and S. R. Honeycombe, "Steels", 3rd Ed., Elsevier USA (2006).

[36] F. Abe, M. Taneike and K. Sawada, "Alloy design of creep resistant 9Cr steel using a dispersion of nano-sized carbonitrides", Int. J. Press. Vessel. Pip. 84 (2007) 3-12.

[37] S. Pillot, Z. Zhao, S. Corre, C. Chauvy, L. Coudreuse, P. Toussaint, Proc. of ASME 2010 Press. Vessel. Pip. Div. Conf. (PVP 2010) 1-14.

[38] M. Hättestrand and H. -O. Andrén, "Evolution of particle size distribution of precipitates in 9% chromium steel using energy filtered transmission electron microscopy", Micron, 32 (2001) 789-797.

[39] Å. Gustafson, M. Hättestrand, “Coarsening of precipitates in an advanced creep resistant 9% chromium steel—quantitative microscopy and simulations”, Mater. Sci. Eng. A333 (2002) 279-286.

[40] M. Hättestrand and H. -O. Andrén, “Influence of strain on precipitation reactions during creep of an advanced 9% chromium steel”, Acta Mater. 49 (2001) 2123-2128.

[41] F. Abe, “Effect of boron on creep deformation behaviour and microstructure evolution in 9% Cr steel at 650 degrees C”, Int. J. Mater. Res. 99 (2008) 387-394.

[42] H. -O. Andrén, “Combining TEM and APFIM techniques to study the microstructure of steels and hardmetals”, Micron 32 (2001) 713-719.

[43] M. Hättestrand, M. Schwind and H. -O. Andrén, “Microanalysis of two creep resistant 9-12% chromium steels”, Mater. Sci. Eng. A250 (1998) 27-36.

[44] M. Hättestrand and H. -O. Andrén, “Boron distribution in 9-12% chromium steels”, Mater. Sci. Eng. A270 (1999) 33-37.

[45] J. Janovec, A. Vyrostkova, M. Svoboda, A. Kroupa and H. J. Grabke, “Evolution of secondary phases in Cr-V low alloy steels during aging”, Metall. Mater. Trans A35 (2004) 751-759.

[46] K. Sawada, K. Kuho and F. Abe, “Creep behaviour and stability of MX precipitates at high temperatures in 9Cr-0.5Mo-1.8W-VNb steel”, Mater. Sci. Eng. A319-321 (2001) 784-787.

[47] K. Sawada, K. Kuho and F. Abe, “Contribution of coarsening of MX carbonitrides to creep strength degradation in high chromium ferritic steel” Mater. Sci. Technol. 19 (2003) 732-738.

[48] M. Taneike, K. Sawada and F. Abe, “Effect of carbon concentration on precipitation behaviour of $M_{23}C_6$ carbides and MX carbonitrides in martensitic 9Cr steel during heat treatment”, Metall. Mater. Trans. A35 (2004) 1255-1262.

[49] K. Yamada, M. Igarshi, S. Muneki and F. Abe, “Creep properties affected by morphology of MX in high-Cr ferritic steels”, ISIJ Intl. 41 (2001) S116-S120.

[50] M. Taneike, F. Abe and K. Sawada, “Creep-strengthening of steel at high temperatures using nano-sized carbonitride dispersions”, Nature, 424 (2003) 294–296.

[51] B. S. Ku and J. Yu, “Effects of Cu addition on the creep rupture properties of a 12% Cr steel”, Scripta Mater. 45 (2001) 205-211.

[52] L. Korcakova, J. Hald and M. A. J. Somers, “Quantification of laves phase particle size particle size in 9CrW steel”, Mater. Charac. 47 (2001) 111-117.

[53] Q. A. Li, “Precipitation of Fe_2W Laves phase and modelling of its direct influence on the strength of a 12Cr-2W steel”, Metall. Mater. Trans. A37 (2006) 89-97.

[54] Y. Murata, T. Koyama, M. Morinaga and T. Miyazaki, “Prediction of the Laves phase morphology in Fe-Cr-W-C quaternary steels with aid of system free energy concept”, ISIJ Intl. 42 (2002) 1423-1429.

[55] B. S. Ku and J. Yu, “Effects of Cu addition on the creep rupture properties of a 12% Cr steel”, Scripta Mater. 45 (2001) 205-211.

[56] A. Strang and V. Vodarek, “Z-phase formation in martensitic 12CrMoVNb steel”, Mater. Sci. Technol. 12 (1996) 552–556.

[57] A. Golpayegani, H.-O. Andrén, H. Danielsen, J. Hald, “A study on Z-phase nucleation in martensitic chromium steels”, Mater. Sci. Eng. A489 (2008) 310–318.

[58] K. Sawada, M. Taneike, K. Kimura and F. Abe, "Effect of nitrogen content on microstructural aspects and creep behaviour in extremely low carbon 9Cr heat-resistant steel", ISIJ Intl. 44 (2004) 1243–1249.

[59] L. Cipolla, H. K. Danielsen, D. Venditti, P. E. D. Nunzio, J. Hald, M. A. J. Somers, "Conversion of MX nitrides to Z-phase in a martensitic 12% Cr steel", Acta Mater. 58 (2010) 669–679.

[60] S. Kou, "Welding Metallurgy", 2nd ed., 2003, John Wiley & Sons, New Jersey.

[61] R. W. Messler, Jr., "Principles of Welding: Processes, Physics, Chemistry and Metallurgy", WILEY-VCH Verlag GmbH & Co. KGaA, Weinheim (2004).

[62] S. A. David, J. A. Siefert and Z. Feng, "Welding and weldability of candidate ferritic alloys for future advanced ultrasupercritical fossil power plants", Sci. Technol. Weld. Join. 18(8) (2013) 631 – 651.

[63] K. Laha, K. S. Chandravathi, P. Parameshwaran, K. B. S. Rao and S. L. Mannan, "Characterization of Microstructures across the Heat-Affected Zone of the Modified 9Cr-1Mo Weld Joint to Understand Its Role in Promoting Type IV Cracking", Metall. Mater. Trans. 38A (2007) 58 - 68.

[64] R. Mythili, P. V. Thomas, S. Saroja, M. Vijaylakshmi and V. S. Raghunathan, "Microstructural modification due to reheating in multipass manual metal arc welds of 9Cr-1Mo steel", J. Nucl. Mater. 312 (2003) 199-206.

[65] R. K. Shiue, K. C. Lan and C. Chen, "Toughness and austenite stability of modified 9Cr-1Mo welds after tempering", Mater. Sci. Eng. A 287 (2000) 10 - 16.

[66] B. Arivazhagan, S. Sundaresan and M. Kamaraj, “Effect of TIG arc surface melting process on weld metal toughness of modified 9Cr-1Mo (P91) steel”, Mater. Lett. 62 (2008) 2817 – 2820.

[67] P. K. Ghosh and U. Singh, "Influence of pre- and post- weld heating on weldability of modified 9Cr-1Mo (V-Nb) steel pipe under shielded metal arc and tungsten inert gas welding process”, Sci. Technol. Weld. Join. 9 (3) (2004) 229 - 236.

[68] T. Watanabe, M. Tabuchi, M. Yamazaki, H. Hongo and T. Tanabe, “Creep damage evaluation of 9Cr-1Mo-V-Nb steel welded joints showing Type IV fracture”, Int. J. Press. Vessel Pip. 83 (2006) 63–71.

[69] H. Hongo, M. Tabuchi and T. Watanabe, “Type IV Creep Damage Behavior in Gr.91 Steel Welded Joints”, Metall. Mater. Trans. 43A (2012) 1163 – 1173.

[70] P. Kumar, “An Overview of Welding and Fabrication Aspects during Manufacture of Nuclear Reactor Components for 500 MWe Prototype Fast Breeder Reactor”, Proc. of International Welding Congress 2014 (IWC 2014), New Delhi, India (2014).

[71] J.-P. Barthoux, “Narrow gap welding of heavy wall thickness materials in nuclear and fossil fuel industries”, Focus on Nuclear Power Generation, November 2008, pp. 36 – 42. Retrieve from http://www.nuclear-exchange.com/pdf/TP_Polysounde.pdf on August 16, 2014.

[72] B. Arivazhagan and M. Vasudevan, “A comparative study on the effect of GTAW processes on the microstructure and mechanical properties of P91 steel weld joints”, J. of Manuf. Proc. 16 (2014) 305 – 311.

[73] S. Sulaiman, “Structure of properties of the heat affected zone of P91 creep resistant steel”, PhD Thesis, University of Wollongong, Wollongong, Australia (2007) [http://ro.uow.edu.au/theses/777].

[74] B. Arivazhagan, S. Sundaresan and M. Kamaraj, “A study on influence of shielding gas composition on toughness of flux-cored arc weld of modified 9Cr–1Mo (P91) steel”, Journal of Materials Processing Technology 209 (2009) 5245 – 5253.

[75] S. Paddea, J. A. Francis, A. M. Paradowska, P. J. Bouchard and I. A. Shibli, "Residual stress distribution in a P91 steel-pipe girth weld before and after post weld heat treatment", Mater. Sci. Eng. A534 (2012) 663 - 672.

[76] P. Mayr, “Weldability of Modern 9%Cr Steels for Application in USC Power Plants”, PhD Thesis, Graz University of Technology (2007).

[77] J. Parker, “Factors affecting type IV creep damage in Grade 91 steel welds”, Mater. Sci. Eng. A578 (2013) 430 – 437.

[78] L. Commin, M. Reith, B. Dafferner, H. Zimmermann, D. Bolich, S. S. Baumgärtner, R. Ziegler, S. Dichiser, T. Fabry, S. Fischer, W. Hildebrand, O. Palussek, H. Ritz and A. Sponda, “A fail-safe and cost effective formation route for blanket first wall”, J. Nucl. Mater. 442 (2013) 538 – 541.

[79] H. Kishimoto, T. Ono, H. Sakasegawa, H. Tanigawa, Y. Konho and A. Kohyama, “Toughness characterization by small punch specimen test technique for HIPed joints of F82H steel aiming at first wall fabrication in fusion”, J. Nucl. Mater. 440 (2013) 622 – 626.

[80] H. Kishimoto, T. Ono, H. Saasegawa, H. Tanigawa, M. Ando, T. Shibayama, Y. Konho and A. Kohyama, “Oxide formation and precipitation behaviors on interface of

F82H steel joints during HIPing and hot pressing”, J. Nucl. Mater. 442 (2013) S546 – S 551.

[81] R. Bhattacharya, Indian TBM Team, “Status of Indian LLCB TBM program and R&D activities”, Fus. Eng. Des. 89 (2014) 1107 – 1112.

[82] B. Huang, Y. Zhai, J. Zhang, C. Li and Q. Wu, “First wall fabrication of 1/3 scale china dual functional lithium lead blanket”, Fus. Eng. Des. 89 (2014) 1181 – 1185.

[83] A. Kundu, P. J. Bouchard, S. Kumar, K. A. Venkata, J. A. Francis, A. Paradowska, G. K. Dey and C. E. Truman, “Residual stresses in P91 steel electron beam welds”, Sci. Technol. Weld. Join. 18(1) (2013) 70 – 75.

[84] W. M. Steen and J. Mazumder, “Laser material processing”, 2010, 4th ed., Springer, 2010.

[85] W. H. Lee, R. K. Shiue and C. Chen, “Mechanical properties of modified 9Cr-1Mo steel welds with notches”, Mater. Sci. Eng. A356 (2003) 153 - 161.

[86] Z. Xu, “Laser welding and post weld heat treatment of modified 9Cr-1VNb steel”, Report No. ANL/NE-12/12, Argonne National Laboratory, Chicago, Illinois (2008).

[87] B. Shanmugarajan, G. Padmanabham, H. Kumar, S. K. Albert and A. K. Bhaduri, “Autogenous laser welding investigations on modified 9Cr-1Mo (P91) steel”, Sci. Technol. Weld. Join. 16(6) (2011) 528 - 534.

[88] Y. V. Harinath, K. A. Gopal, S. Murugan and S. K. Albert, “Study on laser welding of fuel clad tubes and end plugs made of modified 9Cr-1Mo steel for metallic fuel of Fast Breeder Reactors”, J. Nucl. Mater. 435 (2013) 32 - 40.

[89] A. Cardella, E. Rigal, L. Bedel, Ph. Bucci, J. Fiek, L. Forest, L.V. Boccaccini, E. Diegele, L. Giancarli, S. Hermsmeyer, G. Janeschitz, R. Lässer, A. Li Puma, J. D.

Lulewicz, A. Möslang, Y. Poitevin, E. Rabaglino, “The manufacturing technologies of the European breeding blankets”, J. Nucl. Mater. 329 - 333 (2004) 133 - 140.

[90] H. Tanigawa, T. Hirose, K. Shiba, R. Kasada, E. Wakai, H. Serizawa, Y. Kawahito, S. Jitsukawa, A. Kimura, Y. Kohno, A. Kohyama, S. Katayama, H. Mori, K. Nishimoto, R.L. Klueh, M.A. Sokolov , R.E. Stoller , S.J. Zinkle, “Technical issues of reduced activation ferritic/martensitic steels for fabrication of ITER test blanket modules”, Fus. Eng. Des. 83 (2008) 1471–1476.

[91] H. Serizawa, S. Nakamura, M. Tanaka, Y. Kawahito, H. Tanigawa, S. Katayama, “Effect of mechanical restraint on weldability of reduced activation ferritic/martensitic steel thick plates”, J. Nucl. Mater. 417 (2011) 55 - 58.

[92] H. Serizawa, D. Mori, Y. Shirai, H. Ogiwara, H. Mori, “Weldability of dissimilar joint between F82H and SUS316L under fiber laser welding”, Fus. Eng. Des. 88 (2013) 2466 - 2470.

[93] P. Aubert, F. Tavassoli, M. Reith, E. Diegele and Y. Poitevin, “Review of candidate welding processes of RAFM steels for ITER test blanket modules and DEMO”, J. Nucl. Mater. 417 (2011) 43 - 50.

[94] D. J. Hughes, E. Koukovini-Platia, E. L. Heeley, “Residual stress in a laser welded EUROFER blanket assembly using non-destructive neutron diffraction techniques”, Fusion Eng. Des. (2014), http://dx.doi.org/10.1016/j.fusengdes.2013.12.041.

[95] R. C. Reed and H. K. D. H. Bhadesia, “A Simple Model for Multipass Steel Welds”, Acta Metall. Mater. 42(11) (1994) 3663 - 3678.

[96] H. C. Carslaw and J. C. Jaeger, “Conduction of heat in solids”, 1997, Oxford Science Publications, Oxford, UK.

[97] D. Rosenthal, “The theory of moving sources of heat and its application to metal treatments”, Trans. Amer. Soc. Mech. Eng. 68 (1946) 849 – 866.

[98] J. Goldak, A. Chakravarti and M. Bibby, “A new finite-element model for welding heat-sources”, Metall. Mater. Trans. B15 (2) (1984) 299 - 305.

[99] T. Zacharia, A. H. Eraslan, D. K. Aidun and S. A. David, “3-dimensional transient model for arc-welding process”, Metall. Mater. Trans. B20(5) (1989) 645 - 659.

[100] R. L. Ule, Y. Joshi and E. B. Sedy, “A new technique for 3-dimensional transient heat-transfer computations of autogenous arc-welding”, Metall. Mater. Trans. B21(6) (1990) 1033 - 1047.

[101] T. Zacharia, S. A. David and J. M. Vitek, “Effect of evaporation and temperature-dependent material properties on weld pool development”, Metall. Mater. Trans. B22(2) (1991) 233 - 241.

[102] R. T. C. Choo, J. Szekely and R. C. Westhoff, “On the calculation of the free-surface temperature of gas-tungsten-arc weld pools from 1st principles: Part I. modelling the welding arc”, Metall. Mater. Trans. B23(3) (1992) 357 -369.

[103] S. Kumar and S. C. Bhaduri, “3-dimensional finite-element modelling of gas metal-arc welding”, Metall. Mater. Trans. B25(3) (1994) 435 - 441.

[104] S. Kumar and S. C. Bhaduri, “Theoretical investigation of penetration characteristics in gas metal-arc welding using finite-element method”, Metall. Mater. Trans. B26(3) (1995) 611 - 624.

[105] G. Ravichandran, V. P. Raghupathy and N. Ganesan, “Analysis of temperature distribution during circumferential welding of cylindrical and spherical components using the finite element method”, Comput. Struct. 59 (1996) 225 - 255.

[106] J. Haidar and J. J. Lowke, “Predictions of metal droplet formation in arc welding”, J. Phys. D29 (12) (1996) 2951 - 2960.

[107] M. A. Wahab and M. J. Painter, “Numerical models of gas metal arc welds using experimentally determined weld pool shapes as the representation of the welding heat source”, Int. J. Press. Vessel. Pip. 73(1997) 153 - 159.

[108] M. Ushio and C. S. Wu, “Mathematical modelling of three-dimensional heat and fluid flow in a moving gas metal arc weld pool”, Metall. Mater. Trans. B28(3) (1997) 509 - 516.

[109] G. H. Little and A. G. Kamtekar, “The effect of thermal properties and weld efficiency on transient temperatures during welding”, Comput. Struct. 68 (1998) 157 - 165.

[110] I. S. Kim and A. Basu, “A mathematical model of heat transfer and fluid flow in the gas metal arc welding process”, J. Mater. Process. Technol. 77 (1998) 17–24.

[111] W. H. Kim and S. J. Na, “Heat and fluid flow in pulsed current GTA weld pool”, Int. J. Heat Mass Transfer 41 (1998) 3213 -3227.

[112] L. A. Jones, T. W. Eagar and J. H. Lang, “A dynamic model of drops detaching from a gas metal arc welding electrode”, J. Phys. D31(1) (1998) 107 - 123.

[113] M. A. Wahab, M. J. Painter and M. H. Davies, “The prediction of the temperature distribution and weld pool geometry in the gas metal arc welding process”, J. Mater. Process. Technol. 77 (1998) 233 - 239.

[114] C. S. Wu and J. S. Sun, “Modelling the arc heat flux distribution in GMA welding”, Comput. Mater. Sci. 9 (1998) 397 - 402.

[115] C. S. Wu, W. Zheng and L. Wu, “Modelling the transient behaviour of pulsed current tungsten-inert-gas weld pools”, Modell. Simul. Mater. Sci. Eng. 7 (1999) 15 - 23.

[116] Z. Yang and T. DebRoy, “Modelling macro-and microstructures of gas-metal-arc welded HSLA-100 steel”, Metall. Mater. Trans. B30(3) (1999) 483 - 493.

[117] A. Bachorski, M. J. Painter, A. J. Smailes and M. A. Wahab, “Finite-element prediction of distortion during gas metal arc welding using the shrinkage volume approach”, J. Mater. Process. Technol. 93 (1999) 405 - 409.

[118] S. Ohring and H. J. Lugt, “Numerical simulation of a time-dependent 3-D GMA weld pool due to a moving arc”, Weld. J. 78 (1999) 416S - 424S.

[119] R. Komanduri and Z. B. Hou, “Thermal analysis of the arc welding process: part I. General solutions”, Metall. Mater. Trans. B31(6) (2000) 1353 - 1370.

[120] X. T. Tian and Q. Y. Shi, “Preventing welding hot cracking by welding with an intensive trailing cooler”, J. Mater. Process. Technol. 97 (2000) 30 - 34.

[121] E. A. Bonifaz, “Finite element analysis of heat flow in single-pass arc welds”, Weld. J. 79 (2000) 121S - 125S.

[122] Y. Wang and H. L. Tsai, “Effects of surface active elements on weld pool fluid flow and weld penetration in gas metal arc welding”, Metall. Mater. Trans. B32(3) (2001) 501 - 515.

[123] Y. Wang and H. L. Tsai, “Impingement of filler droplets and weld pool dynamics during gas metal arc welding process”, Int. J. Heat Mass Transfer 44 (2001) 2067 - 2680.

[124] R. Komanduri and Z. B. Hou, “Thermal analysis of the arc welding process: part II. Effect of variation of thermophysical properties with temperature”, Metall. Mater. Trans. B32(3) (2001) 483 - 499.

[125] S. W. Wen, P. Hilton and D. C. J. Farrugia, “Finite element modelling of a submerged arc welding process”, J. Mater. Process. Technol. 119 (2001) 203 - 209.

[126] A. A. Reddy, B. Guha and D. R. G. Achar, “Finite element modelling of three-dimensional transient heat transfer in stainless steel (304) pulsed GTA weldments”, Numer. Heat Transfer A - Appl. 41 (2002) 41 - 46.

[127] J. Mackerle, “Finite element analysis and simulation of welding: a bibliography (1976–1996)”, Model. Simul. Mater. Sci. Eng., 4 (1996) 501 – 533.

[128] J. Mackerle, “Finite element analysis and simulation of welding - an addendum: a bibliography (1996–2001)”, Model. Simul. Mater. Sci. Eng., 10 (2002) 295-318.

[129] A. H. Yaghi, T. H. Hyde, A. A. Becker, J. A. Williams and W. Sun, “Residual stress simulation in welded sections of P91 pipes”, J. Mater. Process. Technol. 167 (2005) 480 - 487.

[130] D. Dean and M. Hidekazu, “Prediction of welding residual stress in multi-pass butt-welded modified 9Cr–1Mo steel pipe considering phase transformation effects”, Comput. Mater. Sci. 37 (2006) 209 - 219.

[131] S. H. Kim, J. B. Kim and W. J. Lee, “Numerical prediction and neutron diffraction measurement of residual stresses for a modified 9Cr-1Mo steel weld”, J. Mater. Process. Technol. 209 (2009) 3905 - 3913.

[132] J. W. H. Price, A. Z. Paradowska, S. Joshi, T. Finlayson, C. Semetay and H. Nied, "Comparison of experimental and theoretical residual stresses in welds: the issue of gauge volume", Int. J. Mech. Sci. 50 (2008) 513 - 521.

[133] S. K. Bate, R. Charles and A. Warren, "Finite element analysis of a single bead-on-plate specimen using SYSWELD", Int. J. Press. Vessel. Pip. 86 (2009) 73 - 78.

[134] A. S. Aloraier and S. Joshi, "Residual stresses in flux cored arc welding process in bead-on-plate specimens", Mater. Sci. Eng. A534 (2012) 13 - 21.

[135] J. J. Xu, P. Gilles, Y. G. Duan and C. Yu, "Temperature and residual stress simulations of the NeT single-bead-on-plate specimen using SYSWELD", Int. J. Press. Vessel. Pip. 99 - 100 (2012) 51 - 60.

[136] ESI Group, SYSWELD, Theory Manuals, ESI France, 2012.

[137] S. Joshi, J. Hildebrand, A. S. Aloraier and T. Rabczuk, "Characterization of material properties and heat source parameters in welding simulation of two overlapping beads on a substrate", Comput. Mater. Sci. 69 (2013) 559 - 565.

[138] S. Joshi, C. Semetay, J. W. H. Price, H. F. Nied, "Weld-induced residual stresses in a prototype dragline cluster and comparison with design codes", Thin-Walled Struct. 48 (2010) 89 - 102.

[139] S. A. Tsirkas, P. Papanikos, Th. Kermanidis, "Numerical simulation of the laser welding process in butt-joint specimen", J. Mater. Process. Technol. 134 (2003) 59 - 69.

[140] G. A. Moraitis and G. N. Labeas, "Prediction of residual stresses and distortions due to laser beam welding of butt joints in pressure vessels", Int. J. Press. Vessel. Pip. 86 (2009) 133 - 142.

[141] N. S. Shanmugam, G. Buvanashekaran, K. Sankaranarayanasamy and S. R. Kumar, “A transient finite element simulation of the temperature and bead profiles of T-joint laser welds”, Mater. Des. 31 (2010) 4528 - 4542.

[142] M. Lax, “Temperature rise induced by a laser beam”, J. Appl. Phys. 48 (1977) 3919 - 3924.

[143] Y. I. Nissim, A. Lietoila, R. B. Gold and J. F. Gibbons, “Temperature distributions produced in semiconductors by a scanning elliptical or circular CW laser beam”, J. Appl. Phys. 51 (1980) 274 - 279.

[144] T. Miyazaki and W. H. Giedt, “Heat-transfer from an elliptical cylinder moving through an infinite-plate applied to electron-beam welding”, Int. J. Heat Mass Transfer 25 (1982) 807 - 814.

[145] W. M. Steen, J. Dowden, and M. Davis, P. Kapadia, “A point and line source model of laser keyhole welding”, J. Phys. D21(8) (1988) 1255 - 1260.

[146] J. Dowden, M. Davis and P. Kapadia, “Some aspects of the fluid-dynamics of laser-welding”, J. Fluid Mech. 126 (1983) 123 - 146.

[147] C. Chan, J. Mazumder, M. M. Chen, “A 2-dimensional transient model for convection in laser melted pool”, Metall. Mater. Trans. A15 (1984) 2175 2184.

[148] T. Chande and J. Mazumder, “Estimating effects of processing conditions and variable properties upon pool shape, cooling rates, and absorption-coefficient in laser-welding”, J. Appl. Phys. 56 (1984) 1981 - 1986.

[149] M. Davis, P. Kapadia and J. Dowden, “Solution of a Stefan problem in the theory of laser-welding by the method of lines”, J. Comput. Phys. 60(1985) 534 - 538.

[150] S. Kou and Y. H. Wang, "Three-Dimensional Convection in Laser Melted Pools", Metall. Trans. A17 (1986) 2265 - 2270.

[151] C. L. Chan, J. Mazumder and M. M. Chen, "3-dimensional axisymmetrical model for convection in laser-melted pools", Mater. Sci. Technol. 3 (1987) 306 - 311.

[152] R. Akhter, M. Davis, J. Dowden, P. Kapadia, M. Ley and W. M. Steen, "A method for calculating the fused zone profile of laser keyhole welds", J. Phys. D22(1) (1989) 23 - 28.

[153] K. N. Lankalapalli, J. F. Tu, K. H. Leong and Gartner M, "Laser weld penetration estimation using temperature measurements", J. Manuf. Sci. Eng.-Trans ASME 121 (1999) 179 - 188.

[154] W. Hamoudi and R. Ducharme, "Keyhole welding of C-Mn steel using a 10kW CO_2 laser", Int. J. Join. Mater. 8 (1996) 30-36.

[155] J. M. Dowden, "The Mathematics of Thermal Modelling: An Introduction to the Theory of Laser Material Processing", 2001, Chapman and Hall / CRC Press, New York.

[156] P. G. Klemens, "Heat balance and flow conditions for electron beam and laser welding", J. Appl. Phys. 47 (1976) 2165 - 2174.

[157] J. G. Andrews and D. R. Atthey, "Hydrodynamic limit to penetration of a material by a high-power beam", J. Phys. D9 (1976) 2181 - 2184.

[158] J. Dowden, N. Postaciouglu, M. Davis and P. Kapadia, "A keyhole model in penetration welding with a laser", J. Phys. D20 (1987) 36 - 44.

[159] N. Postaciouglu, P. Kapadia, M. Davis and J. M. Dowden, “Upwelling in the liquid region surrounding the keyhole in penetration welding with a laser”, J. Phys. D20 (1987) 340 - 345.

[160] J. Dowden, S. C. Wu, P. Kapadia and C. Strange, “Dynamics of the vapour flow in the keyhole in penetration welding with a laser at medium welding speeds”, J. Phys. D24 (1991) 519 - 532.

[161] A. Kar, T. Rockstroh and J. Mazumder, “2-dimensional model for laser-induced materials damage-effects of assist gas and multiple reflections inside the cavity”, J. Appl. Phys. 71 (1992) 2560 - 2569.

[162] E. A. Metzbower, “Keyhole formation”, Metall. Mater. Trans. B24 (1993) 875 - 880.

[163] C. Tix and G. Simon, “A transport theoretical-model of the keyhole plasma in penetration laser-welding”, J. Phys. D26 (1993) 2066 - 2074.

[164] T. Klein, M. Vicanek, J. Kroos, I. Decker and G. Simon, “Oscillations of the keyhole in penetration laser-beam welding”, J. Phys. D27 (1994) 2023 - 2030.

[165] A. Kar and J. Mazumder, “Mathematical-modelling of key-hole laser-welding”, J. Appl. Phys. 78 (1995) 6353 - 6360.

[166] P. Solana and G. Negro, “A study of the effect of multiple reflections on the shape of the keyhole in the laser processing of materials”, J. Phys. D30 (1997) 3216 - 3222.

[167] P. Solana and J. L. Ocana, “A mathematical model for penetration laser welding as a free-boundary problem”, J. Phys. D30 (1997) 1300 - 1313.

[168] A. Matsunawa and V. Semak, “The simulation of front keyhole wall dynamics during laser welding”, J. Phys. D30 (1997) 798–809.

[169] P. Kapadia, P. Solana and J. Dowden, “Stochastic model of the deep penetration laser welding of metals”, J. Laser Appl. 10 (1998) 170 - 173.

[170] R. Fabbro and K. Chouf, “Keyhole modelling during laser welding”, J. Appl. Phys. 87 (2000) 4075 – 4083.

[171] R. Fabbro and K. Chouf, “Dynamical description of the keyhole in deep penetration laser welding”, J. Laser Appl. 12 (2000) 142 - 148.

[172] H. Ki, P. S. Mohanty and J. Mazumder, “Modelling of Laser Keyhole Welding: Part I. Mathematical Modelling, Numerical Methodology, Role of Recoil Pressure, Multiple Reflections and Free Surface Evolution”, Metall. Mater. Trans. 33A (2002) 1817 - 1830.

[173] H. Ki, P. S. Mohanty and J. Mazumder, “Modelling of Laser Keyhole Welding: Part II. Simulation of Keyhole Evolution, Velocity, Temperature Profile and Experimental Verification”, Metall. Mater. Trans. 33A (2002) 1831 - 1842.

[174] R. Rai, S. M. Kelly, R. P. Martukanitz and T. Debroy, “A Convective Heat-Transfer Model for Partial and Full Penetration Keyhole Mode Laser Welding of a Structural Steel”, Metall. Mater. Trans. 39A (2008) 98 - 112.

[175] A. P. Mackwood, R. C. Crafer, “Thermal modelling of laser welding and related processes: a literature review”, Optics Laser Technol. 37 (2005) 99 - 115.

[176] N.S. Rossini, M. Dassisti, K. Y. Benyounis and A.G. Olabi, “Methods of measuring residual stresses in components”, Mater. Des. 35 (2012) 572 - 588.

[177] N. Tebedge, G. Alpsten and L. Tall, “Residual-stress measurement by the sectioning method”, Exp. Mech. 13(2) (1973) 88 – 96.

[178] A. T. DeWald and M. R. Hill, “Multi-axial contour method for mapping residual stresses in continuously processed bodies”, Exp. Mech. 46 (2006) 473 - 490.

[179] N. Murugan and R. Narayanan, “Finite element simulation of residual stresses and their measurement by contour method”, Mater. Des. 30(6) (2009) 2067 - 2071.

[180] A. G. Olabi and M. S. J. Hashmi, “Stress relief procedures for low carbon steel (1020) welded components”, J. Mater. Process. Technol. 56 (1996) 552 - 562.

[181] A. Ajovalasit, G. Petrucci and B. Zuccarello, “Determination of non-uniform residual stresses using the ring-core method”, J. Mater. Process. Technol. 118(2) (1996) 224 - 224.

[182] R. H. Leggatt, D. J. Smith, S. D. Smith and F. Faure, “Development and experimental validation of the deep hole method for residual stress measurement”, J. Strain Anal. 31(3) 177 - 186.

[183] A. T. DeWald and M. R. Hill, “Improved data reduction for the deep hole method of residual stress measurement”, J. Strain Anal. 38(1) (2003) 65 - 78.

[184] D. M. Stewart, K. J. Stevens and K. B. Kaiser, “Magnetic Barkhausen noise analysis of stress in steel”, Curr. Appl. Phys. 4(2-4) (2004) 308–311.

[185] H. Y. Ilker, C. Ibrahim and C. G. Hakan, “Non-destructive determination of residual stress state in steel weldments by Magnetic Barkhausen Noise technique, NDT&E Int. 43 (2010) 29-33.

[186] F. Balahcene and J. Lu, “Study of residual stress induced in welded steel by surface longitudinal ultrasonic method”, Proc. SEM Annual Conference on Theoretical, Experimental and Computational Mechanics (1999) 331–334.

[187] T. Leon-Salamanca and D. E. Bray, “Residual stress measurement in steel plates and welds using critically refracted waves”, Res. Nondestruct. Eval. 7(4) (1996) 169–184.

[188] J. H. Norton and D. Rosenthal, “Stress measurement by x-ray diffraction”, Proc. Soc. Exp. Stress Anal., 1(2) (1944) 73–76.

[189] J. H. Norton, D. Rosenthal, Stress measurement by x-ray diffraction, Proc. Soc. Exp. Stress Anal., 1(2) (1944) 81–90. [Very old, consider change]

[190] P. J. Withers, "Mapping residual and internal stress in materials by neutron diffraction", C. R. Phys. 8 (2007) 806 - 820

[191] S. -H. Kim, J. -B. Kim and W. -J Lee “Numerical prediction and neutron diffraction measurement of residual stress for a modified 9Cr-1Mo steel weld”, J. Mater. Process. Technol. 209 (2009) 3905-3913.

[192] G. A. Webster and R. C. Wempory, "Non-destructive measurement of residual stress by neutron diffraction", J. Mater. Process. Technol. 117 (2001) 395 - 399.

[193] W. Wanchuck, E. M. Vyacheslav, M. Pavel, A. Gyu-Baek and B. -S. Seong, "Neutron diffraction measurements of residual stresses in a 50mm thick weld", Mater. Sci. Eng. A528 (2011) 4120 - 4124.

[194] M. J. Park, H. N. Yang, D. Y. Jang, J. S. Kim and T. E. Jin, "Residual stress measurement on welded specimen by neutron diffraction", J. Mater. Process. Technol. 155 - 156 (2004) 1171 - 1177.

[195] A. Paradowska, J. W. H. Price, R. Ibrahim and T. Finlayson, "A neutron diffraction study of residual stress due to welding", J. Mater. Process. Technol. 164 - 165 (2005) 1099 - 1105.

[196] J. W. H. Price, A. Paradowska, S. Joshi and T. Finlayson, "Residual stresses measurement by neutron diffraction and theoretical estimation in a single weld bead", Int. J. Press. Vessel. Pip. 83 (2006) 381 - 387.

[197] M. Hofmann and R. C. Wimpory, "NET TG1: Residual stress analysis on a single bead weld on a steel plate using neutron diffraction at the new engineering instrument ‘STRESS-SPEC’", Int. J. Press. Vessel. Pip. 86 (2009) 122 - 125.

[198] C. Ohms, R. C. Wimpory, D. E. Katsareas and A. G. Youtsos, "NET TG1: Residual stress assessment by neutron diffraction and finite element modelling on a single bead weld on a steel plate", Int. J. Press. Vessel. Pip. 86 (2009) 63 - 72.

[199] S. Pratihar, M. Turski, L. Edwards and P. J. Bouchard, "Neutron diffraction residual stress measurements in a 316L stainless steel bead-on-plate weld specimen", Int. J. Press. Vessel. Pip. 86 (2009) 13 - 19.

[200] D. Thibault, P. Bocher, M. Thomas, M. Gharghouri and M. Côté, "Residual stress characterization in low transformation temperature 13%Cr–4%Nistainless steel weld by neutron diffraction and the contour method", Mater. Sci. Eng. A527 (2010) 6205 - 6210.

[201] W. Wanchuck, E. M. Vyacheslav, C. R. Hubbard, J. H. Lee and S. P. Kwang, "Residual stress determination in a dissimilar weld overlay pipe by neutron diffraction", Mater. Sci. Eng. A528 (2011) 8021 - 8027.

[202] M. Rogante, P. Battistella and F. Rustichelli, "Residual stress measurement by neutron diffraction in AA6082 extruded samples submitted to different quenching rates", J. Alloy. Compd. 378 (2004) 335 - 338.

[203] W. Suder, S. Ganguly, S. Williams, A. M. Paradowska and P. Colegrove, “Comparison of joining efficiency and residual stresses in laser and laser hybrid welding”, Sci. Technol. Weld. Join. 16(3) (2011) 244 - 248.

[204] D. W. Brown, T. M. Holden, B. Clausen, M. B. Prime, T. A. Sisneros, H. Swenson and J. Vaja, "Critical comparison of two independent measurements of residual stress in

an electron-beam welded uranium cylinder: Neutron diffraction and the contour method", Acta Mater. 59 (2011) 864 -873.

[205] S. Ganguly, L. Edwards and M. E. Fitzpatrick, “Problems in using a comb sample as a stress-free reference for the determination of welding residual stress by diffraction”, Mater. Sci. Eng. A528(3) (2010) 1226 - 1232.

[206] A. Kundu, P. J. Bouchard, S. Kumar, G. K. Dey, “Characterisation of Residual Stress in Electron Beam Welded P91 Plates by Neutron Diffraction”, Int. J. Metall. Eng. 2(1) (2013) 79 - 84.

Chapter 3: Materials and Methods

3.1 Description of the Material

ASTM A387 Gr91 steel plates of different thicknesses 6, 10, 30 mm; procured from M/s. Industeel, Belgium in normalized (heated to 1050^{o}C, soaked for 30 min and air cooled) and tempered (heated to 770^{o}C, soaked for 30 min and air cooled) condition, were used in the present study. This is 9Cr-1Mo steel modified with microalloying additions of V and Nb.

3.1.1 Chemistry

Chemical composition of the material, in the test certificate provided by the manufacturer, is presented in Table 3.1. Chemical composition of the material was reconfirmed by carrying out chemical analysis at Analytical Chemistry Division (ACD) of Bhabha Atomic Research Centre (BARC), Mumbai.

Table 3.1: Chemical composition of the steel in wt. % (balance Fe)

	Cr	Mo	C	V	Nb	Mn	Si	P	S	Al	N	Ni	Cu
Test Certificate	8.965	0.901	0.106	0.194	0.073	0.443	0.221	0.018	0.0008	0.010	0.0464	0.212	0.045
ACD, BARC	8.95	0.90	0.11	0.20	0.07	-	-	-	-	-	-	-	-

3.1.2 Mechanical Properties

Tensile properties of the material, as reported in the test certificate, are presented in Table 3.2. These properties were confirmed by carrying out tensile test.

Table 3.2: Tensile properties of 9Cr-1Mo(V, Nb) FMS in as-received condition.

Tensile Properties	Yield Strength (MPa)	Ultimate Tensile Strength (MPa)	%Elongation (A50)
Test Certificate	545	692	24
Our Results	550$\pm$10	710$\pm$10	20$\pm$1

3.2 Experimental Methods

3.2.1 Dilatometry of the Parent Material

Dilatometry was performed using a horizontal dual push-rod type dilatometer (make: MAC Science Co. Ltd., Japan, model: TD 5000S) to characterize the solid state phase transformations – ferrite to austenite on heating and austenite to martensite on cooling. For this purpose, a cylindrical pin (length 14.91 mm and diameter 4 mm) was used as the sample and a cylindrical alumina pin was used as the reference. The sample and the reference pins were heated simultaneously at a rate of 10^{o}C/min from room temperature to 1060^{o}C; soaked for 30 min and cooled to room temperature at 10^{o}C/min. In addition to the phase transformation temperatures, these experiments also provided the coefficients of linear expansion for the three phases – ferrite, austenite and martensite, which were used as inputs for modelling and simulation of laser welding of this steel. The strain associated with these phase transformations is expected to have a significant bearing on the residual stress profile. Therefore, these experiments provided important material data, for example, transformation temperatures and the strain associated with these transformations, for the modelling and simulation of laser welding.

In addition, a set of dilatometric experiments were performed to study the effect of austenitization temperature on the transformation behaviour of the austenite while cooling. For this purpose, the cylindrical pins (15 mm length and 4 mm diameter) made of this steel were heated to different austenitization temperatures – 850^{o}C, 950^{o}C, 1050^{o}C and 1150^{o}C at a rate of 10^{o}C/min and then cooled to room temperature at the same rate, without any soaking at austenitization temperature. The purpose of these experiments was to study transformation behaviour of austenite while cooling in the

HAZ during a welding thermal cycle where the material experiences different austenitization temperatures and hardly any soaking time.

3.2.2 Laser Welding

Laser welding was carried out using high power continuous wave CO_2 laser, (make: Trumpf Laser, Germany, model: TruFlow 10000) with 10 kW maximum power, mounted on a 5-axis CNC machine. The welding head was equipped with a focusing optics of 280 mm focal length, which provided a focused beam diameter of about 0.5 mm. Helium gas at a flow rate of 20 litres per minute was used for shielding the hot and / or molten metal against oxidation and also for avoiding formation of plasma at the work piece surface. The laser welding machine and the set up used for making the weld joints reported in this study are shown in Fig. 3.1. This set up was used for making the weld beads and the weld joints, details of which are presented in the subsequent sections.

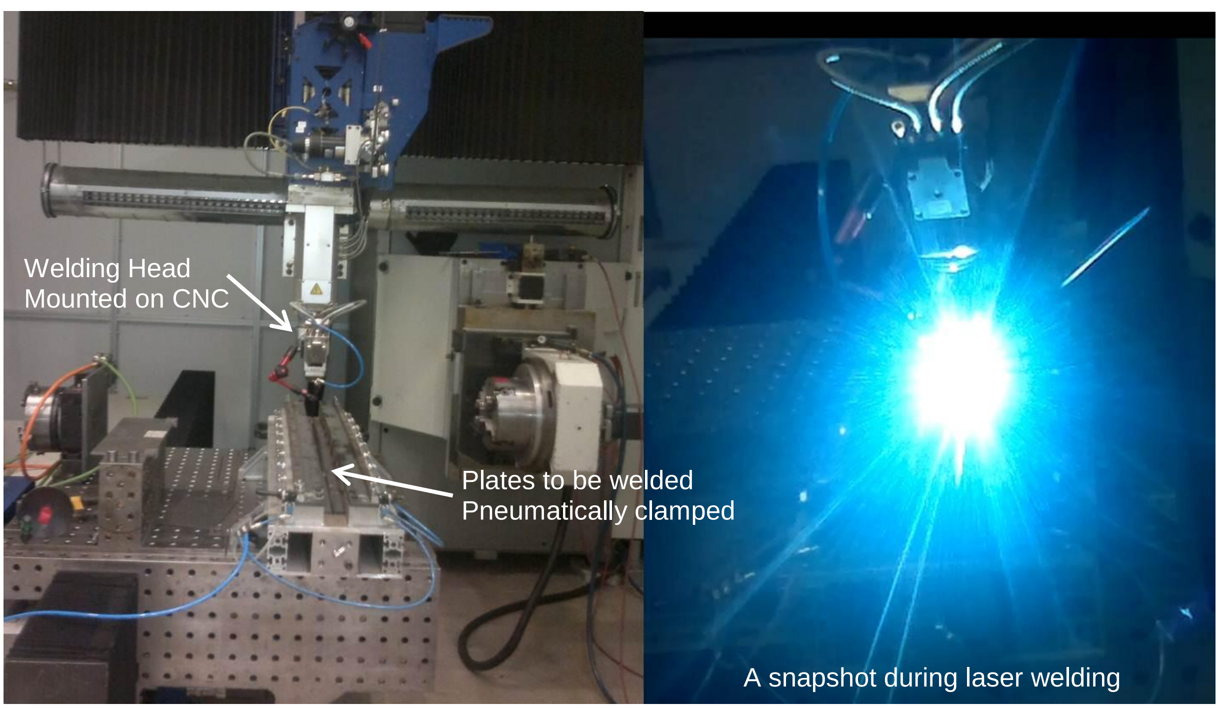

Fig. 3.1: Laser welding set up and a snap shot during laser welding of 9 mm thick plates of 9Cr-1Mo(V, Nb) FMS in square butt configuration.

3.2.2.1 Bead on Plate

Weld beads were produced on 30 mm thick plates of 9Cr-1Mo(V, Nb) FMS. Laser power was varied in 2 - 8 kW range and welding speed was varied in 0.5 - 5.0 m/min range. A total number of 22 weld beads, each of 200 mm length, were produced for different laser power – welding speed combination, details of which are presented in Table 3.3. The purpose of the bead on plate experiments was to generate a process parameter window for selecting optimum parameters for making full penetration sound weld joints with narrow fusion zone and HAZ. All the weld beads showed smooth and continuous appearance and no visible defect. The weld beads thus produced were sectioned to measure depth of penetration for each of the laser power – welding speed combinations.

Table 3.3: Details of Bead on Plate Experiments.

Sl. No.	Laser Power (kW)	Power Density (MW/cm^2)	Welding Speed (m/min)	Interaction Time (ms)	Remarks
1	2	1.02	0.5	60	Wide Bead
2			1.0	30	Narrow Bead
3			1.5	20	Narrow Bead
4			2.0	15	Narrow Bead
5			3.0	10	Narrow Bead
6	4	2.04	0.5	60	Wide Bead
7			1.0	30	Narrow Bead
8			2.0	15	Narrow Bead
9			3.0	10	Narrow Bead
10			4.0	7.5	Very Narrow Bead
11	6	3.06	1.0	30	Wide Bead
12			2.0	15	Narrow Bead
13			3.0	10	Narrow Bead
14			4.0	7.5	Very Narrow Bead
15			5.0	6	Very Narrow Bead
16	8	4.08	0.5	60	Very wide Bead
17			1.0	30	Wide Bead
18			1.5	20	Narrow Bead
19			2.0	15	Narrow Bead
20			3.0	10	Narrow Bead
21			4.0	7.5	Very Narrow Bead
22			5.0	6	Very Narrow Bead

3.2.2.2 Square Butt Joints

Square butt joints were produced between 5 mm thick plates and also between 9 mm thick plates of 9Cr-1Mo(V, Nb) FMS. Weld joints were made at 8 kW laser power for further characterization of the weld joints for microstructure, microhardness, tensile properties and residual stresses. Details of the weld joints and the welding parameters are provided in Table 3.4. The weld joints showed full penetration, nice bead appearance and no visible defect. Weld joints produced between 9 mm thick plates of 9Cr-1Mo(V, Nb) FMS are presented in Fig. 3.2. Some of the laser welded plates were tempered at 770^{o}C for 30 min for microstructural characterization and property evaluation of the weld joints in PWHT condition.

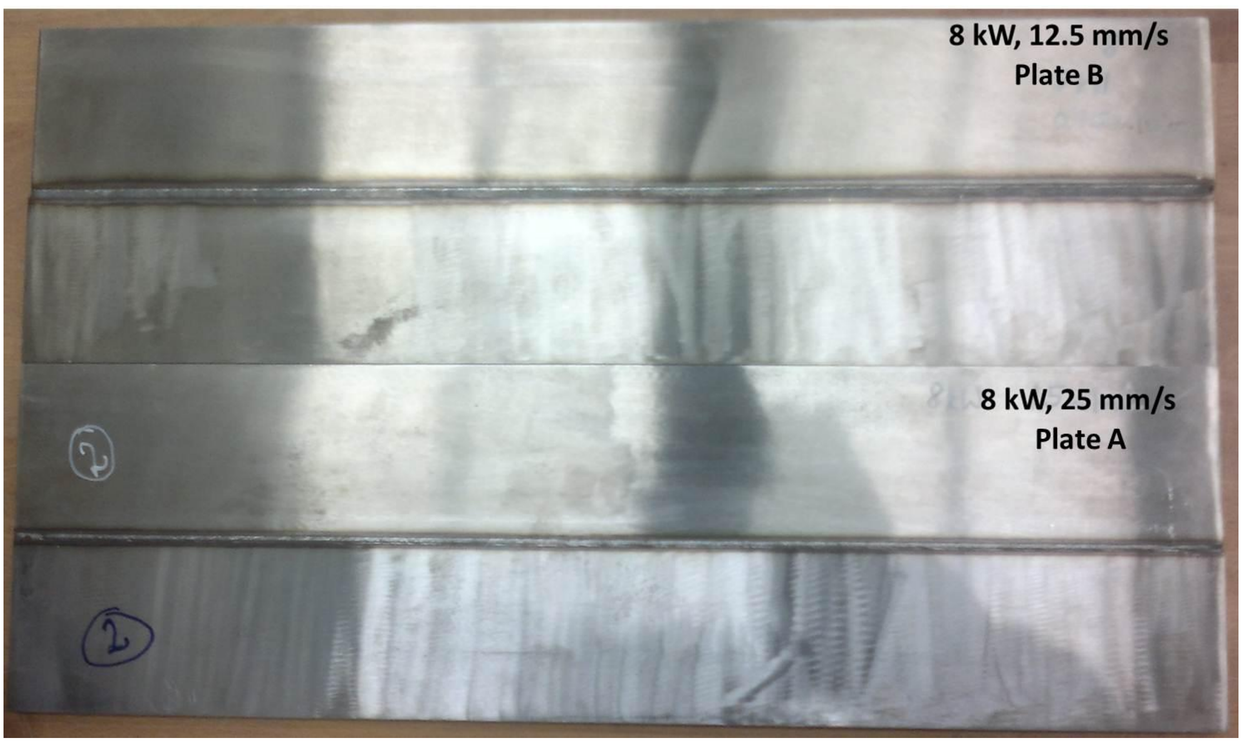

Fig. 3.2: Square butt weld joint produced between 9Cr-1Mo(V, Nb) FMS plates (500(l)x70(w)x9(t) mm3) produced be laser welding at 8 kW laser power and two different welding speeds – 1.5 m/min (25 mm/s) for Plate A and 0.75 m/min (12.5 mm/s) for Plate B. 'l', 'w' and 't' are respectively length, width and thickness of the plate.

Table 3.4: Details of the laser welded joints produced between 9Cr-1Mo(V, Nb) ferritic/martensitic Steel plates.

Sl. No.	Plate Size (mm)	Joint Length (mm)	Joint Thickness (mm)	Laser Power (kW)	Welding Speed (m/min)	Number of Plates
1.	230x115x5	230	5	8	5.0	2
2.	500x70x9	500	9	8	1.5	4
3.	500x70x9	500	9	8	0.75	4

3.2.3 Optical / Scanning Electron Microscopy

Weld joints were sectioned normal to the welding direction to examine the cross-section. The cross-section was ground, polished and then etched using Villella's reagent (ethyl alcohol: 95 ml, hydrochloric acid: 5 ml and picric acid: 1 gm) to reveal the microstructure of different regions – the fusion zone (FZ), the heat affected zone (HAZ) and the parent material (PM), across the weld joint. Microstructure of the different regions was then examined using an optical microscope and a scanning electron microscope (SEM) at different length scales.

3.2.4 Microhardness Measurements

Welding thermal cycle induces metallurgical phase transformations in the fusion zone and the HAZ in 9Cr-1Mo(V, Nb) FMS. This leads to significant variations in hardness across the weld joint. Microhardness measurements were made to capture variation in the hardness of the material across the weld joint. These measurements were made using a Vickers hardness testing machine at a load of 2 N and a dwell time of 10 s. Separation between the successive measurement points was kept small (0.2 mm) in the fusion zone and the HAZ to capture the anticipated steep variation in the microhardness through the narrow HAZ (~ 0. 5 mm) and then increased (0.5 – 1 mm) in the parent metal.

3.2.5 Transmission Electron Microscopy

Microstructural characterization of the material in the different regions across the weld joint at higher resolution was carried out using a transmission electron microscope (TEM) (make: JEOL, model: 2000 FX). This TEM operates at a maximum accelerating voltage of 200 keV and is equipped with an energy dispersive spectroscopy (EDS) unit (make: Oxford, model: X-Max) for micro-chemical analysis. For this purpose specimens were prepared from respective regions – FZ, HAZ and PM. First a thin slice (~ 0.3 mm thick) of material was extracted from the weld joint cross-section using a slow speed diamond saw. This slice was thinned to a thickness < 0.1 mm by grinding it against abrasive papers. Small discs of 3 mm diameter were punched out from this thinned slice to extract specimen from the parent metal. Because of very small width of the fusion zone (~ 1 mm) and the HAZ (~ 0. 5 mm on the either side of FZ) it was not possible to extract separate specimen from the fusion zone and the HAZ. Therefore, 3 mm discs were extracted keeping the fusion zone in the centre. These discs were then thinned by electrolytic jet thinning in 90:10 solution (perchloric acid: ethanol) at -30^{o}C. Microstructural examination of the fusion zone and the parent metal was performed. Subsequently, the central hole in the fusion zone was extended to create thin regions in the HAZ in a Gatan dual ion mill (make: Gatan, model: 600) and microstructural characterization of the HAZ region was then performed in TEM.

Microstructural examination of the fusion zone and the HAZ was performed in the as-welded and also in post weld tempered condition. Post weld tempering leads to formation of carbide and carbonitride precipitates in the fusion zone and the HAZ.

Micro-chemical characterization of these precipitates was performed using Energy Dispersive Spectroscopy (EDS) unit attached to the transmission electron microscope.

3.2.6 Tensile Property Evaluation

3.2.6.1 Tensile Tests for the Parent Material and the Weld Joints

Room temperature tensile properties of the parent material and the laser welded joints were measured by carrying out tensile tests. Transverse tensile tests were performed for weld joints, keeping the fusion zone in the centre of the tensile test specimen. Full thickness tensile test specimens were used for 5 mm thick butt joints. For 9 mm thick butt joints, half thickness tensile test specimens were used. Tensile test specimens were prepared by wire electro-discharge machining. Drawing of the tensile test specimen for the parent metal and the weld joints are presented in Figs. 3.3(a) and (b) respectively.

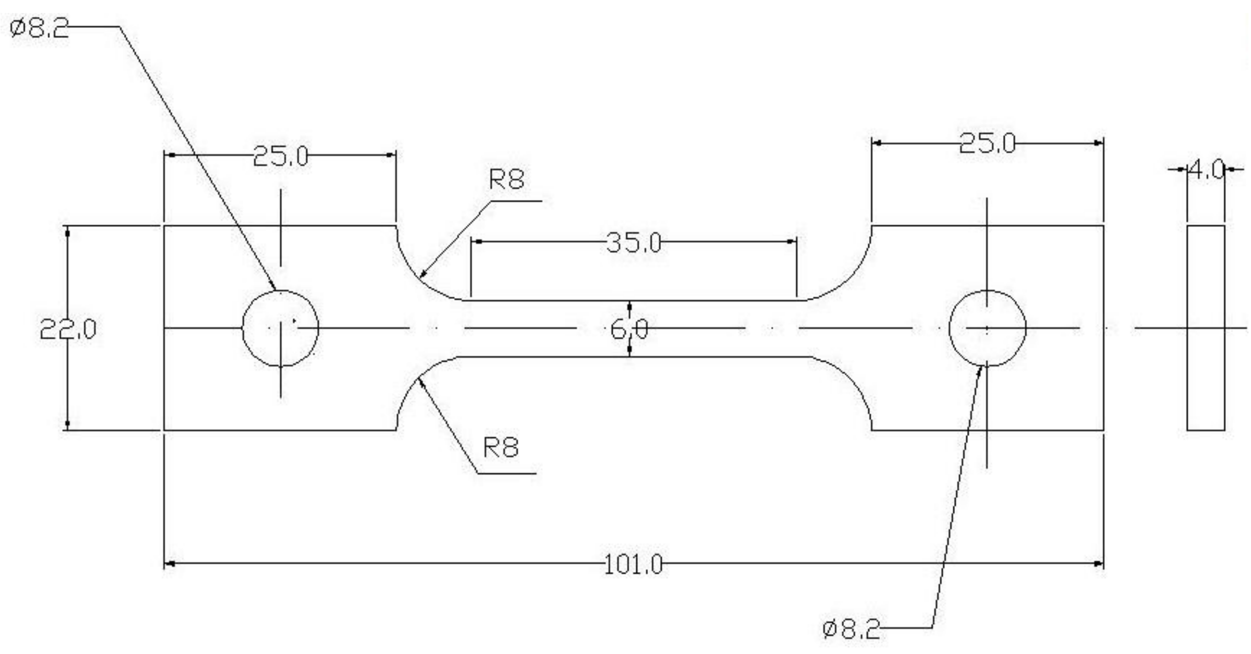

Fig. 3.3(a): Drawing of the tensile test specimen used for evaluation of tensile properties of the parent metal at room temperature as well as at elevated temperatures. All dimensions are in mm.

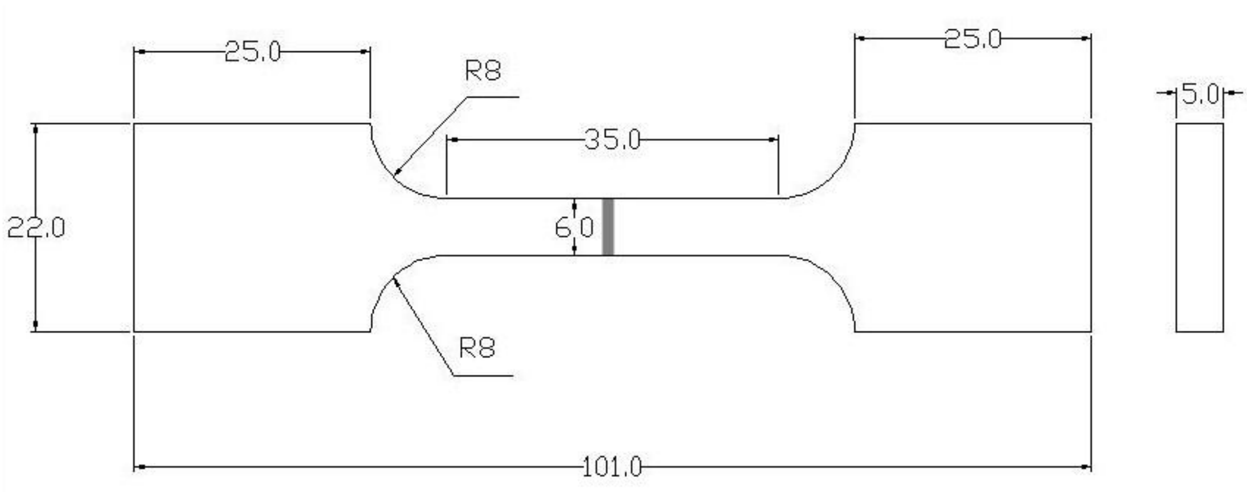

Fig. 3.3(b): Drawing of the transverse tensile test specimen used for evaluation of tensile properties of the weld joint in as welded and also in postweld heattreated conditions. All dimensions are in mm.

Tensile tests were performed at a strain rate of 5x10^{-4} s^{-1} and a strain gage (25.4 mm) was used to measure elongation in the initial part of deformation (up to ~ 2% elongation). For subsequent deformation, cross-head displacement was converted into strain using the entire gage length (35 mm) and compliance of the loading train was also considered. For welded joints, cross-weld tensile tests were performed in as welded and also in post weld tempered (770^{o}C for 30 minutes followed by air cooling) conditions.

3.2.6.2 Elevated Temperature Tensile Test for the Parent Material

Elevated temperature tensile tests were conducted to measure phase-dependent tensile properties of this steel. The material, 9Cr-1Mo-0.2V-0.07Nb-0.1C FMS, in as received condition - normalized (1050^{o}C for 30 minutes followed by air cooling) and tempered (770^{o}C for 30 minutes followed by air cooling), designated as Tempered Martensite (TM), was used in these experiments. Flat/rectangular tensile test specimens (Fig. 3.3(a)) were extracted from the as-received material by wire electro-discharge machining. A tensile test machine equipped with a split furnace, having heating rate controls and three thermocouples for monitoring the temperatures in different zones along the length of the tensile test specimen, was used to conduct these tests. The tensile test specimen in the TM condition was heated to the test temperatures (27^{o}C to 800^{o}C range) at a rate of 3^{o}C/min, soaked for 30 min, and then the tensile tests were conducted at a strain rate of 5 x 10^{-4} s^{-1}. In order to generate martensitic structure, designated as M, some of the tensile test specimens, made from the material in the TM condition, were normalized again (solutionized at 1050^{o}C for 30 minutes followed by air cooling) in a separate furnace. These normalized tensile test specimens were tested at different test temperatures (27^{o}C to 400^{o}C range) adopting a procedure similar to that for the TM condition. A metastable austenitic condition, designated as A, was produced *in-situ* in the tensile test setup. For this purpose, the tensile test specimen, made from the material in the TM condition, was mounted on the tensile test machine and heated in the split furnace (attached to the tensile test machine) to 1050^{o}C at a heating rate of 3^{o}C/minutes, soaked for 30 minutes, and cooled at a nominal rate of 10^{o}C/minute. This cooling rate from the austenitic phase field was sufficient to retain the metastable austenite in this material right up to the test temperature [1 – 2]. Thermocouple readings were recorded while cooling of the tensile test specimens to the test temperature. Once it reached the test temperature, the furnace was switched on and the test temperature was set. The tensile test specimen was allowed to stabilize at the test temperature for 5 minutes and the tensile tests were then conducted at a strain rate of 5 x 10^{-4} s^{-1}. Tensile tests for metastable austenitic condition were conducted in the range of 400^{o}C to 800^{o}C. Tensile test conditions for the three structural designations - TM, M, and A, are presented in Fig. 3.4. The test temperatures and the structural conditions of the material during the tensile tests are also marked with dark squares on the dilation curve of this material (Fig. 3.5) produced at a similar cooling rate.

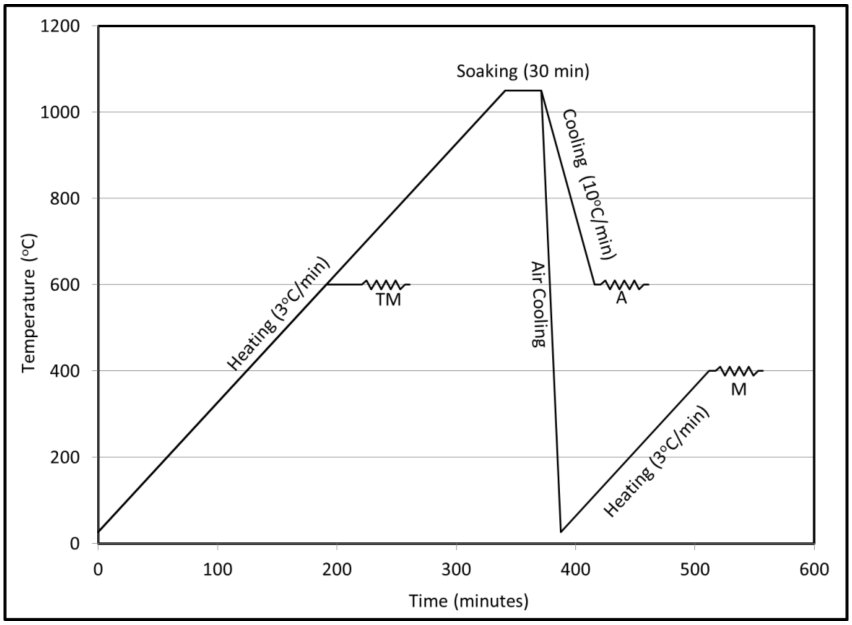

Fig. 3.4: Tensile test conditions for tempered martensitic (TM), martensitic (M) and metastable austenitic (A) employed in this study.

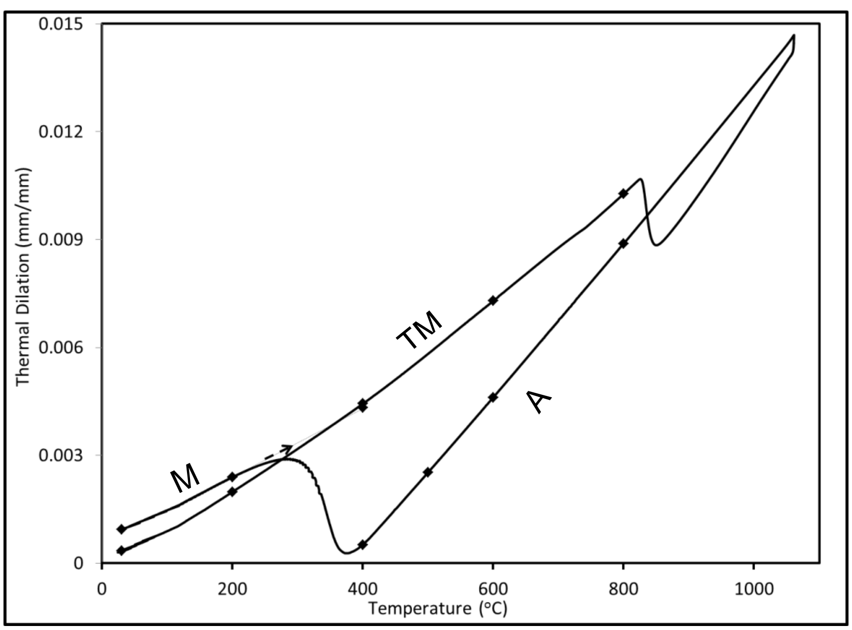

Fig. 3.5: Tensile test conditions are marked with dark squares on the dilation curve of 9Cr-1Mo(V, Nb) FMS produced at a heating and cooling rate of 10 ^{o}C/min.

An extensometer was used to measure strain for the tests conducted at room temperature. For elevated temperature tests, crosshead displacements were converted into strain. Corrections for machine compliance were made using elevated temperature elastic modulus of carbon steel for TM and M conditions, and that of austenitic steel for 'A' condition. Elevated temperature elastic modulus for carbon steel and austenitic stainless steel was obtained by linear fitting of the data in the literature [3]. Some important tensile properties such as yield strength (YS), uniform elongation (UE), and ultimate tensile strength (UTS) (true stress) of this material under different test conditions were derived from the respective engineering stress–strain curves. The fractured, tensile test specimens were allowed to cool in the furnace because rapid cooling of the same, to retain the as-tested microstructure, was not possible in the existing experimental setup. Optical metallography and TEM studies were performed on the samples extracted from the uniformly elongated region of the fractured specimens tested in the metastable austenitic phase field.

3.2.7 Neutron Diffraction for Residual Stress Measurements

Residual stress measurements were carried out by neutron diffraction. Laser welded plates of 9 mm thickness produced at 8 kW power and welding speeds – 1.5 m/min (Plate A) and 0.75 m/min (Plate B) were used in these measurements. Details of laser welding conditions – A and B, are presented in section 3.2.2.2. Neutron diffraction measurements were made along three principal orthogonal directions – longitudinal, normal and transverse. Longitudinal direction is the translational direction of welding, the normal direction is perpendicular to the welding direction passing through the thickness of the plate and the transverse direction is in the plane of the plate and perpendicular to the other two directions.

Neutron diffraction for residual stress measurements was carried out at Institut Laue-Langevin (ILL), Grenoble, France on the SALSA instrument. The neutron source at this facility is an experimental nuclear reactor with 58 MW thermal power. All measurements were made using {211} crystal reflection of the material, with a monochromatic beam of wavelength λ = 1.648 Å. Diffraction peak from {211} planes is most commonly used for residual stress measurements in the ferritic steels, because elastic properties of the material along this direction is representative of the bulk of the material. This wavelength resulted in a scattering angles close to 90^o, thereby giving essentially a cuboidal gauge volume. Fig. 3.6(a) shows a schematic of neutron diffraction measurement and the actual set up for neutron diffraction measurements performed at at ILL, Grenoble, France and reported in this study is shown in Fig. 3.6(b).

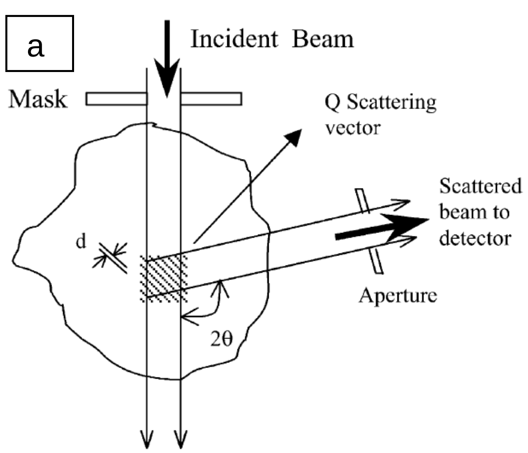

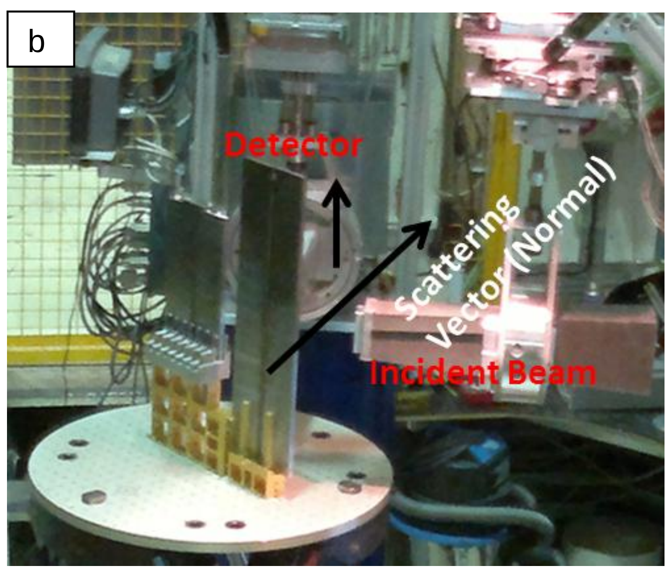

Fig. 3.6: Schematic of neutron diffraction (a) and actual set up for neutron diffraction measurements at ILL, Grenoble (b), reported in this study.

Source and detector slit combinations were chosen to define gauge volumes, in the sample, small enough to capture the rapid variations in strain; expected across the weld and in the through-thickness direction of the plate. For measurements of lattice spacing in the longitudinal direction, a gauge volume of 0.8 mm x 0.8 mm x 2 mm was chosen, and an extended volume (in the longitudinal direction) of 0.8 mm x 0.8 mm x 20 mm was chosen for measurements of lattice spacing in the transverse and the normal directions. Measurement points were placed at close spacings (at 0.5 mm) near the weld line and sparsely thereafter. The lines along which neutron diffraction measurements were made are shown schematically in Figs. 3.7(a) and 3.7(b) for welding conditions (A) and (B) respectively.

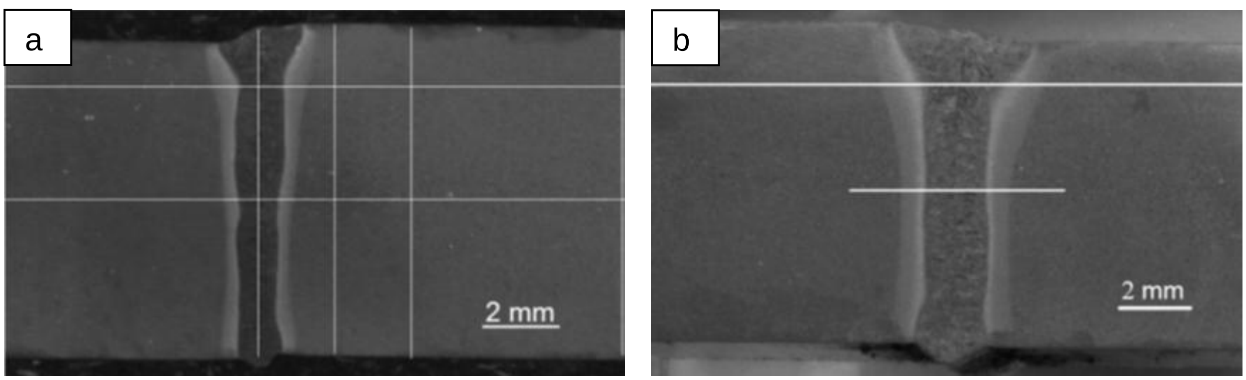

Fig. 3.7 (a): Macrograph showing joint cross-section in Plate A (welded at 8 kW and 1.5 m/min) and (b): Macrograph showing joint cross-section in Plate B (welded at 8 kW and 0.75 m/min) with neutron diffraction measurement lines marked. Measurement line is 1.5 mm and 4.5 mm below the left top surface.

Values of the stress-free lattice spacing, d_0, for (211) planes were required to determine the measured residual strains. Invariably, it is difficult to determine reliable values of the stress-free lattice parameters in the vicinity of narrow weldments. Several approaches that can be used have been documented by Withers et al.. [4]. In the present case, the very narrow width of the fusion zone (~ 1.2 mm) and HAZ (~ 0.6 mm) means that steep changes in d_0 were expected. Therefore, it was decided to use a “comb sample” spanning the weld as illustrated in Fig. 3.8.

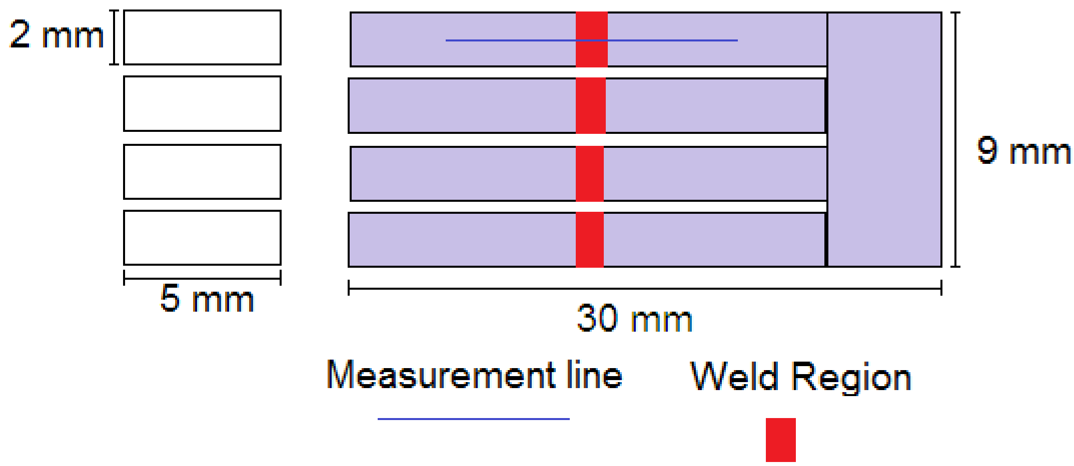

Fig. 3.8: Sketch showing the comb sample used for d_0 measurements.

The comb was machined from a cross-sectional slice of the material (approximately 5 mm thick) that had been extracted from near the end of the laser welded plate. Four transverse “prongs” spanning the weld line, each about 2 mm thick, were created by making three EDM cuts through the thickness of the slice as shown in Fig. 3.8. Whilst such samples are often considered to be free of “macrostress”, significant remnant stresses in a similar comb extracted from an aluminium alloy plate have been reported [5]. This may be even more important in the present case because of the short residual stress length-scales involved. To mitigate this potential uncertainty, strains were measured in the three orthogonal directions – longitudinal, transverse and normal, in the comb prongs and a state of plane stress (for the normal plane) was assumed to exist within the prongs in order to derive values for d_0. Measurements for the *d*-spacing in the three orthogonal directions were made at different points across the weld in the top most prong. A gauge volume of 0.8 x 0.8 x 2.0 mm^3 was used for measurements in the longitudinal and normal directions and an extended gauge volume of 0.8 x 0.8 x 5.0 mm^3 was used for measurements in the transverse direction. Stress-free lattice parameter (d_0) values were derived assuming a plane stress condition in the topmost prong as described below.

The stress along a principal direction x can be written as [4]

$$\sigma_x = \frac{E}{(1+\nu)(1-2\nu)}\left[(1-\nu)\varepsilon_x + \nu(\varepsilon_y + \varepsilon_z)\right] \tag{3.1}$$

Where σ_x is component of stress along x-direction and ε_x, ε_y, ε_z are strain components in principal directions x, y and z respectively, and E (218 MPa) and ν (0.3) are the Young's modulus and Poisson's ratio respectively.

If σ_x is relieved by cutting a thin strip normal to the x-direction; then

$$\frac{E}{(1+\nu)(1-2\nu)}\left[(1-\nu)\varepsilon_x + \nu(\varepsilon_y + \varepsilon_z)\right] = 0 \tag{3.2}$$

and making the substitution $\varepsilon_x = \frac{d_x - d_0}{d_0}$ (3.3)

gives $d_0 = \frac{(1-\nu)d_x + \nu(d_y + d_z)}{(1+\nu)}$ (3.4)

This expression was used to derive d_0 values for the fusion zone and the HAZ. The approach assumes isotropic material properties (i.e. low texture) and that values of d_0 are direction-independent (i.e. negligible microstresses are present owing to the influence of plastic strain). For the parent metal, the average d_0 value of ten different measurements on a small piece of material cut from the far end of the plate was used.

The diffraction angle, 2θ, determined from the measured position of the diffraction peak, was used to derive the lattice spacing, d, using Bragg's Law,

$$\lambda = 2d\sin\theta \tag{3.5}$$

The lattice spacing along three orthogonal directions of the welded plate – longitudinal, transverse and normal, were calculated using the corresponding diffraction peaks from different measurement points. These values were then used to calculate strain values ε_x, ε_y and ε_z in the three directions using suitable d_0 values as described above. Using these strain values, the residual stress along the three orthogonal directions – σ_x, σ_y and σ_z were calculated for all the measurement points using equation (3.1). Errors in the individual lattice spacing measurements were derived from the error in the location of the diffraction peak centre, arising from the Gaussian fit. This exercise was carried out for all the measurements on the plate as well as on the combs. The error propagation was applied in the derivation of all values for d_0 (using a plane stress assumption) and for values of residual strain and residual stress along the three principal directions.

3.3 Modelling and Simulation using SYSWELD

Thermo-metallurgical and thermo-mechanical modelling and simulation of laser welding was performed to compute temporal evolution and spatial distribution of temperature, phase-fraction and stresses resulting from laser welding of 9 mm thick plates of 9Cr-1Mo(V, Nb) FMS in square butt configuration. The thermo-metallurgical and thermo-mechanical analyses were sequentially coupled.

3.3.1 Geometry and Mesh Model

A three dimensional (3D) mesh model of a plate of size 90 x 70 x 9 mm^3 was prepared for these computations. Mesh model of only one plate was prepared to take advantage of the symmetry offered by the square-butt configuration. Element size was kept very fine 0.1x0.2x0.25 mm^3 in the fusion zone due to fine heat source size and increased gradually away from it, to minimize the computation time. The model consisted of

279744 3D-elements and is presented in Fig. 3.9. A two dimensional skin was extracted for heat exchange with the air at ambient temperature (30^oC). Welding line, welding direction and the nodes for application of the clamps were defined.

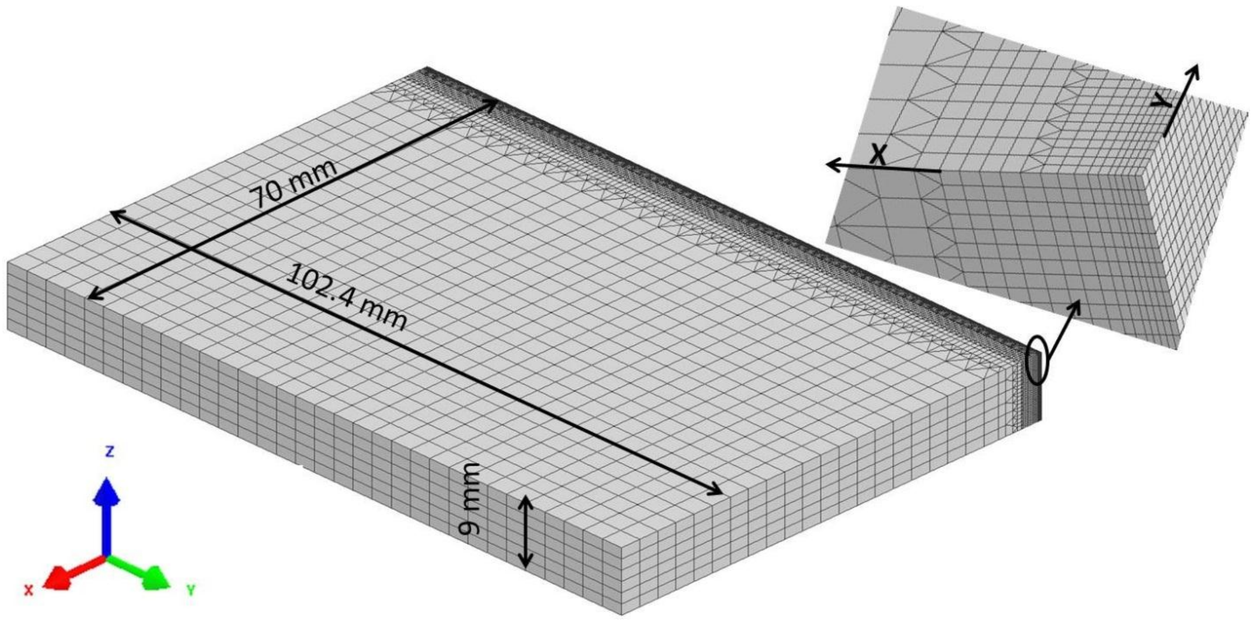

Fig. 3.9: Three dimensional mesh model of the plate used for laser welding simulation. Part of the plate near the joint line is shown in greater detail.

3.3.2 Material Properties

Temperature dependent physical properties of this material, presented in Fig. 3.10, were compiled from the literature [6 - 7] and used in these computations. Room temperature specific density of the material was taken as 7.85, which was made temperature dependent by considering thermal dilation and volumetric changes associated with solid state phase transformation. Latent heat of fusion was not considered in these computations due to exorbitantly high computational time requirement. This steel has tempered martensitic structure, which transforms into austenite on heating between Ac_1 (820^oC) and Ac_3 (900^oC) and the austenite transforms into martensite upon air cooling below Ms temperature (375^oC).

Temperature dependent mechanical properties for different phase-fields – as transformed martensite, tempered martensite and austenite, were obtained by carrying out elevated temperature tensile tests in respective phase-fields, as described in section 3.2.6.2. These experimentally measured values, presented in Figs. 3.11 through 3.13, were used in these computations. Thermal expansion coefficients and phase transformation temperatures were obtained by carrying out dilatometry of this material (described in section 3.2.1) and were used in these computations. Softening temperature was considered to be 1200^{o}C above which mechanical behaviour of the material was not considered.

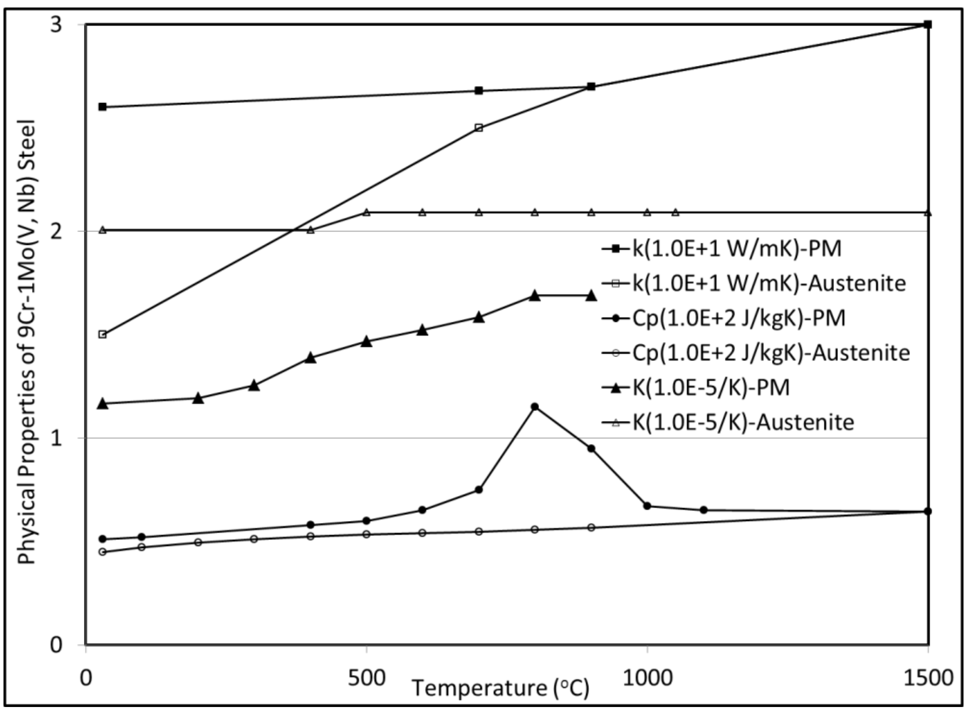

Fig. 3.10: Physical properties of 9Cr-1Mo(V, Nb) steel used in this simulation ('k' is thermal conductivity, 'Cp' is heat capacity and 'K' is thermal expansion coefficient) [6 – 7].

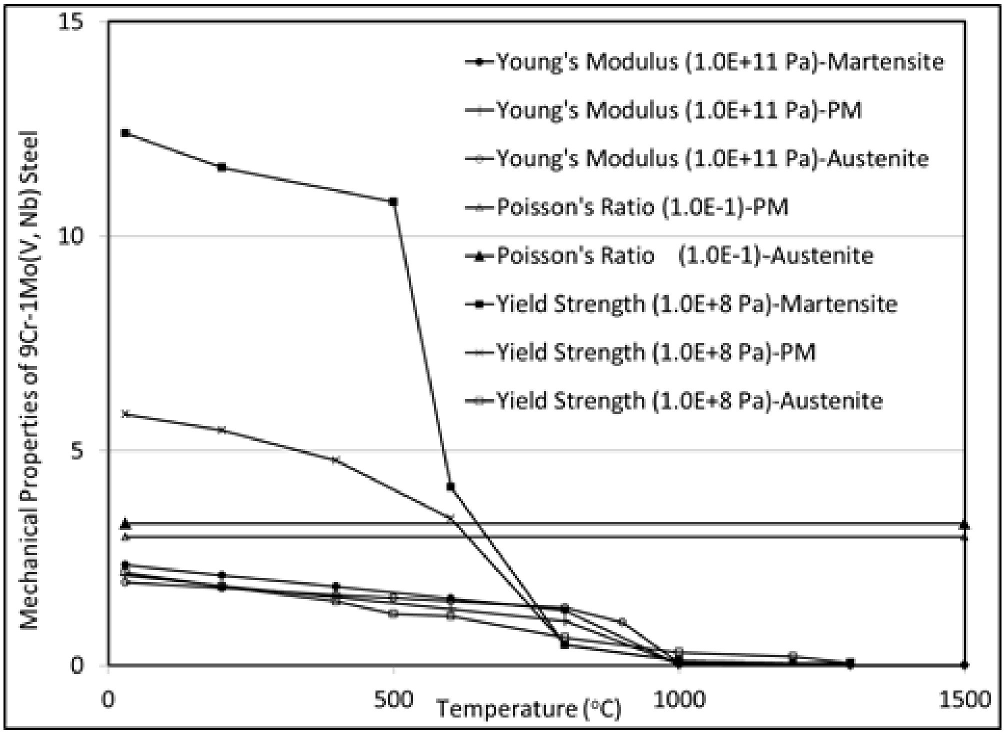

Fig. 3.11: Mechanical properties of 9Cr-1Mo(V, Nb) steel used in this simulation.

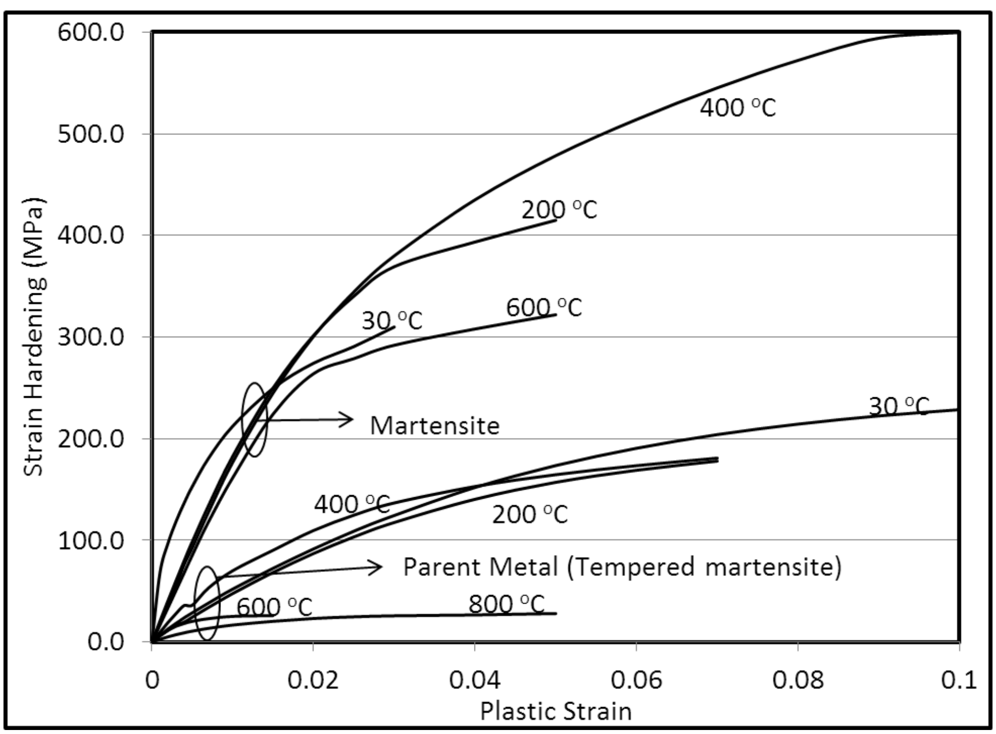

Fig. 3.12: Strain hardening behaviour of the 9Cr-1Mo(V, Nb) steel in tempered martensitic (parent metal) and as transformed martensitic condition.

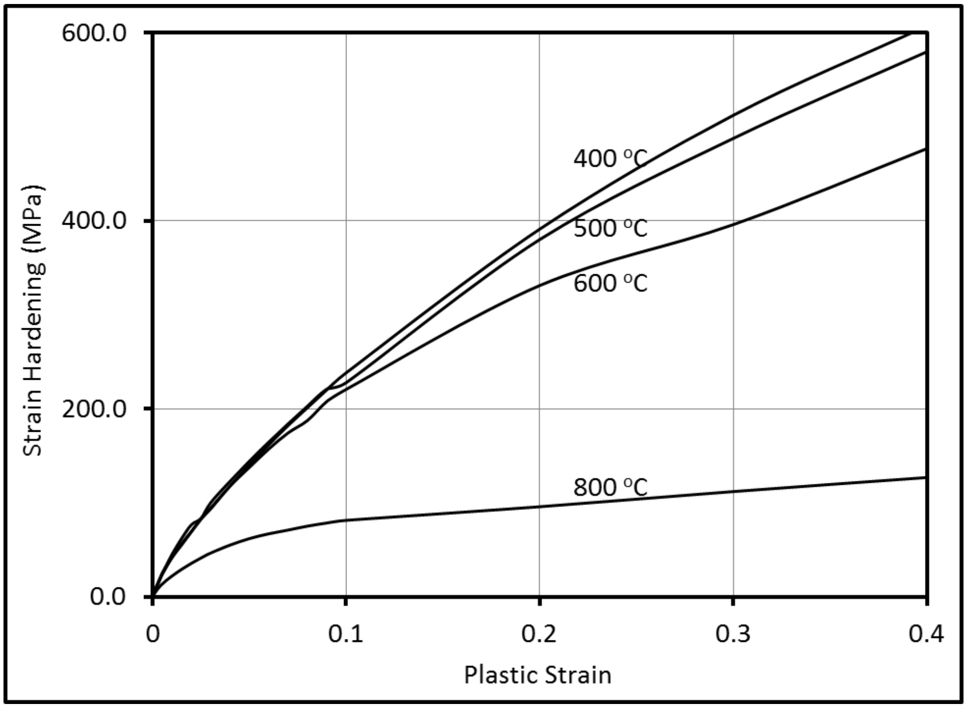

Fig. 3.13: Strain hardening behaviour of the 9Cr-1Mo(V, Nb) steel in metastable austenitic condition.

3.3.3 Heat Source Definition

Proper heat source definition is necessary for realistic simulation of a welding process. SYSWELD offers some standard form of heat sources like surface Gaussian, double ellipsoid and 3D Gaussian [8] with provision for calibrating the actual heat source parameters using the experimental data like depth and width of the fusion zone cross-section. A 3D Gaussian heat source (Fig. 3.14 (a)) has a form of a cone / truncated cone with heat intensity following a Gaussian profile in radial direction and a linear profile along the axis of the cone. This heat source can be represented by means of top and bottom radii and height of the truncated cone. A double ellipsoidal heat source (Fig. 3.14(b)) is made of two semi-ellipsoids – one in the front and another in the rear of the heat source. The intensity distribution in this heat source can be represented by means of three geometrical parameters a, b and c, which are semi-major axes of the semi-ellipsoids. This software package also allows for combining these standard heat source forms. In addition, there is a provision for using user defined heat source. 3D Gaussian and double ellipsoid heat sources are used for simulating beam welding processes and conventional arc welding processes respectively [6 - 18].

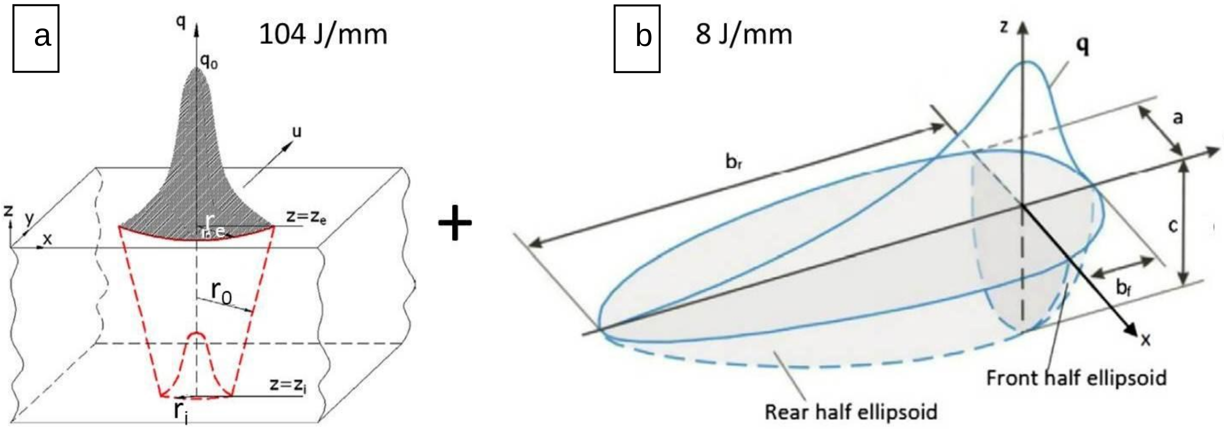

$$q(x,y,z) = q_0 exp\left(-\frac{x^2+y^2}{{r_0}^2(z)}\right) \qquad q_f(x,y,z) = q_0 exp\left(-\left(\frac{x^2}{a^2}+\frac{y^2}{{b_f}^2}+\frac{z^2}{c^2}\right)\right)$$

$$r_0(z) = r_0 + \frac{r_i - r_e}{z_i - z_e}\,(z - z_e) \qquad q_r(x,y,z) = q_0 exp\left(-\left(\frac{x^2}{a^2}+\frac{y^2}{{b_r}^2}+\frac{z^2}{c^2}\right)\right)$$

Fig. 3.14: Schematic representation of combined (a) 3D Gaussian and (b) double ellipsoid heat source used in this simulation.

However, a careful observation of cross-section of laser welded joint shows that it has a nail like profile with small nail-head and a large nail-body. While the body of the nail-shaped fusion zone can be represented by a 3D Gaussian heat source, realistic representation of the nail head requires a double ellipsoid heat source. Therefore, a linear combination of a 3D Gaussian and a double ellipsoid heat source (Fig. 3.13) was used to represent the welding heat source during these computations. These two types of heat sources have been extensively used and described in the literature [6 - 18]. 70% of the laser beam energy (120 J/mm) was assumed to be absorbed by the work piece and the total absorbed energy was divided between the 3D Gaussian and the double ellipsoid heat source in the ratio of 93:7 (104:8 J/mm); based on heat source calibration exercise using dedicated heat source fitting tool available in SYSWELD 2012.

3.3.4 Transient Thermo-metallurgical Computations

Transient thermo-metallurgical computation was done for laser welding at 8 kW laser power and 1.5 m/min (25 mm/s) welding speed to compute transient temperature-field and transient metallurgical phase-field. Computation of transient temperature-field involved solving the heat conduction equation (Equation 3.7) with a moving heat source (described in the previous section) as heat input, in combination with a combined convection-radiation cooling condition (Equation 3.8) on the skin of the plate.

Heat Conduction Equation:

$$\nabla.(k\nabla T) + \dot{q} - \rho c\dot{T} = 0 \tag{3.7}$$

Where, k is thermal conductivity, ρ is density, c is specific heat capacity and T is temperature.

Combined convection-radiation heat exchange coefficient (h)

$$h = 25 + se(T + T_o)(T^2 + T_o^2) \qquad (in\, Wm^{-2}K^{-1}) \tag{3.8}$$

Where, Stefan's constant s = 5.67 x 10^{-8} $Wm^{-2}K^{-4}$, emissivity (e) of steel was taken as 0.8 and T is absolute temperature.

For metallurgical computations this material was considered as three phase material – ferrite (the starting material), austenite and martensite. Metallurgical computations involved computation of the phase fraction as a function of temperature. Reactions for phase transformation were defined between corresponding transformation temperatures. Ferrite to austenite transformation was defined between (Ac_1 = 820°C and Ac_3 = 900°C) and this transformation was computed according to Leblond's equation [19]. Martensitic transformation was defined for austenite cooling below Ms temperature (375°C) and martensite phase fraction was computed according to Koistinen-Marburger equation (Equation 3.9) [20].

Leblond Equation [19]

$$\frac{dP(T)}{dt} = f(\dot{T})\frac{P_{eq}(T) - P(T)}{\tau(T)} \tag{3.9}$$

Where P(T) is proportion of phase, t is time, T is temperature, $P_{eq}(T)$ is equilibrium phase fraction and τ is delay time.

Koistinen-Marburger Equation [20]

$$P(T) = 1 - \exp(-0.011(Ms - T)) \tag{3.10}$$

Where P(T) is fraction of martensite at a temperature lower than the martensite start temperature, Ms, which was taken as 375°C from dilatometric experiment on this material, see Section 3.2.1.

An optimized time step of 8 ms was used by the software for computations during welding (when heat source was on) and subsequently increased by 1.5 times for successive computations. Computations were carried out in 574 time steps and results were stored in 574 cards – one card corresponding for one time step. Total computation time for the thermo-metallurgical computation was 67080 s (18 hours and 38 minutes).

3.3.5 Transient Thermo-mechanical Computations

The plate was clamped to mimic actual clamping condition as closely as possible. Plates were rigidly clamped in the through thickness direction on all the nodes, 4 mm farther from the weld centre line, to simulate the pneumatic clamping used during the welding process. These clamps were kept for 300 s from the start of welding and removed afterwards. Additionally, symmetry clamps were applied on the longitudinal (along welding line) – normal (along plate thickness) plane as only one plate has been modelled. The four extreme corners of the plate, farthest from the weld centre line were rigidly clamped in all the three directions (x, y and z) to prevent rigid body motion of the plate.

Sequentially coupled, non-linear thermo-mechanical analysis was performed. Results of transient thermo-metallurgical computations stored in 574 cards (time steps) were read and mechanical analysis was performed at each time step. Thermo-mechanical computations involved solving Hook's law with thermal and transformational strains; in conjugation with von-Mises yielding criteria. Isotropic strain hardening of the material was considered for these computations. Displacement, strain and stress-fields were computed for each of the 574 time steps. Total computation time for thermo-mechanical computation was 400636 s (111 hours and 17 minutes).

References

[1] B. J. Ganesh, S. Raju, A. K. Rai, E. Mohandas, M. Vijayalakshmi, K. B. S. Rao and B. Raj, “Differential scanning calorimetry study of diffusional and martensitic phase transformations in some 9wt% Cr low carbon ferritic steels”, Mater. Sci. and Technol. 27(2) (2011) 500-512.

[2] K. Haarmann, J. C. Vaillant, W. Bendick and A. Arbab, The T91/P91 Book, Vallourec and Mannessmann Tubes, (1999) 14-29.

[3] G.E. Dieter, “Mechanical Metallurgy”, SI Metric ed., McGraw Hill Book Company, Singapore, 1988, p. 281.

[4] P. J. Withers, "Mapping residual and internal stress in materials by neutron diffraction", C. R. Phys. 8 (2007) 806 – 820.

[5] S. Ganguly, L. Edwards and M. E. Fitzpatrick, “Problems in using a comb sample as a stress-free reference for the determination of welding residual stress by diffraction”, Mater. Sci. Eng. A528(3) (2010) 1226 - 1232.

[6] A. H. Yaghi, T. H. Hyde, A. A. Becker, J. A. Williams and W. Sun, “Residual stress simulation in welded sections of P91 pipes”, J. Mater. Process. Technol. 167 (2005) 480 - 487.

[7] S. H. Kim, J. B. Kim and W. J. Lee, “Numerical prediction and neutron diffraction measurement of residual stresses for a modified 9Cr-1Mo steel weld”, J. Mater. Process. Technol. 209 (2009) 3905 - 3913.

[8] ESI Group, SYSWELD, Theory Manuals, ESI France, 2012.

[9] D. Dean and M. Hidekazu, “Prediction of welding residual stress in multi-pass butt-welded modified 9Cr–1Mo steel pipe considering phase transformation effects”, Comput. Mater. Sci. 37 (2006) 209 - 219.

[10] J. W. H. Price, A. Z. Paradowska, S. Joshi, T. Finlayson, C. Semetay and H. Nied, “Comparison of experimental and theoretical residual stresses in welds: the issue of gauge volume”, Int. J. Mech. Sci. 50 (2008) 513 - 521.

[11] S. K. Bate, R. Charles and A. Warren, “Finite element analysis of a single bead-on-plate specimen using SYSWELD”, Int. J. Press. Vessel. Pip. 86 (2009) 73 - 78.

[12] A. S. Aloraier and S. Joshi, “Residual stresses in flux cored arc welding process in bead-on-plate specimens”, Mater. Sci. Eng. A534 (2012) 13 - 21.

[13] J. J. Xu, P. Gilles, Y. G. Duan and C. Yu, “Temperature and residual stress simulations of the NeT single-bead-on-plate specimen using SYSWELD”, Int. J. Press. Vessel. Pip. 99 - 100 (2012) 51 - 60.

[14] S. Joshi, J. Hildebrand, A. S. Aloraier and T. Rabczuk, “Characterization of material properties and heat source parameters in welding simulation of two overlapping beads on a substrate”, Comput. Mater. Sci. 69 (2013) 559 - 565.

[15] S. Joshi, C. Semetay, J. W. H. Price, H. F. Nied, “Weld-induced residual stresses in a prototype dragline cluster and comparison with design codes”, Thin-Walled Struct. 48 (2010) 89 - 102.

[16] S. A. Tsirkas, P. Papanikos, Th. Kermanidis, “Numerical simulation of the laser welding process in butt-joint specimen”, J. Mater. Process. Technol. 134 (2003) 59 - 69.

[17] G. A. Moraitis and G. N. Labeas, “Prediction of residual stresses and distortions due to laser beam welding of butt joints in pressure vessels”, Int. J. Press. Vessel. Pip. 86 (2009) 133 - 142.

[18] N. S. Shanmugam, G. Buvanashekaran, K. Sankaranarayanasamy and S. R. Kumar, “A transient finite element simulation of the temperature and bead profiles of T-joint laser welds”, Mater. Des. 31 (2010) 4528 - 4542.

[19] J. Leblond and J. Devaux, “A new kinetic model for anisothermal metallurgical transformations in steels including effects of austenite grain size”, Acta Metall. 32 (1984) 137– 146.

[20] D. P. Koistinen and R. E. Marburger, “A general equation prescribing the extent of the austenite - martensite transformation in pure iron–carbon alloys and plain carbon steels”, Acta Metall. 7 (1959) 59 – 60.

Chapter 4: Microstructure, Phase Transformation and Phase-dependent Tensile Behaviour of 9Cr-1Mo(V, Nb) FMS

4.1 Introduction

P/T/Gr91 steel, also known as modified 9Cr-1Mo steel or 9Cr-1Mo(V, Nb) steel is a high temperature material of interest to ultra-supercritical power plants and next generation nuclear reactors [1-6]. This is a martensitic steel and used in tempered martensitic condition. The final microstructure of this steel is obtained by employing a heat treatment, which involves normalizing at a temperature in the range of 1050 – 1080^oC and tempering at a temperature in 730 – 780^oC range. This is highly hardenable, low carbon steel and therefore, normalizing produces a lath martensitic microstructure within prior austenite grains. The normalized microstructure gets transformed into elongated subgrain structure decorated with submicron (~100 nm) size $M_{23}C_6$ type carbides and nanometer (~ 10 – 20 nm) size MX type carbonitrides. Microstructure of this steel, resulting from its standard heat treatment is well characterized in the literature [7 - 11]. Microstructural characterization of the as-received material was performed at different length scales to obtain the starting microstructure before its laser welding.

Because of high alloying content, this steel is highly hardenable. Therefore, when cooled from the austenitic phase field, transforms into martensite even at very slow cooling rates (~ 5^oC/min). The Ms temperature of this steel is about 400^oC. Phase transformation in this steel is well characterized in the literature [12 - 13]. However, the effect of austenitization temperature on transformation behaviour of austenite, while cooling, is not well reported. Austenitization temperature and time becomes important because, it determines solute content of the austenite formed during austenitization, which in turn determines hardenability of the austenite. Lower austenitization temperature may lead to an austenite leaner in solute content due to insufficient dissolution of carbide precipitates. This austenite is expected to be less hardenable than that indicated by nominal composition of the steel. Such austenite can therefore, transform into ferrite as well as bainite, instead of the usual martensitic transformation in this steel. This material experiences lower austenitization temperature and time during welding in the outer HAZ region. Therefore, it is desirable to understand the effect of austenitization temperature on the transformation behaviour of austenite in this steel. Dilatometry is one of the important and commonly employed methods to study phase transformations involving change in specific volume of the phases. This method relies on change in length of the specimen caused by phase-transformations, which is recorded continuously while the specimen is subjected to a thermal cycle across different phase-fields. When a ferritic/martensitic steel specimen is heated, its length increases with temperature until austenitic transformation commences. Ferritic to austenitic phase-transformation results in decrease in length of the specimen until the transformation is over. Subsequent heating leads to increase in length due to thermal expansion of austenite. When the specimen is cooled from austenitic phase-field, it undergoes thermal contraction until transformation of austenite commences. Austenite transforms into ferrite/bainite/martensite or into a mix of these phases, depending on its hardenability and the cooling rate employed during dilatometry. These transformations are associated with increase in length of the specimen. After these transformations are complete, subsequent cooling leads to thermal contraction. Thus dilatometry provides phase-transformation temperatures in ferritic / martensitic steels, which provides insight of the transformation behaviour of austenite. Different aspects of phase transformation behaviour of steel have been studied and reported in the literature [14 – 16]. Sulaiman [14] has used dilatometry to measure phase transformation temperatures in P91 steel. Ning et al. [15] have used dilatometry to study phase transformation mechanism of minor stressed T91 steel using dilatometry. They have reported that Ms temperature increases by application of compressive stress, however, beyond a critical stress Ms temperature starts to decrease. Wang et at [16] have studied martensitic transformation behaviour of deformed supercooled austenite in a medium-carbon Si–Al-rich alloy steel using dilatometry. They have reported decrease in Ms temperature due to deformation of supercooled austenite. They have attributed the decrease in the Ms temperature to strengthening of austenite due to deformation. However, there is no reported study on the effect of austenitization temperature on the transformation behaviour of austenite in 9Cr-1Mo(V, Nb) FMS. This work reports the effect of austenitization temperature on the transformation behaviour of austenite in this steel, studied using dilatometry.

This steel, like any other martensitic steel, shows hysteresis in the phase field, as it transforms from tempered martensite (TM) to austenite (A) in the temperature range 820 – 900^{o}C while heating, and then from austenite to martensite (M) in 375 – 225^{o}C range while cooling [12 - 13]. Thus, depending on the thermal cycle that this steel is subjected to, there are two regimes of phase field hysteresis – Regime I (RT – 375^{o}C), in which either TM or M can exist and Regime II (375 – 820^{o}C), in which either TM or A can exist. Such thermal cycles, causing excursion through the three different phase fields – TM, A, and M, are associated with several thermo-mechanical processes including welding of this steel. Therefore, this steel is subjected to hysteresis in the phase field with each welding pass. The three phase fields – TM, A, and M, differ substantially in terms of basic crystal structure as well as microstructure. As the structure of a material forms the basis of its mechanical properties, it is natural that structural hysteresis in this steel will induce phase-dependence in its tensile behaviour. Phase-dependent tensile properties are expected to have a strong influence on the evolution of displacement and stress fields during welding. Therefore, quantitative assessment of phase-dependent tensile behaviour is essential for modelling and simulation endeavours, for computing the displacement and stress-fields, resulting from welding of this steel. Though substantial literature exists on the phase transformation behaviour of metastable austenitic phase field of different grades of steel under stress as well as plastic deformation [17 - 20], and tensile tests of supercooled austenite in high hardenability low carbon steel have also been reported [21], there is no published literature quantifying phase-dependence in the tensile behaviour of this steel. Due to non-availability of information on the phase-dependent mechanical properties of this steel, computational efforts in this direction have relied on published literature on elevated temperature mechanical properties of either austenitic stainless steel or those of TM condition of this steel [22 - 24]. Inferences drawn from such computational studies may lead to erroneous conclusions and often, understanding of the underlying process remains incomplete. Therefore, Dean et al. [23] suggested using data on phase-dependent mechanical properties for improving accuracy of the computed results.

Phase-dependent tensile properties of 9Cr-1Mo(V, Nb) ferritic/martensitic steel in its three different phases– TM, A, and M were evaluated by performing elevated temperature tensile tests. Additionally, an attempt has been made to correlate tensile properties of the metastable austenite with microstructural changes during the tensile test, which could be inferred from the room temperature microstructure of the fractured samples. Results of microstructural characterization, dilatometry and elevated temperature tensile tests of the three phases – TM, A and M of 9Cr-1Mo(V, Nb) FMS are presented and discussed in this chapter.

4.2 Microstructure of the As-received Material

The as-received material was in normalized (1050^{o}C) and tempered (770^{o}C) condition. Representative optical micrograph of the as-receive material is presented in Fig. 4.1. This micrograph was produced using Villella's reagent on a polished surface of the as-received material. This is a typical tempered martensitic microstructure. Prior austenite grains and lath packets are clearly resolved in this micrograph.

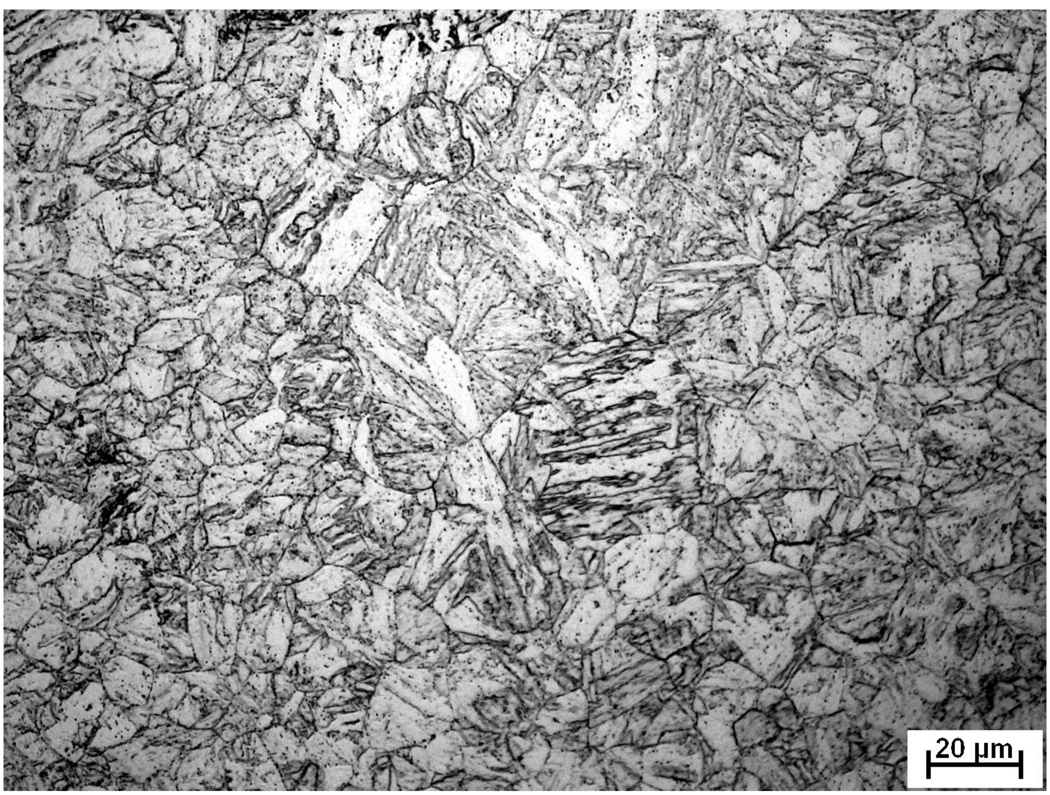

Fig. 4.1: Representative optical micrograph of 9Cr-1Mo(V, Nb) FMS. Prior austenite grains and substructures within can be clearly seen in this micrograph.

Representative micrograph of the as-received 9Cr-1Mo(V, Nb) FMS obtained by scanning electron microscope are presented in Figs. 4.2 and 4.3. The scanning electron micrgraph at lower magnification (Fig. 4.2) shows a large number of submicron precipitates, distributed uniformly. The scanning electron micrographs at higher magnification (Fig. 4.3) shows there are two type of precipitates, the larger precipitates are approximately 100 nm in size while the smaller precipitates are approximately 10 nm in size. The bigger precipitates (~ 100 nm) are reported in the literature to be $M_{23}C_6$ carbides, where M is mainly Cr, which is partly substituted with Fe, Mn, Mo etc. [10 - 11]. The smaller precipitates (~ 10 nm) are reported as MX type carbonitrides where M is mainly V and Nb [10 - 11]. Transmission electron micrograph of this steel is presented in Fig. 4.4. The tranmission electron micrograph shows that the $M_{23}C_6$ type carbides are along the elongated subgrain boundaries. Microstructure of the as-received material is consistent with with that reported in the literautre for 9Cr-1Mo(V, Nb) FMS in normalized and tempered condition.

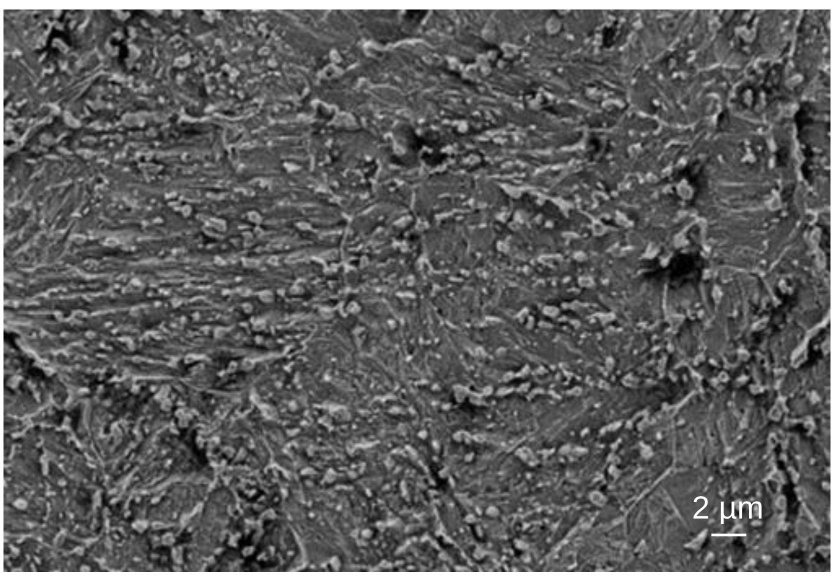

Fig. 4.2: Representative scanning electron micrograph of 9Cr-1Mo(V, Nb) FMS. The micrograph shows uniformly distributed submicron carbide precipitates.

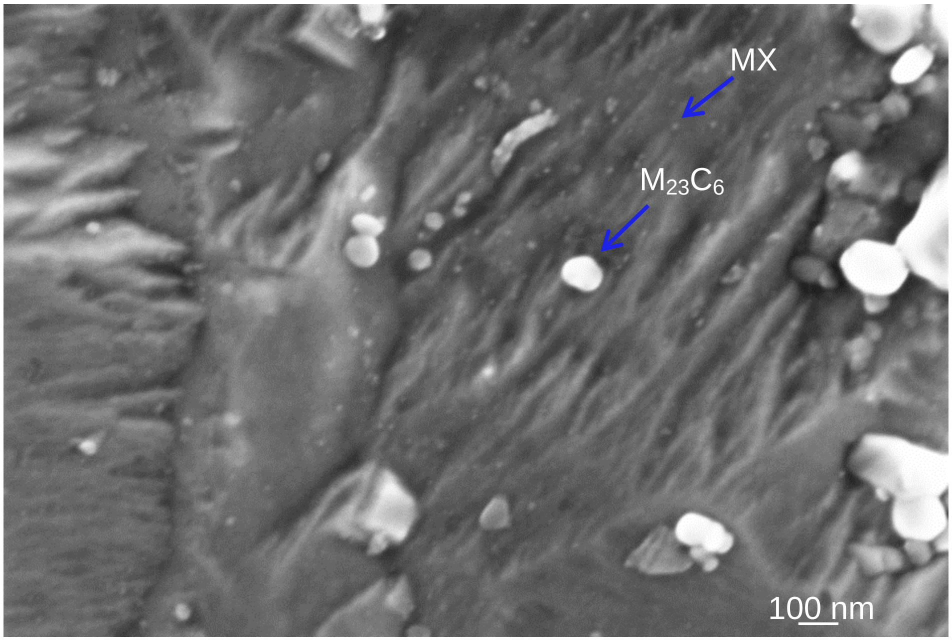

Fig. 4.3: Representative scanning electron micrograph of 9Cr-1Mo(V, Nb) FMS. The micrograph shows $M_{23}C_6$ and MX precipitates.

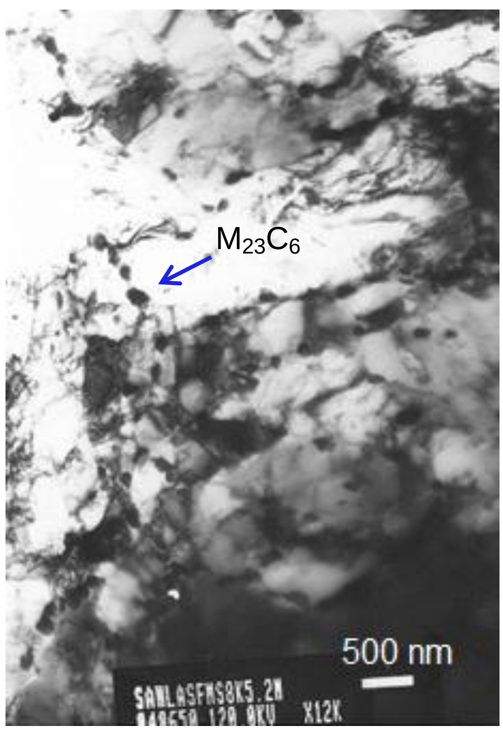

Fig. 4.4: Representative transmission electron micrograh of 9Cr-1Mo(V, Nb) FMS. The micrograph shows carbide precipitates along the elongated subgrain boundaries and also within the subgrains.

4.3 Effect of Austenitization Temperature on Transformation of Austenite

Dilatometry curves for 9Cr-1Mo(V, Nb) FMS heated to different austenitization temperature and subsequently cooled to room temperature, at a heating and cooling rates of 10^{o}C/min, are presented in Figs. 4.5 (a – d). The tempered martensite starts to transform into austenite at ~ 830^{o}C (Ac_1) while heating. These dilatometry curves clearly show the effect of austenitization temperature on the transformation behaviour of austenite while cooling. The specimen austenitized at 950^{o}C and higher temperatures transformed from austenite to martensite, below Ms temperature (~ 375^{o}C), while cooling as shown in Figs. 4.5 (b – d). However, the specimen austenitized at 850^{o}C, transformed from austenite to ferrite plus carbide, while cooling. The transformation temperature of austenite was also much higher (780 – 720^{o}C) (Fig. 4.5a) than Ms temperature of this steel (~375^{o}C). This implies that hardenability of the austenite formed at 850^{o}C is significantly lesser than that of the austenite formed at 950^{o}C and higher temperatures. This can be explained on the basis of carbide dissolution and solute content of the resulting austenite. Degree of completion of ferrite to austenite transformation, dissolution of carbide / carbonitride precipitates and therefore, solute content of the austenite depends on the superheat above Ac_1 temperature and the time above this temperature. If superheat is not sufficient, ferrite to austenite transformation and dissolution of the carbides will not be complete. Insufficient dissolution of carbide, results in austenite with significantly lower solute content than that indicated by the nominal composition. Hardenability of austenite depends on the solute content and therefore, lower austenitizing temperature leads to formation of austenite with lower solute content and therefore, of lesser hardenability. In case of 9Cr-1Mo(V, Nb) FMS, solvus temperature of $M_{23}C_6$ type carbide is higher than 850^oC (Fig. 1.5). Therefore, the austenite produced by heating this steel at 850^oC is expected to be depleted of alloying elements like C, Cr, Mo, V and Nb. Therefore, it showed lesser hardenability and transformed into ferrite plus carbide.

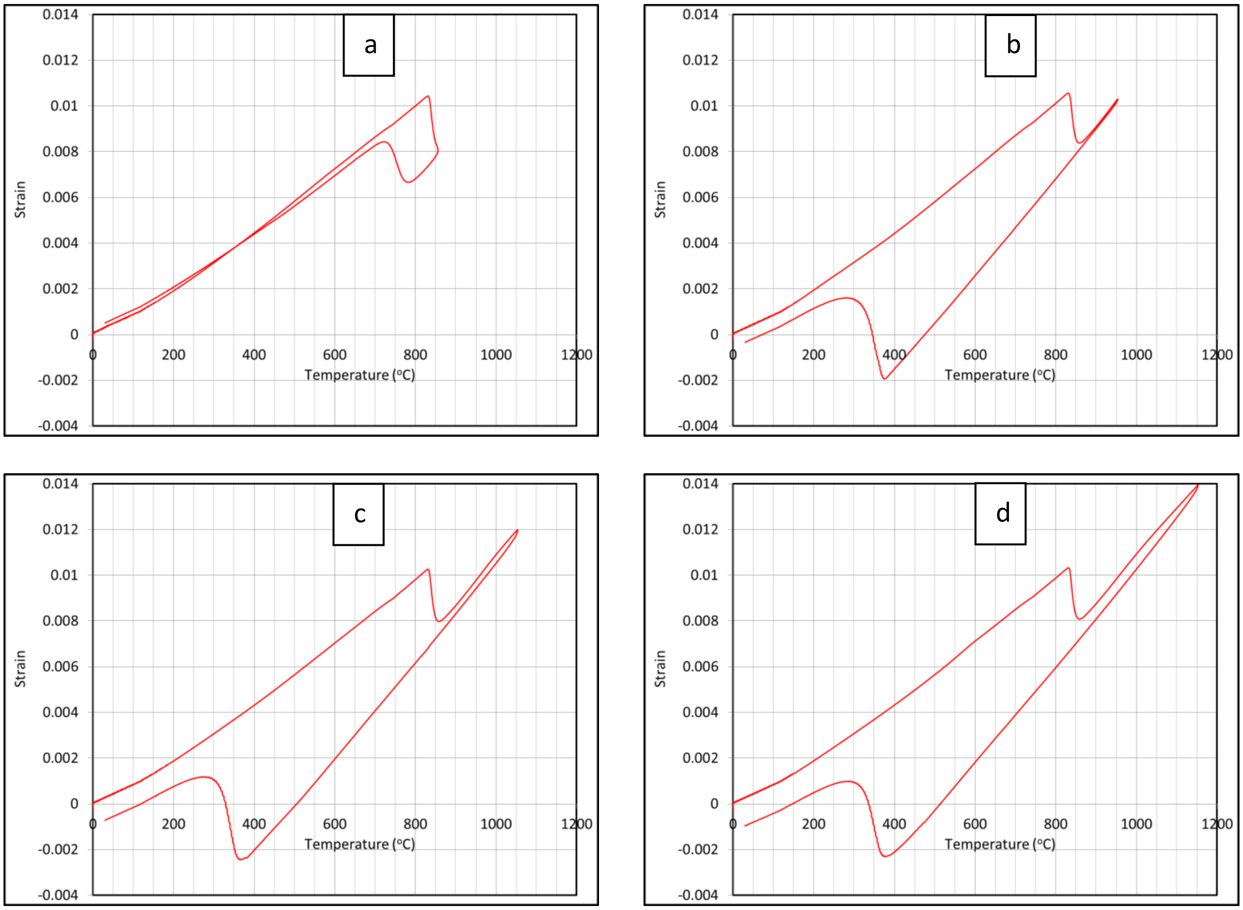

Fig 4.5: Dilation curve of 9Cr-1Mo(V, Nb) FMS austenitized at different temperatures – a. 850^oC, b. 950^oC, c. 1050^oC and d. 1150^oC.

It is important to mention that outer part of the HAZ, bordering the parent metal, experiences lower superheat over the Ac_1 temperature and the time of exposure is also very small. The austenite formed in this region is therefore, expected to exhibit lesser hardenability and transform into ferrite as well as bainite. These transformation products have inferior creep properties than the martensite. These results are important to understand formation of type IV cracking in the weld joints in this material.

4.4 Phase-Dependent Tensile Behaviour of 9Cr-1Mo(V, Nb) FMS

Engineering stress-strain curves of 9Cr-1Mo(V, Nb) FMS tested at different temperatures in 30 – 800^{o}C range in TM, A, and M phase fields are presented in Fig. 4.6. The contrast in the tensile behaviour of the three phases is obvious with the martensitic conditions showing much higher yield strength and significantly lower elongation as compared to the metastable austenitic condition at a given test temperature. This contrast is also a manifestation of phase dependence in the tensile behaviour of this material, as it presents two completely different tensile curves at the same test temperature. This can be attributed to the difference in the strength and work-hardening behaviour of the different phases. Ranking of the three phases – TM, A, and M in terms of strength and elongation, and superior work hardening behaviour of the metastable austenite over that of the martensitic conditions is also clear from these tensile curves. Some important tensile properties such as yield strength (YS), uniform elongation (UE) and ultimate tensile strength (UTS) (true stress) of this material under different test conditions were derived from the respective engineering stress-strain curves. These values are presented in Fig. 4.7 as (YS, UE, UTS) triplet near the dark squares, marking test conditions on the dilation curve of this material.

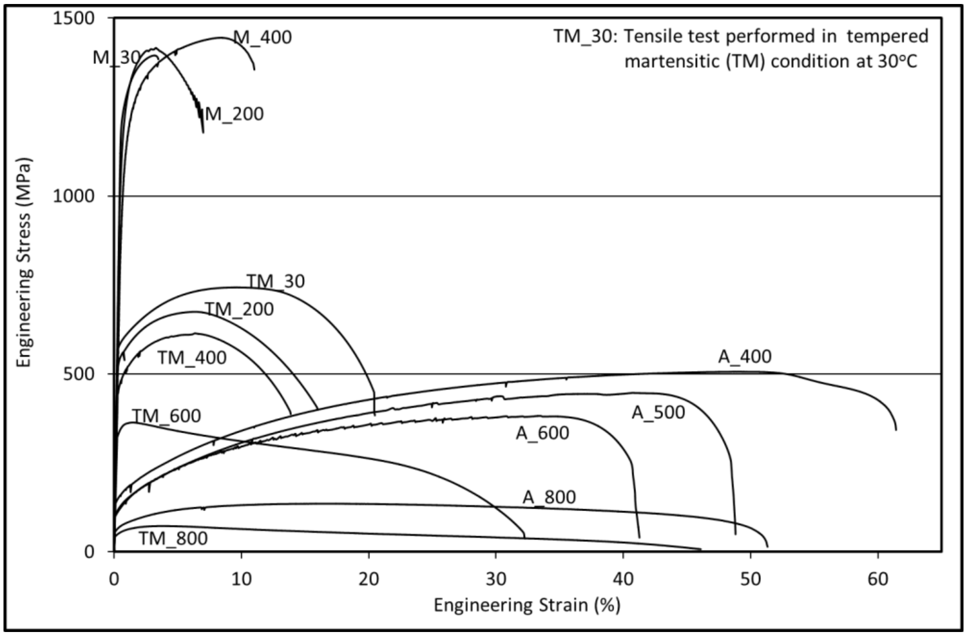

Fig. 4.6: Engineering stress-strain curve of 9Cr-1Mo(V, Nb) FMS in three different phase fields - tempered martensite (TM), metastable austenite (A) and as transformed martensite (M) at different test temperatures in RT – 800^{o}C range.

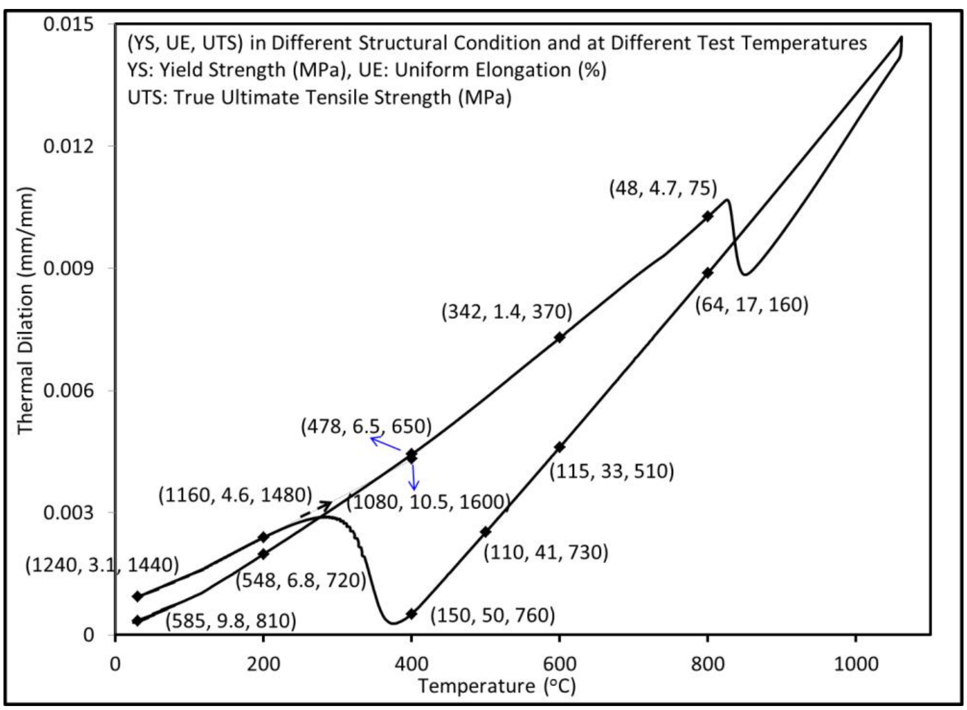

Fig. 4.7: Phase-dependence in tensile properties (YS, UE, UTS) of 9Cr-1Mo(V, Nb) FMS marked on its dilation curve at a heating and cooling rate of 10^{o}C/min.

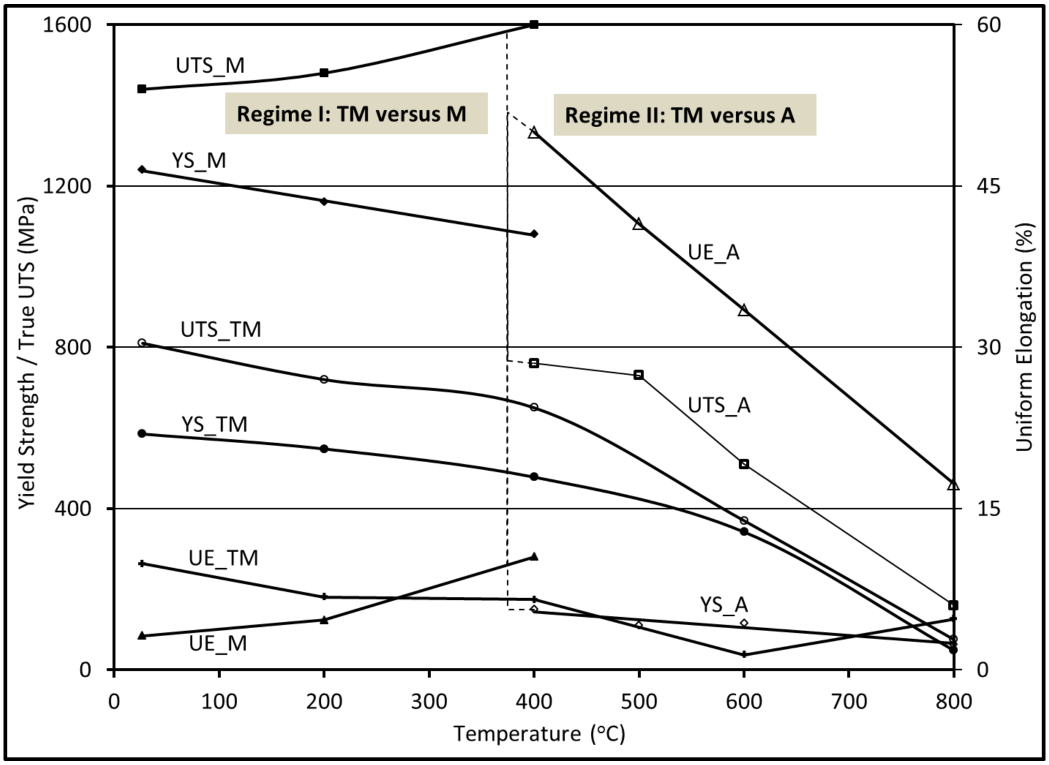

Fig. 4.8: Variation of the tensile properties like yield strength (YS), true ultimate tensile strength (UTS) and uniform elongation (UE) with test temperature of 9Cr-1Mo(V, Nb) FMS in three phase fields - tempered martensitic (TM), metastable austenitic (A) and as transformed martensitic (M). YS_M stands for yield strength of the material in as transformed martensitic condition.

Variation of the tensile properties - YS, UTS (true stress), and UE of this material with test temperature for the three different conditions (TM, A, and M), is presented in Fig. 4.8. Phase-dependence in the tensile behaviour of this material can be seen as difference in the tensile properties of the different structural conditions, which can exist, at a common test temperature while heating and cooling. For clarity, this plot can be divided into two regimes of the test temperature – Regime I (RT – 375^{o}C) in which TM and M conditions can exist and Regime II (375 – 800^{o}C) in which TM and A conditions can exist. Throughout the Regime I, as-transformed martensite shows more than twice YS and UTS than that of tempered martensite. As-transformed martensite also shows significantly lower UE as compared to that of tempered martensite, except at 400^{o}C at which UE of the as transformed martensite (8.7%) is greater than that of the tempered martensite (6.5%). Besides, in Regime I, even though YS of as-transformed martensite shows the expected inverse correlation with the test temperature, its UTS shows direct correlation, which is anomalous. These two apparently anomalous results need further work for satisfactory explanation.

In Regime II, YS of the tempered martensite decreases from 478 MPa to 48 MPa (90% drop) as temperature increases from 400^{o}C to 800^{o}C. On the other hand, YS of the metastable austenite falls from 150 MPa to 64 MPa and thus shows relatively much smaller (60%) drop over the same temperature range. Thus YS of the metastable austenite is not only significantly lower than that of the tempered martensite at a given temperature; it is less temperature-sensitive as well. This is primarily due to relatively lower and less temperature-sensitive Peierls-Nabarro stress of face-centred cubic structure, than that of body-centred cubic structure [25]. Additionally, much coarser microstructure and absence of carbide precipitates in the metastable austenite also contribute to its lower YS than that of the tempered martensite.

Interestingly, differences in the UTS (true stress) are much smaller in magnitude and opposite in direction than those in the YS. Thus, at a common test temperature, while YS of the metastable austenite is lower, it's UTS (true stress) is higher than the corresponding values of the tempered martensite. This results in much higher UTS to YS difference for the metastable austenite than that for tempered martensite. Also, throughout Regime II, the metastable austenite shows nearly one order higher UE than that shown by the tempered martensite. This is a manifestation of superior work hardening behaviour of the metastable austenite as compared to tempered martensite. This has important implication for the stress-field evolution during welding process, when the metastable austenite in the fusion zone and the heat affected zone can accommodate much larger stress than its YS by deforming plastically and getting work hardened under influence of the thermal contraction induced forces of tensile nature. Uniform elongation of the metastable austenite shows inverse correlation with the test temperature, decreasing from 50% to 17% over the test temperature range of 400 – 800^{o}C. This is apparently anomalous as positive correlation is expected for a homogeneous microstructure. Room temperature microstructures of the tensile samples tested in the metastable austenitic conditions provided a possible explanation for this anomaly as discussed in the next section.

4.5 Microstructure of Fractured Metastable Austenitic Tensile Specimen

Optical and TEM micrographs of the tensile test specimen tested in the metastable austenitic condition at different test temperatures (400 – 800^{o}C) and allowed to cool in the furnace are presented in Figs. 4.9 through 4.11. The experimental set-up used in the present study did not allow rapid cooling of the fractured specimen, therefore, as-tested microstructure could not be preserved. Slow cooling of the fractured samples could have introduced some changes in the microstructure, which include recrystallization and diffusional phase transformation of the deformed austenite. In view of this, only very limited inferences could be drawn from these microstructures. The optical micrograph (Fig. 4.9a) of the sample tested at 400^{o}C shows profuse micro-deformation bands within the deformed prior austenite grains and the TEM micrograph (Fig. 4.9b) shows the micro-deformation bands swamped with submicron as-transformed martensite laths. These micro-deformation bands are formed within the austenite grains due to plastic deformation during the tensile test and subsequently get inherited by the product microstructure as the deformed austenite gets transformed into bainite/martensite [16, 17]. There is no signature of recrystallization of the parent austenite phase tested at 400^{o}C, which is natural as the test temperature is lower than 0.4T_m.

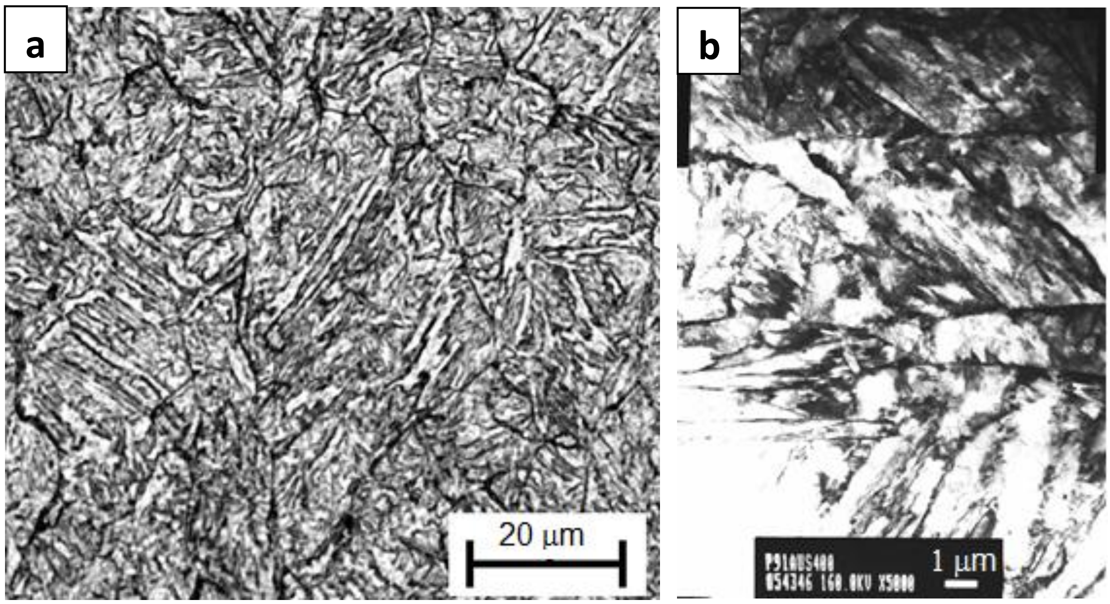

Fig. 4.9: Room temperature microstructure of metastable austenite tensile tested at 400^{o}C (a) optical micrograph showing deformation bands within prior austenite grains and (b) TEM bright field image of the deformation bands swamped with martensite lath.

However, the metastable austenite specimens tested at higher temperatures – 500^{o}C, 600^{o}C (Fig. 4.10a) and 800^{o}C (Fig. 4.11a) show varying degree of recrystallization in the deformed prior austenite phase field. Partial recrystallization of the parent austenite phase field provides a possible explanation for inverse correlation between UE and test temperature for the metastable austenitic condition. It is reasonable to expect that the recrystallization being incomplete can create an inhomogeneous microstructure consisting of work-hardened and soft recrystallized austenite grains. This inhomogeneity of the microstructure can cause necking and thus limit UE during the tensile test. Onset of recrystallization requires larger plastic deformation at lower test temperatures and vice-versa. Therefore, onset of necking and thus UE shows inverse correlation with the test temperature.

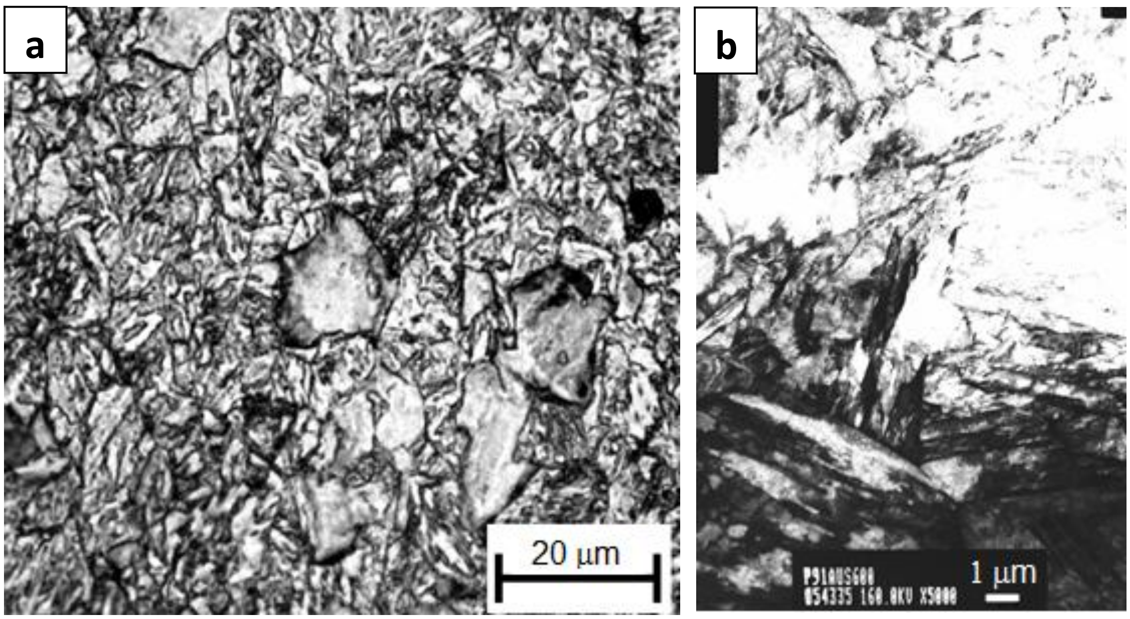

Fig. 4.10: Room temperature microstructure of metastable austenite tensile tested at 600^{o}C (a) optical micrograph showing deformed and also some recrystallized prior austenite grains and (b) TEM bright field image showing bainitic region.

In addition to the lath martensitic structure, the metastable austenite tested at 600^{o}C shows some bainitic regions (Fig. 4.9b) and that tested at 800^{o}C shows ferritic (Fig. 4.11b) as well as bainitic regions (Fig. 4.11c). Presence of the ferritic region is expected as the fractured samples were left in the furnace to cool after the tensile test, so the cooling rate was low and also because plastic deformation is known to shift the continuous cooling transformation (CCT) curves towards left [18]. However, the bainitic regions were not expected as the CCT curve of this material does not show any bainitic transformation [13]. This difference could be due to the fact that the parent austenite was deformed prior to transformation and that is not accounted for in the case of the CCT curve. These results, however, suggest that under the conditions of deformation and stress, this material can transform into bainite as well. Therefore, further work is required to modify the CCT curve of this material to include the effect of stress and prior deformation on phase transformation of this material.

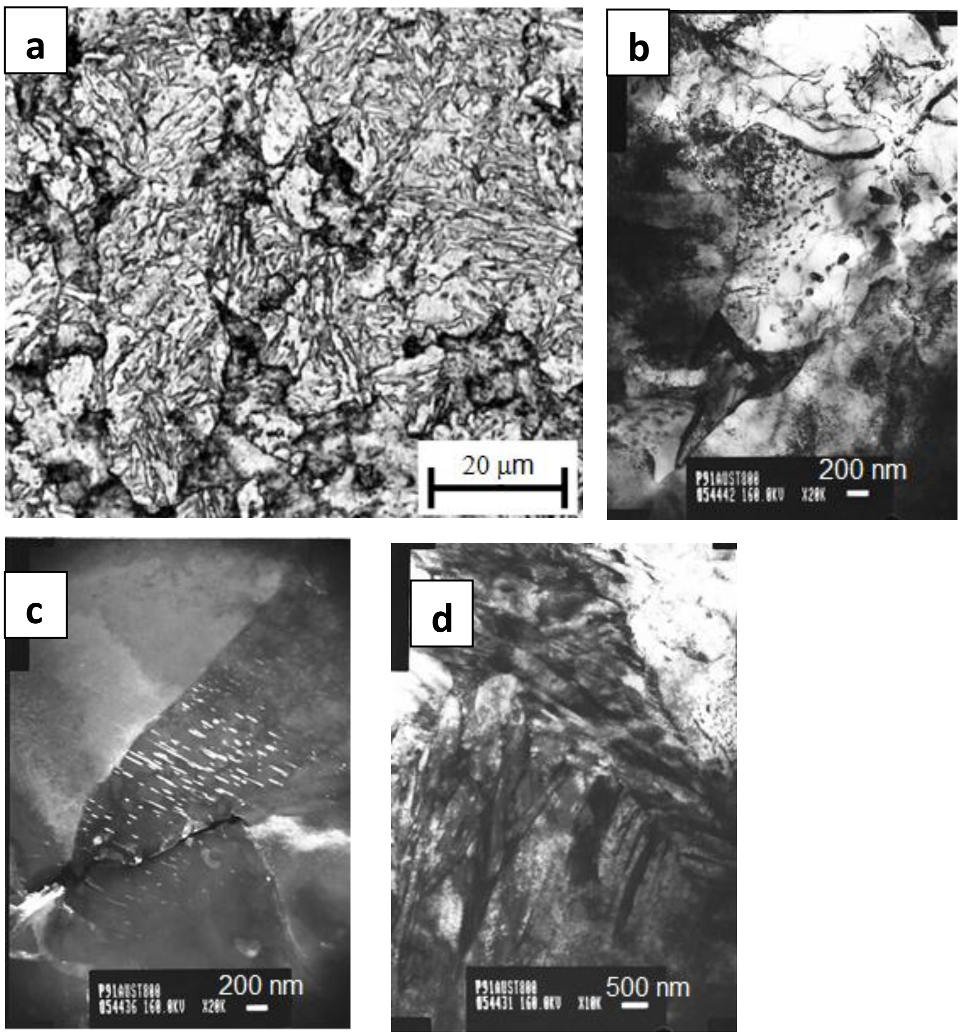

Fig. 4.11: Room temperature microstructure of metastable austenite tensile tested at 800^{o}C (a) optical micrograph showing deformed and as well as partially recrystallized prior austenite grains and (b) TEM bright field image of ferrite plus carbide region, (c) TEM dark field image of bainitic region and (d) TEM bright field image of martensite laths.

4.6 Conclusions

Microstructural characterization and dilatometry of the as-received 9Cr-1Mo(V, Nb) FMS in normalized and tempered condition were done. In addition, phase-dependent (elevated temperature) tensile tests of this steel were also performed and this is being reported for the first time. From this study following conclusions can be drawn.

(i) The microstructure of 9Cr-1Mo(V, Nb) FMS showed elongated subgrains within prior austenite grains of ~ 20 µm size. Submicron $M_{23}C_6$ type carbides (~ 100 nm) decorated the prior austenite grain boundaries as well as the subgrain boundaries. In addition, MX type carbonitrides of size about 10 nm were also observed within the subgrains. This microstructure is consistent with that reported in the literature for this steel.

(ii) Austenitization temperature showed significant influence on the transformation behaviour of austenite during cooling, in this steel. While cooling, the austenite transformed into martensite (Ms ~ 375^{o}C), for austenitization temperatures of 950^{o}C and higher, while it transformed into ferrite plus carbide for austenitization temperature of 850^{o}C. This was due to loss of hardenability of the austenite due to insufficient dissolution of carbides at lower austenitization temperatures.

(iii) The results showed considerable influence of the underlying phases – tempered martensite, metastable austenite and as-transformed martensite, on different tensile properties – yield strength, uniform elongation and ultimate tensile strength, of this material during heating and cooling due to hysteresis in the phase field.

(iv) This material in the metastable austenitic condition showed one order higher uniform elongation and superior work hardening characteristics as compared to that in the tempered martensitic condition in the 400 - 800^{o}C temperature range.

(v) The metastable austenitic phase field of this material showed higher uniform elongation with decreasing deformation temperature. Therefore, this material can be a promising candidate for ausforming.

(vi) Bainitic transformation products observed in the room temperature microstructure of metastable austenite, deformed at 600^{o}C and at higher temperatures cannot be explained on the basis of the existing CCT curve. Therefore, effect of stress and deformation on the transformation of the deformed austenite in this material requires further investigation.

(vii) This work is relevant for 8-12%Cr ferritic/martensitic steels, including reduced activation ferritic martensitic steels, produced under different grades for a variety of high temperature applications as the phase transformation behaviour is very similar within this group.

References

[1] F. Masuyama, "History of power plants and progress in heat resistant steels", ISIJ Intl. 41(6) (2001) 612–625.

[2] R. L. Klueh, "Elevated temperature ferritic and martensitic steels and their application to future nuclear reactors", Int. Mater. Rev. 50(5) (2005) 287 - 310.

[3] A. Shibli and F. Starr, "Some aspects of plant and research experience in the use of new high strength martensitic steel P91" Int. J. of Press. Vessels Pip. 84(1 - 2) (2007) 114 -122.

[4] R. L. Klueh and A. T. Nelson, "Ferritic/martensitic steels for next-generation reactors", J. Nucl. Mater. 371 (1 - 2) (2007) 37-52.

[5] K. H. Mayer and F. Masuyama, "The development of creep-resistant steels" in Creep-Resistant Steels, F. Abe, T U Kern and R. Viswanathan Eds.; Woodhead Publishing Limited, Cambridge, UK, (2008) 15-77 .

[6] H. Tanigawa, K. Shiba, A. Möslang, R.E. Stoller, R. Lindau, M.A. Sokolov, G.R. Odette, R.J. Kurtz and S. Jitsukawa, "Status and key issues of reduced activation ferritic/martensitic steels as the structural material for a DEMO blanket", J. Nucl. Mater. 417 (1 – 3) (2011) 9-15.

[7] H. Kitahara, R. Ueji, N. Tsuji and Y. Minamino, "Crystallographic features of lath martensite in low-carbon steel", Acta Mater 54 (2006) 1279-1288.

[8] S. Morito, X. Huang, T. Furuhara, T. Maki and N. Hansen, "The morphology and crystallography of lath martensite in alloy steels", Acta Mater 54 (2006) 5323-5331.

[9] F. Abe, M. Taneike and K. Sawada, "Alloy design of creep resistant 9Cr steel using a dispersion of nano-sized carbonitrides", Int. J. Press. Vessel. Pip. 84 (2007) 3-12.

[10] I. Holzer, “Modelling and simulation of strengthening in complex martensitic 9-12%Cr steel and binary Fe-Cu alloy”, PhD. Thesis, Graz University of Technology, Graz (2010).

[11] A. Aghajani, “Evolution of microstructure during long-term creep of a tempered martensite ferritic steel”, PhD Thesis, Ruhr University, Bochum, Germany (2009).

[12] B. J. Ganesh, S. Raju, A. K. Rai, E. Mohandas, M. Vijayalakshmi, K. B. S. Rao, and B. Raj, “Differential scanning calorimetry study of diffusional and martensitic phase transformations in some 9 wt% Cr low carbon ferritic steels”, Mater. Sci. and Technol. 27(2) (2011) 500-512.

[13] K. Haarmann, J. C. Vaillant, W. Bendick and A. Arbab, The T91/P91 Book, Vallourec and Mannessmann Tubes, (1999) 14-29.

[14] S. Sulaiman, “Structure of properties of the heat affected zone of P91 creep resistant steel”, PhD Thesis, University of Wollongong, Wollongong, Australia (2007) [http://ro.uow.edu.au/theses/777].

[15] B. Ning, Q. Shi, Z. Yan, J. Fu, Y. Liu and L. Bie, “Variation of martensite phase transformation mechanism in minor-stressed T91 ferritic steel”, J. Nucl. Mater. 393 (2009) 54–60.

[16] T. S. Wang, M. Zhang, Y. H. Wang, J. Yang and F. C. Zhang, “Martensitic transformation behaviour of deformed supercooled austenite”, Scripta Mater. 68(2) (2013) 162 - 165.

[17] M. C. Tsai, C. S. Chiou, J. S. Du and J. R. Yang, “Phase transformation in AISI 410 stainless steel”, Mater. Sci. Eng. A332(1 - 2) (2002) 1-10.

[18] F. Xiao, B. Liao, G. Qiao and S. Guan, “Effect of hot deformation on phase transformation kinetics of 86CrMoV7 steel”, Mater. Charact. 57 (4 - 5) (2006) 306 - 313.

[19] N. Tsuji and T. Maki, “Enhanced structural refinement by combining phase transformation and plastic deformation in steels”, Scripta Mater. 60 (2009) 1044 - 1049.

[20] H. G. Lambers, S. Tschumak, H. J. Maier and D. Canadinc, “Role of Austenitization and Pre-Deformation on the Kinetics of the Isothermal Bainitic Transformation”, Metall. Mater. Trans. A40 (2009) 1355 - 1366.

[21] Y. Yogo, M. Kamiyama, T. Iwata, N. Iwata and T. Ishikawa, “Measurement of Flow Stress in Supercooled Austenite for High Hardenability Steel”, Metall. Mater. Trans. A43 (2012) 893 - 899.

[22] A. H. Yaghi, T. H. Hyde, A. A. Becker, J. A. Williams and W. Sun, “Residual stress simulation in welded sections of P91 pipes”, J. Mater. Process. Technol. 167 (2005) 480 - 487.

[23] D. Dean and M. Hidekazu, “Prediction of welding residual stress in multi-pass butt-welded modified 9Cr–1Mo steel pipe considering phase transformation effects”, Comput. Mater. Sci. 37 (2006) 209 - 219.

[24] S. H. Kim, J. B. Kim and W. J. Lee, “Numerical prediction and neutron diffraction measurement of residual stresses for a modified 9Cr-1Mo steel weld”, J. Mater. Process. Technol. 209 (2009) 3905 - 3913.

[25] R. W. Hertzberg: Deformation and Fracture Mechanics of Engineering Materials, 4th ed., John Wiley and Sons Inc., 1995, pp. 62-64.

Chapter 5: Laser Welding of 9Cr-1Mo(V, Nb) FMS and Weld Joint Characterization

5.1 Introduction

9Cr-1Mo FMS modified with optimized microalloying additions of V and Nb, is a high temperature material of interest to ultra-supercritical power plants and next generation nuclear reactors [1 - 7]. This material forms the basis for development of the reduced activation ferritic/martensitic steels (RAFMS), which is the structural material for the test blanket modules for fusion reactors [8 - 14]. This steel is joined by different conventional arc welding processes like Manual Metal Arc Welding, Gas Tungsten Arc Welding, Submerged Arc Welding etc. [15 - 21]. However, these are high heat input processes and require multiple passes with preheating as well as inter-pass heating of the component. High heat input associated with these conventional welding processes results in higher distortion / residual stresses as well as a wider heat affected zone (HAZ), which in turn has adverse impact on the integrity of the weld joints. A premature failure mechanism in weld joint of Cr-Mo ferritic martensitic steels, known as type IV cracking, is often attributed to microstructural changes in the HAZ [15]. As the extent of microstructural changes in the HAZ is governed by the quantum of heat supplied to carry out welding, therefore, it has been suggested that low heat input processes like laser and electron beam welding can minimize type IV cracking susceptibility of weld joints [21 - 22]. Besides, these welding processes can produce a thick weld joint with narrow fusion zone and HAZ without any filler material. Distortion of the weld joint is negligible because of low heat input. Owing to these benefits, laser welding of 9Cr ferritic/martensitic steels (FMS) has recently evinced considerable interest [22 - 29].

Fabrication activities for test blanket modules (TBM) for International Thermonuclear experimental Test Reactor (ITER) has provided a fresh impetus for research activities in laser and electron beam welding of 9Cr FMS. The TBMs being developed by different participants in ITER, have fairly complex design and therefore, it is very challenging to fabricate them, even after employing the state of the art in technology. Fabrication of TBM requires making a large number of weld joints of varying thickness to be made and the distortion allowance is very minimal. Therefore, laser and electron beam welding is being used for fabrication of different subcomponents of TBM and also for integrating these subcomponents into the final TBM assembly. Laser welding is being adopted in ~ 2 – 12 mm thick joints, while EB welding is being used for up to 90 mm thick joints by Japan for joining side plates and back plates with the first wall [25 - 29].

9Cr-1Mo(V, Nb) FMS is a highly hardenable material and undergoes complete martensitic transformation upon cooling from austenitic phase-field, even at very low cooling rates ~5^{o}C/min [30]. Thermal cycles imposed by welding heat source, therefore, induce phase transformations as well as significant microstructural changes. Strength of a thermal cycle is qualitatively defined as a function of superheat and residence time of the material above a critical temperature required to cause a change. Strength of the weld thermal cycle weakens gradually from the fusion zone towards the parent metal. This leads to formation of a graded heat affected zone in the welded 9Cr-1Mo(V, Nb) FMS. The microstructural variations across the weld joint, including that in the graded HAZ resulting from welding of 9Cr-1Mo(V, Nb) FMS has been discussed in detail in the literature [15, 17]. However, literature on laser welding of this steel is rather limited [22, 23]. Shanmugarajan et al. [22] have reported laser welding studies for 6 mm thick plate of P91 steel using continuous wave CO_2 laser (Power 3.5 kW). They have studied laser welds produced by varying heat input in the range of 168 J/mm to 1500 J/mm. They have reported increase in width of the fusion zone and the HAZ with increasing heat input. Further, at lower heat input up to 420 J/mm, they did not observe any soft inter-critical region; which was observed at heat inputs exceeding 700 J/mm. At lower heat inputs (up to 420 J/mm) they did not observe any δ-ferrite in the fusion zone, which was present in the fusion zone of the joints made at heat inputs exceeding 700 J/mm.

Lee et al. [23] produced and characterized full penetration laser welds on 5 mm thick plates of 9Cr-1Mo(V, Nb) FMS in normalized condition (1040^{o}C, 30 minutes), using 5 kW continuous wave CO_2 laser (Rofin-Sinar 850). They produced two weld beads, overlapping 6% at the root, on each plate to produce wide enough fusion zone for further characterization. The welds were tempered at 250^{o}C, 540^{o}C and 750^{o}C for 1 hour. They have characterized the welds and the parent metal for microstructure, impact toughness, notch tensile strength and fatigue crack growth, in air as well in hydrogen atmosphere. However, these studies have not dwelt upon cross-weld microstructural variation resulting from laser welding.

Laser welding differs significantly from the conventional welding processes due to its high power density, resulting in deeper penetration with significantly lower heat input. This results in high thickness to width aspect ratio of the fusion zone plus HAZ region. High thickness to width aspect ratio of the fusion zone and the HAZ also influences the constraints imposed on the material in this zone, dilating under the influence of steep temperature gradient as well as solid state phase transformations. Lower heat input also results in rapid cooling in the fusion zone and the HAZ region, which results in relatively weaker thermal cycle for recrystallization and grain coarsening due to lower residence time above the critical temperatures. This work reports variation of microstructure across the weld joint in laser welded 9Cr-1Mo(V, Nb) FMS and the important features of the microstructure have been discussed in terms of the synergistic effect of various factors influencing microstructural evolution during laser welding.

5.2 Depth of Penetration and Joining Efficiency

Depth of penetration, for the weld beads produced on a 30 mm thick plate of 9Cr-1Mo(V, Nb) FMS at different laser power (2 – 8 kW) and welding speed (0.5 – 5.0 m/min), was measured at the mid-length cross-section. Depth of penetration was measured from the top surface of the plate to the lowest point in the fusion zone. Variation of the depth of penetration with welding speed, for different laser powers in 2 – 8 kW range, is presented in Fig. 5.1.

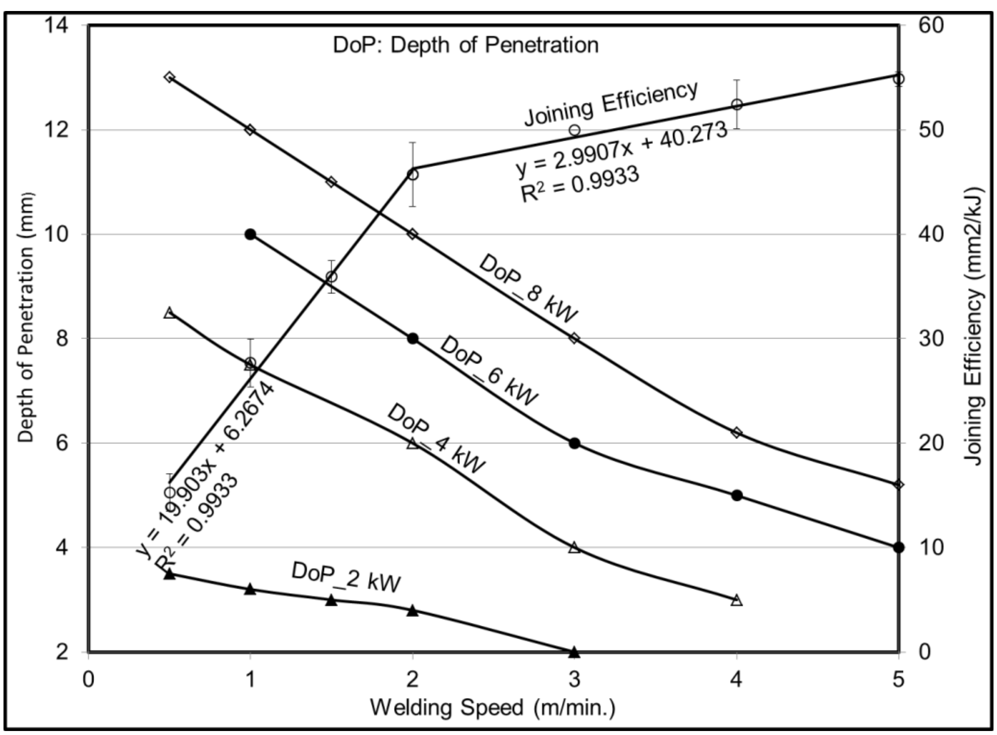

Fig. 5.1: Variation of depth of penetration of weld beads produced on 9Cr-1Mo(V, Nb) FMS at different laser powers and joining efficiency with welding speed.

For a given laser power, the depth of penetration decreases with increasing welding speed and for a given welding speed the depth of penetration increases with increasing laser power. This variation is very much on the expected lines and can be explained by energy balance. From this data, joining efficiency for each of the weld bead was calculated using the following equation.

$$J.\ E. = (v \times d) / P \qquad \text{............} \ (5.1)$$

J. E. = Joining efficiency (mm^2/kJ)

v = speed of welding (mm/s)

d = Depth of penetration (mm)

P = Laser power (kW)

Joining efficiency is a measure of the parting area which can be fused together per unit of energy supplied by the laser beam. Higher joining efficiency implies that a larger fraction of the supplied energy is being used for achieving the intended purpose of fusing the interface and not for broadening of the fusion zone and the HAZ. Joining efficiency showed a positive correlation with the welding speed; this is because at higher welding speed more of the supplied energy is being utilized in through thickness direction than that in the lateral direction.

Average joining efficiency of the weld beads at different laser powers (2 – 8 kW) was plotted against welding speed. The variation of average joining efficiency with welding speed could be fitted into the following linear equations.

$$J.\ E. = 19.903 \times v + 6.2674 \qquad 0.5 \leq v \leq 2.0$$

$$= 2.9907 \times v + 40.273 \qquad 2.0 \leq v \leq 5.0$$

Where J. E. is joining efficiency in mm^2/kJ and 'v' is the welding speed in m/min.

It can be seen that, as the welding speed increased from 0.5 m/min to 2.0 m/min, the joining efficiency increased rapidly. However, the incremental rate of increase in the joining efficiency with increasing welding speed was much lower at higher welding speeds (beyond 2.0 m/min). This can be explained in terms of competitive rate of heat transfer in the desired (through thickness) and undesired (transverse) direction with respect to the welding direction. Heat transfer in the through thickness direction occurs almost instantly by keyhole formation and radiation mechanism and that in the transverse direction is predominantly by melt pool convection and also by conduction in the solid. While lowering the welding speed serves to increase the depth of penetration by depositing more energy; a larger fraction of the deposited energy is carried away in the transverse direction by melt pool convection and thus joining efficiency is lower and the reverse is true when the welding speed is increased. However, beyond a certain welding speed, the welding speed to melt pool velocity ratio saturates and therefore, the incremental gain in the joining efficiency is significantly lower.

Also, increasing the welding speed leads to lower depth of penetration and therefore, a trade-off has to be made between joining efficiency and the depth of penetration, while choosing the optimum welding speed. From the results of the present experiments it emerged that the trade-off is at a welding speed of 2.0 m/min.

In conventional arc welding processes, linear heat input (power/speed) (kJ/mm) is used as a measure of heat input. The macro-structural as well as microstructural features associated with the weld joint are discussed in terms of this parameter (linear heat input). This works well because the heat transfer is 3-dimensional. Sometimes this practice, of discussing the macro-structural as well as microstructural features associated with the weld joint on the basis of linear heat input, is extended to laser welded joints also [22]. However, this does not seem to be a good practice as the heat transfer in case of deep penetration welding (for example laser and electron beam welding) is 2-dimensional. It must be noted that same linear heat input can be supplied by proportionately varying the laser power and welding speed. However, the outcome in terms of depth of penetration, heat transfer from the fusion zone to the parent metal, shape and size of the fusion zone and the HAZ and the microstructural features in the fusion zone and the HAZ can be vastly different for the two laser power – welding speed combinations, with same linear heat input. For a fixed linear heat input, high laser power - welding speed combination produces a deeper and narrower fusion zone and HAZ than that at lower laser power and proportionately lower welding speed. Therefore, linear heat input is not a good parameter to discuss the macro and microstructural features associated with a laser / electron beam welded joints; rather joining efficiency is a much better parameter.

Higher joining efficiency also implies that a larger cross-section is available for diffusion of the same amount of thermal energy being deposited near the joint and therefore, rapid heating and cooling of the material outside of the heat deposition zone by the welding heat source. This leads to a narrow fusion zone and HAZ for the weld joints produced at higher joining efficiency and vice-versa. Macrograph of the weld beads produced on a 30 mm thick plates of 9Cr-1Mo(V, Nb) at 8 kW laser power and different welding speeds - (a) 0.5 m/min, (b) 1.0 m/min, (c) 1.5 m/min and (d) 2.0 m/min is presented in Figs. 5.2(a) through Fig. 5.2(d). It may be noted that for the weld beads produced at 8 kW laser power, joining efficiency increases from 15 mm^2/kJ to 42

mm^2/kJ; when welding speed increased from 0.5 m/min to 2.0 m/min. With increasing joining efficiency, the lateral spread of the fusion zone and the the HAZ gets markedly restricted.

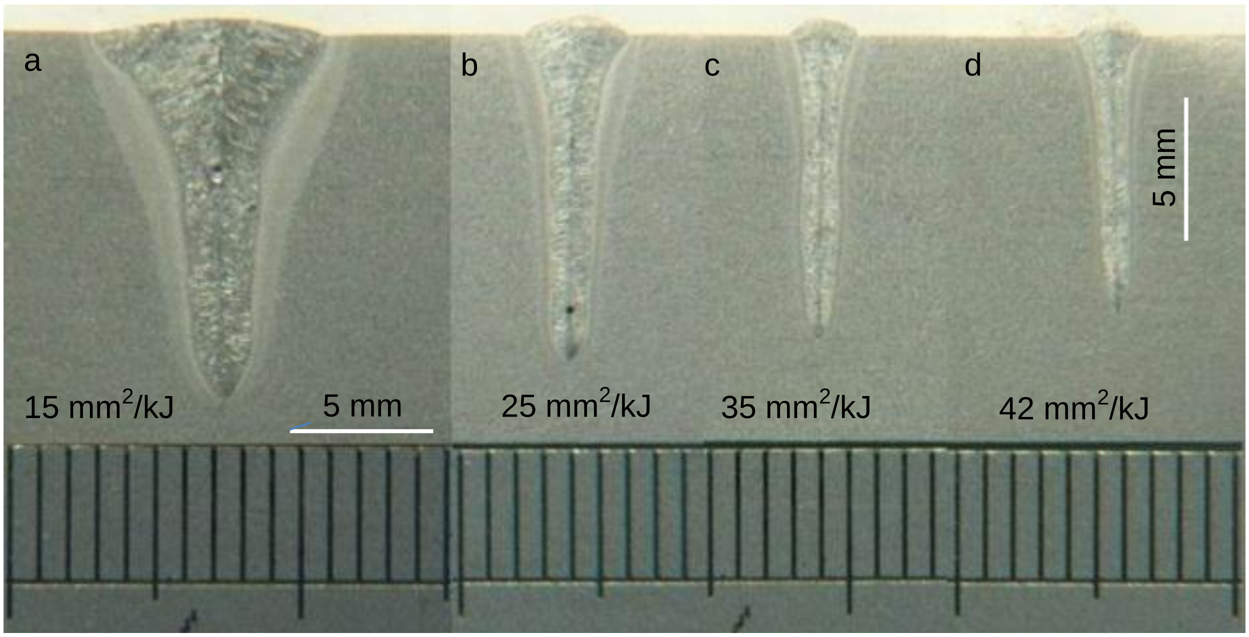

Fig. 5.2: Macrograph of laser weld beads produced at 8 kW laser power and welding speed of (a) 0.5 m/min, (b) 1.0 m/min, (c) 1.5 m/min and (d) 2.0 m/min. Joining efficiency for these weld beads are respectively 15 mm^2/kJ, 25 mm^2/kJ, 35 mm^2/kJ and 42 mm^2/kJ.

5.3 Cross-Weld Microstructural Variation in As-welded Condition

Macrographs showing cross-section of the laser welded joints produced at 8 kW laser power and two different welding speeds 1.5 m/min and 0.75 m/min, are presented in Figs. 5.3(a) and 5.3(b) respectively. These macrographs show a deep and narrow fusion zone and HAZ. Such a deep and narrow fusion zone and HAZ with high depth to width aspect ratio is a characteristic of the weld joints produced by high power density energy sources like focused laser and electron beams. Shape of the fusion zone resembles that of a nail with a small head and a long body. While the long body of the fusion zone forms through keyhole mechanism, a small nail head forms at the top surface because of surface tension gradient induced melt pool convection. The fusion zone and the HAZ are significantly wider in case of the weld joint produced at same laser power but slower welding speed (0.75 m/minute) and lower joining efficiency (14 mm^2/kJ) than that in case of the weld joint produced at higher welding speed (1.5 m/minute) and higher joining efficiency (28 mm^2/kJ).

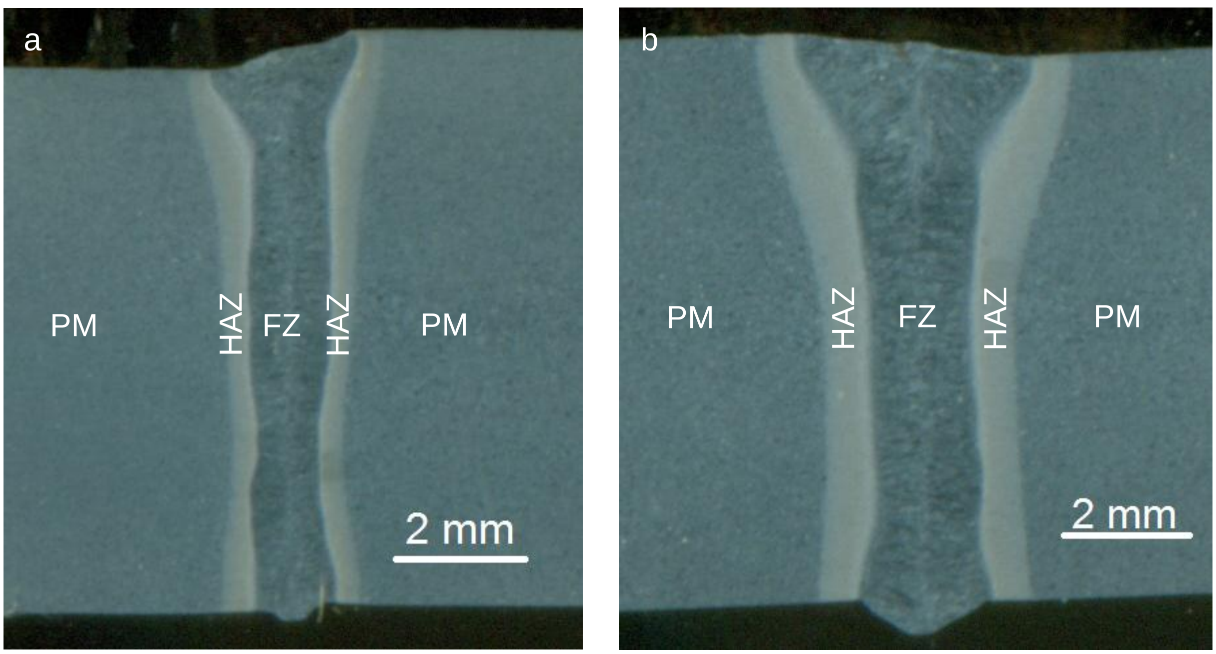

Fig. 5.3: Macrographs of laser welded joint in 9Cr-1Mo(V, Nb) FMS produced at 8 kW power and two different welding speeds (a) 1.5 m/min (Plate A) and (b) 0.75 m/min (Plate B).

Microstructure of the parent metal consists of tempered martensitic subgrains decorated with $M_{23}C_6$ type carbides and MX carbonitrides within prior austenite grains of ~ 20 µm size and has been discussed in detail in Chapter 4. There was no significant difference in the microstructure of the different regions the HAZ as well as the FZ in the plates welded at same laser power (8 kW) but two different welding speeds 1.5 m/min and

0.75 m/min. Optical micrograph of the HAZ region in in the plate welded at 8 kW laser power and 1.5 m/min welding speed is shown in Fig. 5.4(a). This micrograph shows as-transformed martensitic structure within prior austenite grains of varying size. The austenite grains are formed by phase transformation of ferrite to austenite, which then grows in size. The extent of ferrite to austenite transformation depends on the superheat above Ac_1 temperature. Growth of the austenite grains depends on combined effect of the superheat and time spent above grain growth temperature. Strength of the thermal cycle weakens progressively with increasing distance from the fusion line. This has resulted in progressively smaller prior austenite grains with increasing distance from the fusion line.

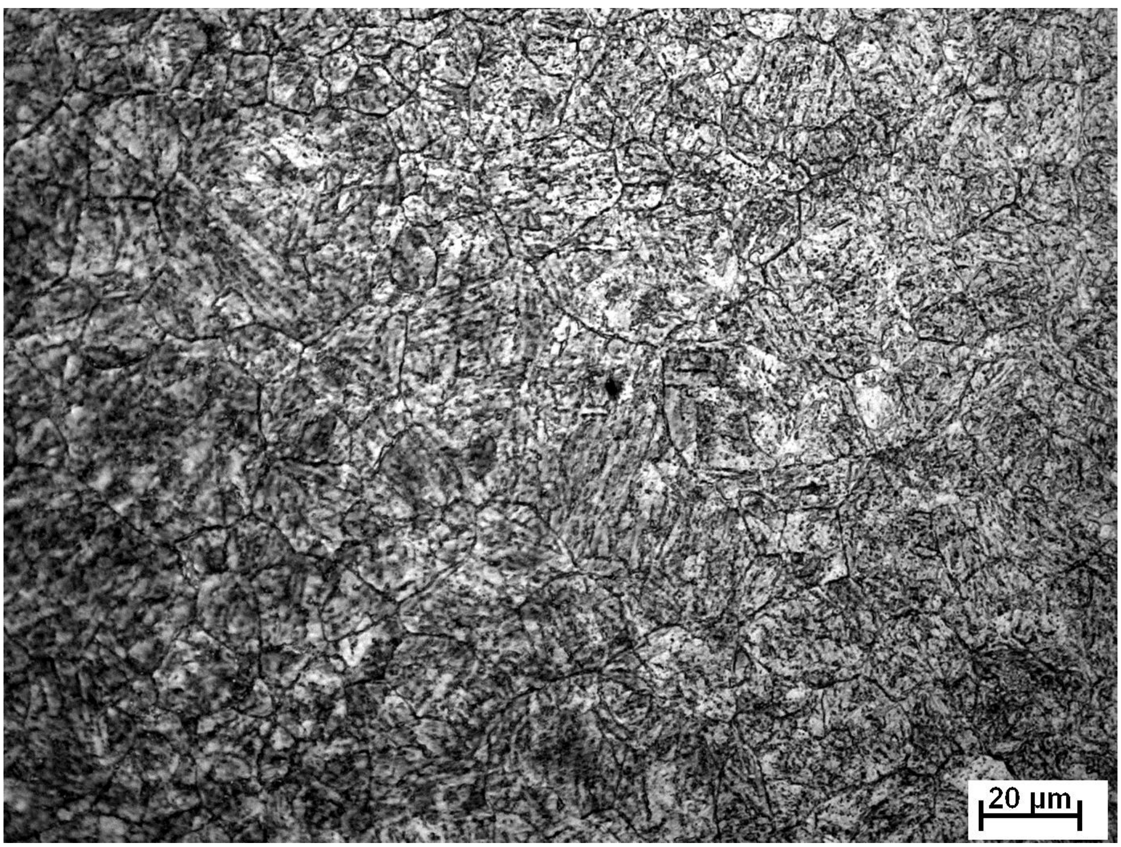

Fig. 5.4(a): Optical micrograph of the HAZ region in the plate welded at 8 kW laser power and 1.5 m/min welding speed showing prior austenite grains of varying size.

In case of arc welded joints in this steel five different zones – PMZ (partially melted zone), CGHAZ (coarse grained HAZ), FGHAZ (fine grained HAZ), ICHAZ (intercritical HAZ) and SCHAZ (subcritical HAZ) form as weld thermal cycle is very strong due to high heat input and therefore longer residence time for the material above the respective critical temperatures. However, in these laser welded joints no CGHAZ was observed. This can be explained by lower heat input resulting in rapid cooling and therefore short residence time for the material above the critical temperature for grain coarsening, which is ~ 1100^{o}C. This argument is supported by the scanning electron micrograph from the HAZ region (Fig. 5.4(b)), which shows incomplete dissolution of the carbide precipitates present in the original microstructure.

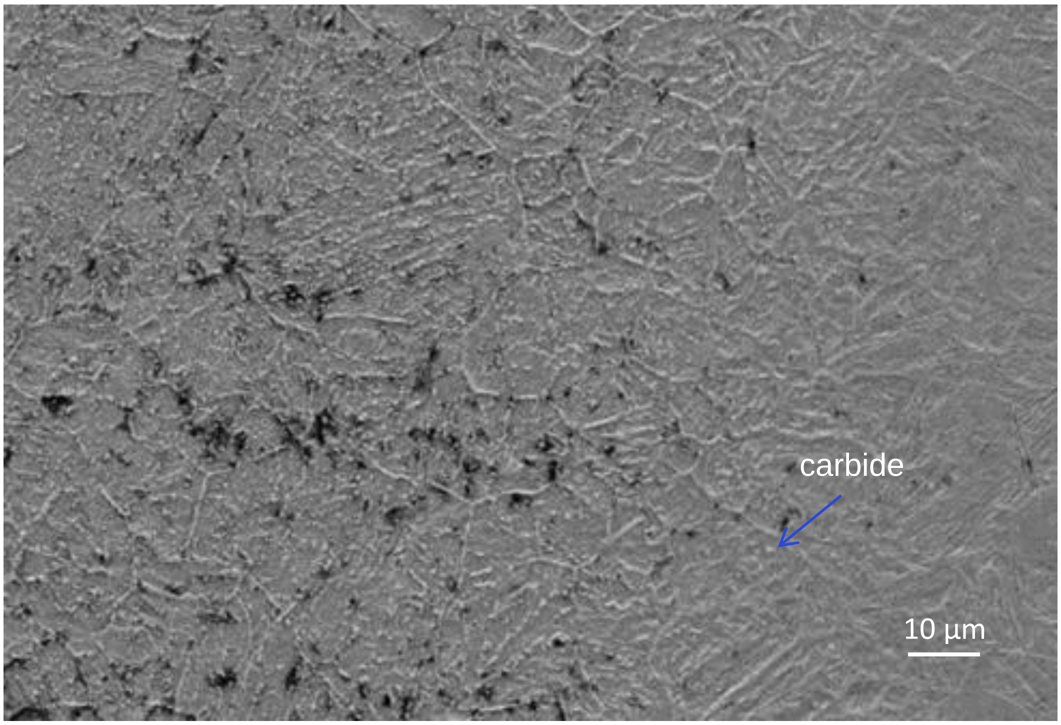

Fig. 5.4(b): Scanning electron micrograph of the HAZ region in the plate welded at 8 kW laser power and 1.5 m/min welding speed, showing presence of undissolved carbide/carbonitride precipitates.

TEM micrographs from the HAZ region are presented in Figs. 5.4(c) and 5.4(d). Figure 5.4(c) shows some fine undissolved carbide precipitates, in the HAZ region, and thus confirms incomplete dissolution of the carbide precipitates. Incomplete dissolution of carbide precipitates, because of short residence time of the material at the higher temperatures, did not allow grain coarsening to take place in the HAZ region.

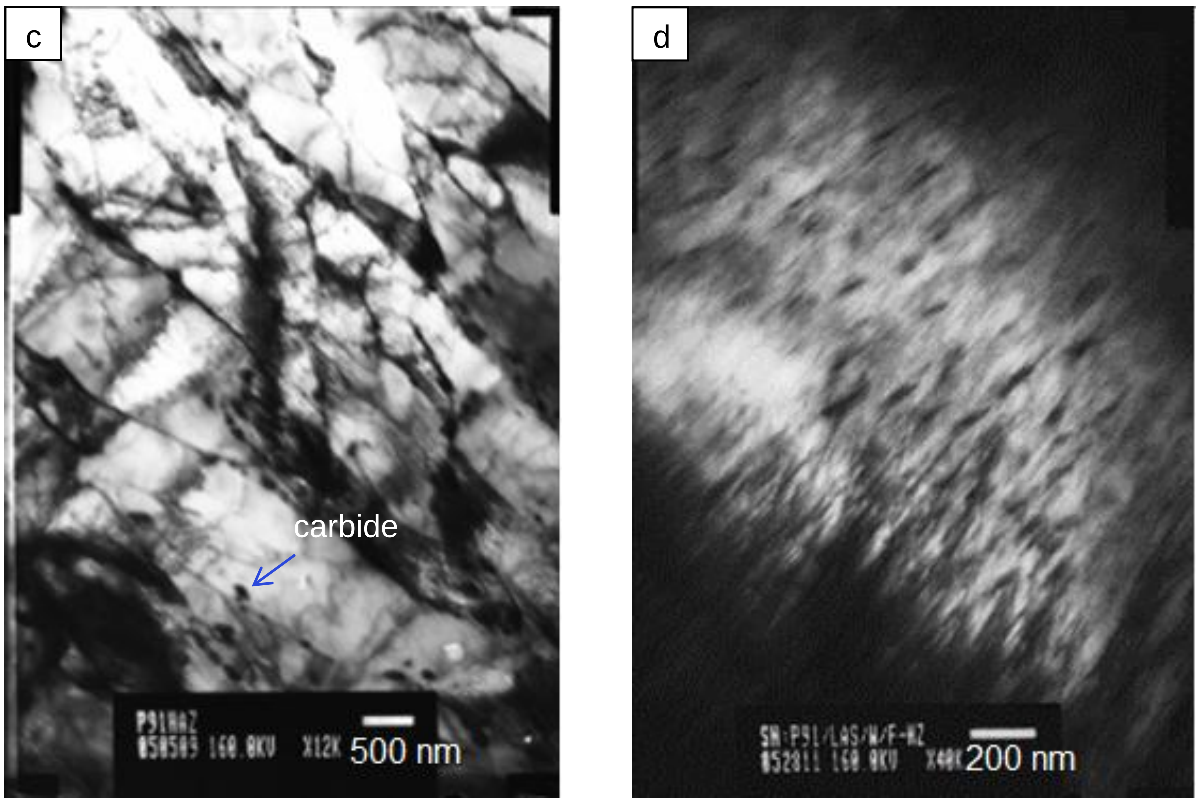

Fig. 5.4: TEM micrographs from the HAZ region in in the plate welded at 8 kW laser power and 1.5 m/min welding speed showing (c) incomplete dissolution of carbide precipitates and (d) presence of bainitic region.

In addition to incomplete carbide precipitates, the HAZ region also showed bainitic region (Fig. 5.4(d)). This steel is highly hardenable and therefore, not expected to undergo bainitic transformation, at least at the high cooling rates experienced by the material in the HAZ region. Presence of the bainitic region can be explained by loss of hardenability of the steel resulting from incomplete dissolution of the carbide precipitates at lower peak temperatures experienced in the outer HAZ region (i.e. the HAZ region closer to the parent metal). It has been discussed in Chapter 4, how lower austenitization temperature can lead of loss of hardenability to the extent that this steel can undergo even diffusional transformation at a cooling rate at which it is expected to undergo only martensitic transformation.

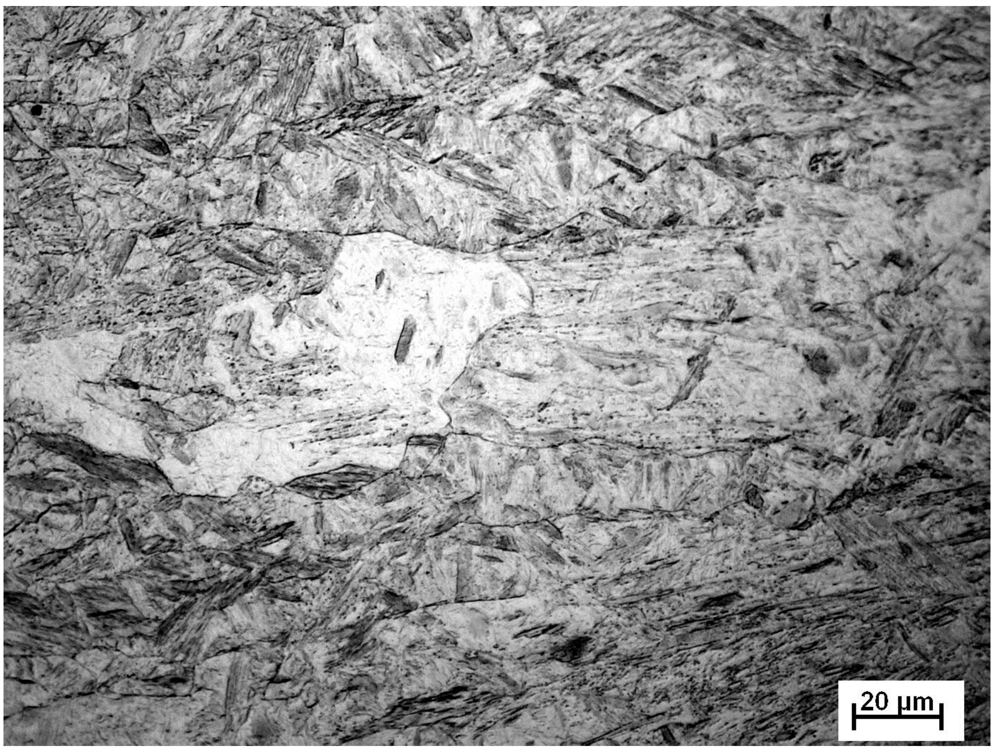

Fig. 5.4(e): Optical micrograph of the fusion zone in the plate welded at 8 kW laser power and 1.5 m/min welding speed showing columnar prior austenite grains.

Optical micrograph of the fusion zone in the plate welded at 8 kW laser power and 1.5 m/min welding speed is presented in Fig. 5.4(e). This micrograph shows as-transformed martensitic structure within columnar prior austenite grains. Columnar morphology is a result of solidification under steep temperature gradient generally associated with the melt produced by high intensity heat sources like laser and electron beam. The direction of solidification is normal to the fusion line and the columnar morphology has prevailed right up to the weld centreline. Besides, this microstructure is a homogeneous as-transformed martensite and no δ-ferrite was observed. This is consistent with the results reported by Shanmugarajan et al. [22] for the laser welded joints made with comparable heat input.

SEM micrograph of the fusion zone is presented in Fig. 5.4(f). This micrograph shows that the fusion zone is a homogeneous single phase and no precipitate is present in this zone.

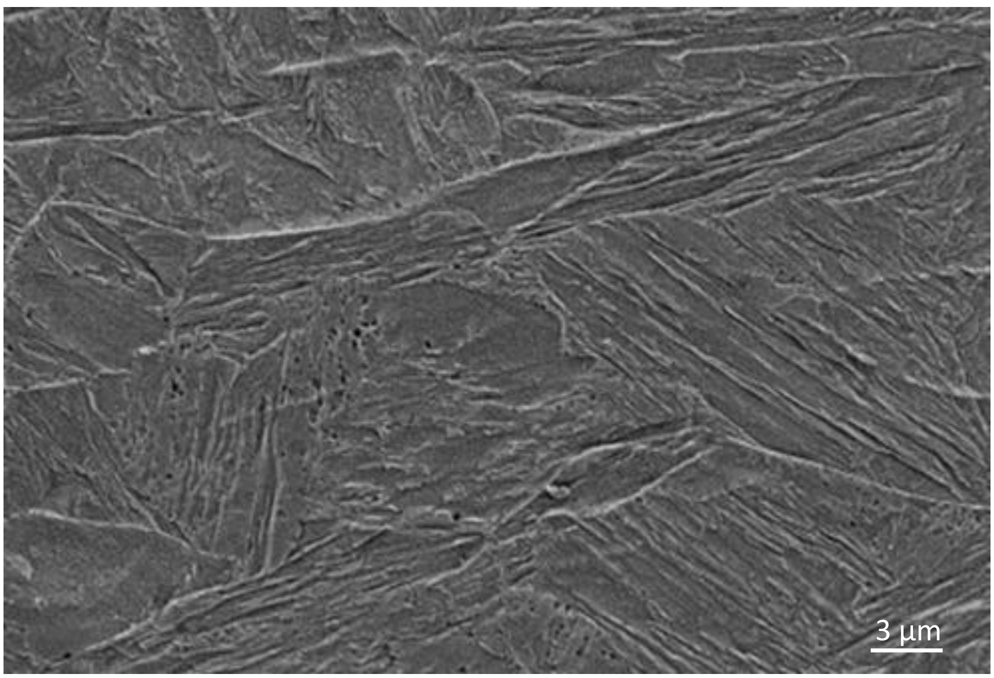

Fig. 5.4(f): SEM micrograph of the FZ region in the plate welded at 8 kW laser power and 1.5 m/min, showing absence of any precipitate in this zone.

TEM micrographs from the fusion zone are presented in Figs. 5.4(g) and 5.4(h). These micrographs confirm that the fusion zone is indeed a homogeneous single phase and there are no carbide precipitates in this zone. This differs from microstructure of the fusion zone of multipass arc welded joints in which succeeding passes cause re-austenitization and tempering of the material deposited by the preceding passes and thus creating a heterogeneous microstructure comprised of as-transformed martensite, δ-ferrite as well as different carbide precipitates [17].

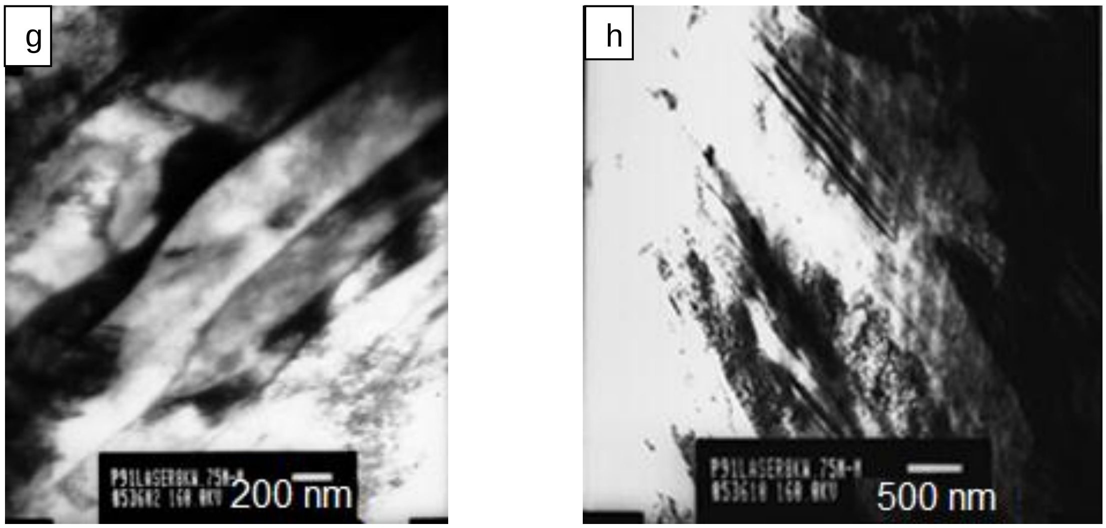

Fig. 5.4: TEM micrographs from the fusion zone region in laser welded 9Cr-1Mo(V, Nb) FMS showing (g) lath martensite and (h) twinned martensite.

This is a low carbon steel and therefore, transforms predominantly as lath martensite (Fig. 5.4(g)), however, in addition to lath martensite, significant fraction of twinned martensite was also observed (Fig. 5.4(h)). Twinned martensite has also been reported in the fusion zone of this steel by Lee et al. [23]. However, they have reported that the twinned martensite formed during PWHT by decomposition of retained austenite in the inter-lath region. In our case, no retained austenite was observed and the twinned martensite was observed in as-welded condition. This may be explained by suppression of the Ms temperature due to work-hardening resulting from plastic deformation of the austenite in the fusion zone, prior to its transformation. Wang et al. [31, 32] have reported that higher strength of austenite, resulting from work hardening, suppresses Ms temperature by mechanical stabilization of austenite. Martensitic transformation at lower temperatures results in twinned martensite. Austenite in the high aspect ratio fusion zone contracts under greater constraint and therefore, is likely to experience significant plastic deformation and work hardening. This can result in significant suppression of the Ms temperature and this explains significant fraction of twinned martensite in the fusion zone, even though it is not generally observed in this steel.

5.4 Microstructure of Weld Joint in Post Weld Heat Treated Condition

Optical micrograph of the HAZ of the laser welded 9Cr-1Mo(V, Nb) FMS plate, in post weld heat treated condition is presented in Fig. 5.5a. Fine grained character of the HAZ region can be clearly seen in this micrograph.

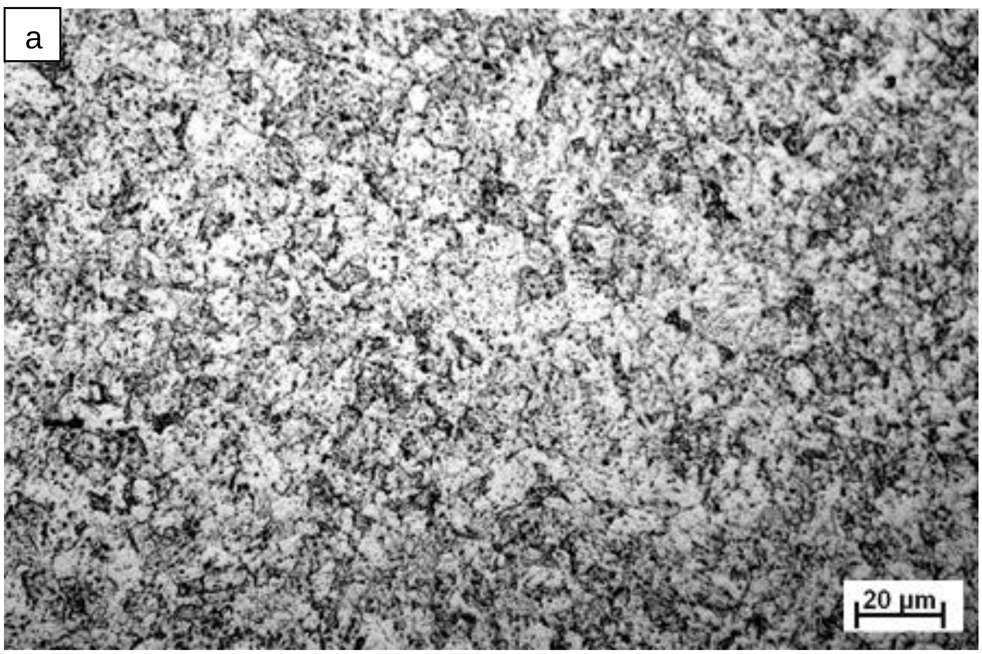

Fig. 5.5(a): Optical Micrograph of the HAZ in the laser welded 9Cr-1Mo(V, Nb) FMS in postweld heat treated condition showing fine grained character.

SEM micrograph of the HAZ of the laser welded 9Cr-1Mo(V, Nb) FMS plate, in post weld heat treated condition is presented in Figs. 5.5b and 5.5c. Figure 5.5b shows subgrain structure and $M_{23}C_6$ type carbides (~ 100 – 200 nm size range). Etch pits resulting from removal of carbide precipitates during etching are also seen in this micrograph. SEM micrograph at higher magnification shows fine MX type carbonitrides as well, in addition to $M_{23}C_6$ type carbides.

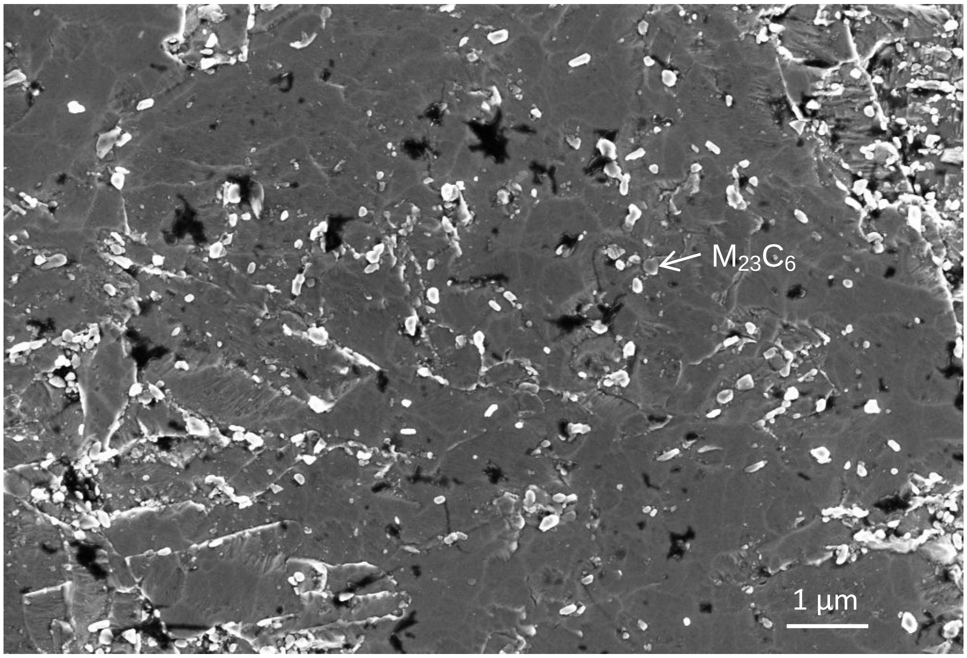

Fig. 5.5(b): SEM micrograph of the HAZ in laser welded 9Cr-1Mo(V, Nb) FMS in postweld heat treated condition.

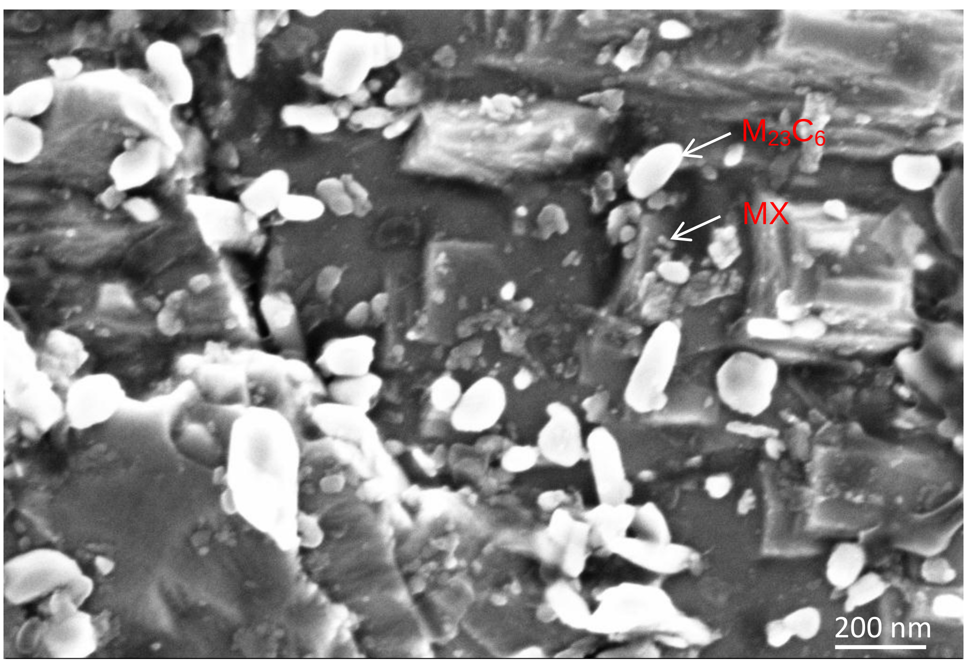

Fig. 5.5(c): SEM micrograph of the HAZ in laser welded 9Cr-1Mo(V, Nb) FMS in postweld heat treated condition.

Optical micrograph of the fusion zone in the laser welded 9Cr-1Mo(V, Nb) FMS plate in postweld heat treated condition is presented in Fig. 5.5(d). Columnar morphology of the prior austenite grains is also very clear in this micrograph. This implies that post weld tempering did not alter morphology of the prior austenite grains, which was expected also. Optical micrographs suggest that postweld tempering has resulted in uniform precipitation of precipitates.

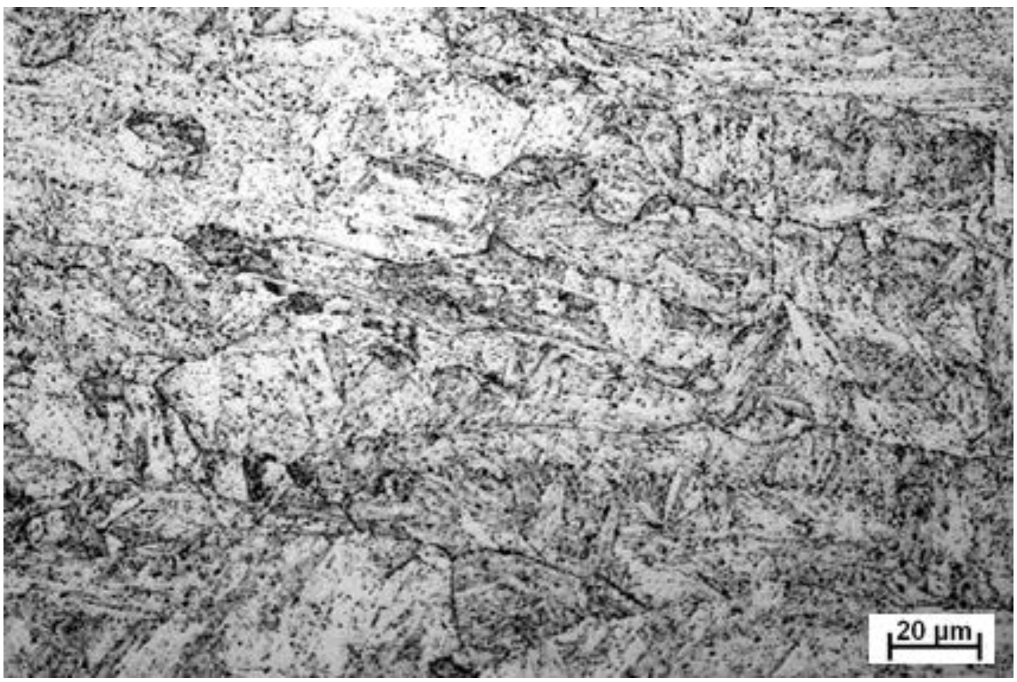

Fig. 5.5(d): Optical micrograph of the fusion zone in the laser welded 9Cr-1Mo(V, Nb) FMS plate in postweld heat treated condition.

SEM micrograph of the fusion zone in the laser welded 9Cr-1Mo(V, Nb) FMS plate in postweld heat treated condition is presented in Fig. 5.5(e). Prior austenite grain boundary, other interfaces, subgrain structure and uniform distribution of precipitates are seen in this micrograph. SEM at further higher magnification shows two different kinds of precipitates – $M_{23}C_6$ carbides and MX type carbonitrides, present in this micrograph.

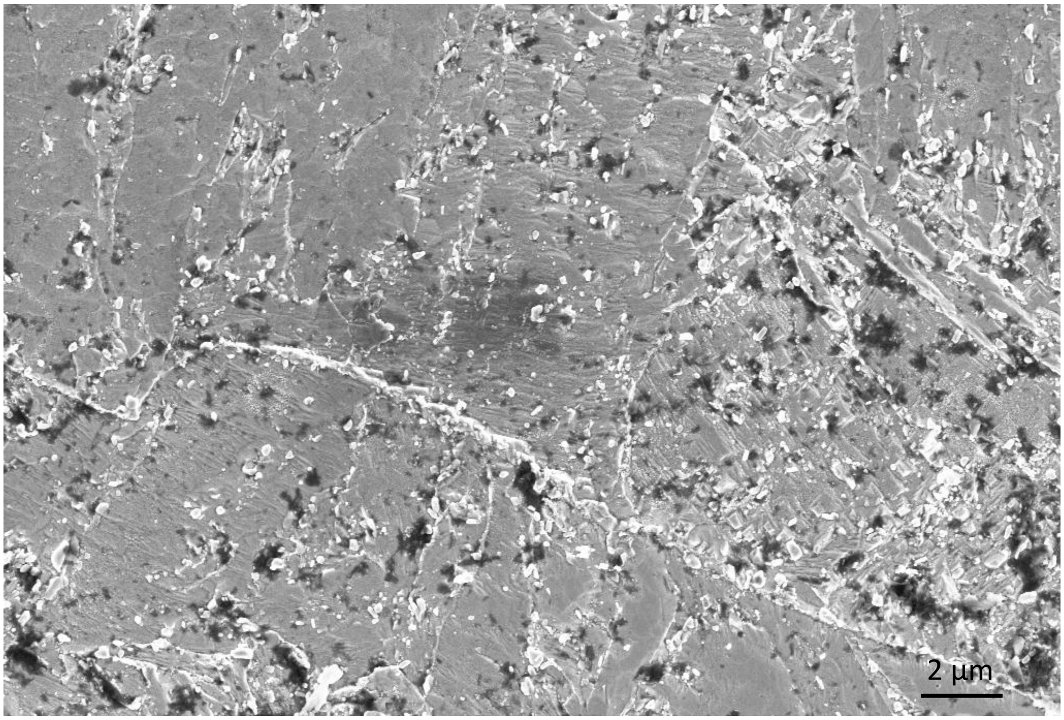

Fig. 5.5(e): SEM micrograph of the FZ in the laser welded 9Cr-1Mo(V, Nb) FMS in postweld heat treated condition showing subgrain structure and precipitates.

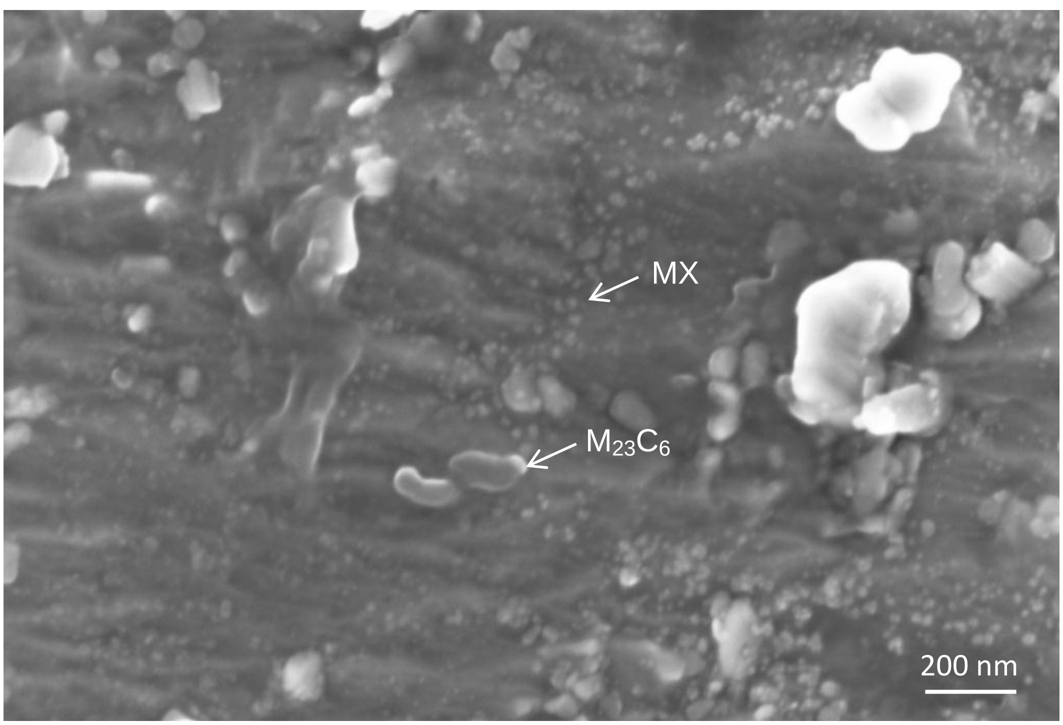

Fig. 5.5(f): SEM micrograph of the FZ in the laser welded 9Cr-1Mo(V, Nb) FMS in postweld heat treated condition showing uniform distribution of precipitates.

TEM micrograph from the fusion zone in postweld heat treated condition shows these precipitates at higher magnification (Fig. 5.5(g)). There are two types of precipitates. The bigger precipitates are ~ 100 - 200 nm in size range and these are along subgrain boundaries and also along prior austenite grain boundaries. EDS spectrum of these particles (Fig. 5.5(h)) shows these are Cr carbide in which some Cr has been replaced by other metals like Fe and Mo. These carbides are well characterized and reported in the literature as $M_{23}C_6$ carbides, where M is mainly Cr which has been partly replaced with Fe and Mo [4]. In addition there are very fine (~ 10 nm) precipitates dispersed within the subgrain. These precipitates have been reported in the literature as MX type carbides [4]. Thus it can be seen PWHT has restored the microstructure of the fusion zone to that of the parent metal except for the morphology of the prior austenite grains.

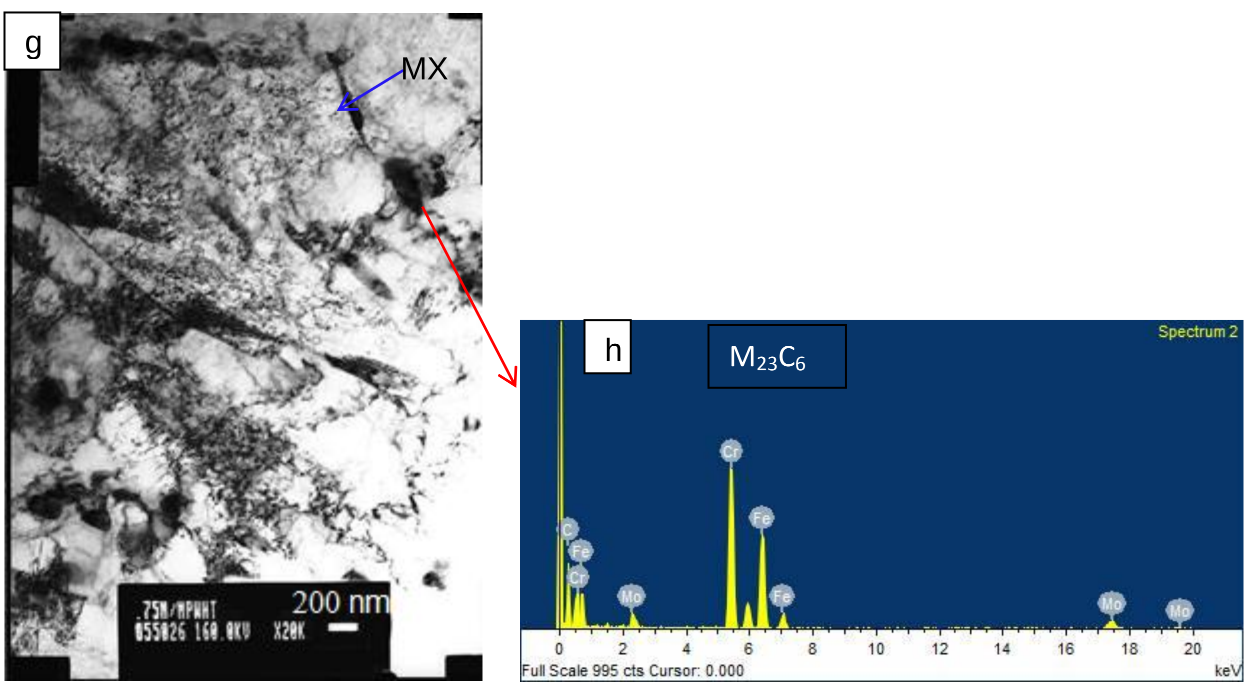

Fig. 5.5: TEM micrograph of the fusion zone in postweld heat treated condition (g) and EDS spectrum of $M_{23}C_6$ type carbide precipitate in the fusion zone (h).

5.5 Microhardness and Cross-Weld Tensile Strength

Cross weld microhardness profile for the weld joints, in as-welded condition, in 9Cr-1Mo(V, Nb) FMS made at 8 kW laser power and two different welding speeds – 1.5 m/min (W1) and 0.75 m/min (W2), is presented in Fig. 5.6. In both the weld joints, the fusion zone showed much higher hardness (~ 450 – 500 HVN) than the parent metal (~ 230 HV). The transition in the cross-weld hardness profile is very steep through the HAZ as this zone is very narrow. Higher hardness of the HAZ and the fusion zone is on account of the martensitic transformation in these regions under influence of the weld thermal cycle. As-transformed martensite is much harder than the tempered martensite (the parent metal in this case) and therefore, the fusion zone and the HAZ showed significantly higher hardness compared to the parent metal. Slower welding speed (0.75 m/min), while keeping the laser power unchanged at 8 kW led to wider fusion zone and HAZ. This resulted in relatively wider as-transformed martensitic region, which is reflected in the cross-weld hardness profile. Also, the martensite in the HAZ region is expected to have lesser carbon (in the solution) on the parent metal side than that near the fusion zone and hardness of the as-transformed martensite depends on its carbon content. Therefore, the HAZ region adjacent to the parent metal showed lower hardness than that adjacent to the fusion zone.

Cross weld hardness profile of the W1 (weld joint made at 8 kW and 1.5 m/min) in post weld tempered condition at different temperatures – 750^{o}C, 760^{o}C and 770^{o}C is also present in Fig. 5.6. Postweld tempering led to significant reduction in the hardness of the fusion zone and the HAZ region. As a result of PWHT, hardness of the fusion zone has reduced to ~ 280 HVN for 750^{o}C and ~260 – 270 HVN for 760^{o}C and 770^{o}C.

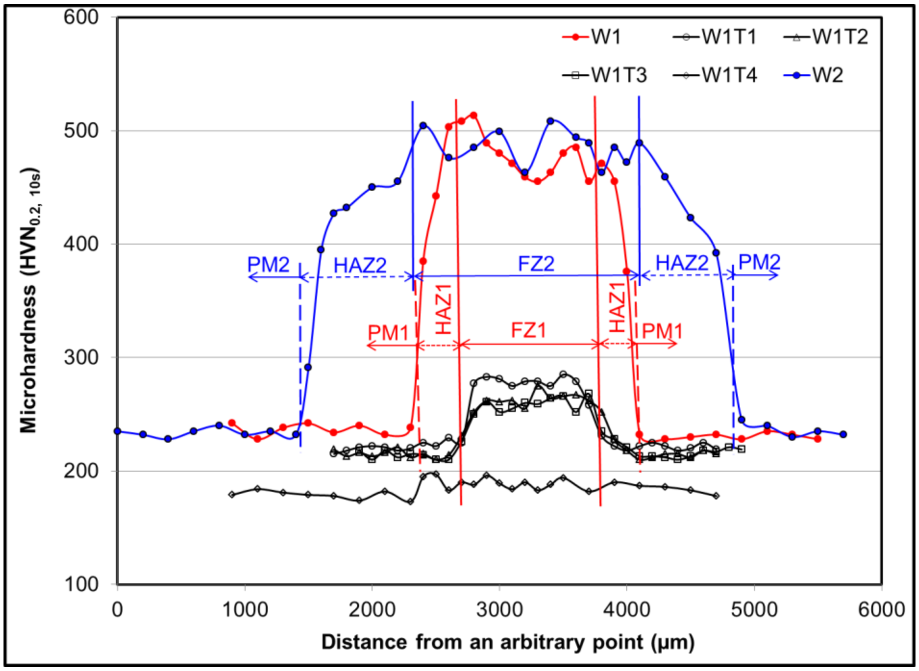

Fig. 5.6: Cross-weld microhardness profile for laser welded joints at 8 kW laser power and two different welding speeds – 1.5 m/min (W1) and 0.75 m/min (W2) in as welded condition. Cross-weld microhardness profile of W1 in post weld heat treated conditions different temperatures: W1T1 (750^{o}C, 30 min), W1T2 (760^{o}C, 30 min), W1T3 (770^{o}C, 30 min) and W1T4 (770^{o}C, 120 min) are also superimposed for comparison.

Interestingly, while the fusion zone has retained some of the hardening even after PWHT, it was not so with the HAZ. The HAZ region has lost all the hardening during PWHT, which it had acquired during welding. This suggests faster tempering kinetics in the HAZ region than that in the fusion zone region. This can be explained by presence of fine undissolved carbides in the HAZ region, which accelerated tempering; while absence of these precipitates explains incomplete tempering and therefore, retention of some hardening in the fusion zone. Also, no inter-critical softening was observed in the cross-weld hardness profile. This result is consistent with that reported in the literature for laser welded joint between 6 mm thick plate in this material, produced at comparable heat input. This can be explained by low heat input associated with laser welding. Due to low heat input, the material does not get over tempered in the inter-critical zone and therefore, no softening in the inter-critical zone. Post weld tempering at 770^{o}C for 2 hrs. led to significant softening across the weld joint with hardness reducing to 180 – 200 HVN.

Representative tensile curves of the parent metal and the weld joint in as-welded and also in post weld heat treated condition are presented in Fig. 5.7. The tensile curves (engineering stress – strain curves) show a typical ductile behaviour for the material in all the three conditions. Important tensile properties derived from these tensile test curves are presented in Table 5.1. The parent metal showed highest elongation (~ 20%), while the weld joint in as welded condition showed least elongation (18%). However, the loss in the elongation due to welding is only marginal (~ 2%). Besides, this loss in elongation was nearly completely recovered by post weld tempering of the weld joint at a cost of marginal decrease in the yield strength and ultimate tensile strength.

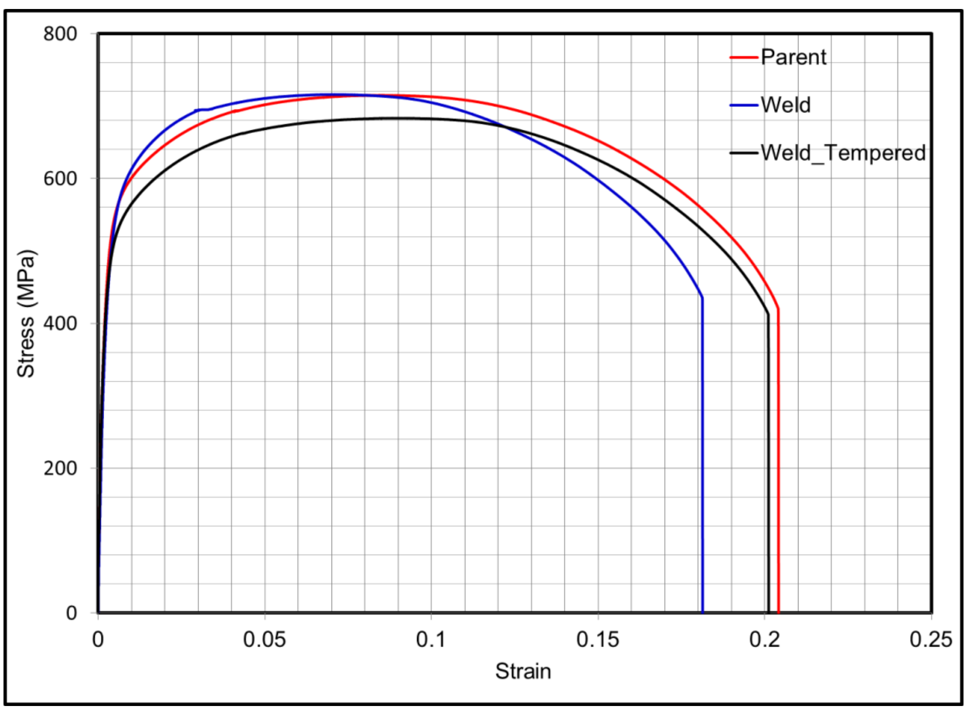

Fig. 5.7: Representative tensile curves (engineering stress – strain curves) of the parent metal and the laser welded joints in as-welded and also in postweld heat treated condition (770^{o}C, 30 min).

Table 5.1: Tensile properties of the parent metal and the laser welded joint.

	Parent Metal	As-Welded	Postweld Heat Treated
Yield Strength (MPa)	550$\pm$10	550$\pm$10	500$\pm$10
Ultimate Tensile Strength (MPa)	710$\pm$10	710$\pm$10	680$\pm$10
Total Elongation (%)	20$\pm$1	18$\pm$1	20$\pm$1

Fractured tensile test specimen of the parent metal and also the weld joint in as-welded as well as in the postweld heat treated condition are presented in Fig. 5.8. The fractured specimen showed significant necking prior to fracture, which is characteristic of a ductile material. The fusion zone is marked with an arrow for the cross-weld tensile test specimen. The cross-weld tensile specimen always fractured in the parent metal, far away from the fusion zone as well as the HAZ, for the as-welded and also for the post-weld heat treated specimen. This implies that the weld joints are stronger that the parent metal. This also confirms that weld joints were sound and defect-free. Because, the weld-joints always fractured in the parent metal, therefore, the strength properties like yield strength and ultimate tensile strength measured from these tensile curves and reported in Table 5.1 essentially belongs to the parent metal and not the HAZ or the fusion zone. In the as-welded condition the fusion zone and the HAZ resembles closely to the material in normalized condition. Therefore, as a first approximation, strength and elongation of the fusion zone and the HAZ can be taken as strength and elongation of the material in normalized condition. These values were measured and reported in Chapter 4 as part of characterization of as-received material. These values show significantly higher strength and lower elongation values for the material in as-transformed martensitic condition. This explains why the cross-weld tensile specimen always fractured in the parent metal and showed marginally lower elongation than that shown by the parent metal.

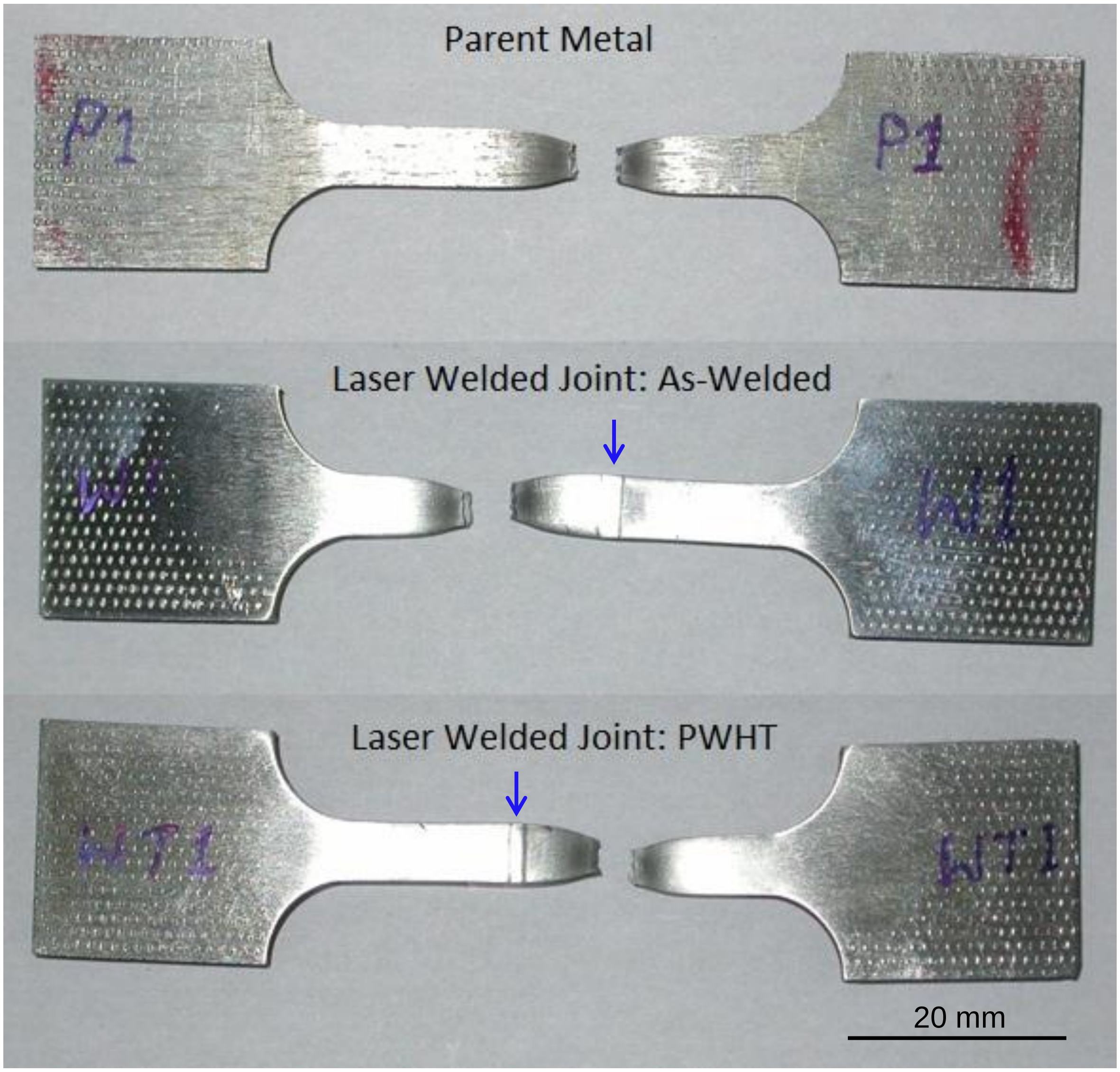

Fig. 5.8: Fractured tensile specimen of 9Cr-1Mo(V, Nb) FMS – parent metal and the laser welded joints in as-welded as well as in the postweld heat treated condition, showing significant necking before fracture and fracture was always in the parent metal proving strength and soundness of the weld joints.

5.6 Conclusions

Laser weld joints were made between 9 mm thick plates and bead on plate studies were made on 30 mm thick plates of 9Cr-1Mo(V, Nb) FMS using high power (10 kW) continuous wave CO_2 laser. Based on these studies following conclusions can be drawn.

(i) The joining efficiency increased from 15 mm^2/kJ to 55 mm^2/kJ with welding speed increasing from 0.5 m/min to 5.0 m/min. This implies better utilization of laser energy for fusing the parting surface at higher welding speeds.

(ii) The rate of increase in joining efficiency with welding speed, which is very steep in 0.5 – 2.0 m/min range, becomes moderate beyond this welding speed.

(iii) The depth of penetration decreased with increasing welding speed. Therefore, welding speed of 2.0 m/min acted like a trade-off between joining efficiency and depth of penetration or joint thickness.

(iv) Microstructure of the fusion zone showed as-transformed lath martensitic structure within columnar prior austenite grains. In addition to lath martensite, significant fraction of twinned martensite was also observed. Presence of twinned martensite can be explained by suppression of Ms temperature in the fusion zone due to work hardening of austenite.

(v) Microstructure of the HAZ showed as-transformed lath martensite within equiaxed prior austenite grains. These prior austenite grains formed because of phase transformation the parent metal (ferrite) into austenite grains and subsequent growth of the austenite grains. Because extent of phase-transformation and grain growth depends on time and superheat above Ac_1 temperature, therefore, progressively smaller prior austenite grains were observed from the fusion line towards the parent metal.

(vi) No coarsening of prior austenite grains were observed in the HAZ. This contrasts from the HAZ of arc welded joint in this material, in which grain coarsening is invariably present. This can be explained by low heat input associated with laser welding process, resulting in shorter residence time above grain coarsening temperature.

(vii) Undissolved carbide precipitates were also observed in the HAZ. This can also be explained by rapid heating and cooling rates associated with laser welding, resulting in insufficient time for carbide dissolution.

(viii) Some bainitic transformation products were also observed in the HAZ. This can be explained by formation of relatively leaner (in solute) austenite due to partial carbide dissolution. This austenite with lower alloying content transformed into bainite on account of lower hardenability.

(ix) Cross-weld microhardness profile showed significant hardening of the fusion zone (~ 450 – 500 HVN) than that of the parent metal (~ 230 HVN). Therefore, transition in the hardness profile through the narrow HAZ was very steep. High hardness of the fusion zone and the HAZ was on account of martensitic transformation.

(x) Postweld tempering resulted in significant softening (from ~ 500 HVN to ~ 260 – 280 HVN) of the fusion zone and the HAZ. Hardness of the HAZ became equal to that of the parent metal while hardness of the fusion zone was in 260 -280 HVN. No inter-critical softening was observed.

(xi) Postweld tempering of the weld joint restored all the microstructural features like subgrain structure, $M_{23}C_6$ type carbides and MX type carbonitrides in the fusion zone and HAZ except morphology of the prior austenite grains.

(xii) The cross-weld tensile test specimen, in as-welded and also in the postweld heat treated condition, always fractured in the parent metal in ductile manner. Tensile test showed that the weld joints were sound and stronger than the parent metal. Elongation of the cross-weld tensile test specimen (~ 18%) was marginally lower than that of the parent metal (~20%). However, this loss in elongation was nearly completely recovered by postweld tempering at 770^{o}C for 30 minutes.

References

[1] R. I. Jaffee, “Metallurgical problems and opportunities in coal-fired steam power plants, Metall. Trans. 10(2) (1979) 139-164.

[2] F. Masuyama, “History of power plants and progress in heat resistant steels”, ISIJ Intl. 41(6) (2001) 612–625.

[3] I. Holzer, “Modelling and simulation of strengthening in complex martensitic 9-12%Cr steel and binary Fe-Cu alloy”, PhD. Thesis (2010), Graz University of Technology, Graz

[4] A. Aghajani, “Evolution of microstructure during long-term creep of a tempered martensite ferritic steel”, PhD Thesis (2009), Ruhr University, Bochum, Germany

[5] K. H. Mayer and F. Masuyama, “The development of creep-resistant steels” in Creep-Resistant Steels, F. Abe, T U Kern and R. Viswanathan Eds.; Woodhead Publishing Limited, Cambridge, UK, (2008) 15-77 .

[6] D. V. Thornton and K. H. Mayer, “European high temperature materials development” in Advanced Heat Resistant Steels for Power Generation, R. Viswanathan and J.W. Nutting, Eds.; IOM Communications Ltd., London, (1999) 349-365.

[7] F. Masuyama, “New developments in steels for power generation boilers”, in Advanced Heat Resistant Steels for Power Generation, R. Viswanathan and J.W. Nutting, Eds.; IOM Communications Ltd., London, (1999) 33-48.

[8] G. J. Butterworth and O. N. Jarvis, “Comparison of Transmutation and Activation effects in five ferritic alloys and AISI 316 stainless steel in a fusion reactor spectrum”, J. Nucl. Mater. 122 - 123 (1984) 982 – 988.

[9] M. Tamura, H. Hayakawa, M. Tanimura, A. Hishinuma and T. Kondo, “Development of potential low activation ferritic and austenitic steels, J. Nucl. Mater. 141-143 (1986) 1067-1073.

[10] D. G. Doran, A. F. Rowcliffe and F. M. Mann, “Prospects for reduced activation alloys”, J. Nucl. Mater. 141- 143 (1086) 1074 – 1080.

[11] R. L. Klueh, D. S. Giles and T. A. Lechtenberg, “Development of ferritic steels for reduced activation: The US program”, J. Nucl. Mater. 141-143 (1986) 1081-1087.

[12] D. Dulieu, K. W. Topholme and G. J. Butterworth, “Development of low-activation martensitic stainless steels, J. Nucl. Mater. 141-143 (1986) 1097-1101.

[13] T. Noda, F. Abe, H. Araki and M. Okada, “Development of low activation ferritic steels”, J. Nucl. Mater. 141-143 (1986) 1102-1106.

[14] C.-Y. Hsu and T. A. Lechtenberg, “Microstructure and mechanical properties of unirradiated low activation ferritic steel”, J. Nucl. Mater. 141-143 (1986) 1107-1112.

[15] K. Laha, K. S. Chandravathi, P. Parameshwaran, K. B. S. Rao and S. L. Mannan, “Characterization of Microstructures across the Heat-Affected Zone of the Modified 9Cr-1Mo Weld Joint to Understand Its Role in Promoting Type IV Cracking", Metall. Mater. Trans. 38A, (2007) 58 - 68.

[16] S. Pillot, Z. Zhao, S. Corre, C. Chauvy, L. Coudreuse and P. Toussaint, “Thick Plates in Grade 91 for Fourth Generation Nuclear Reactors”, Proc. of ASME 2010 Pressure Vessels and Piping Division Conference (PVP 2010), July 18-22, 2010 Washington, USA.

[17] R. Mythili, P. V. Thomas, S. Saroja, M. Vijaylakshmi and V. S. Raghunathan, "Microstructural modification due to reheating in multipass manual metal arc welds of 9Cr-1Mo steel", J. Nucl. Mater. 312 (2003) 199-206.

[18] R. K. Shiue, K. C. Lan and C. Chen, "Toughness and austenite stability of modified 9Cr-1Mo welds after tempering", Mater. Sci. Eng. A 287 (2000) 10 - 16.

[19] P. K. Ghosh and U. Singh, "Influence of pre- and post- weld heating on weldability of modified 9Cr-1Mo (V-Nb) steel pipe under shielded metal arc and tungsten inert gas welding process”, Sci. Technol. Weld. Join. 9 (3) (2004) 229 - 236.

[20] S. Paddea, J. A. Francis, A. M. Paradowska, P. J. Bouchard and I. A. Shibli, "Residual stress distribution in a P91 steel-pipe girth weld before and after post weld heat treatment", Mater. Sci. Eng. A 534 (2012) 663 - 672.

[21] S. K. Albert, M. Tabuchi, H. Hongo, T. Watanabe, K. Kubo and M. Matsui, “Effect of Welding Process and Groove Angle on Type IV Cracking Behaviour of Weld Joints of a Ferritic Steel”, Sci. Technol. Weld. Join. 10 (2) (2005) 149-157.

[22] B. Shanmugarajan, G. Padmanabham, H. Kumar, S. K. Albert and A. K. Bhaduri, “Autogenous laser welding investigations on modified 9Cr-1Mo (P91) steel”, Sci. Technol. Weld. Join. 16(6) (2011) 528 - 534.

[23] W. H. Lee, R. K. Shiue and C. Chen, “Mechanical properties of modified 9Cr-1Mo steel welds with notches”, Mater. Sci. Eng. A356 (2003) 153 - 161.

[24] Z. Xu, “Laser welding and post weld heat treatment of modified 9Cr-1VNb steel”, Report No. ANL/NE-12/12, Argonne National Laboratory, Chicago, Illinois (2008).

[25] A. Cardella, E. Rigal, L. Bedel, Ph. Bucci, J. Fiek, L. Forest, L.V. Boccaccini, E. Diegele, L. Giancarli, S. Hermsmeyer, G. Janeschitz, R. Lässer, A. Li Puma, J. D.

Lulewicz, A. Möslang, Y. Poitevin, E. Rabaglino, “The manufacturing technologies of the European breeding blankets”, J. Nucl. Mater. 329 - 333 (2004) 133 - 140.

[26] H. Tanigawa, T. Hirose, K. Shiba, R. Kasada, E. Wakai, H. Serizawa, Y. Kawahito, S. Jitsukawa, A. Kimura, Y. Kohno, A. Kohyama, S. Katayama, H. Mori, K. Nishimoto, R.L. Klueh, M.A. Sokolov , R.E. Stoller , S.J. Zinkle, “Technical issues of reduced activation ferritic/martensitic steels for fabrication of ITER test blanket modules”, Fus. Eng. Des. 83 (2008) 1471–1476.

[27] H. Serizawa, S. Nakamura, M. Tanaka, Y. Kawahito, H. Tanigawa, S. Katayama, “Effect of mechanical restraint on weldability of reduced activation ferritic/martensitic steel thick plates”, J. Nucl. Mater. 417 (2011) 55 - 58.

[28] H. Serizawa, D. Mori, Y. Shirai, H. Ogiwara, H. Mori, “Weldability of dissimilar joint between F82H and SUS316L under fiber laser welding”, Fus. Eng. Des. 88 (2013) 2466 - 2470.

[29] P. Aubert, F. Tavassoli, M. Reith, E. Diegele and Y. Poitevin, “Review of candidate welding processes of RAFM steels for ITER test blanket modules and DEMO”, J. Nucl. Mater. 417 (2011) 43 - 50.

[30] B. J. Ganesh, S. Raju, A. K. Rai, E. Mohandas, M. Vijayalakshmi, K. B. S. Rao, and B. Raj, “Differential scanning calorimetry study of diffusional and martensitic phase transformations in some 9 wt% Cr low carbon ferritic steels”, Mater. Sci. and Technol. 27(2) (2011) 500-512.

[31] T. S. Wang, M. Zhang, Y. H. Wang, J. Yang and F. C. Zhang, “Martensitic transformation behaviour of deformed supercooled austenite”, Scripta Mater. 68(2) (2013) 162 - 165.

[32] H. K. D. H. Bhadeshia and R. W. K. Honeycombe, "Steels: Microstructure and Properties", 3rd Edition, Elsevier, New York, USA (2006).

[33] A. Aghajani, "Evolution of microstructure during long-term creep of a tempered martensite ferritic steel", PhD Thesis, Ruhr University, Bochum, Germany (2009).

Chapter 6: Residual Stress Mapping by Neutron Diffraction in Laser Welded 9Cr-1Mo(V, Nb) FMS Plates

6.1 Introduction

Ferritic-martensitic steels, and in particular grade 91 steel (9Cr-1Mo(V, Nb)), find extensive application in supercritical power generation plants, nuclear power systems and in the petrochemical industry owing to their excellent combination of elevated temperature strength, thermal fatigue resistance and immunity from stress corrosion cracking in aqueous and chloride environments [1 – 4]. Moreover they are candidate materials for structural components in many advanced reactor systems like the Very High Temperature Reactor and the Sodium Fast Reactor owing to their low susceptibility to irradiation embrittlement [2, 5]. Different welding techniques such as Manual Metal Arc welding, Submerged Arc Welding and Gas Tungsten Arc Welding are used to fabricate components and assemblies from ferritic-martensitic steels of this type [5 - 21]. Laser welding is a versatile joining process with high power density and low thermal input. It can weld different alloys from sub-millimeter up to 20 mm section thicknesses in different joint configurations without the need for any filler material. Major advantages of the laser welding process include the narrow width of the fused zone and the HAZ, and minimal distortion of the components being welded owing to the low heat input. There is also some evidence to suggest that welds made with high-energy beam processes such as laser or electron beam welding may be more resistant to type IV cracking than welds made with conventional arc welding processes [9].

Very high values of residual stress approaching the yield strength of the parent material and weld filler are generally introduced in the vicinity of welded joints [17]. Temperature excursions associated with the thermal cycle of a welding pass induce localized thermal dilation that is accommodated by the elasto-plastic responses of the structure. In turn this is accommodated by cyclic stress-strain behaviour of the materials, the self-restraint of the structure and any applied restraint. In addition, for material systems like P91, the strains associated with the solid-state austenite to martensite transformation of the material in the fusion zone and the HAZ can have a profound impact on the residual stress profile [17, 22, 23]. Paddea et al. [17] have reported residual stresses in P91 steel-pipe girth weld before and after post weld heat treatment. They have reported significant compressive stresses in the fusion zone of the last pass, which has been attributed to martensitic transformation during cool down of the weld joint. They have also demonstrated that martensitic transformation in constrained volume leads to compressive stresses by conducting “Satoh Test”. In this test a P91 steel specimen was allowed to cool from austenitic phase-field under constrained condition and this resulted in introduction of compressive stresses as the specimen cooled below its Ms temperature. Dean et al. [22] have reported computation of residual stresses in multi pass arc welded joints in P91 steel pipe considering the effect of solid state phase transformation. Kim et al. [23] have reported computed as well as experimentally measured (by neutron diffraction) residual stresses in multi pass arc welded joints in P91 steel. Both these studies have shown that martensitic transformation of austenite has significant compressive effect on the residual stressed in the fusion zone.

Quantitative characterization of the residual stress distribution around the welded joint is important, to understand the factors governing its evolution, to assess how such stresses may affect the life and integrity of components in-service, and also to design mitigation treatments including optimization of the post-weld heat treatment (PWHT).

Residual stress around a weld joint can be measured by surface based techniques such as centre-hole drilling, magnetic methods and X-ray diffraction or volumetric techniques such as deep hole drilling, the contour method, neutron diffraction or synchrotron diffraction [24]. Surface based techniques provide limited information about the residual stress field, whilst volumetric strain relief methods are invasive or destructive. Neutron diffraction was selected for the present work for several reasons. First, it is a non-destructive method that can provide quantitative information about three or more components of the stress tensor in the structures made from steel up to a few tens of millimeters thick [25]. Secondly, a fine gauge volume can be selected to resolve the rapid variations in residual stress on short length-scales expected in narrow width laser welds. Thirdly, the neutron diffraction technique is well established having been applied widely to characterize residual stresses in welded joints [17, 22 - 45].

Measurements of the residual stress fields around P91 welded joints, made by different methods, including neutron diffraction, have been reported by several workers [17, 22, 23]. However, these weld joints were made by arc welding processes in multiple passes. There is no published work on residual stress measurements in laser welded joints in 9Cr-1Mo(V, Nb) FMS. The present work provides a detailed analysis of residual stress measurements by neutron diffraction. Keyhole laser welds are also of interest as they are expected to show a residual stress profile that is significantly different from that introduced by conventional multi-pass welding processes. This is on account of the high through-thickness to width aspect ratio of the fusion zone and the HAZ and also because they are single pass welds. This chapter presents results of the residual stress measurements using neutron diffraction in 9 mm thick plates of 9Cr-1Mo(V, Nb) FMS welded at 8 kW laser power and two different welding speeds – 1.5 m/min (Plate A) and 0.75 m/min (Plate B) using a continuous wave CO_2 laser, details of the welding process are described in Chapter 3. The results reported here will provide a set of high quality measured residual stress data that can be used to validate modelling and simulation endeavours. Such models can be harnessed to explore the effects of different processing conditions on the residual stress profile, as well as for providing the starting conditions for PWHT stress relaxation studies.

6.2 Neutron Diffraction Peak FWHM Analysis

The representative neutron diffraction peak for {112} planes obtained from identical gauge volume (0.8x0.8x2.0 mm^3) in the parent metal and the fusion zone are presented in Figs. 6.1a and 6.1b respectively. It can be seen that the diffraction peak from the parent metal is much sharper (full width at half maxima (FWHM) ~ 0.5^o) than that from the fusion zone (FWHM ~ 1.4^o). Wider diffraction peak implies higher microstresses within the gauge volume. This shows that microstresses are much higher in the fusion zone than that in the parent metal. The fusion zone structure is as-transformed martensite, which has high dislocation density that explains higher microstresses and therefore, wider neutron diffraction peaks.

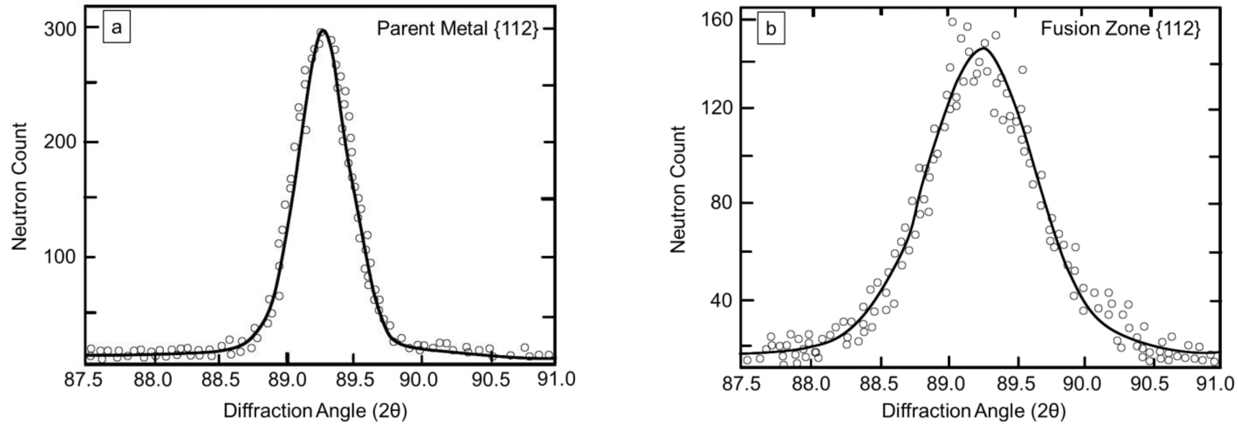

Fig. 6.1: Representative neutron diffraction patterns from (a) The parent metal and (b) The fusion zone in laser welded 9 mm thick plates of 9Cr-1Mo(V, Nb) FMS obtained at ILL, France.

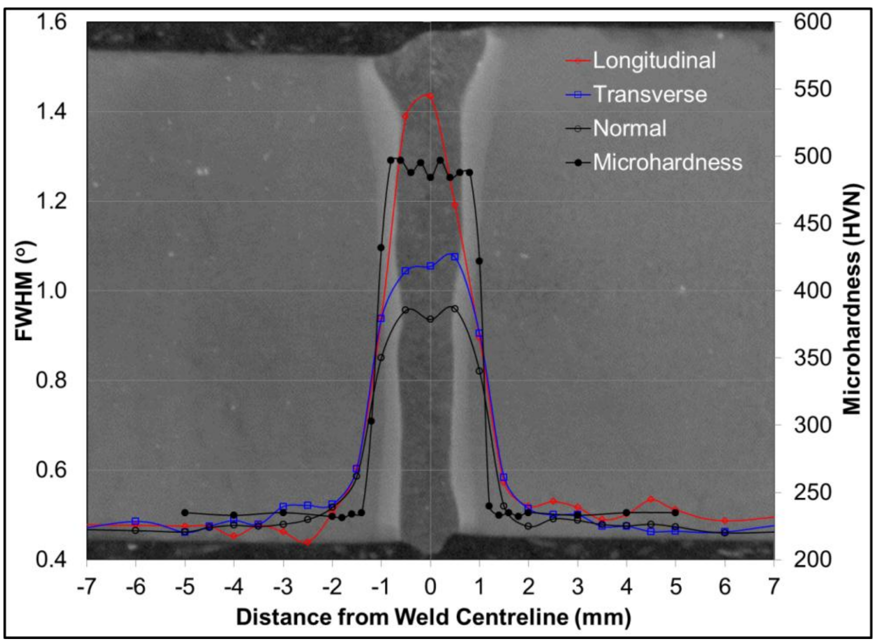

Fig. 6.2: Cross-weld variation of FWHM of the neutron diffraction peaks in 9 mm thick laser welded (laser power: 8 kW and welding speed: 1.5 m/min) plate of 9Cr-1Mo(V, Nb) FMS, showing significant broadening of the diffraction peak in the fusion zone, due to martensitic transformation.

The variation in the FWHM of the {112} neutron diffraction peak across the weld joint for measurements along the longitudinal, transverse and normal directions at mid-length of Plate A (8 kW, 1.5 m/min), is shown in Fig. 6.2. A cross-weld microhardness profile from a similar location is superimposed in this figure. A similar pattern was observed in all the cross-weld measurement scans. The variation in FWHM is symmetric about the weld centre line and exhibits an interesting trend. FWHM of the diffraction peak remains ~ 0.5^{o} for the parent metal and increases rapidly through the narrow HAZ to become as high as 1.4^{o} for the measurements along the longitudinal direction and ~ 1^{o} for the measurements along the transverse and the normal directions in the welded region. The regions of higher FWHM showed one-to-one correlation with the regions which have undergone a martensitic transformation due to the welding thermal cycle. The correlation is so strong that the FWHM may be used as an important signature for the fusion zone (FZ) and the HAZ, which have undergone a martensitic transformation during welding. The higher values of FWHM of the diffraction peaks are due to a variation of strains on the microscopic length scale within the gauge volume. Such variations can arise from plastic deformation during cooling and / or the solid state phase transformation. However, further experimentation and simulation work is needed to confirm and elucidate the contributing mechanisms.

The FWHM of the diffraction peak in the weld region for the longitudinal component is significantly greater (~ 40%) than that for the transverse and normal components. This could be due to texture in the prior austenite grains leading to the selection of different variants along the three measured directions – longitudinal, transverse and normal. This can however, be confirmed only with a detailed Electron Back Scattered Diffraction (EBBSD) analysis. It may also be due to the smaller gauge volume used for the longitudinal measurements compared with that used for measurements of the other two components, noting that larger gauge volumes tend to give sharper diffraction peaks than smaller volumes assuming other parameters such as count time, material chemistry and crystal structure etc. remain the same. Whilst a sharp diffraction peak is preferred, as it implies a lower error, a small gauge volume had to be employed, due to fine length scales of the fusion zone and the HAZ, for measuring the longitudinal component in order to capture the steep gradients in stress across the weldment.

6.3 Cross-weld Residual Strain and Residual Stress Profiles in Plate A at 1.5 mm below the Top Surface

The measured residual strain profile, across the low heat input weld (320 J/mm) in Plate A, at mid-length cross-section and 1.5 mm depth below the top surface is shown in Fig. 6.3. As expected, the three components (longitudinal, transverse and normal) of residual strain show a high degree of symmetry across the weld centre-line. Interestingly the longitudinal component shows a bimodal distribution with a trough coincident with the weld centre-line and the two peaks lying 2 mm on either side of the centre in the parent metal near the HAZ – PM interface. The peak value of the longitudinal component of residual strain is ~ 1900 micro-strain. The normal component shows a similar profile, but with a lower peak magnitude (~ 500 micro-strain) at 1.5 mm on either side of the weld centre-line. The transverse component of residual strain, however, shows the opposite trend. It has a peak (~ 650 micro strain) coinciding with the weld centre-line and two troughs (~ -900 micro-strain) at 1.5 mm on either side of the weld centre-line.

Similar characteristics are seen in the cross-weld residual stress profile (Fig. 6.4). The longitudinal component of residual stress shows a low tensile trough (~ 50 MPa) in the weld centre which rises rapidly to a peak value of ~500 MPa at 2 mm on either side of it.

The regions with peak residual stresses are in the parent metal just outside the metallurgical HAZ, as is evident from a comparison of the cross-weld microhardness profile and the residual stresses at the same location. Similar results have been reported by Mark et al. [42] for residual stress profiles across a single pass weld in SA508 steel, which also undergoes a bainitic/martensitic transformation while cooling from the austenite phase field. The normal component shows a similar trend, with a trough in the weld centre (~ 100 MPa) and rising rapidly to peak values (~ 200 MPa) at 1.5 mm on either side of the centre-line. The transverse component shows the opposite trend with the peak (~ 200 MPa) coinciding with the weld centre and two troughs (~$\pm$10 MPa) at 1.5 mm on either side of it.

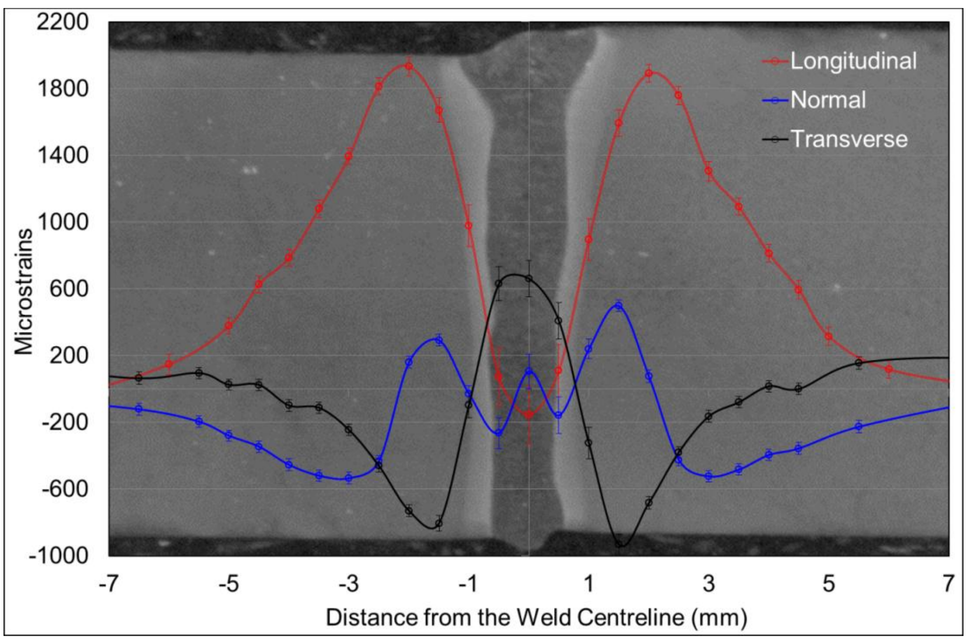

Fig. 6.3: Cross weld residual strain profile in Plate A (laser power: 8 kW and welding speed: 1.5 m/min) at 1.5 mm below top surface.

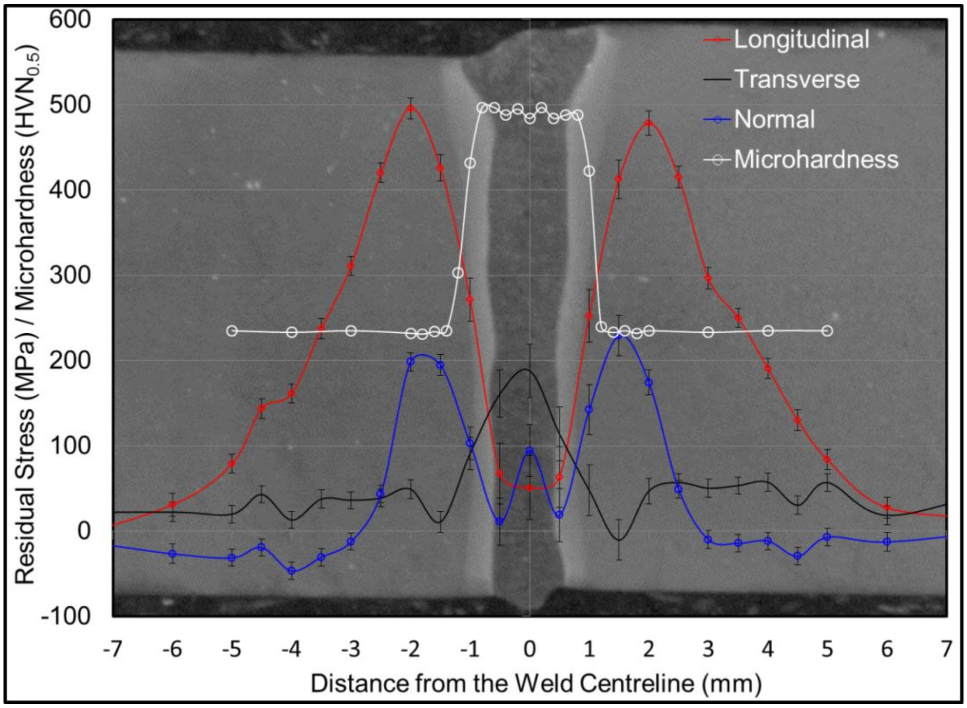

Fig. 6.4: Cross-weld residual stress profile, showing variation of the three principal components – longitudinal, transverse and normal of the residual stress at mid-length cross-section and 1.5 mm below top surface in the laser welded plate at 8 kW laser power and 1.5 m/min welding speed.

The measured strain and stress profiles are nearly symmetric. This gives confidence in the quality of results, and the experimental procedure, which involved remounting of the sample after measurements of the longitudinal component of strain, to obtain corresponding data in the other two orthogonal directions. Thus, further measurements were focused on only one side of the welded joint.

The trough in the longitudinal residual strain and stress profiles at the weld centreline can be attributed to strains associated with the martensitic transformation during cool down of the weld joint. The regions which were heated to a temperature above the Ac_1 during heating cycle undergo austenitic transformation and subsequently undergo martensitic transformation during cool down of the joint. These regions form the fusion zone and the HAZ. Martensitic transformation is associated with a significant volumetric expansion in the fusion zone and the HAZ and therefore, induces significant compressive stresses as the transformation is taking place in a constrained volume. The tensile peaks are in the regions heated to a temperature just below the Ac_1 temperature, as these regions experience only contraction during cooling of the weld joint. This M-shaped profile contrasts with a non-transforming material, where a single tensile peak would be expected at and near the weld centre-line, dropping to low compressive stresses in the far field [37]. In 9Cr-1Mo(V, Nb) FMS, martensitic transformation strains have been observed to have a similar influence on the residual stresses in a multi-pass pipe girth weld, where compressive stresses were measured in the region of the last weld pass [17]. Paddea et al. [17] have demonstrated the compressive effect of martensitic transformation in a P91 steel specimen by carrying out Satoh test. In this test, a cylindrical specimen of P91 steel was allowed to expand freely while being heated at $50^{o}C/s$ to a temperature above Ac_3 to austenitize it. Subsequently, the specimen was clamped and then allowed to cool while monitoring the stresses generated during the cool down. It was reported that compressive stresses developed in the specimen as it cooled down below its Ms temperature [17]. Another interesting feature observed in this figure (Fig 6.4) is the cross-weld profile of the normal component of residual stress, which has the same shape as the profile of the longitudinal component, although with lower peaks. The common shape of the profiles suggests that the factors controlling the evolution of the two are similar in nature and related to the strains associated with the martensitic transformation occurring under constraint. Because of the large aspect ratio (depth to width) of the laser weld fusion zone, the thickness of the weld bead (i.e. the plate) provides significant restraint against the dilatational component of the strain. In the longitudinal direction, the effective restraint length is much longer giving a larger compressive effect. The adjacent tensile peaks in the longitudinal and normal components of the stress profile may be viewed as reactions to the compressive trough in the respective profiles at the weld centre-line. In contrast, the spatial profile of the transverse stress component is similar to that shown by the normal component of residual stress in multi-pass arc welds [17]. This is because, the aspect ratio of the weld beads (depth to width) is much smaller in multi-pass arc welds. The impact of solid state austenite to martensite phase transformation discussed here finds support from other measurements made on Plate A and also on Plate B (8 kW, 0.75 m/min) as discussed below.

6.4 Cross-weld Residual Stress Profiles in Plate A at 4.5 mm below the Top Surface

The cross-weld residual stress profiles for plate A at 4.5 mm below the top surface (mid-thickness plane) of the plate are shown in Fig. 6.5. The profiles for all three components of stress – longitudinal, transverse and normal - are similar to those at a depth of 1.5 mm (Fig. 6.4) but show differences in magnitudes at the troughs and peaks in the respective profiles. For example, the trough in the normal component at the mid-thickness plane is deeper (~-150 MPa) and the peaks are higher (~350 MPa) than those in the equivalent locations in the profile at a depth of 1.5 mm (Figure 6.4). These differences can be attributed to relatively greater restraint experienced by the martensitic transformation strains at the mid-thickness plane than that near the surface. The profiles of the transverse component of the residual stress from the two locations (1.5 mm and 4.5 mm) are nearly similar.

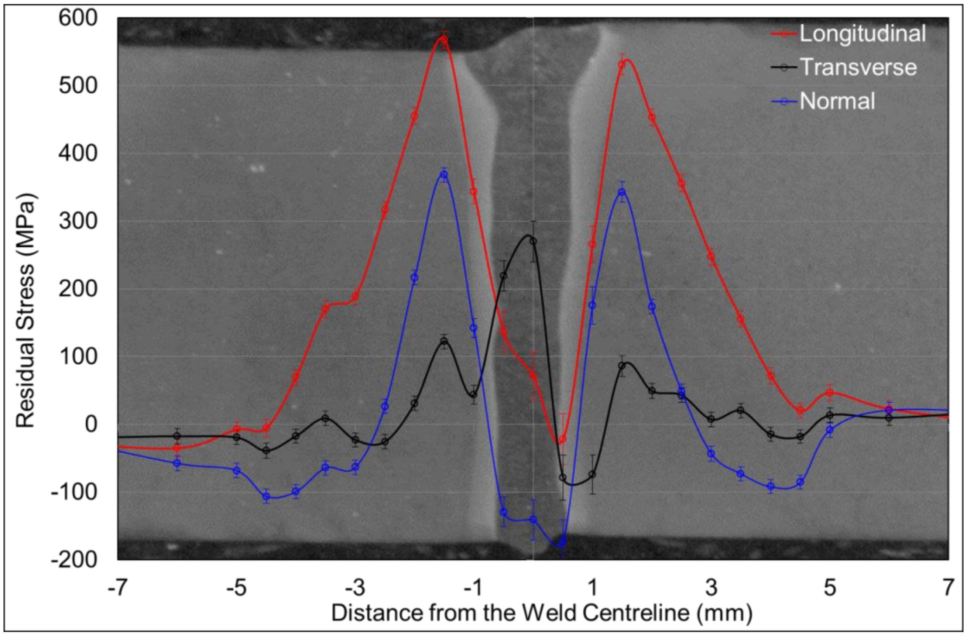

Fig. 6.5: Cross weld residual stress profile in Plate A (laser power: 8 kW and welding speed: 1.5 m/min, plate thickness: 9 mm) at 4.5 mm below surface.

An important difference between the cross-weld residual stress profiles at mid-thickness and at 1.5 mm depth is that, the distance between the tensile peaks is narrower at mid-thickness (± 1.5 mm from the weld centre-line compared with ± 2 mm). This is because the width of the fusion zone plus HAZ is smaller at the mid-thickness plane than at 1.5 mm below the top surface, again noting that it is the martensitic transformation in the fusion zone and HAZ that governs the width of the trough in the residual stress profile.

6.5 Through-thickness Residual Stress Profiles

Through-thickness profiles of the longitudinal, transverse and normal components of residual stress at the weld centre-line in Plate A are shown in Fig. 6.6. It can be observed that the uncertainties associated with these weld metal measurements are much higher (~±30 MPa) than those in the parent metal region (~±10 MPa (Figs. 6.4 and 6.5)). This is on account of higher microstresses in the fusion zone and the HAZ as compared to the same in the parent metal. The transverse component of residual stress is most tensile, the normal component most compressive and the longitudinal component lies in between. The final state of residual stress in the weld metal is the result of competition between thermal contraction and martensitic transformation induced expansion of the material. In the normal direction, thermal contraction will be smaller than that in the longitudinal direction; therefore, the normal component of residual stress is more compressive than the longitudinal component. Residual stress below the mid thickness plane is more compressive than that above the mid plane. This is because, the heat source is applied from the top side, leading to less heat input below the mid-thickness plane and therefore, the dilative martensitic transformation commences first in this region, producing a more compressive region than that above.

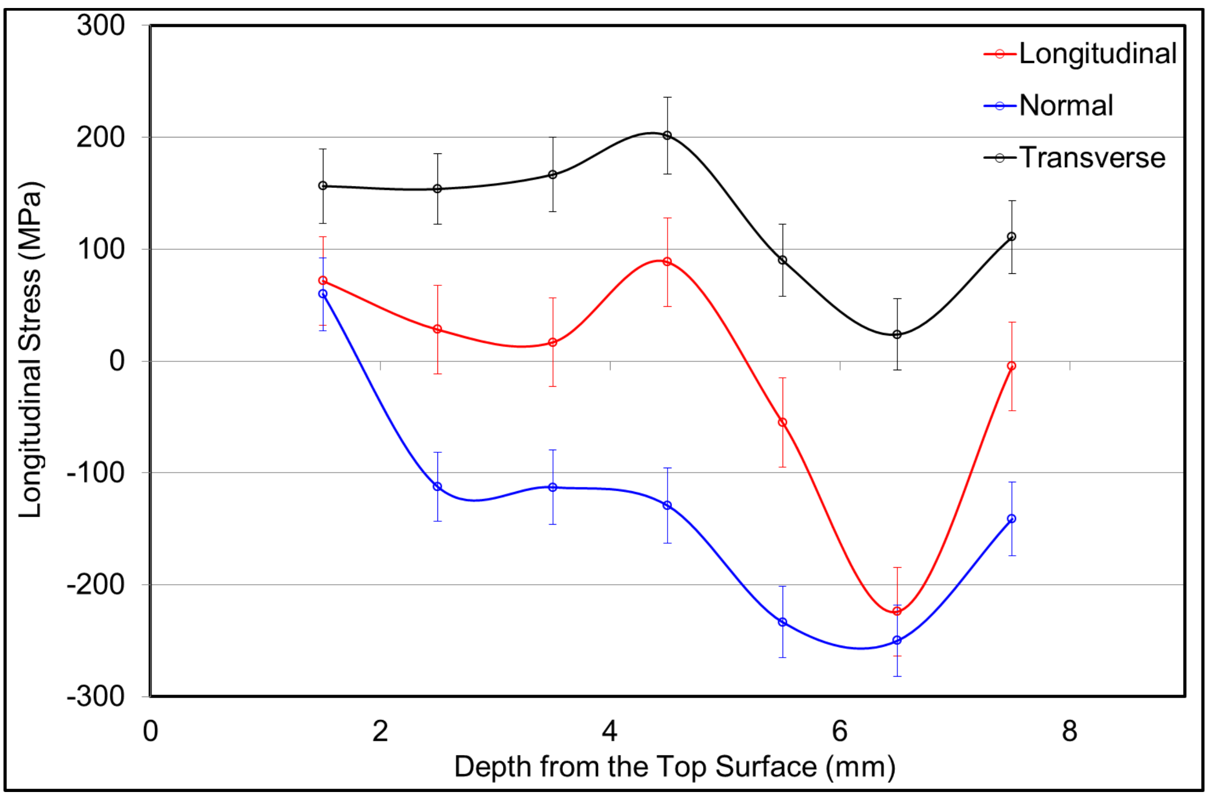

Fig. 6.6: Through-thickness profiles of the longitudinal, transverse and normal components of residual stress in Plate A (laser power: 8 kW and welding speed: 1.5 m/min, plate thickness: 9 mm) along the weld centreline.

The variation in residual stresses through the thickness at the weld centre-line is most likely to be associated with differential cooling between the bottom and top of the weld. Greater heat is input by the laser welding process at the top surface; it can be noted from Figs.5.3 and 5.4 that the fusion zone and the HAZ are slightly narrower towards the bottom side of the plate. This means that the bottom of the welded plate will cool faster than the top and lead to a resultant residual stress distribution controlled by the combined influences of differential thermal contraction, different degrees of martensitic transformation and self-constraint. Thermo-metallurgical and thermo-mechanical modelling and simulation of welding is probably the best way to understand the complex mechanical behaviour involved. This sort of residual stress profile with a compressive zone below the mid-thickness plane and tensile zone above contrasts from that observed in the case of multi-pass arc-welded joints in this material [17] where significantly higher tensile residual stress develops below the mid-thickness plane relative to above it. This is on account of the thermal cycles associated with the succeeding passes introducing martensitic dilation and more compressive stresses in the fusion zone and HAZ and corresponding tensile reactions in the weld metal deposited by the preceding passes.

Residual stress maps for longitudinal and normal components on the mid-length cross-section of the low heat input welded plate were generated on one side of the weld centre-line; using the through thickness measurements along the weld centre-line and along the measurement lines at distances of 2 mm, 4 mm and 10 mm from it. For distances of 15 mm and 30 mm the weld centre-line, values from cross-weld measurements at 1.5 and 4.5 mm below the top surface were used to generate these plots. The plots were generated using MATLAB. Figs. 6.7 and 6.8 respectively show maps of the longitudinal and normal components respectively of the residual stress on one side of the welded joint. These maps show that the cross-weld profiles for the longitudinal and the normal components represented in Figs. 6.4 and 6.5 exist through the entire thickness of the plate. It can also be seen from these maps that the cross-weld profiles of the longitudinal and normal components of stress are very similar in nature, i.e. both components show a low tensile or compressive trough in the weld centre and two tensile peaks on the either side of the joint in the parent metal adjacent to the PM-HAZ boundary.

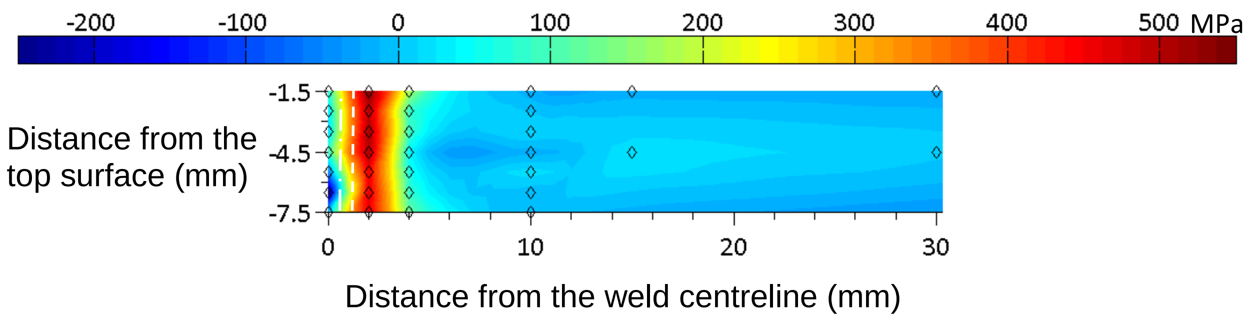

Fig. 6.7: Map of the longitudinal component of residual stress in Plate A (laser power: 8 kW and welding speed: 1.5 m/min, plate thickness: 9 mm) at the mid-length cross-section in the one side of the weld centreline. White lines are marked for the fusion line and the HAZ boundary.

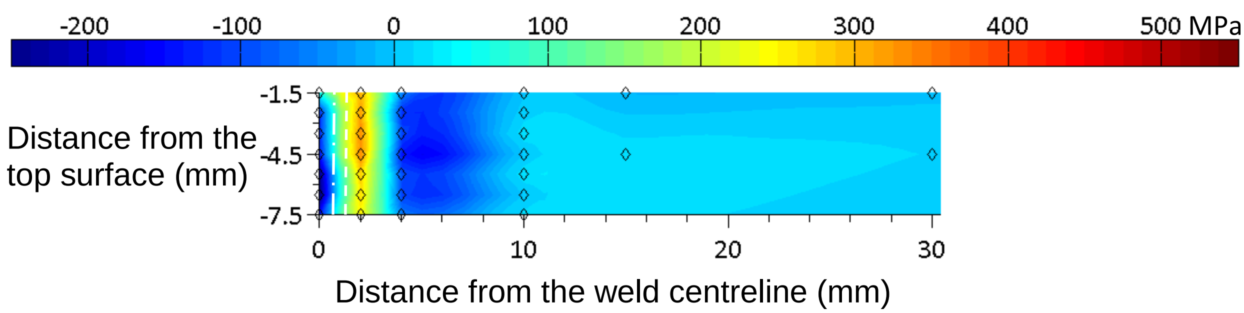

Fig. 6.8: Map of the normal component of residual stress in Plate A (laser power: 8 kW and welding speed: 1.5 m/min, plate thickness: 9 mm) at the mid-length cross-section in the one side of the weld centreline. White lines are marked for the fusion line and the HAZ boundary.

6.6 Effect of Welding Speed on the Residual Stress Profile

Figs. 6.9, 6.10 and 6.11 compare cross-weld profiles of the longitudinal, normal and transverse components of residual stress respectively in Plates A and B, which were welded at the same laser power (8 kW) but with different welding speeds (Plate A: 1.5 m/min and Plate B: 0.75 m/min respectively) giving low and high heat input conditions. A cross-weld microhardness profile is also superimposed. The shapes and peak magnitudes of the profiles from the two plates are almost identical. However, it can be seen that the lower welding speed has led to both broadening and deepening of the trough in the cross-weld profiles of residual stress in both the longitudinal and normal directions. The increased width of the trough correlates with the wider fusion zone in Plate B which experienced nearly double the heat input of Plate A; compare the fusion zones in Figs. 5.3 and 5.4. These results further illustrate how the martensitic transformation in the fusion zone and HAZ of a laser welded joint in 9Cr-1Mo(V, Nb) FMS leads to reduced levels of residual stress in the weld region.

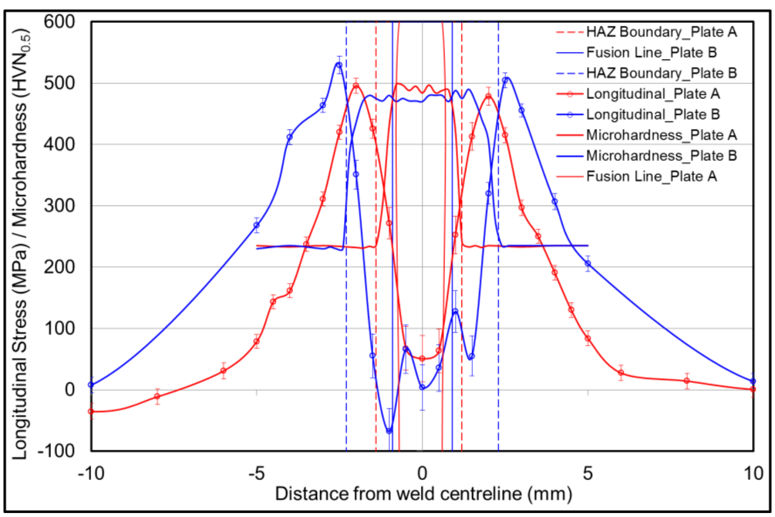

Fig. 6.9: Cross weld profile of the microhardness and the longitudinal component of residual stress in Plate A (laser power: 8 kW and welding speed: 1.5 m/min, plate thickness: 9 mm) and Plate B (laser power: 8 kW and welding speed: 0.75 m/min, plate thickness: 9 mm) at 1.5 mm below top surface.

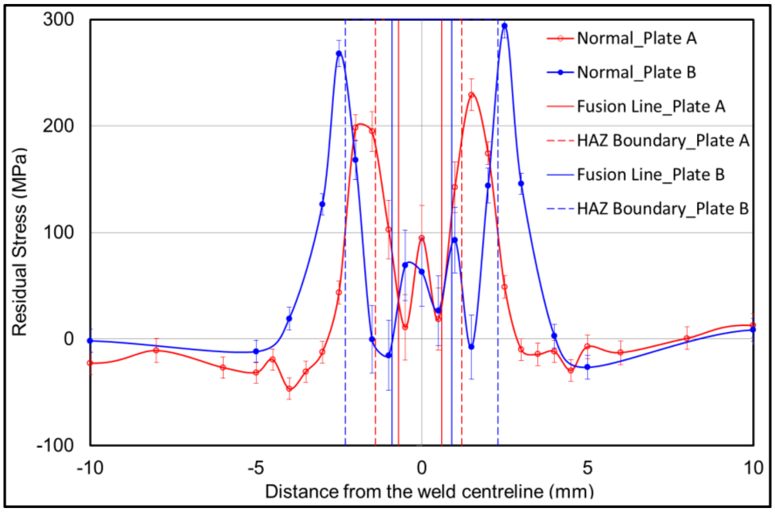

Fig. 6.10: Cross weld profile of the normal component of residual stress in Plate A (laser power: 8 kW and welding speed: 1.5 m/min, plate thickness: 9 mm) and Plate B (laser power: 8 kW and welding speed: 0.75 m/min, plate thickness: 9 mm) at 1.5 mm below top surface.

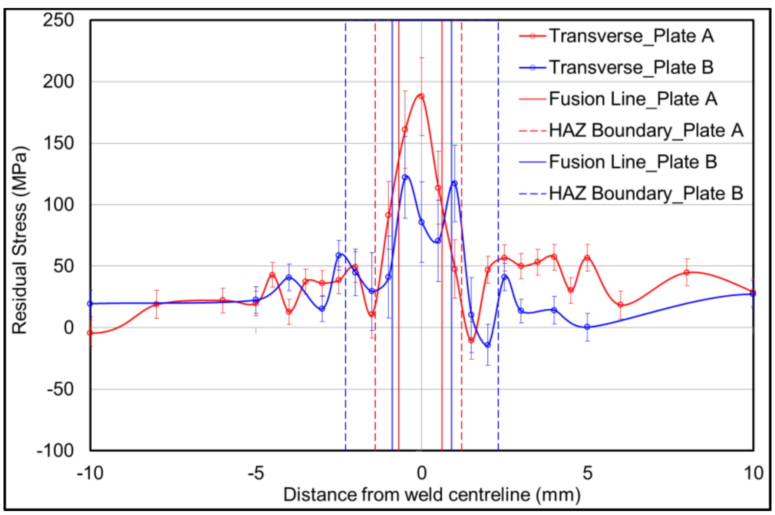

Fig. 6.11: Cross weld profile of the transverse component of residual stress in Plate A (laser power: 8 kW and welding speed: 1.5 m/min, plate thickness: 9 mm) and Plate B (laser power: 8 kW and welding speed: 1.5 m/min, plate thickness: 9 mm) at 1.5 mm below top surface.

6.7 Conclusions

Neutron diffraction was used to measure residual stresses in 9 mm thick laser welded plates of 9Cr-1Mo(V, Nb) FMS. Laser welding had been performed using a high power CO_2 laser at 8 kW laser power and two different welding speeds – 1.5 m/min (Plate A) and 0.75 m/min (Plate B) resulting in two different heat inputs – 320 J/mm (Plate A) and 640 J/mm (Plate B). Following conclusions were drawn from these measurements.

(i) Neutron diffraction peaks from the fusion zone were much wider (FWHM ~ 1.4^o) than those from the parent metal (FWHM ~0.5^o). The HAZ region showed intermediate values for the FWHM of the diffraction peaks. FWHM of the neutron diffraction peaks showed one to one correlation with the regions which have experienced martensitic transformation due to laser welding. Wider diffraction peaks in the fusion zone and the HAZ were due to higher micro-stresses in these regions resulting from the martensitic transformation of austenite.

(ii) FWHM of the diffraction peaks also exhibited gauge volume effect and / or direction dependence with larger gauge volume (0.8 x 0.8 x 20 mm^3) along the transverse and the normal direction resulting in relatively narrower peaks (FWHM ~ 0.9^o - 1.2^o) than the smaller gauge volume (0.8 x 0.8 x 2.0 mm^3) along the longitudinal directional (FWHM ~ 1.4^o). The effect of the measurement direction and size of the gauge volume could not be separated in these measurements.

(iii) Cross-weld profiles of the longitudinal and normal components of residual stress in the laser welds showed a low tensile or compressive trough (-250 to

100 MPa) in the welded fusion zone and high tensile peaks (500 to 600 MPa for the longitudinal component and 200 to 350 for the normal component) in the parent metal near the HAZ-PM interface on the either side of the weld joint.

(iv) There was little variation in residual stresses through the plate thickness except in the fusion zone, where the longitudinal and the normal stresses are more compressive in the bottom half of the weld zone. This contrasts with conventional multi-pass welds in P91 steel where the residual stress is more tensile in the bottom side than in the top side.

(v) The widths of the fusion zone (1.2 mm for the low heat input and 1.8 mm for high heat input) and the low tensile / compressive troughs in the residual stress profiles (2 mm wide for low heat input and 3 mm for high heat input) were wider and marginally deeper for the high heat input weld joint compared with the low heat input weld joint, but the peak magnitudes of the residual stresses were similar.

(vi) There is clear evidence of a very strong influence of the strains associated with the martensitic transformation on the magnitude and spatial profile of all three components of residual stress in both welded plates.

(vii) The significant components of the residual stress in the laser welds are in the longitudinal and normal directions. This contrasts with conventional multi-pass welds where longitudinal component is the most significant, while the transverse and the normal components are comparable and relatively not significant. This is mainly owing to high aspect ratio (depth to width ratio) of the fusion zone and the HAZ in the laser welds.

References

[1] F. Masuyama, “History of power plants and progress in heat resistant steels”, ISIJ Intl. 41(6) (2001) 612–625.

[2] R. L. Klueh, “Elevated temperature ferritic and martensitic steels and their application to future nuclear reactors”, Int. Mater. Rev. 50(5) (2005) 287 - 310.

[3] K. Laha, K. S. Chandravathi, P. Parameshwaran, K. B. S. Rao and S. L. Mannan, “Characterization of Microstructures across the Heat-Affected Zone of the Modified 9Cr-1Mo Weld Joint to Understand Its Role in Promoting Type IV Cracking", Metall. Mater. Trans. 38A (2007) 58 - 68.

[4] K. H. Mayer and F. Masuyama, “The development of creep-resistant steels” in Creep-Resistant Steels, F. Abe, T U Kern and R. Viswanathan Eds.; Woodhead Publishing Limited, Cambridge, UK, (2008) 15-77 .

[5] S. Pillot, Z. Zhao, S. Corre, C. Chauvy, L. Coudreuse, P. Toussaint, Proc. of ASME 2010 Press. Vessel. Pip. Div. Conf. (PVP 2010) 1-14.

[6] R. K. Shiue, K. C. Lan and C. Chen, "Toughness and austenite stability of modified 9Cr-1Mo welds after tempering", Mater. Sci. Eng. A 287 (2000) 10 - 16.

[7] R. Mythili, P. V. Thomas, S. Saroja, M. Vijaylakshmi and V. S. Raghunathan, "Microstructural modification due to reheating in multipass manual metal arc welds of 9Cr-1Mo steel", J. Nucl. Mater. 312 (2003) 199-206.

[8] P. K. Ghosh and U. Singh, "Influence of pre- and post- weld heating on weldability of modified 9Cr-1Mo (V-Nb) steel pipe under shielded metal arc and tungsten inert gas welding process”, Sci. Technol. Weld. Join. 9 (3) (2004) 229 - 236.

[9] S. K. Albert, M. Tabuchi, H. Hongo, T. Watanabe, K. Kubo and M. Matsui, "Effect of Welding Process and Groove Angle on Type IV Cracking Behaviour of Weld Joints of a Ferritic Steel", Sci. Technol. Weld. Join. 10 (2) (2005) 149-157.

[10] T. Watanabe, M. Tabuchi, M. Yamazaki, H. Hongo and T. Tanabe, "Creep damage evaluation of 9Cr-1Mo-V-Nb steel welded joints showing Type IV fracture", Int. J. Press. Vessel Pip. 83 (2006) 63–71.

[11] S. Sulaiman, "Structure of properties of the heat affected zone of P91 creep resistant steel", PhD Thesis, University of Wollongong, Wollongong, Australia (2007) [http://ro.uow.edu.au/theses/777].

[12] P. Mayr, "Weldability of Modern 9%Cr Steels for Application in USC Power Plants", PhD Thesis, Graz University of Technology (2007).

[13] B. Arivazhagan, S. Sundaresan and M. Kamaraj, "Effect of TIG arc surface melting process on weld metal toughness of modified 9Cr-1Mo (P91) steel", Mater. Lett. 62 (2008) 2817 – 2820.

[14] J.-P. Barthoux, "Narrow gap welding of heavy wall thickness materials in nuclear and fossil fuel industries", Focus on Nuclear Power Generation, (2008) 36 – 42. Retrieve from http://www.nuclear-exchange.com/pdf/TP_Polysounde.pdf on August 16, 2014.

[15] B. Arivazhagan, S. Sundaresan and M. Kamaraj, "A study on influence of shielding gas composition on toughness of flux-cored arc weld of modified 9Cr–1Mo (P91) steel", J. Mater. Proc. Technol. 209 (2009) 5245 – 5253.

[16] H. Hongo, M. Tabuchi and T. Watanabe, "Type IV Creep Damage Behavior in Gr.91 Steel Welded Joints", Metall. Mater. Trans. 43A (2012) 1163 – 1173.

[17] S. Paddea, J. A. Francis, A. M. Paradowska, P. J. Bouchard and I. A. Shibli, "Residual stress distribution in a P91 steel-pipe girth weld before and after post weld heat treatment", Mater. Sci. Eng. A534 (2012) 663 - 672.

[18] J. Parker, “Factors affecting type IV creep damage in Grade 91 steel welds”, Mater. Sci. Eng. A578 (2013) 430 – 437.

[19] S. A. David, J. A. Siefert and Z. Feng, “Welding and weldability of candidate ferritic alloys for future advanced ultrasupercritical fossil power plants”, Sci. Technol. Weld. Join. 18(8) (2013) 631 – 651.

[20] P. Kumar, “An Overview of Welding and Fabrication Aspects during Manufacture of Nuclear Reactor Components for 500 MWe Prototype Fast Breeder Reactor”, Proc. of International Welding Congress (IWC 2014), New Delhi, India (2014).

[21] B. Arivazhagan and M. Vasudevan, “A comparative study on the effect of GTAW processes on the microstructure and mechanical properties of P91 steel weld joints”, J. of Manuf. Process. 16 (2014) 305 – 311.

[22] D. Dean and M. Hidekazu, “Prediction of welding residual stress in multi-pass butt-welded modified 9Cr–1Mo steel pipe considering phase transformation effects”, Comput. Mater. Sci. 37 (2006) 209 - 219.

[23] S. H. Kim, J. B. Kim and W. J. Lee, “Numerical prediction and neutron diffraction measurement of residual stresses for a modified 9Cr-1Mo steel weld”, J. Mater. Process. Technol. 209 (2009) 3905 - 3913.

[24] N.S. Rossini, M. Dassisti, K. Y. Benyounis and A.G. Olabi, “Methods of measuring residual stresses in components”, Mater. Des. 35 (2012) 572 - 588.

[25] P. J. Withers, "Mapping residual and internal stress in materials by neutron diffraction", C. R. Phys. 8 (2007) 806 - 820

[26] G. A. Webster and R. C. Wempory, "Non-destructive measurement of residual stress by neutron diffraction", J. Mater. Process. Technol. 117 (2001) 395 - 399.

[27] W. Wanchuck, E. M. Vyacheslav, M. Pavel, A. Gyu-Baek and B. -S. Seong, "Neutron diffraction measurements of residual stresses in a 50mm thick weld", Mater. Sci. Eng. A528 (2011) 4120 - 4124.

[28] M. J. Park, H. N. Yang, D. Y. Jang, J. S. Kim and T. E. Jin, "Residual stress measurement on welded specimen by neutron diffraction", J. Mater. Process. Technol. 155 - 156 (2004) 1171 - 1177.

[29] A. Paradowska, J. W. H. Price, R. Ibrahim and T. Finlayson, "A neutron diffraction study of residual stress due to welding", J. Mater. Process. Technol. 164 - 165 (2005) 1099 - 1105.

[30] J. W. H. Price, A. Paradowska, S. Joshi and T. Finlayson, "Residual stresses measurement by neutron diffraction and theoretical estimation in a single weld bead", Int. J. Press. Vessel. Pip. 83 (2006) 381 - 387.

[31] M. Hofmann and R. C. Wimpory, "NET TG1: Residual stress analysis on a single bead weld on a steel plate using neutron diffraction at the new engineering instrument 'STRESS-SPEC'", Int. J. Press. Vessel. Pip. 86 (2009) 122 - 125.

[32] C. Ohms, R. C. Wimpory, D. E. Katsareas and A. G. Youtsos, "NET TG1: Residual stress assessment by neutron diffraction and finite element modelling on a single bead weld on a steel plate", Int. J. Press. Vessel. Pip. 86 (2009) 63 - 72.

[33] S. Pratihar, M. Turski, L. Edwards and P. J. Bouchard, "Neutron diffraction residual stress measurements in a 316L stainless steel bead-on-plate weld specimen", Int. J. Press. Vessel. Pip. 86 (2009) 13 - 19.

[34] D. Thibault, P. Bocher, M. Thomas, M. Gharghouri and M. Côté, "Residual stress characterization in low transformation temperature 13%Cr–4%Ni stainless steel weld by neutron diffraction and the contour method", Mater. Sci. Eng. A527 (2010) 6205 - 6210.

[35] W. Wanchuck, E. M. Vyacheslav, C. R. Hubbard, J. H. Lee and S. P. Kwang, "Residual stress determination in a dissimilar weld overlay pipe by neutron diffraction", Mater. Sci. Eng. A528 (2011) 8021 - 8027.

[36] M. Rogante, P. Battistella and F. Rustichelli, "Residual stress measurement by neutron diffraction in AA6082 extruded samples submitted to different quenching rates", J. Alloy. Compd. 378 (2004) 335 - 338.

[37] W. Suder, S. Ganguly, S. Williams, A. M. Paradowska and P. Colegrove, “Comparison of joining efficiency and residual stresses in laser and laser hybrid welding”, Sci. Technol. Weld. Join. 16(3) (2011) 244 - 248.

[38] D. W. Brown, T. M. Holden, B. Clausen, M. B. Prime, T. A. Sisneros, H. Swenson and J. Vaja, "Critical comparison of two independent measurements of residual stress in an electron-beam welded uranium cylinder: Neutron diffraction and the contour method", Acta Mater. 59 (2011) 864 -873.

[39] S. Ganguly, L. Edwards and M. E. Fitzpatrick, “Problems in using a comb sample as a stress-free reference for the determination of welding residual stress by diffraction”, Mater. Sci. Eng. A528(3) (2010) 1226 - 1232.

[40] A. Kundu, P. J. Bouchard, S. Kumar, K. A. Venkata, J. A. Francis, A. Paradowska, G. K. Dey and C. E. Truman, “Residual stresses in P91 steel electron beam welds”, Sci. Technol. Weld. Join. 18(1) (2013) 170 – 175.

[41] A. Kundu, P. J. Bouchard, S. Kumar, G. K. Dey, “Characterisation of Residual Stress in Electron Beam Welded P91 Plates by Neutron Diffraction”, Int. J. Metall. Eng. 2(1) (2013) 79 - 84.

[42] A. F. Mark, J. A. Francis, H. Dai, M. Turski, P. R. Hurrell, S. K. Bate, J. R. Kornmeier and P. J. Withers, “On the evolution of local material properties and residual stress in a three-pass SA508 steel weld”, Acta Mater. 60 (2012) 3268–3278.

Chapter 7: Modelling and Simulation of Laser Welding of 9Cr-1Mo(V, Nb) FMS

7.1 Introduction

Ferritic/Martensitic steels with 8-12 wt. % Cr and microalloying additions of V and Nb are materials for high temperature applications in ultra-supercritical (USC) thermal power plants [1-3]. Fe-9Cr-1Mo(V, Nb), also known as P/T/F/Gr91 steel in its different product forms; is a prominent member of ferritic/martensitic steel family. This material and its reduced activation variants are candidate structural material for next generation of nuclear reactors including fusion reactors [2, 4]. This material is joined by different conventional welding processes like Shielded Metal Arc Welding (SMAW), Gas Tungsten Arc Welding (GTAW), Submerged Arc Welding (SAW) [4 - 21]. However, these welding processes are high heat input processes; require multiple passes with preheating and inter-pass heating of the parts to be joined and therefore, produce more distortion. Beam welding processes like laser and electron beam welding on the other hand are single pass processes, require no preheating and the distortion is negligible. Besides, the weld joints produced by the conventional processes lead to inter-critical softening in the parent metal-HAZ boundary region due to the combined effect of high heat input, preheating, multiple passes and inter-pass heating [8, 10]. This softening is reported to cause type IV cracking [8, 10]. Inter-critical softening has not been observed in case of laser and electron beam welded joints and therefore, this has raised an expectation to produce weld joints with superior type IV crack resistance using these welding processes [8]. Due to these benefits laser and electron beam welding of these steels have recently drawn attention of material scientists and engineers [22 - 24].

Transient thermo-metallurgical and thermo-mechanical computations during simulation of the welding process provide better insight of the process in terms of evolution of the thermal-field, phase-field, displacement-field and stress-field in and around the weld joints and is very useful tool for design and development of engineering components and fabrication methodology for the same. This is because, while the final or residual displacement and stress fields can be measured experimentally; evolution of the same while the joint is being made can be appreciated only through simulation of the process. This insight can be used to modify the welding process itself to produce the desired displacement-field and stress-field. Besides, experimental measurement may not be feasible on every component and therefore, the results of the computations can be used to get a better idea of the residual stress-field present around a weld joint in a component going for service. Significant amount of work has been done on simulation of weld joint in this material by different finite element (FE) based software like ANSYS, ABAQUS and SYSWELD [25 - 34] for thermo-metallurgical and thermo-mechanical computations. Yaghi et al. [25] have reported residual stress simulation using ABAQUS in multi-pass arc welded section of P91 pipes. They have used an axisymmetric model for this simulation and have computed through thickness residual stress profiles along the weld centre line and the HAZ region. However, solid state phase transformation (SSPT) of the austenite to martensite was not considered in their model. Deng el al [26] have reported computation of welding residual stresses using ABAQUS in multi-pass arc welded modified 9Cr-1Mo steel pipe in butt configuration, considering SSPT effects. They have used an axisymmetric model and also considered the effects of volumetric and/or yield strength change arising out of SSPT of austenite into martensite during welding. They have reported that the volume and yield strength changes associated with SSPT of austenite to martensite during welding have significant effects on residual stress and must be considered for computation of stresses arising out of welding of this material. Due to lack of mechanical properties of the low temperature austenite, they have used properties of the base metal itself and have suggested use of phase-dependent mechanical properties for further improvements in the computed results. Kim et al. [27] have reported numerical computation using ABAQUS and experimental measurements using neutron diffraction of residual stresses for a modified 9Cr-1Mo steel weld joints. They have used material property data from Yaghi et al. [25] and have not used phase-dependent material property data. The weld joints were produced in butt and fillet configurations using arc welding methods. They had not implemented SSPT of austenite into martensite; however, based on the experimental results they felt that this should be considered for arriving at more reliable results. Price et al. [28] have reported comparison of the residual stress in welds computed using SYSWELD and that measured experimentally using neutron diffraction. They have used metal inert gas deposited weld beads on low carbon steel. Their results show that longitudinal component of the residual stress is the most significant and the normal and transverse components are much smaller and comparable to each-other. Bate et al. [29] have reported thermo-metallurgical and thermo-mechanical computations using SYSWELD for bead on plate specimen produced by tungsten inert gas welding. They have presented transient temperature evolution and residual stress profiles on the weld bead cross-section. Aloraier et al. [30] have reported computation of residual stresses in flux cored arc welding process in bead on plate specimen for a boiler and pressure vessel steel (Fe-1.35Mn-0.155C) using SYSWELD. They have presented temperature distribution at different instant of time and residual stress field. Xu et al. [31] have reported transient thermo-metallurgical and thermo-mechanical computations using SYSWELD for bead on plate specimen, of an austenitic stainless steel (SS316L), produced by automated tungsten inert gas welding. They have presented residual stress profiles as well as temporal evolution of temperature and stress field. This work clearly shows the effect of heating, melting and post-solidification cooling on the evolution of stress field. Tsirkas et al. [32] have reported thermo-mechanical computation of laser welding in 4 mm thick plate of AH36 ship building steel using SYSWELD. However, the results are limited to the temperature contours and displacement contours. Moraitis et al. [33] have reported thermo-mechanical computation of laser welding in high strength steel and an aluminium alloy using ANSYS. They have reported transient temperature field and residual stress profiles across the weld joint and through thickness of the weld joint. However, details of the steel in terms of composition and properties and also if any SSPT has been considered is not reported in this paper. Shanmugam et al. [34] have reported transient thermal computation using SYSWELD for T-joint in austenitic stainless steel (SS304L) made by laser welding.

Based on review of the existing literature, it was observed that substantial literature exists on thermo-metallurgical and thermo-mechanical computation for weld joints in different materials including those in 9Cr-1Mo(V, Nb) steel produced by arc as well as beam welding processes. However, there is no published work on thermo-metallurgical and thermo-mechanical computation for laser welded joints in 9Cr-1Mo(V, Nb) steel.

None of the previous work on thermo-mechanical computation of weld joints in this material has used phase-dependent mechanical properties of this material. Also, literature on the temporal evolution of stress-field is rather limited [31] and none of the previous work has dwelled upon the stress-field in the parent austenite phase-field in the vicinity of the weld joint. This chapter presents results of thermo-metallurgical and thermo-mechanical computations using SYSWELD for laser welding of 9 mm thick plate of 9Cr-1Mo(V, Nb) steel for the first time. SSPT of the material has been considered and phase-dependent mechanical properties have been used in these computations. Computed residual stress profile has been compared with that measured by neutron diffraction in the same plate (presented in chapter 6). Temporal evolution of the stress-field has been discussed and correlated with different thermo-metallurgical processes associated with welding. The state of stress in austenitic phase-field prior to its transformation has also been discussed.

7.2 Temperature Field

Computed fusion zone (regions which exceeded T_m = 1520^{o}C) and HAZ (regions which exceeded Ac_1 = 820^{o}C) placed adjacent to the cross-section of the actual weld joint is presented in Fig. 7.1. Reasonably good agreement between the computed fusion zone and the HAZ and that obtained experimentally can be seen in this figure. The computed profile also shows a nail-shaped narrow fusion zone (half width ~0.6 mm) much like the actual laser welded joint. Fusion zone as well as HAZ is very narrow in both cases primarily due to low heat input associated with laser welding process. These results suggest that heat source used for this simulation was indeed a close approximation for the actual heat source used for laser welding.

Weld thermal cycle at different points, at varying distance from the weld centre line along mid-thickness line at mid-length cross-section is presented in Fig. 7.2. It can be seen that as the heat source approaches the mid-length region, temperature of the region shoots up rapidly and exceeds the melting point in no time and the material melts almost instantly in the fusion zone. As the heat source moves away, the melt solidifies very quickly (within 130 ms) due to rapid heat extraction by the steel plate itself, which acts as a very strong heat sink. Thus there is high cooling rate of the order of 10^4 $^{o}C/s$ for the melt. Such very steep heating and cooling curves for the fusion zone are invariably associated with all the fusion welding processes and the computed results confirm to that reported in the literature [29, 31, 33, 34]. The spatial gradient of temperature in the fusion zone is also very high due to narrow fusion zone. Therefore, fusion zone has columnar solidification structure. This material transforms from austenite to martensite at a cooling rate as low as $0.08^{o}C/s$ [35] and in this case the cooling rate for the austenite is of the order of 10^2 $^{o}C/s$. Therefore, microstructure of the fusion zone is fully martensitic within columnar prior austenite grains (Fig. 7.2). These results are in agreement with the computational and experimental studies reported for the weld joints in this material [24, 25, 27].

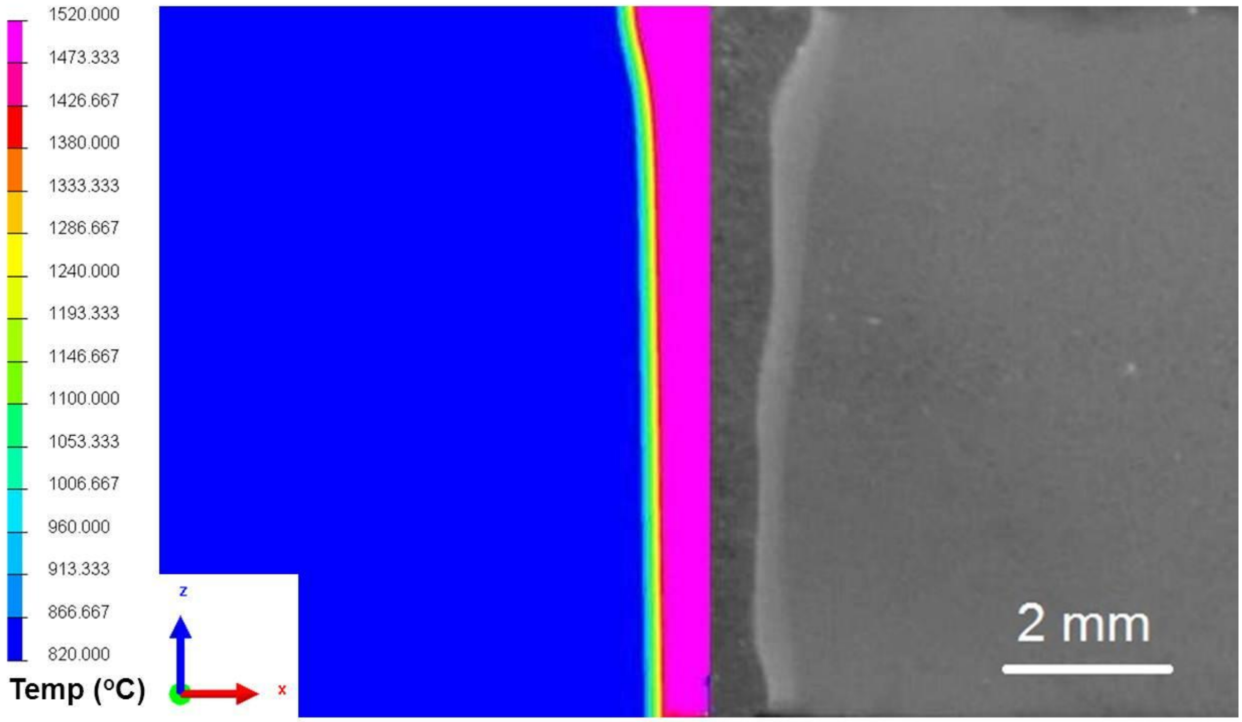

Fig. 7.1: Computed (left) and actual macrograph (right) showing cross-section of the laser welded joint produced in 9Cr-1Mo(V, Nb) ferritic/martensitic steel at 8 kW laser power and 25 mm/s (1.5 m/min) welding speed.

Rapidly rising and relatively slowly falling temperature time curves of nearly similar nature were observed for all the points at varying distance in the vicinity of the weld centre line. The line joining the peak temperatures of nodes at varying distance from the weld centre line is also shown in Fig. 7.2. It can be seen that the peak temperature of a node goes on decreasing and time to reach the peak temperature goes on increasing with increasing distance from the weld centre line. This is because, the thermal energy is flowing outward from the weld region and it takes more time to reach a node at a larger distance.

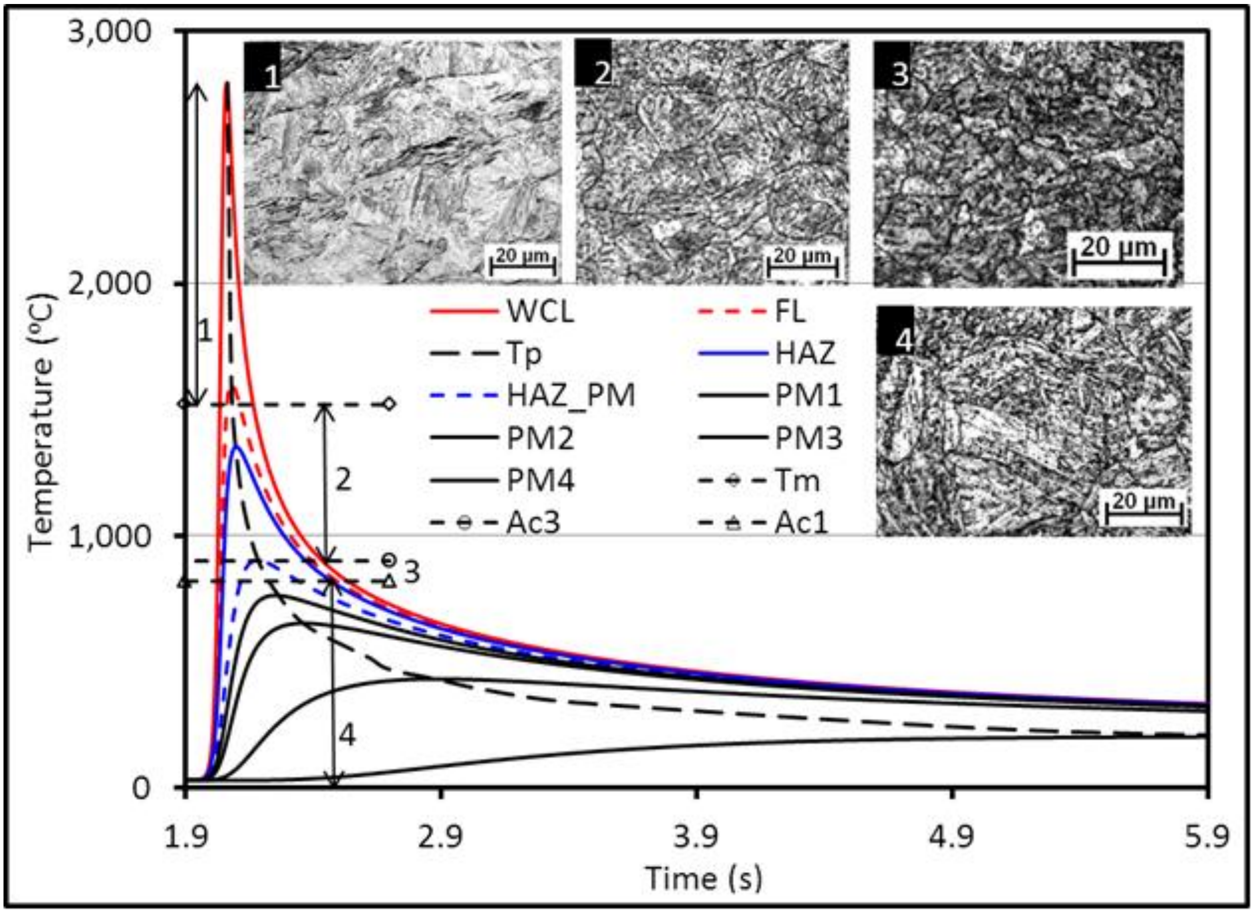

Fig. 7.2: Computed thermal cycle in different regions – weld centre line (WCL), fusion line (FL), heat affected zone (HAZ), HAZ-parent metal (PM) boundary and different points in the parent metal with distance increasing from the WCL along mid-thickness line at mid-length cross-section. Peak temperature at different points at increasing distance from WCL is also joined. Microstructure of the material subjected to different thermal cycles – (1) Fusion Zone (FZ), (2) Heat Affected Zone (FZ side), (3) Heat Affected Zone (PM side) and (4) PM is also shown.

Thermal cycles in the HAZ show that this region remains above Ac_1 temperature for less than 0.5 s and therefore, coarsening of prior austenite grains was not expected. This is because, coarsening of prior austenite grains require complete dissolution of the carbides and time for migration of the grain boundaries. However, the computation shows that high temperature does not stay in the HAZ for sufficient time to support kinetics of carbide dissolution and coarsening of prior austenite grains. Microstructure of the HAZ region is also inserted in Fig. 7.2 and it can be seen that size of prior austenite grains is comparable to that of the parent metal (~ 20 μm). Similarly, thermal cycle in inter-critical HAZ region shows that this region experiences the inter-critical temperature for less than 0.2 s and it is therefore, does not suffer from over tempering and hence no inter-critical softening was observed in the cross-weld microhardness profile (Section 5.5, Chapter 5). Microstructure of the inter-critical region is presented in Fig. 7.2. Relatively finer prior austenite grains, hinting at partial austenitization of the material in this region during heating, can be seen in this micrograph. Microstructure of the parent metal is also included for comparison. This microstructure consists of tempered martensite laths within equiaxed prior austenite grains of 20 μm average size.

7.3 Isotropic Hardening and Residual Stress Profile

7.3.1 Cross-Weld Profile

Variation of three the components – longitudinal (along the welding direction), normal (along the thickness direction) and transverse (normal to the parting surface being welded) of the residual stress and its von-Mises equivalent with distance from the weld centre line at 1.5 mm below top surface on mid-length cross-section is presented in Fig. 7.3. Variation of isotropic hardening (local yield strength of the material) and martensite phase-fraction resulting from welding is also superimposed on this plot. From this plot it can be seen that local yield strength of the material in the fusion zone and the HAZ is more than twice than that of the parent metal. Variation of the local yield strength of this material shows one to one correspondence with the martensite phase fraction. Thus increase in the local yield stress in the fusion zone and HAZ is on account of the martensitic transformation of this material; as martensite of this steel is much stronger than the parent metal in tempered martensitic condition (Fig. 4.5). At a distance of 2 mm from the weld centre line, there is marginal increase in the local yield strength of the parent metal. This is on account of strain hardening of the material.

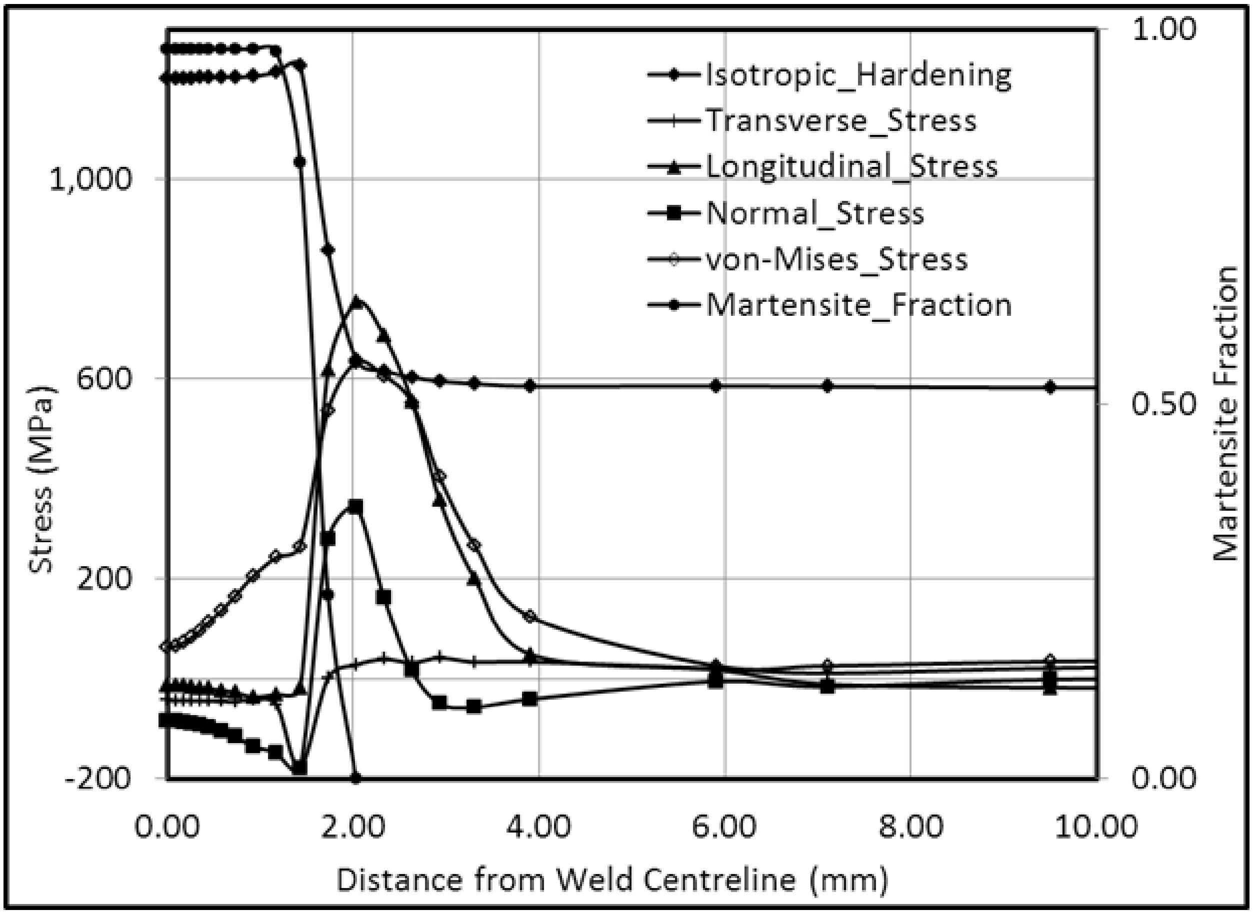

Fig. 7.3: Variation of isotropic hardening (local yield strength), residual stress (longitudinal, normal, transverse and von-Mises equivalent) and martensite phase-fraction with distance from the weld centreline in laser welded joint in 9Cr-1Mo(V, Nb) ferritic/martensitic steel.

Among the three components of the residual stress, the longitudinal component shows the greatest magnitude followed by the normal component and the transverse component is the least significant. The longitudinal and the normal components show similar profiles with a trough in the fusion zone and the HAZ and a peak at 2 mm from the weld centre line, which coincides with zero martensite phase fraction. The peak value of the longitudinal and normal components as well as the von-Mises equivalent of the residual stress lies in the parent metal region bordering the HAZ. Similar profiles for the three components of the residual stress were obtained by neutron diffraction measurements on this weld joint, which has been reported in Chapter 6. The trough in the residual stress profile in the vicinity of the weld joint is on account of SSPT of austenite into martensite, because this transformation is dilative in nature [24]. This kind of profile with trough in the fusion zone and the HAZ accompanied by peaks in the parent metal bordering HAZ has been reported in the literature for weld joints in martensitic steel made by conventional welding processes as well [26]. However, this effect is clearer in case of laser welded joints, because it is a single pass joining process and therefore, effect of the martensitic transformation associated with first pass is not camouflaged by thermal dilation effects of the succeeding passes, as in case of arc welding processes.

In case of the weld joints produced by conventional arc welding processes, the thickness to width aspect ratio of the each pass is low (~1) and therefore, the normal and transverse components of the residual stress are comparable in the magnitude. However, in case of beam welded joints the thickness to width aspect ratio is very high (~10) and therefore, the normal component becomes much more pronounced than the transverse component. This argument finds support from these results.

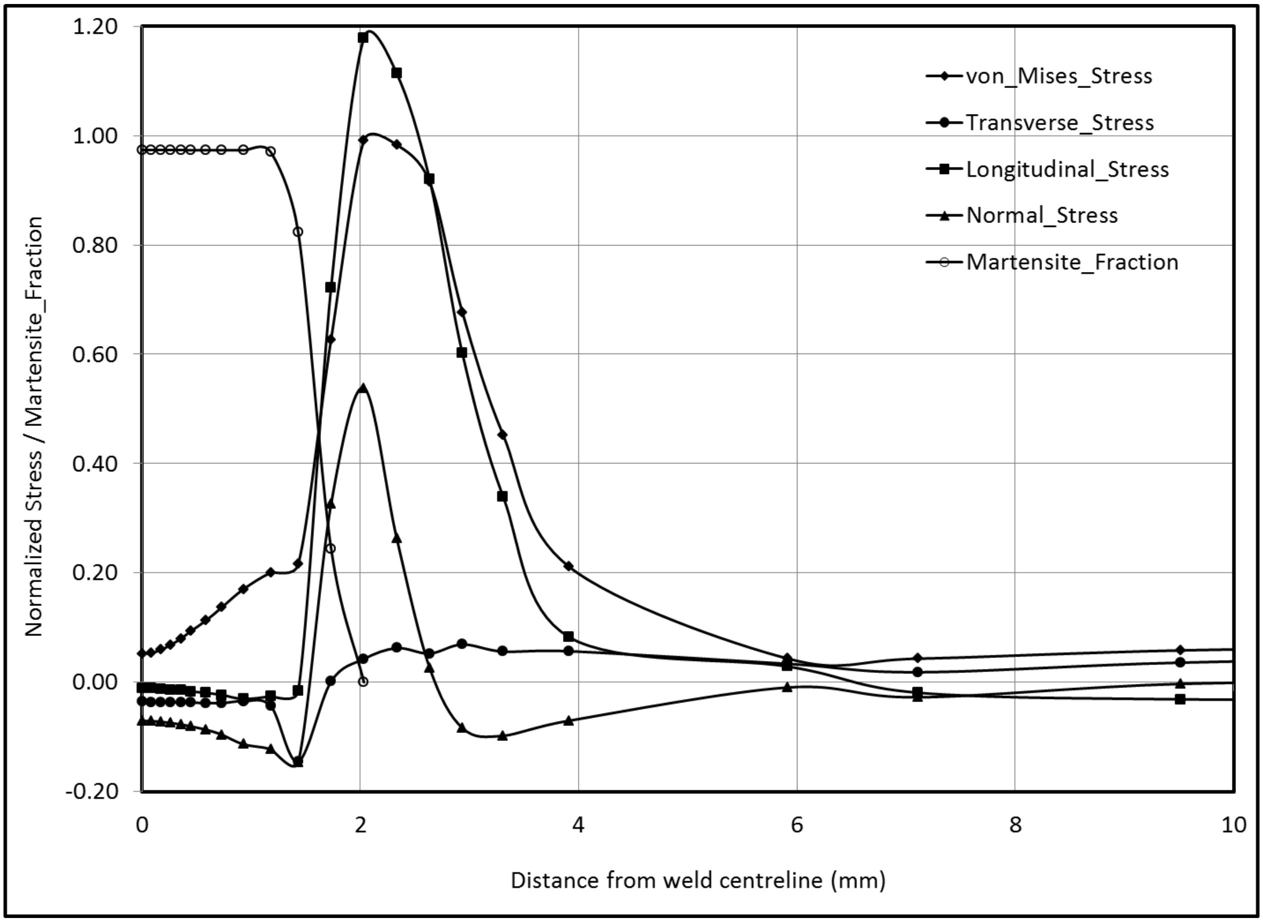

Fig. 7.4: Variation of residual stress (longitudinal, normal, transverse and von-Mises) normalized with local yield strength of the material and martensite phase-fraction with distance from the weld centreline in laser welded joint in 9Cr-1Mo(V, Nb) ferritic/martensitic steel.

Variation of the normalized (by local yield strength) values of the longitudinal, the normal and the transverse components and von-Mises equivalent of the residual stress with distance from the weld centre line at 1.5 mm below top surface on mid-length cross-section is presented in Fig. 7.4. Variation of the martensite phase fraction is also superimposed. It can be seen that the maximum value of the von-Mises equivalent of the residual stress is 1; this means the state of the residual stress is elastic, even though peak value of the longitudinal component of the residual stress is ~ 20% higher than the yield stress. This reconfirms that the computed results do make sense.

Longitudinal component of the residual stress in the vicinity of the weld joint is generally the most significant and it has been consistently reported to exceed the yield strength of the material [36]. In this plot also it can be seen that the normal component with peak value ~50% of the yield strength is the other significant component of the residual stress besides the longitudinal component and the transverse component is the least significant with magnitude within $\pm$10% of the yield strength. The value of von-Mises equivalent of the residual stress being as high as the local yield strength suggests this region (at 2 mm from the weld centre line) might have undergone plastic deformation. This is indeed so because value of the local yield strength in this region is greater than that of the parent metal even though there is no martensitic transformation (Fig. 7.3). Therefore, this increase can only be explained by strain hardening which can occur only if material undergoes plastic deformation. From these results it can be inferred that the regions bordering HAZ and parent metal undergo plastic deformation during laser welding. Further work is required to explore if this plastic deformation has anything to do with type IV cracking of the welded joints in this material as type IV cracking occurs in these locations [8, 10].

Comparison of the computed values of the longitudinal component of the residual stress with that measured by neutron diffraction, reported in Chapter 6, is presented in Fig. 7.5. It can be seen that computed profile show reasonably good match with the measured one in terms of shape and location of the peak; however, there are differences too. The computed profile is steeper and shows significantly higher peak value than the measured one. This can be on account of larger gauge volume (0.8 x 0.8 x 2 mm^3 and 0.8 x 0.8 x 20 mm^3) employed in neutron diffraction measurements, leading to averaging of the residual stresses over a larger volume, than the element size (0.1 x 0.2 x 0.25 mm^3 to 0.3 x 0.4 x 0.5 mm^3 in the region of interest) employed in these computations. Smaller element size and gauge volume are preferred respectively for computation and measurement of the stress field due to steep variation in this case.

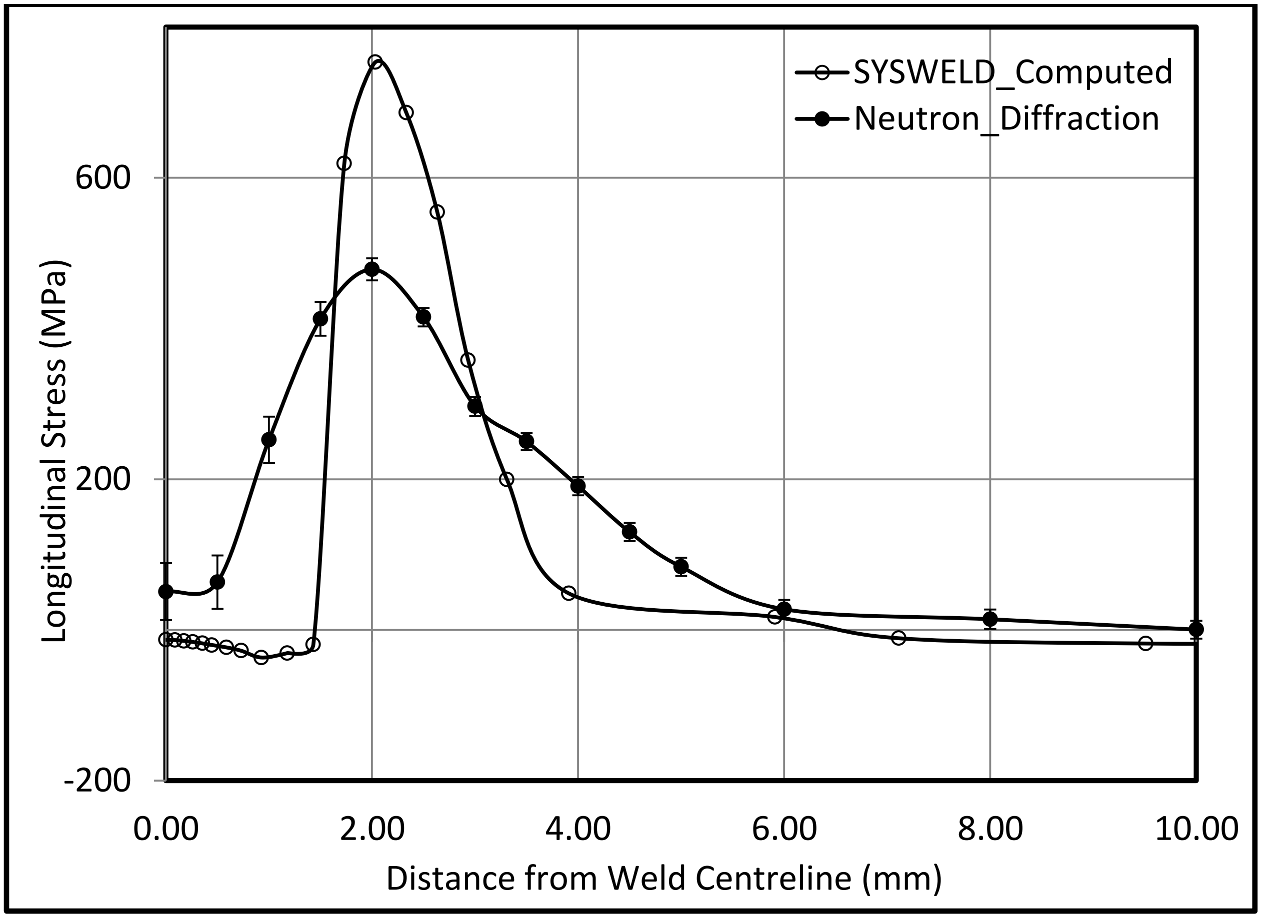

Fig. 7.5: Comparison of the computed (using SYSWELD) and experimentally measured (using Neutron Diffraction) values of longitudinal component of the residual stress profiles across laser welded joint in 9Cr-1Mo(V, Nb) ferritic/martensitic steel.

However, it is practically not possible to lower the gauge volume further for neutron diffraction measurements. Therefore, measurements using reduced gauge volume at a synchrotron sources will be required to improve the accuracy of the measured stress profile in this case. Improvements will be required on the computation side as well. In the present case martensite has been assigned a single set of properties, thus no differentiation has been made between the martensite in the fusion zone and the HAZ. However, it has been seen in these computations that the thermal cycles in the HAZ may not be sufficient for complete dissolution of the carbides and therefore, martensite in the HAZ will have lower carbon and therefore, lower strength as distance from the fusion line increases. This effect need to be mapped experimentally to generate material property data in the HAZ and then employed suitably in the computation of the residual stress field. These two improvements – one on the measurement side and another on the modelling and simulation side is expected to narrow down the differences between the measured and the experimental profiles of the residual stress.

7.3.2 Through - thickness Profile

Variation of longitudinal, normal and transverse components and von-Mises equivalent of the residual stress along the weld centre line is presented in Fig. 7.6. The transverse component is mostly low tensile, normal component is significantly compressive and the longitudinal component is between these two. This order of the three components of the residual stress is consistent with that measured by neutron diffraction and reported in chapter 6. Further, through thickness profiles of the three components of residual stress are not symmetric across the mid-thickness plane. The lower half is under relatively compressive state of stress than the upper half. This can be explained by the fact that the thermal loading condition is not symmetric, as the heat source has been applied from the top surface during welding. Therefore, the region below the mid-thickness plane received lesser heat input than that above and cooled to the Ms temperature earlier than the upper half.

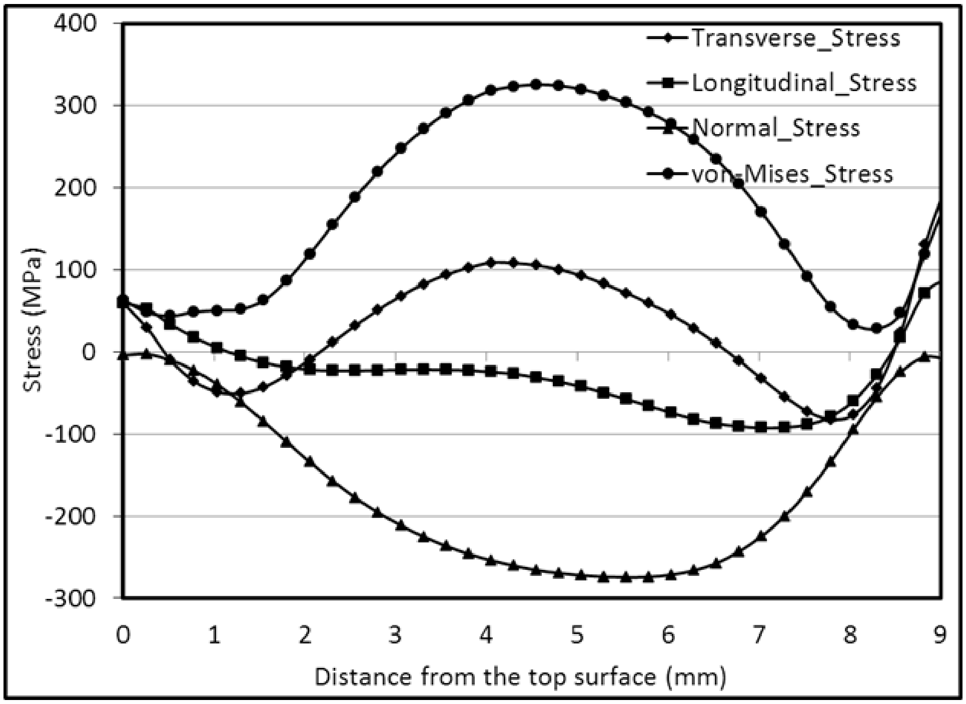

Fig. 7.6: Through thickness residual stress profile along the weld centreline, showing region below mid-thickness to be under relatively compressive stress as compared to that above.

To support this argument, a part of the cooling curves from three points - 0.5 mm, 4.5 mm and 8.5 mm below the top surface is presented in Fig. 7.7. Martensite phase fraction of the corresponding regions is also plotted on the same curve. It can be seen that at 8.5 mm depth the material reached the Ms temperature ~300 ms before it did at mid-thickness level and above that. Therefore, martensitic transformation commenced first in the lower half, which is obvious from the temporal evolution of martensite phase fraction presented in this figure. Thus the region between the mid-thickness plane and the bottom surface experienced martensitic transformation under greater restraint than that above and this resulted in relatively compressive stress field below mid-thickness region than that above in the fusion zone. This result was also observed by neutron diffraction measurements reported elsewhere (Section 6.5, Chapter 6). Thus the computed and the measured profiles converge to support that the regions below mid-thickness is under relatively compressive state of stress than that above. This finding contrasts with that reported in case of the weld joints produced between pipes by multipass arc welding processes; which showed high tensile residual stresses in the root side and compressive stresses on the outer surface [25]. This difference can be explained by the fact that in case of multipass joints, part of the material deposited in the preceding pass experiences only thermal dilation and no SSPT during next subsequent passes. Therefore, only the weld metal deposited in the final pass experiences compressive residual stresses and those deposited in the preceding passes experience high tensile residual stress.

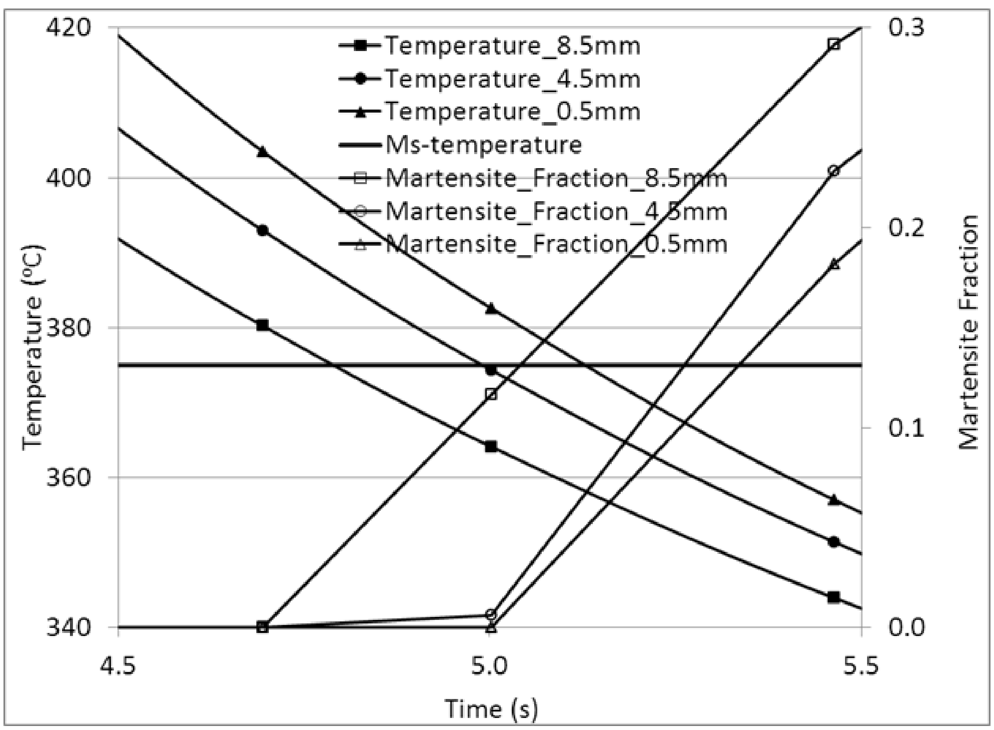

Fig. 7.7: Cooling curve and martensite phase evolution at three different depths (8.5 mm, 4.5 mm and 0.5 mm) along the weld centreline. It is evident that along the weld centreline the martensitic transformation proceeds from the bottom side towards the top surface.

7.3.3 Temporal Evolution of Stress Field

Temporal evolution of longitudinal stress, temperature and austenite and martensite phase-fraction in a small volume (3D element) at the weld centre line is presented in Fig. 7.8. This plot clearly shows the effect of different factors causing development of stress field during welding.

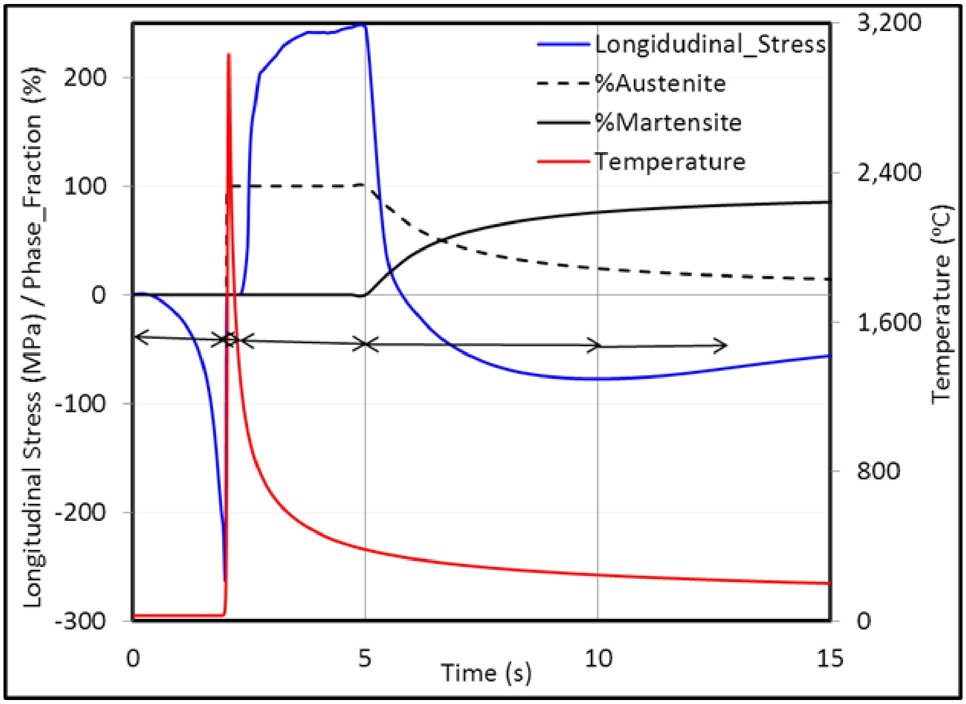

Fig. 7.8: Temporal evolution of longitudinal stress, temperature and phase-fraction in a small volume (3D element) at the weld centreline. Effect of (1) rapid heating of preceding regions (2) rapid heating of the element (3) contraction of solidified weldment, (4) transformation of austenite into martensite and (5) contraction of martensite on the evolution of the stress-field can be seen very clearly.

Region 1 (in time domain) shows evolution of high compressive stresses. This is due to rapid thermal expansion of the material as heat source approaches the region under consideration. Once the heat source comes too close softening or annealing effect takes place and stress level rises rapidly to zero and stays there till the region melts and solidifies again (Region 2). After that the solidified regions starts to contract and tensile stresses start to develop into it. The stress remains tensile and goes on increasing till the Ms temperature is reached (Region 3). Once, Ms temperature is reached, martensitic transformation of austenite (which is dilative in nature) commences; and this leads to rapid evolution of compressive stresses (Region 4). After sufficient transformation has occurred, effect of thermal contraction of the material dominates and the stresses start to become progressively tensile (Region 5). Temporal evolution of stresses in weld joints of P91 steel is not reported in the literature and therefore, cannot be compared. However, temporal profile of the longitudinal stress resulting from TIG weld bead on SS316L has been reported by Xu et al. [31]. It shows only two regions – Region 1 i.e. compressive stresses arising due to approaching heat source and region 3 i.e. tensile stresses arising due to localized contraction during cool down of the weld. Our results are consistent with those reported by Xu et al. [31] in region 1 and 3. Absence of region 2 is surprising as the stress must remain zero for the time duration, when the material remains molten. However, this time duration is too short as compared to the time scale used for plotting temporal evolution and that might be the reason, why region 2 is missing from the plot reported by Xu et al. [31]. The absence of region 4 and beyond is due to the fact that there is no SSPT in SS316L. Thus temporal profiles of the stresses provide effect of different contributing factors and also possible points of intervention during the process itself, to suitably alter the stress field. Temporal evolution of the stress field is something that cannot be determined experimentally and can only be computed. Knowledge of the temporal evolution of stress field is important not only to delineate the effects of different contributing factors but also for devising any intervention during welding to introduce desired modification in the stress-field.

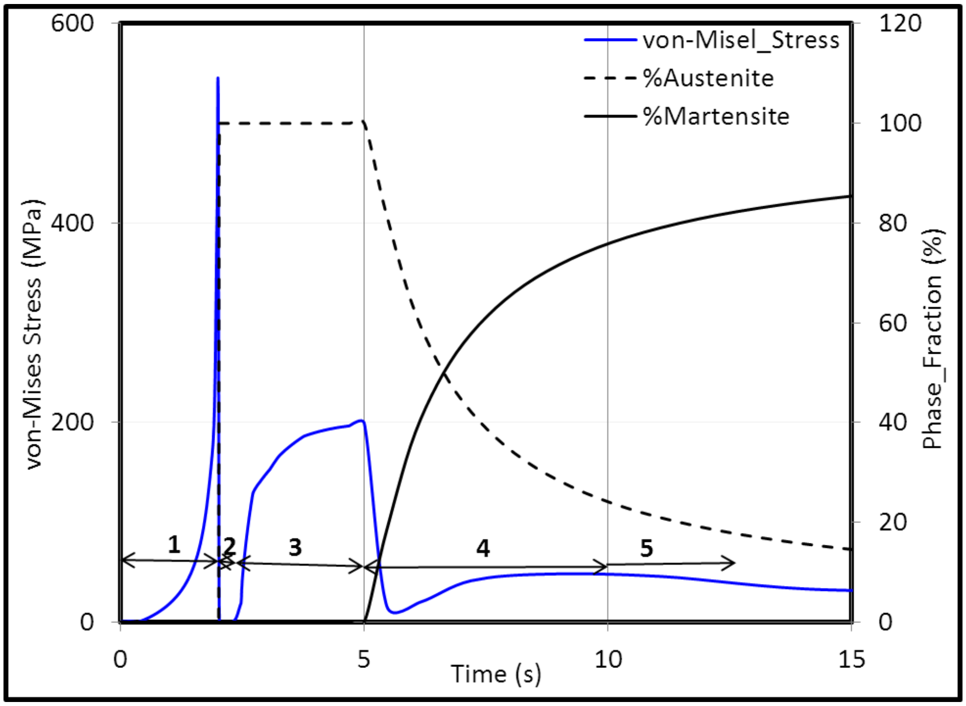

Fig. 7.9: Temporal evolution of von-Mises stress, temperature and phase-fraction in a small volume (3D element) at the weld centreline. Effect of (1) rapid heating of preceding regions (2) rapid heating of the element (3) contraction of solidified weldment, (4) transformation of austenite into martensite and (5) contraction of martensite on the evolution of the stress-field can be seen very clearly.

Temporal evolution of von-Mises stress, temperature and phase-fraction in a small volume (3D element) at the weld centre line is presented in Fig. 7.9. This figure also delineates the effect of different contributing factors on evolution of the stress field. However, this figure presents a very interesting result. In region 3 i.e. between 2.2 to 5s, when the material is completely austenitic, von-Mises stress is much higher than yield strength of the austenite at the corresponding temperature (Fig. 4.6). This implies that the austenite had undergone plastic deformation and therefore, work hardened while the weld joint cooled to Ms temperature. This is something that cannot be seen in the resulting microstructure as the solid state martensitic transformation, which occurs below Ms temperature (~ 375 ^oC), camouflages the effects of plastic deformation of the parent austenite to a great extent. Work hardening of the parent austenite has another implication, that it lowers the Ms temperature [37]. To what extent the Ms gets suppressed need to be found out experimentally and fed back into these computations as material data input for further improvements in the computed results.

7.3.4 Stress Field in Supercooled Austenite

While the final or residual stress field can be experimentally measured, one has to rely solely on computations to know the stress field in the material at the intermediate time steps. While there can be so many of the intermediate time steps, one important time step is when the heat source is removed. In this simulated welding process, the heat source is removed after 4.09 s as it traverses the entire length of the weld seam by then.

Through thickness stress profile along weld centre line at the mid-length cross-section of the welded plate at 4.09 s is presented in Fig. 7.10. Three-dimensional austenite phase-field at this time is also inserted. It can be seen that at this point in time the fusion zone was fully austenitic at the mid-length cross-section; therefore, this stress field is in the austenitic phase field. The fusion zone is predominantly in tensile stress field as all the three components – longitudinal, transverse and normal are tensile in most part of it. Also, the von-Mises stress and isotropic hardening (local yield strength) of the material have same magnitude and this is much higher than the yield strength of the austenite (Fig. 4.6). This implies that the austenite had undergone and continued to undergo plastic deformation and therefore, strain-hardening. At the mid-thickness level, all the three components – longitudinal, transverse and normal are tensile in nature. This means that the austenite was not only deforming, it was doing so under tensile triaxial state of stress. Fortunately austenite has sufficient ductility to prevent any structural discontinuity under the tensile triaxial state of stress. This profile is vastly different from the final or residual stress profile (Fig. 7.6). The difference between the state of stresses shown in Fig. 7.6 and Fig. 7.10 also shows the effect of the martensitic transformation on evolution of stress.

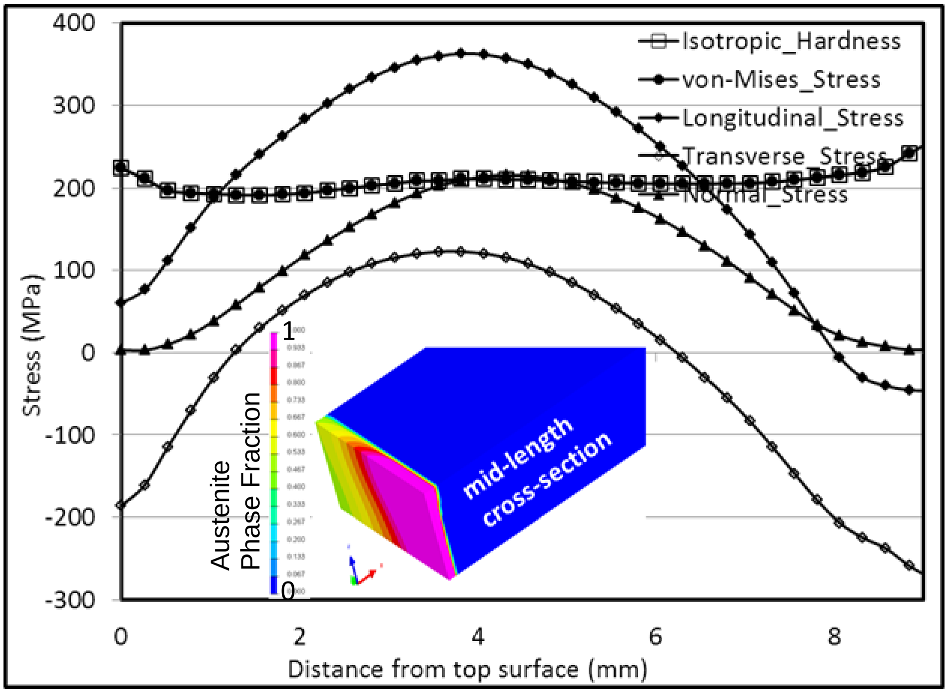

Fig. 7.10: Through thickness stress profile along weld centreline at the mid-length cross-section of the welded plate at 4.09 s. Three-dimensional austenite phase-fields at this time is also inserted. Plastic deformation of austenite and tri-axial stress in the mid-thickness region is evident.

Cross-weld stress profile at 1.5 mm below the top surface of the welded plate at 4.09 s is presented in Fig. 7.11. This profile also confirmed that the austenitic phase field had undergone plastic deformation. However, it is worth noticing the difference between the stress profiles at 4.09 s presented in Fig. 7.11 and the final or residual stress field at the same location presented in Fig. 7.3. The residual stress profile (Fig. 7.3) showed that the residual stresses died down beyond 5 mm. This may give a false impression that during the laser welding process only 5 mm on the either side was subjected to significant levels of stress. However, the stress profile in Fig. 7.11 revealed that the region affected by significant stress level was much wider and it was as wide as 10 mm on the either side of the weld joint. Thus it can be inferred that the computed temporal stress profiles, which cannot be measured, reveal much more than that revealed by the residual stress profile which can be computed as well as measured.

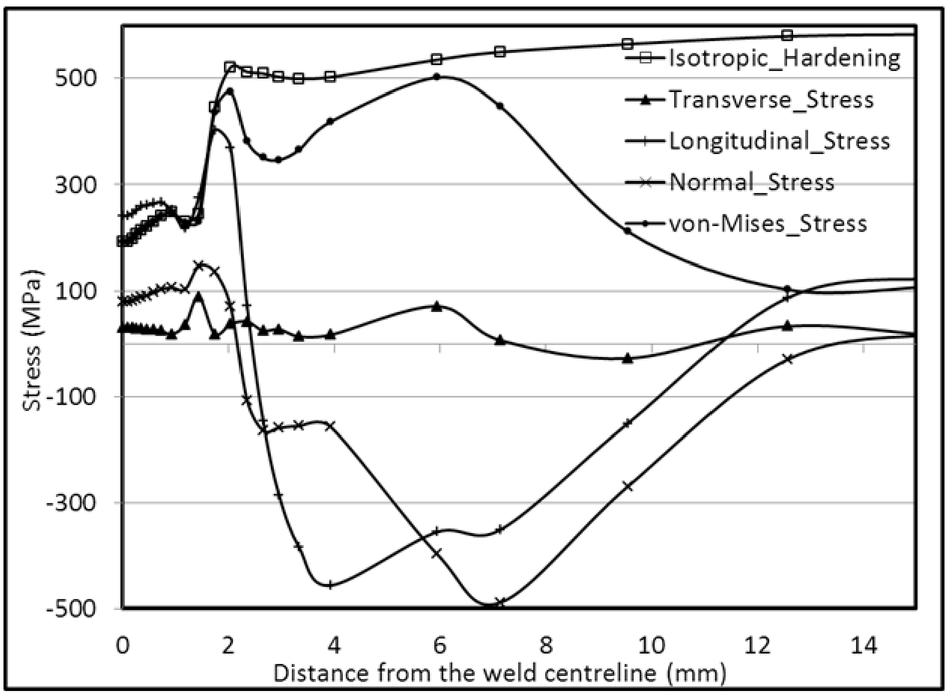

Fig. 7.11: Cross-weld stress profile at 1.5 mm below the top surface of the welded plate at 4.09 s. Plastic deformation of austenite is evident.

7.4 Conclusions

Temporal and spatial evolution of temperature, metallurgical phase and stress field resulting from laser welding of 9 mm thick 9Cr-1Mo(V, Nb) steel at 8 kW laser power and 1.5 m/min (25 mm/s) welding speed were computed using finite element based simulation and solution package SYSWELD. Following conclusions can be drawn from this computational study.

(i) Computed fusion zone and HAZ profiles show reasonably good agreement with the actual weld joint cross-section.

(ii) The temporal evolution of the thermal field shows that the material stays in the HAZ temperature zone (Ac_1 to Tm) for very short time (less than 0.5 s) and the fusion zone and the HAZ cools to Ms temperature at an average cooling rate exceeding 100^oC/s. Therefore, there is no coarsening of the austenite grains in the HAZ and all the austenite gets transformed into martensite while cooling.

(iii) Spatial variation of the three components of the residual stress shows that the longitudinal and the normal components are significant while the transverse component is the least significant. Cross-weld profiles of the longitudinal and the normal components of the residual stress show trough in the fusion zone and the HAZ and a peak in the parent metal bordering the HAZ. The peak value of the longitudinal component is 20% higher than the local yield strength and that of the von-Mises equivalent is equal to the local yield strength. The cross-weld profiles of the residual stress also show mild plastic deformation leading to work-hardening of the parent metal adjacent to the metallurgical HAZ. The computed residual stress profiles show reasonably good agreement with that measured by neutron diffraction.

(iv) Through thickness profile of longitudinal, transverse and normal components of the residual stress show that the region below mid-thickness is in the state of compressive stress than that above. This can be attributed to martensitic transformation commencing first in the bottom side of the plate.

(v) Temporal evolution of the stress-field clearly delineates the effect of different factors contributing to the evolution of the stress-field in the material. Martensitic transformation brings in compressive effect in the longitudinal component of stress by more than 300 MPa and it has compressive effect of varying magnitude on all the three components of the stress. Temporal evolution of the stress field also shows that the austenitic phase-field undergoes significant plastic deformation and therefore, work hardening prior to its transformation into martensite. Besides, the stress-field at an intermediate time step shows that the region affected by the stress due to welding process is much wider (~ 10 - 12 mm on the either side of the joint) than that suggested by the final or residual stress-field (~ 5 mm on either side of the joint).

References

[1] F. Masuyama, “History of power plants and progress in heat resistant steels”, ISIJ Intl 41(6) (2001) 612–625.

[2] R. L. Klueh, “Elevated temperature ferritic and martensitic steels and their application to future nuclear reactors”, Int. Mater. Rev. 50(5) (2005) 287 - 310.

[3] K. H. Mayer and F. Masuyama, “The development of creep-resistant steels” in Creep-Resistant Steels, F. Abe, T U Kern and R. Viswanathan Eds.; Woodhead Publishing Limited, Cambridge, UK, (2008) 15-77 .

[4] S. Pillot, Z. Zhao, S. Corre, C. Chauvy, L. Coudreuse, P. Toussaint, Proc. of ASME 2010 Press. Vessel. Pip. Div. Conf. (PVP 2010) 1-14.

[5] R. K. Shiue, K. C. Lan and C. Chen, "Toughness and austenite stability of modified 9Cr-1Mo welds after tempering", Mater. Sci. Eng. A 287 (2000) 10 - 16.

[6] R. Mythili, P. V. Thomas, S. Saroja, M. Vijaylakshmi and V. S. Raghunathan, "Microstructural modification due to reheating in multipass manual metal arc welds of 9Cr-1Mo steel", J. Nucl. Mater. 312 (2003) 199-206.

[7] P. K. Ghosh and U. Singh, "Influence of pre- and post- weld heating on weldability of modified 9Cr-1Mo (V-Nb) steel pipe under shielded metal arc and tungsten inert gas welding process”, Sci. Technol. Weld. Join. 9 (3) (2004) 229 - 236.

[8] S. K. Albert, M. Tabuchi, H. Hongo, T. Watanabe, K. Kubo and M. Matsui, “Effect of Welding Process and Groove Angle on Type IV Cracking Behaviour of Weld Joints of a Ferritic Steel”, Sci. Technol. Weld. Join. 10 (2) (2005) 149-157.

[9] T. Watanabe, M. Tabuchi, M. Yamazaki, H. Hongo and T. Tanabe, “Creep damage evaluation of 9Cr-1Mo-V-Nb steel welded joints showing Type IV fracture”, Int. J. Press. Vessel Pip. 83 (2006) 63–71.

[10] K. Laha, K. S. Chandravathi, P. Parameshwaran, K. B. S. Rao and S. L. Mannan, “Characterization of Microstructures across the Heat-Affected Zone of the Modified 9Cr-1Mo Weld Joint to Understand Its Role in Promoting Type IV Cracking", Metall. Mater. Trans. 38A (2007) 58 - 68.

[11] S. Sulaiman, “Structure of properties of the heat affected zone of P91 creep resistant steel”, PhD Thesis, University of Wollongong, Wollongong, Australia (2007) [http://ro.uow.edu.au/theses/777].

[12] P. Mayr, “Weldability of Modern 9%Cr Steels for Application in USC Power Plants”, PhD Thesis, Graz University of Technology (2007).

[13] B. Arivazhagan, S. Sundaresan and M. Kamaraj, “Effect of TIG arc surface melting process on weld metal toughness of modified 9Cr-1Mo (P91) steel”, Mater. Lett. 62 (2008) 2817 – 2820.

[14] J.-P. Barthoux, “Narrow gap welding of heavy wall thickness materials in nuclear and fossil fuel industries”, Focus on Nuclear Power Generation, (2008) 36 – 42. Retrieve from http://www.nuclear-exchange.com/pdf/TP_Polysounde.pdf on August 16, 2014.

[15] B. Arivazhagan, S. Sundaresan and M. Kamaraj, “A study on influence of shielding gas composition on toughness of flux-cored arc weld of modified 9Cr–1Mo (P91) steel”, J. Mater. Process. Technol. 209 (2009) 5245 – 5253.

[16] H. Hongo, M. Tabuchi and T. Watanabe, “Type IV Creep Damage Behavior in Gr.91 Steel Welded Joints”, Metall. Mater. Trans. 43A (2012) 1163 – 1173.

[17] S. Paddea, J. A. Francis, A. M. Paradowska, P. J. Bouchard and I. A. Shibli, "Residual stress distribution in a P91 steel-pipe girth weld before and after post weld heat treatment", Mater. Sci. Eng. A534 (2012) 663 - 672.

[18] J. Parker, "Factors affecting type IV creep damage in Grade 91 steel welds", Mater. Sci. Eng. A578 (2013) 430 – 437.

[19] S. A. David, J. A. Siefert and Z. Feng, "Welding and weldability of candidate ferritic alloys for future advanced ultrasupercritical fossil power plants", Sci. Technol. Weld. Join. 18(8) (2013) 631 – 651.

[20] P. Kumar, "An Overview of Welding and Fabrication Aspects during Manufacture of Nuclear Reactor Components for 500 MWe Prototype Fast Breeder Reactor", Proc. of International Welding Congress 2014 (IWC 2014), New Delhi, India (2014).

[21] B. Arivazhagan and M. Vasudevan, "A comparative study on the effect of GTAW processes on the microstructure and mechanical properties of P91 steel weld joints", J. of Manuf. Proc. 16 (2014) 305 – 311.

[22] W. H. Lee, R. K. Shiue and C. Chen, "Mechanical properties of modified 9Cr-1Mo steel welds with notches", Mater. Sci. Eng. A356 (2003) 153 - 161.

[23] Z. Xu, "Laser welding and post weld heat treatment of modified 9Cr-1VNb steel", Report No. ANL/NE-12/12, Argonne National Laboratory, Chicago, Illinois (2008).

[24] A. Kundu, P. J. Bouchard, S. Kumar, K. A. Venkata, J. A. Francis, A. Paradowska, G. K. Dey and C. E. Truman, "Residual stresses in P91 steel electron beam welds", Sci. Technol. Weld. Join. 18(1) (2013) 170 – 175.

[25] A. H. Yaghi, T. H. Hyde, A. A. Becker, J. A. Williams and W. Sun, “Residual stress simulation in welded sections of P91 pipes”, J. Mater. Process. Technol. 167 (2005) 480 - 487.

[26] D. Dean and M. Hidekazu, “Prediction of welding residual stress in multi-pass butt-welded modified 9Cr–1Mo steel pipe considering phase transformation effects”, Comput. Mater. Sci. 37 (2006) 209 - 219.

[27] S. H. Kim, J. B. Kim and W. J. Lee, “Numerical prediction and neutron diffraction measurement of residual stresses for a modified 9Cr-1Mo steel weld”, J. Mater. Process. Technol. 209 (2009) 3905 - 3913.

[28] J. W. H. Price, A. Z. Paradowska, S. Joshi, T. Finlayson, C. Semetay and H. Nied, “Comparison of experimental and theoretical residual stresses in welds: the issue of gauge volume”, Int. J. Mech. Sci. 50 (2008) 513 - 521.

[29] S. K. Bate, R. Charles and A. Warren, “Finite element analysis of a single bead-on-plate specimen using SYSWELD”, Int. J. Press. Vessel. Pip. 86 (2009) 73 - 78.

[30] A. S. Aloraier and S. Joshi, “Residual stresses in flux cored arc welding process in bead-on-plate specimens”, Mater. Sci. Eng. A534 (2012) 13 - 21.

[31] J. J. Xu, P. Gilles, Y. G. Duan and C. Yu, “Temperature and residual stress simulations of the NeT single-bead-on-plate specimen using SYSWELD”, Int. J. Press. Vessel. Pip. 99 - 100 (2012) 51 - 60.

[32] S. A. Tsirkas, P. Papanikos, Th. Kermanidis, “Numerical simulation of the laser welding process in butt-joint specimen”, J. Mater. Process. Technol. 134 (2003) 59 - 69.

[33] G. A. Moraitis and G. N. Labeas, “Prediction of residual stresses and distortions due to laser beam welding of butt joints in pressure vessels”, Int. J. Press. Vessel. Pip. 86 (2009) 133 - 142.

[34] N. S. Shanmugam, G. Buvanashekaran, K. Sankaranarayanasamy and S. R. Kumar, “A transient finite element simulation of the temperature and bead profiles of T-joint laser welds”, Mater. Des. 31 (2010) 4528 - 4542.

[35] B. J. Ganesh, S. Raju, A. K. Rai, E. Mohandas, M. Vijayalakshmi, K. B. S. Rao, and B. Raj, “Differential scanning calorimetry study of diffusional and martensitic phase transformations in some 9 wt% Cr low carbon ferritic steels”, Mater. Sci. and Technol. 27(2) (2011) 500-512.

[36] W. Woo, Z. Feng, X. L. Wang XL and S. A. David, “Neutron diffraction measurements of residual stress in friction stir welding: A review”, Sci. Technol. Weld. Join. 16(1) (2011) 23-32.

[37] T. S. Wang, M. Zhang, Y. H. Wang, J. Yang and F. C. Zhang, “Martensitic transformation behaviour of deformed supercooled austenite”, Scripta Mater. 68(2) (2013) 162 - 165.

Chapter 8: Summary and Conclusions

Ferritic martensitic steels (FMS) are structural and functional material for ultra-supercritical power plants and next generation nuclear reactors. 9Cr-1Mo(V, Nb) FMS is a prominent member of this family of the ferritic/martensitic steels. This material is joined by different conventional arc welding processes. However, process complexities, high heat input and resultant wider fusion zone, heat affected zone, residual stress affected zone and higher joint distortions limit application of the conventional arc welding processes for fabrication of high end components like Test Blanket Module (TBM) for the International Thermonuclear Experimental Reactor (ITER). To overcome these limitations, laser welding and electron beam welding of these steels has evinced considerable interest. However, reported literature on laser welding of 9Cr-1Mo(V, Nb) FMS in terms of microstructure and residual stresses is rather limited.

Detailed experimental and computational study of laser welding of 9Cr-1Mo(V, Nb) FMS was done in this work. Laser welding experiments were performed using a high power (up to 10 kW) continuous wave CO_2 laser. Laser welding parameters were optimized based on the weld beads produced over a range of parameters (laser power: 2 – 8 kW and welding speed: 0.5 – 5.0 m/min) and square butt joints between 9 mm thick plates of 9Cr-1Mo(V, Nb) FMS were made. Residual stress measurements in the laser welded 9 mm thick plates of 9Cr-1Mo(V, Nb) FMS were performed by neutron diffraction at Institut Laue-Langevin (ILL), Grenoble, France. In addition, modelling and simulation studies of laser welding was performed, using a finite element based welding and heat treatment simulation solution software – SYSWELD, for computation of temporal evolution and spatial distribution of temperature and stresses. Some hitherto unexplored attributes of the physical metallurgy of 9Cr-1Mo(V, Nb) FMS, required for understanding the evolution of microstructure and residual stresses during welding of this steel, were also studied. The present study has revealed some interesting results regarding phase transformation behaviour and mechanical behaviour of this steel during welding. Besides, the HAZ as well as the fusion zone in the laser welded joints in this steel, present some interesting microstructural features generally not observed / reported in the arc welded joints in this steel. The results are summarized in this chapter.

8.1 Austenitization Temperature and Transformation of Austenite while Cooling

This steel is highly hardenable because of high alloying content and therefore, when cooled from austenitic phase-field, it transforms completely into martensite even at very low cooling rates ~ $5^{o}C/min$ [1 - 2]. High hardenability is beneficial in obtaining uniform martensitic microstructure even in relatively thick sections, by cooling in still air from its standard normalizing temperatures in the range of 1040 – $1080^{o}C$. However, this material does not experience its standard normalizing temperature in the HAZ during welding. Different regions of the HAZ experience different austenitization temperatures between Ac_1 (~$820^{o}C$) to melting temperature for very short duration. The austenitization temperature and time combination determines the extent of dissolution of the carbide / carbonitride precipitates and therefore, affects chemistry and hardenability of the resulting austenite in the HAZ. This can affect transformation behaviour and transformation products of the austenite in the different part of the HAZ. Therefore, study of the effects of the austenitization temperature on transformation behaviour of austenite in 9Cr-1Mo(V, Nb) FMS is essential to understand the microstructural evolution in the HAZ. Though, physical metallurgy and cross-weld microstructure of this steel are well characterized and reported in the literature [2, 3], effect of austenitization temperature on phase-transformation behaviour of austenite in the HAZ region has not been given due consideration.

Therefore, dilatometry was performed to study the effect of austenitization temperature on the phase-transformation behaviour of the austenite in this steel. The austenitization temperatures were varied in the range of 850^{o}C – 1150^{o}C and soaking was not done at the austenitization temperatures to simulate the condition prevalent in the HAZ.

It was observed that the austenitization temperatures of 950^{o}C and above resulted in martensitic transformation of the austenite while cooling below the Ms temperature (~375^{o}C) (Figs. 4.5(b - d), Chapter 4). However, austenitization temperature of 850^{o}C resulted in diffusional transformation of austenite during cooling at much higher temperature (780 – 720^{o}C) (Figs. 4.5(a), Chapter 4) than its Ms temperature (~375^{o}C).

This implies that austenitization temperatures above 950^{o}C leads to dissolution of sufficient carbides and thus ensures sufficient hardenability for martensitic transformation of austenite during cooling. On the other hand austenitization temperature of 850^{o}C is insufficient to ensure dissolution of carbide precipitates and this leads to significant deterioration in the hardenability of the austenite. As a result the austenite transforms into diffusional ferrite. The computed phase-diagram of 9Cr-1Mo(V, Nb) FMS by Igarshi et al. [4] shows that solvus temperature of $M_{23}C_6$ carbide precipitates is ~900^{o}C and that of MX type carbonitride precipitates is ~1180^{o}C. Therefore, it was expected that the carbide / carbonitride precipitates were not to dissolve at austenitization temperatures below 900^{o}C.

Phase transformation behaviour of austenite in the HAZ region has significant influence on the final microstructure, residual stresses and performance of the weld joint in service [2, 5 - 7]. The HAZ adjacent to the fusion line experiences higher austenitization temperatures, while those near the parent metal experience lower austenitization temperatures. In addition, the material in the HAZ experiences the austenitization temperatures for very short duration; typically less than 500 ms in case of laser welding (computed result, Fig. 7.2, Chapter 7), due to high cooling rates associated with welding process. The combined effect of lower austenitization temperature and duration leads to insufficient carbide dissolution, mainly in the HAZ adjacent to the parent metal. Insufficient carbide dissolution leads to formation of austenite, which is lean in solute content and therefore exhibits lower hardenability than that indicated by nominal composition of the steel.

The austenitization temperature of 850^{o}C corresponds to the intercritical region of the HAZ. Softening in the intercritical HAZ (ICHAZ) has been long suggested as a potential contributor to the creep damage localization in this region, leading to failure by Type – IV cracking [8, 9]. So far the intercritical softening has been attributed to the over-tempering of the tempered-martensite in ICHAZ [8, 9]. However, the present study suggests that in addition to the over-tempering of the tempered-martensite in the HAZ region, it is the diffusional transformation of the austenite (formed at lower austenitization temperatures) in the ICHAZ and the FGHAZ, which contributes to the intercritical softening. The diffusional transformation product of austenite (ferrite) is inherently soft and has very low dislocation density than the diffusionless transformation products (bainite and martensite). Therefore, lower austenitization temperature in the

FGHAZ / ICHAZ leading to diffusional transformation can be a possible explanation for lower creep strength and failure by Type-IV cracking of the welded joints in this material.

8.2 Phase-dependent Tensile Behaviour of 9Cr-1Mo(V, Nb) FMS

In 9Cr-1Mo(V, Nb) FMS, the martensite (as-transformed or tempered) transforms into austenite while heating at much higher temperatures (Ac_1 ~820^oC) and the austenite transforms into martensite at much lower temperatures (Ms ~375^oC). This leads to hysteresis in the phase-field in the ferritic/martensitic steels. The three phases – as-transformed martensite, tempered martensite and supercooled austenite can be present at a given temperature during welding in different regions. These three phases are expected to show entirely different tensile behaviour owing to the differences in their crystal structure as well as microstructure. Quantitative knowledge of the tensile behaviour of the three phases at different temperatures is essential for accurate computation of the residual stress by modelling and simulation of welding of this steel. However, there is no published literature on the phase-dependent tensile behaviour of this steel at different temperatures. An attempt was made to address this gap by conducting tensile test of the three phases – as-transformed martensite, tempered martensite and supercooled austenite, of this steel at different temperatures in the range of RT to 800^oC. These tests provided valuable phase-dependent tensile properties of this steel. These results are discussed in Chapter 4 in detail. Phase-dependence in the tensile properties of this steel can be appreciated by comparing the yield strength, uniform elongation and ultimate tensile strength (true stress) of the three phases of this steel at a common test temperature of 400^oC. These values are presented in Table 8.1.

Table 8.1: Tensile properties of the three phases – as-transformed martensite, tempered martensite (Parent Metal) and supercooled austenite at 400^{o}C.

	As-transformed Martensite	**Tempered Martensite (Parent Metal)**	**Supercooled Austenite**
Yield Strength (MPa)	1080	478	150
Ultimate Tensile Strength (true stress) (MPa)	1600	650	760
Uniform Elongation (%)	10.5	6.8	50

At 400^{o}C, the steel showed significantly higher strength and lower elongation in martensitic (as-transformed as well as tempered) condition than that in supercooled austenitic condition. This information is vital for modelling and simulation of welding of this steel for accurate computation of the stress and deformation fields and also for the correct interpretation of the resulting residual stress field and the microstructure. These results were used in modelling and simulation of laser welding of 9Cr-1Mo(V, Nb) performed as part of the present work.

Supercooled austenitic phase of this steel showed inverse correlation with temperature. Uniform elongation of the supercooled austenite decreased from 50% at 400^{o}C to 17% at 800^{o}C (Fig. 4.8, Chapter 4). Partial recrystallization was observed in the microstructure of the fracture tensile samples tested in the supercooled austenitic condition (Figs. 4.10(a) and 4.11(a), Chapter 4). Partial recrystallization of the supecooled austenite resulted in a mechanically heterogeneous mix of soft recrystallized grains and work hardened grains. This heterogeneity led to necking. At higher temperature, recrystallization commences at lower deformation than that at lower temperature. This explains the observed inverse correlation of uniform elongation of supercooled austenite with temperature in 9Cr-1Mo(V, Nb) FMS.

8.3 Joining Efficiency and Welding Speed

Joining efficiency (mm^2/kJ) gives the area of the parting surface which is fused with one kJ of the energy supplied by the heat source. Higher joining efficiency therefore, implies minimal undesired thermal effects like HAZ, residual stresses and joint distortion. Owing to high power density, beam (Laser and Electron) welding processes are associated with one order higher joining efficiency (~ 15 – 25 mm^2/kJ) as compared to arc welding processes (~ 1 – 3 mm^2/kJ) [10]. Joining efficiency in case of laser welding depends on the factors like quality of the laser beam, laser power, welding speed and mode (conduction / keyhole) of welding.

Effect of welding speed on joining efficiency during laser welding of 9Cr-1Mo(V, Nb) FMS was studied as a part of the present work. For this purpose a large number (22) of weld beads were produced on 30 mm thick plates, for a range of laser power (2 – 8 kW) and welding speed (0.5 – 5.0 m/min) combinations. Joining efficiency increased from ~ 15 mm^2/kJ at the welding speed of 0.5 m/min to ~ 55 mm^2/kJ at the welding speed of 5.0 m/min (Fig. 5.1, Chapter 5). Similar values for joining efficiency have been reported by Suder et al. [11] while performing laser welding at 4 kW and 7 kW laser power using a high power (8 kW) fiber laser. This shows that joining efficiency in keyhole mode is not dependent on the type of laser is being used for welding. Besides, the values of the joining efficiency obtained in the present work and also that reported by Suder et al. [11] are nearly twice than that reported by Steen et al. [10]. This difference can be attributed to progressively improved laser beam quality over time.

The increase in the joining efficiency with welding speed was very much expected as the increased welding speed reduces the time for lateral spread of the deposited laser energy into the work piece. Lateral spread of the deposited energy of the laser beam occurs through two mechanisms. In the weld pool, it is diverging flow of the melt under surface tension gradient and in the solid it is conduction of the thermal energy under temperature gradient. High welding speed or short interaction time of the laser beam with the substrate shortens solidification time of the melt, which in turn minimizes lateral spread of the thermal energy by melt pool convection.

It was interesting to note that significant part of the gain in the joining efficiency (15 mm^2/kJ – 45 mm^2/kJ) was accrued with relatively smaller increase in the welding speed from 0.5 m/min to 2.0 m/min and increasing the welding speed beyond that led to only marginal increase in the joining efficiency (Fig. 5.1, Chapter 5). At the same time, depth of penetration decreased significantly with increasing welding speed at a given laser power. Therefore, the welding speed of 2.0 m/min can be treated as a trade-off between joining efficiency and depth of penetration.

8.4 Cross-weld Microstructure, Microhardness and Tensile Properties of Laser Welded Joints in 9Cr-1Mo(V, Nb) FMS

Welding is known to produce a graded variation in the microstructure across the welded joints in 9Cr-1Mo(V, Nb) steel. Under influence of the heat supplied for welding, this steel undergoes different phase-transformations and other metallurgical changes. The extent of microstructural variations in the fusion zone and the HAZ depends on the magnitude of the thermal energy and the number of passes used. In conventional arc welding processes multiple passes are used, leading to formation of a heterogeneous microstructure within the fusion zone itself and a wide and a graded HAZ. The resulting cross-weld variation in the microstructure also induces variation in the hardness across the weld joint and therefore, tensile strength and in-service performance of the weld joint. These aspects has been reported and discussed at length in the literature [3, 12] for arc welded joints in this steel. However, the literature covering these aspects of laser welded joints are rather limited [13]. Microstructural characterization, microhardness measurements and tensile property evaluation of the laser welded joints in 9Cr-1Mo(V, Nb) FMS were performed as a part of the present work.

Laser welded joints at 8 kW laser power and 1.5 m/min welding speed showed a deep (9 mm) and narrow fusion zone (~ 1.1 mm) and HAZ (0.5 mm on the either side of the fusion zone) and those welded at same power (8 kW) but slower speed (0.75 m/min), which showed slightly wider fusion zone (~ 1.8 mm) and HAZ (~ 1.5 mm on the either side of the fusion zone) (Figs. 5.3a and 5.3b, Chapter 5). Wider fusion zone and HAZ in case of slower welding speed is on account of larger heat input.

Microstructure of the fusion zone, in as-welded condition, comprised of as-transformed martensite within columnar prior austenite grains (Fig. 5.4e, Chapter 5). In addition to the lath martensite, twinned martensite was also observed (Figs. 5.4g and 5.4h, Chapter 5). The microstructure was fully homogeneous and no δ-ferrite or carbide / carbonitride precipitates were observed. Microstructure of the HAZ consisted of as-transformed martensite within prior austenite grains of progressively smaller sizes from the fusion line towards the parent metal side (Fig. 5.4a, Chapter 5). However, there was no appreciable coarsening of the prior austenite grains in the HAZ. Incomplete dissolution of the carbide precipitates and bainitic transformation product of austenite was also observed in the HAZ (Figs. 5.4c and 5.4d, Chapter 5). Post weld heat treatment of the weld joints at 770^{o}C led to tempering of the fusion zone and the HAZ by rearrangement of the dislocations and precipitation of the carbide and carbonitride precipitates (Figs. 5.5b and 5.5d, Chapter 5).

Cross-weld microhardness profile, in as-welded condition, showed significant hardening in the fusion zone and the HAZ. The fusion zone showed hardness in 450 – 500 HVN range, which is nearly twice of that of the parent metal (~230 – 240 HVN) (Fig. 5.6, Chapter 5). Variation in the hardness was very steep through the narrow HAZ. This hardening is on account of the martensitic transformation and is not acceptable for end use. Therefore, welded joints in this steel are invariably tempered. Postweld tempering (770^{o}C for 30 min) led to significant softening in the fusion zone and the HAZ, however, no inter-critical softening was observed. After tempering, hardness of the HAZ became comparable to that of the parent metal, however that of the FZ remained slightly higher (~ 260 – 280 HVN) (Fig. 5.6, Chapter 5).

Cross-weld tensile tests in as-welded condition yielded yield strength of 550 MPa and UTS of 720 MPa, which is nearly same as that of the parent metal (Fig. 5.7, Chapter 5). This is because the joints failed in the parent metal (Fig. 5.8, Chapter 5). In post weld heat treated condition, the strength values decreased marginally (yield strength: 500 MPa and UTS: 680 MPa). Here again the joints failed in the parent metal only during cross-weld tensile test. This shows that the weld joints were sound and stronger than the parent metal. Elongation of the as-welded joint (18%) was only marginally lower than that of the parent metal (21%) and this loss was nearly completely recovered by post weld tempering of the weld joints. These results are in agreement with that reported in the literature for laser welded joints in 6 mm thick plates of P91 steel [14].

Fully homogenous martensitic structure of the fusion zone of the laser welded joints in as-welded condition is because of single pass. This differs from the heterogeneous microstructure comprising of as-transformed martensite, re-austenitized and re-transformed martensite and zones tempered to varying extent and resulting carbide / carbonitride precipitates; produced as a result of multiple passes in case of arc welded joints [12]. Presence of twinned martensite in the fusion zone microstructure can be explained by mechanical stabilization of the austenite, due to work hardening while cooling under constraint to the transformation temperature, leading to suppression of martensitic transformation temperature [14].

In the heat affected zone, during heating, as the tempered martensite is heated above Ac_1 temperature, ferrite transforms into martensite by nucleation and growth mechanism. The extent of the nucleation and growth depends on the superheat and the residence time above Ac_1 temperature. Because, these parameters vary across the HAZ therefore, austenite grains of progressively varying sizes are formed. This explains presence of the prior austenite grains of varying sizes in the HAZ (Fig. 5.4a, Chapter 5). In case of arc welding, due to slower heating and cooling the HAZ experiences greater residence time above Ac_1 temperature and therefore, coarsening of austenite grains takes place near the fusion line, which reflects as coarse grained HAZ (CGHAZ) [12]. However, in case of laser welding, due to rapid heating and cooling the HAZ experiences very short residence time above Ac_1 temperature and therefore, coarsening of austenite grains does not take place even near the fusion line. This explains absence of CGHAZ in laser welded joints in 9Cr-1Mo(V, Nb) FMS (Fig. 5.4a, Chapter 5). Rapid heating and cooling in the HAZ, also results in insufficient time for complete dissolution of the carbide particles. This produces relatively lean austenite with lower hardenability that sometimes transforms into bainite. This explains presence of some bainitic transformation products in the HAZ (Fig. 5.4d, Chapter 5).

Inter-critical softening is invariably present in the arc welded joints in this steel due to over tempering and this is responsible for premature failure of the welded joints by Type-IV cracking. However, inter-critical softening was absent in laser welded joints. Absence of the inter-critical softening again shows that due to low heat input and therefore, rapid heating and cooling during laser welding, the inter-critical HAZ did not undergo any over tempering. This is one of the reasons why laser and EB welded joints are reported to have better creep performance than the arc welded joints in this steel [15].

8.5 Residual Stresses in Laser Welded 9Cr-1Mo(V, Nb) FMS by Neutron Diffraction

Residual stresses are invariably associated with welded joints because of localized thermal dilation of material and in certain alloys, like 9Cr-1Mo(V, Nb) FMS, also because of solid state phase transformations. Residual stresses have a significant bearing on in-service performance of welded components and therefore, accurate and reliable measurement of the same is necessary. Among the various experimental methods available for residual stress measurements, neutron diffraction is a versatile non-invasive method for measuring stresses present in a small volume of the element of interest within a thick weld joint. In the present work, neutron diffraction was performed for measurement of residual stresses in two plates of 9 mm thick 9Cr-1Mo(V, Nb) FMS, laser welded at 8 kW power and different welding speeds – 1.5 m/min and 0.75 m/min. Three orthogonal components (longitudinal, transverse and normal) of the residual stresses were measured at different points across the weld joint as well as through the thickness of the plate.

These measurements showed that the region affected by the residual stresses is significantly wider (~ 5 mm on the either side of the weld centreline) than the metallurgical HAZ (Fig. 6.4, Chapter 6). The longitudinal component of the residual stress was most significant followed by the normal component and the transverse component was least significant. The longitudinal component and the normal components of the residual stress showed similar cross-weld profiles with a trough in the fusion zone and a peak on the either side of it, in the parent metal adjoining the HAZ. The width of the compressive/low tensile trough and therefore distance between the tensile peaks on the either side of the weld joint was more for the weld joint produced at the same laser power and lower welding speed (Fig. 6.9, Chapter 6). There was no significant variation in the residual stresses along thickness of the plate, except in the fusion zone, which was in relatively compressive state of stress below mid-thickness plane than that above (Figs. 6.7 and 6.8, Chapter 6). The neutron diffraction peaks obtained from the fusion zone and the HAZ were significantly wider (FWHM ~ 0.9^{o} – 1.4^{o}) than that obtained from the parent metal (FWHM ~ 0.5^{o}) (Figs. 6.1 and 6.2, Chapter 6). Besides, the neutron diffraction peak width exhibited a systematic variation across the weld joint and showed one to one correlation with the regions which have undergone martensitic transformation during laser welding (Fig. 6.2, Chapter 6).

The compressive/low tensile residual stresses in the fusion zone and high tensile residual stress peaks on the either side of it, is a direct consequence of the martensitic transformation of austenite during cool down of the weld joint. In the materials, where no martensitic transformation is present, localized contraction of the weld joint produces high tensile stresses in the fusion zone and the HAZ and a balancing compressive stress of low magnitude spread over a much wider region in the parent metal. However, in case of 9Cr-1Mo(V, Nb) FMS the material in the fusion zone and the HAZ, transforms from austenite to martensite during cool down of the weld joint. This phase transformation is associated with volumetric expansion and this expansion is constrained. Also the product phase (martensite) is much stronger than the parent phase (austenite). Therefore, this phase transformation brings in significant amount of compressive stresses in the fusion zone and the HAZ, which nearly nullifies the tensile stresses resulting from localized thermal contraction. The parent metal just outside the HAZ, however, experiences only thermal contraction and no volumetric expansion and therefore, tensile stresses develop in this zone. In addition this region also experiences tensile reaction of the compressive stresses brought in the fusion zone and the HAZ by the martensitic transformation. Therefore, tensile residual stress peaks are present in the parent metal just outside the HAZ.

The bainitic and the martensitic transformations in the fusion zone and HAZ are known to introduce compressive effect on the residual stress [6, 7, 16 - 19], this has not been quantified in case of laser welded joints in 9Cr-1Mo(V, Nb) FMS. All the reported work on the residual stress measurements in weld joints in 9Cr-1Mo(V, Nb) FMS or other bainitic/martensitic steel were concerned with the arc welded joints [6, 7, 16, 19]. In case of arc welding multiple passes are involved and the succeeding passes altered the stress/residual stress field produced by the preceding passes. This made it difficult to deduce the effect of the martensitic transformation on the residual stresses from those measurements. Electron beam welding can be considered to introduce similar kind of residual stresses in this material as that introduced by laser welding. Kundu et al. [17, 18] in their recent work on residual stress measurements in electron beam welded 9Cr-1Mo(V, Nb) FMS have also reported similar cross-weld residual stress profiles as that obtained in the present work on laser welded joints.

Another interesting observation concerned relative significance of the three orthogonal components (longitudinal, normal and transverse) of the residual stress. In the arc welded joints, the longitudinal component of the residual stress remains most significant and the other two components – normal and transverse are comparable and not so significant [16]. However, in the present work, it was observed that there was a clear order among the three components of the residual stress: longitudinal > normal > transverse (Fig. 6.4, Chapter 6). This order of the three components of the residual stress also shows similarity with the physical dimensions of the region, which experienced martensitic transformation during welding, along these directions. Since, martensitic transformation has a lasting impact on the residual stresses in the laser welded joints in this steel, it can be concluded that the high thickness to width aspect ratio of the weld joint is responsible for inducing this order among the three components of the residual stress.

Through thickness variation in the residual stresses was not significant except in the fusion zone. The fusion zone showed relatively compressive state of stresses below mid-thickness than that above. This is markedly different from that observed in case of multipass arc welded joints in this steel. Paddea et al. [16] have reported tensile stresses in the root side and below the mid-thickness and compressive stresses on the top surface side. This is because, the compressive stress resulting from martensitic transformation is preserved in case of the closing passes forming the top surface, while the preceding weld deposit gets the tensile reaction and also tensile stresses due to localized contraction. This is not so in the case of laser welded joints as there is only one pass and the entire fusion zone solidifies and undergoes martensitic transformation almost simultaneously. Thus balancing of the residual stresses in case of laser welding is predominantly across the joint; while it is across as well as through the thickness of the joint, in case of arc welding.

Significantly wider neutron diffraction peaks obtained from the fusion zone (FWHM ~ 0.9^{o} – 1.4^{o}) and the HAZ than those from the parent metal (~0.5^{o}) are on account of higher micro-stresses present in those regions (Figs.6.1 and 6.2, Chapter 6). These micro-stresses arise from martensitic transformation. As the diffraction peak width showed one to one correlation with martensitic transformation, it can be used as a marker for the measurement location, during neutron diffraction. This is very important while measuring residual stresses in laser and electron beam welded joints using neutron diffraction. This is because, the length scales of the fusion zone and the HAZ are very small and it is quite tedious to ensure that the diffraction measurements are indeed being made from the intended locations.

8.6 Modelling and Simulation of Laser Welding in 9Cr-1Mo(V, Nb) FMS

Modelling and simulation provides better insight into a process. This is because experimental observation of many changes of interest is either difficult or not possible during the actual process, but the same can be computed by modelling and simulation of the process. For example the final or residual stress resulting from welding can be experimentally measured, but its evolution during welding cannot be measured. Modelling and simulation of a process also allows better visualization of a process, particularly, when the process is fast. Therefore, modelling and simulation of laser welding was carried out for better visualization and deeper insight of the thermo-metallurgical and thermo-mechanical changes taking place during laser welding of 9Cr-1Mo(V, Nb) FMS at 8 kW laser power and 1.5 m/min welding speed.

The computed and the experimentally observed profiles of the fusion zone and HAZ (Fig. 7.1, Chapter 7) showed reasonably good agreement. This suggests that the heat source model used in these computations was a good representation of the actual heat source and therefore, the computed results could be relied upon. Temporal evolution of temperature in the fusion zone showed almost instant heating and melting and then rapid cooling of the melt. The peak temperatures at increasing distance from the weld centreline showed an asymptotically falling trend (Fig. 7.2, Chapter 7). The computed results showed very small residence time above Ac_1 temperature (~0.5 s) for the material in the HAZ and still smaller time (~200 ms) in the inter-critical temperature range.

Almost instant heating and melting is because of very high rate of energy input resulting from the high power density (4 MW/cm^2) and welding speed (1.5 m/min). Rapid cooling of the melt is on account of much lower energy input, which is sucked out by nearly infinite heat sink, the plates being welded. However, cooling rate of the melt is relatively lower than the heating rate. This is because heating rate is governed by the rate of energy input, which is process controlled (power density and welding speed) while the cooling rate is governed by the property of the material (thermal diffusivity). This also explains why heating rates in the HAZ and the parent metal are much lower than those in the fusion zone, as it is diffusion of the heat within the material which causes heating of these zones and not the direct supply of energy from the laser beam, which heats up and melts the material in the fusion zone. Heating of the HAZ and the parent metal is because of the heat flowing outward from the fusion zone and this explains the asymptotically falling peak temperatures with increasing distance from the fusion line.

Rapid solidification of the melt resulted in the formation of columnar grains in the fusion zone. The columnar grains originated at the fusion line and grew nearly perpendicular right up to the weld centreline. Short residence time (~ 500 ms) of the material above Ac_1 temperature in HAZ explains incomplete dissolution of the carbide / carbonitride in this zone. This also explains why coarsening of the prior austenite grains was not appreciable in the HAZ and why CGHAZ was not observed. This is because of insufficient time for dissolution of the carbides and for growth of the austenite grains formed by transformation of ferrite grains while heating above Ac_1. Short residence time (~ 200 ms) of the material in the inter-critical temperature range explains absence any softening of the material in the inter-critical zone in the cross-weld microhardness profile presented and discussed in Chapter 5 (Section 5.5).

The computed residual stress profile across the weld joint (Fig. 7.3, Chapter 7) showed low tensile / compressive trough in the fusion zone and a high tensile peak in the parent metal, much like that observed by neutron diffraction measurements. The location of the high tensile peak was at 2 mm from the weld centreline in the cross-weld residual stress profiles obtained by computation. This result also agrees well with that obtained from the neutron diffraction measurements (Fig. 7.5, Chapter 7). The order of significance of the three orthogonal components of the residual stress was also the same – longitudinal > normal > transverse; in computed as well as measured results. Though there was difference in terms of the magnitude of the tensile peaks. The computed peak values are considerably higher than that obtained by neutron diffraction measurements.

Reasonably good agreement between the computed and the measured residual stress profiles in terms of nature of the profile, location of the high tensile peaks and the relative significance of the three orthogonal components (longitudinal, normal and transverse) of the residual stress certifies the modelling and simulation work. The differences in the computed and the experimentally measured residual stresses were in terms of the magnitude of the tensile peak. This can be explained by the fact that gauge volume in case of neutron diffraction measurements was 0.8 x 0.8 x 2mm^3 and this is too large to capture the stress gradient present across the weld joint, considering the length scales of the fusion zone (~ 1.2 mm) and HAZ (~ 0.5 mm). On the other hand sufficiently fine elements (~ 0.1 x 0.1 x 0.25 mm^3 to 0.3 x 0.4 x 0.5 mm^3) could be employed in modelling and simulation work near the weld centreline to capture the high stress gradient resulting from laser welding of 9Cr-1Mo(V, Nb) FMS. Therefore, it can be inferred that the residual stress values measured by neutron diffraction presents an average value over a much larger region and therefore, expected to be lower than the actual value due to steep stress gradient present within the volume.

Computation of the temporal evolution of the stress-field revealed the effect of different events associated with laser welding of 9Cr-1Mo(V, Nb) FMS – rapid heating of the material during approach of the laser beam to the point of interest, softening and melting by the laser beam, post solidification contraction, solid state transformation of austenite into martensite and subsequent thermal contraction of the martensite; on evolution of the stress-field resulting from laser welding (Fig. 7.8, Chapter 7). Most striking is the effect of the solid state transformation of austenite into martensite which contributed ~300 MPa compressive stresses in the longitudinal component of the residual stress. Another very important result was the state of stresses in the austenitic phase field of the 9Cr-1Mo(V, Nb) FMS in the fusion zone. In the mid-thickness region the austenite was under triaxial tensile stresses (Fig 7.9, Chapter 7). von-Mises equivalent of the stresses in the austenitic phase-field in the fusion zone, prior to its transformation into martensite, was ~ 200 MPa. This value is ~ 33% higher than the yield stress of the austenite in this steel (Chapter 4) and this shows that austenite had undergone plastic deformation and therefore, work hardening prior to its transformation into martensite. It was also, observed that the stress affected zone during laser welding was much wider (~ 10 – 12 mm) than that indicated by the final or the residual stress profile (~ 5 mm) on the either side of the weld centreline (Figs. 7.4 and 7.10, Chapter 7). It is worth mentioning that there is hardly any experimental technique which can extract this information considering the high speed of the laser welding process and therefore rapid nature of the associated changes. Also, there is hardly any literature quantifying the effect of martensitic transformation on the residual stresses or reporting the nature and the quantum of the stresses in the austenite phase-field prior to its transformation into martensite. All these interesting results were obtained in the present work. While it is not possible to obtain a direct proof of plastic deformation and work hardening of the austenitic phase-field prior to its transformation into martensite, indirect evidence is present in the final microstructure. This steel normally transforms into lath martensite, because of low carbon content. However, significant fraction of twinned martensite was present in the fusion zone. This implies that the martensitic transformation in the fusion zone had occurred at lower temperatures, than the usual transformation temperatures for this steel. This is possible only if the austenite was work hardened by plastic deformation prior to its transformation, as work hardening is known to suppress Ms temperature of austenite [14]. The stress field in the material during laser welding was present in a much wider region than that indicated by the final or the residual stresses. This information can be very useful in implementing suitable clamping during laser welding of this steel.

From these results it can be concluded that modelling and simulation of laser welding has provided a deeper insight of the process as well as many results scientific and engineering importance, which cannot be obtained by the actual experiments. These studies are important for fabrication of the components of the next generation nuclear reactors for which 9Cr FMS are the candidate structural material.

8.7 Suggestion for Further Work

Laser and Electron Beam welding of thick sections of 8-12Cr FMS is of interest, as these steels are the structural material for the next generation power plants and nuclear reactors, including the fusion reactor. In the present work an attempt has been made to study laser welding of 9Cr-1Mo(V, Nb) FMS in terms of microstructure, mechanical properties and residual stresses by experiment and modelling and simulation. However, the following points may have to be addressed for comprehensive understanding of the issues related to laser welding of 8-12Cr FMS/RAFMS, unambiguously. A brief description of the area of interest for the further studies is enumerated below.

It was realized in the present work that neutron diffraction was not good enough to capture the steep gradient in the residual stresses present across the laser welded joints in 9Cr FMS and therefore, further measurements using synchrotron radiation is suggested for further improvements in the cross-weld residual stress profile. It was also realized that there was variation in the transformation temperatures and mechanical properties of the transformation products of austenite across the HAZ, as a result of variation in the austenitization temperature and this need to be implemented in the modelling and simulation work for improving the accuracy of the computed residual stresses. However, sufficient material data was not available to implement this variation. Sufficient material data should be generated on the mechanical properties of the transformation products of austenite as a function of austenitization temperature and this variation should be implemented in the modelling and simulation work. Present modelling and simulation studies also suggested significant plastic deformation and work hardening of the austenitic phase prior to its martensitic transformation during cool down of the weld joint. This is expected to suppress martensitic transformation temperatures of the steel and therefore, affect the residual stresses. This effect could not be implemented in the modelling and simulation during the present work. However, this material data should be generated and implemented in the modelling and simulation work for improving the accuracy of the computed residual stresses.

The present study suggests that 9Cr-1Mo(V, Nb) FMS is a good candidate for ausforming. Therefore, a detailed study of the ausforming behaviour of 9Cr-1Mo(V, Nb) FMS should be performed to assess the suitability of this process for shaping of this steel into different forms including U-shape for fabrication of the FW (First Wall) of the TBM (Test Blanket Module) for The ITER (International Thermonuclear Experimental Reactor).

References

[1] K. Haarmann, J. C. Vaillant, W. Bendick and A. Arbab, The T91/P91 Book, Vallourec and Mannessmann Tubes, (1999) 14-29.

[2] B. J. Ganesh, S. Raju, A. K. Rai, E. Mohandas, M. Vijayalakshmi, K. B. S. Rao, and B. Raj, “Differential scanning calorimetry study of diffusional and martensitic phase transformations in some 9 wt% Cr low carbon ferritic steels”, Mater. Sci. and Technol. 27(2) (2011) 500-512.

[3] S. A. David, J. A. Siefert and Z. Feng, “Welding and weldability of candidate ferritic alloys for future advanced ultrasupercritical fossil power plants”, Sci. Technol. Weld. Join. 18(8) (2013) 631 – 651.

[4] M. Igarshi, S. Muneki and F. Abe, “Microstructure control of martensite phase matrix in advanced ferritic steels for USC boilers to achieve long term stability”, in Materials for advanced power engineering – 6th Liege Conference (1998) 637-646.

[5] S. Sulaiman, “Structure of properties of the heat affected zone of P91 creep resistant steel”, PhD Thesis, University of Wollongong, Wollongong, Australia (2007) [http://ro.uow.edu.au/theses/777].

[6] D. Dean and M. Hidekazu, “Prediction of welding residual stress in multi-pass butt-welded modified 9Cr–1Mo steel pipe considering phase transformation effects”, Comput. Mater. Sci. 37 (2006) 209 - 219.

[7] S. H. Kim, J. B. Kim and W. J. Lee, “Numerical prediction and neutron diffraction measurement of residual stresses for a modified 9Cr-1Mo steel weld”, J. Mater. Process. Technol. 209 (2009) 3905 - 3913.

[8] K. Laha, K. S. Chandravathi, P. Parameshwaran, K. B. S. Rao and S. L. Mannan, “Characterization of Microstructures across the Heat-Affected Zone of the Modified 9Cr-1Mo Weld Joint to Understand Its Role in Promoting Type IV Cracking", Metall. Mater. Trans. 38A (2007) 58 - 68.

[9] J. Parker, “Factors affecting type IV creep damage in Grade 91 steel welds”, Mater. Sci. Eng. A578 (2013) 430 – 437.

[10] W. M. Steen and J. Mazumder, “Laser material processing”, 4th ed., Springer (2010).

[11] W. Suder, S. Ganguly, S. Williams, A. M. Paradowska and P. Colegrove, “Comparison of joining efficiency and residual stresses in laser and laser hybrid welding” Sci. Technol. Weld. Join. 16(3) (2011) 244 – 248.

[12] H. Cerjak and P. Mayr, “Creep strength of welded joints of ferritic steels” in Creep-Resistant Steels, F. Abe, T U Kern and R. Viswanathan Eds.; Woodhead Publishing Limited, Cambridge, UK, (2008) 472 - 503.

[13] B. Shanmugarajan, G. Padmanabham, H. Kumar, S. K. Albert and A. K. Bhaduri, “Autogenous laser welding investigations on modified 9Cr-1Mo (P91) steel”, Sci. Technol. Weld. Join. 16(6) (2011) 528 - 534.

[14] T. S. Wang, M. Zhang, Y. H. Wang, J. Yang and F. C. Zhang, “Martensitic transformation behaviour of deformed supercooled austenite”, Scripta Mater. 68(2) (2013) 162 - 165.

[15] S. K. Albert, M. Tabuchi, H. Hongo, T. Watanabe, K. Kubo and M. Matsui, “Effect of Welding Process and Groove Angle on Type IV Cracking Behaviour of Weld Joints of a Ferritic Steel”, Sci. Technol. Weld. Join. 10 (2) (2005) 149-157.

[16] S. Paddea, J. A. Francis, A. M. Paradowska, P. J. Bouchard and I. A. Shibli, "Residual stress distribution in a P91 steel-pipe girth weld before and after post weld heat treatment", Mater. Sci. Eng. A534 (2012) 663 - 672.

[17] A. Kundu, P. J. Bouchard, S. Kumar, K. A. Venkata, J. A. Francis, A. Paradowska, G. K. Dey and C. E. Truman, “Residual stresses in P91 steel electron beam welds”, Sci. Technol. Weld. Join. 18(1) (2013) 170 – 175.

[18] A. Kundu, P. J. Bouchard, S. Kumar, G. K. Dey, “Characterisation of Residual Stress in Electron Beam Welded P91 Plates by Neutron Diffraction”, Int. J. Metall. Eng. 2(1) (2013) 79 - 84.

[19] A. F. Mark, J. A. Francis, H. Dai, M. Turski, P. R. Hurrell, S. K. Bate, J. R. Kornmeier and P. J. Withers, “On the evolution of local material properties and residual stress in a three-pass SA508 steel weld”, Acta Mater. 60 (2012) 3268–3278.

List of Publications from this Work

International Journals: 04

1. **Santosh Kumar**, A. Kundu, K. A. Venkata, A. Evans, C. E. Truman, J. A. Francis, K. Bhanumurthy, P. J. Bouchard and G. K. Dey, "Residual stresses in laser welded ASTM A387 Grade 91 steel plates", **Materials Science & Engineering A575 (2013) 160–168.**
2. **Santosh Kumar**, R. P. Kushwaha, B. C. Maji, K. Bhanumurthy and G. K. Dey, "Phase-dependence in the tensile behaviour of 9Cr-1Mo(V, Nb) ferritic/martensitic steel", **Metallurgical and Materials Transactions A45(2) (2014) 531 - 536.**
3. **Santosh Kumar**, Reena Awasthi, C. S. Viswanadham, K. Bhanumurthy and G. K. Dey, "Thermo-metallurgical and thermo-mechanical computations for laser welded joint in 9Cr-1Mo(V, Nb) steel", **Materials and Design 59 (2014) 211–220.**
4. **Santosh Kumar**, C. S. Viswanadham, S. Bhattacharya, S. B. Roy, K. Bhanumurthy and G. K. Dey, "Experimental and simulation studies on helium channel reconstruction for TBM fabrication by high power laser welding", **Fusion Science and Technology 65(2) (2014) 199-204.**

International Conferences: 04

1. **Santosh Kumar**, A. Kundu, K. A. Venkata, A. Evans, K. Bhanumurthy, P. J. Bouchard, and G. K. Dey, "Neutron Diffraction: The State of Art in Non-invasive Stress-field Mapping", **Aisa Pacific Conference on Non-Destructive Testing (APCNDT 2013)**, Mumbai, India
2. **Santosh Kumar,** Evan Alex, P. J. Bouchard and G. K. Dey, "Residual Stress Measurements by Neutron Diffraction in P91 Laser Welded Joints", **International Symposium on Neutron Scattering (ISNS 2013)**, Mumbai, India.
3. **Santosh Kumar,** R. P. Kushwaha, K. Bhanumurthy and G. K. Dey, "Microstructural characterization of deformed supercooled austenite of P91 steel", **International Conference on Electron Microscopy (EMSI 2013)**, Kolkata, India.
4. **Santosh Kumar,** C. S. Viswanadham, S. Bhattacharya, K. Bhanumurthy and G. K. Dey, "Laser Welding of ASTM A387 Grade 91 Steel and Microstructural Characterization of the Weld Joints", **2nd International Conference on Nuclear Materials (NuMAT 2012)**, Osaka, Japan

National Conferences: 02

1. **Santosh Kumar,** R. P. Kushwaha, A. Ghosh, K. Bhanumurthy and G. K. Dey, "Effect of Austenitization Temperature on Transformation of Austenitic Phase in P91 Steel", **National Metallurgical Day, Annual Technical Meeting (NMD-ATM 2014)**, Pune, India.
2. **Santosh Kumar,** R. P. Kushwaha, A. Ghosh, K. Bhanumurthy and G. K. Dey, "Residual stresses in laser welded 9Cr-1Mo(V, Nb) ferritic/martensitic steel: A computational study", **(NMD-ATM 2014)**, Pune, India.

List of Figures

List of Tables

List of Symbols

Symbol	Description
A_1	Ferrite to austenite start temperature in steel
A_3	Ferrite to austenite finish temperature in steel
Ac	Transformation temperatures in steel during heating at a finite rate
Ac_1	Ferrite to austenite start temperature during heating of steel
Ac_3	Ferrite to austenite finish temperature during heating of steel
Ae	Equilibrium transformation temperatures in steel
Ae_1	Ferrite to austenite start equilibrium temperature in steel
Ae_3	Ferrite to austenite finish equilibrium temperature in steel
Ae_4	Austenite to δ-ferrite start equilibrium temperature in steel
Ar	Transformation temperatures in steel during cooling at a finite rate
Ar_1	Austenite to ferrite finish temperature during cooling of steel
Ar_3	Austenite to ferrite start temperature during cooling of steel
α	Ferrite, a body centred cubic form of iron and steel below A_1 temperature
α'	Martensite, a body centred cubic form of steel
γ	Austenite, a face centred cubic form of iron and steel
δ-ferrite	A high temperature a body centred cubic form of iron and steel
λ	Wavelength
d	Interplaner spacing of crystallographic planes
do	Interplaner spacing of crystallographic planes in stress-free condition
ε	Strain
σ	Stress
E	Young's Modulus
ν	Poisson's ratio
(hkl)	Miller index of a crystallographic plane
k	Thermal conductivity
c, c_p	Heat capacity
K	Coefficient of linear expansion
q	Heat density (energy per unit volume)

r_o	Bottom radius of the truncated conical heat source
r_e	Top radius of the truncated conical heat source
z	Height of the truncated conical heat source
a, b, c	Length of semi-principal axes of ellipsoidal heat source
f	Front
r	Rear
∇	Del operator
ρ	Density
T	Temperature
h	Heat transfer coefficient
s	Stefan's constant
e	Emissivity
T_o	Temperature of ambient
P(T)	Phase fraction at temperature T
Peq	Equilibrium phase fraction
t	Time
τ	Delay time or time lag
P	Laser power
d	Depth of penetration
v	Welding speed

List of Abbreviations

Abbreviation	Description
FMS	Ferritic / martensitic steel
RAFMS	Reduced activation ferritic / martensitic steel
CLAM	Chinese low activation martensitic steel
In-RAFMS	Indian reduced activation ferritic / martensitic steel
N&T	Normalized and tempered
CHT	Continuous heating transformation
CCT	Continuous cooling transformation
DSC	Differential scanning calorimetry
MMAW	Manual metal arc welding
SMAW	Shielded metal arc welding
GTAW	Gas tungsten arc welding
DCEP	Direct current electrode positive
DCEN	Direct current electrode negative
A-TIG	Activated tungsten inert gas
NG-TIG	Narrow gap tungsten inert gas
GMAW	Gas metal arc welding
MIG	Metal inert gas
FCAW	Flux cored arc welding
SAW	Submerged arc welding
UDW	Uniaxial diffusion welding
HIPing	Hot isostatic pressing
EBW	Electron beam welding
PWHT	Post weld heat treatment
FZ	Fusion zone
HAZ	Heat affected zone
PMZ	Partially melted zone
CGHAZ	Coarse grained heat affected zone
FGHAZ	Fine grained heat affected zone

ICHAZ	Intercritical heat affected zone
SCHAZ	Subcritical heat affected zone
PM	Parent Material
TM	Tempered martensite
M	Martensite
A	Austenite
YS	Yield strength
UE	Uniform elongation
UTS	Ultimate tensile strength
SEM	Scanning electron microscope
TEM	Transmission electron microscope
EDS	Electron dispersive spectroscopy
TBM	Test blanket module
ITER	International thermonuclear experimental reactor
HPDL	High power diode laser
Nd-YAG	Neodymium-yttrium aluminium garnet
CNC	Computer numerical control
SCC	Stress corrosion cracking
CMM	Co-ordinate measuring machine
EDM	Electro-discharge machining
MBN	Magnetic Barkhausen noise
2D	Two dimensional
3D	Three dimensional
RT	Room temperature
J. E.	Joining efficiency
FWHM	Full width at half maximum
SSPT	Solid state phase transformation
BARC	Bhabha Atomic Research Centre
HBNI	Homi Bhabha National Institute
ILL	Institut-Laue Langevin

EPSRC	Engineering and Physical Sciences Research Council
CEA	Commissariat à l'Energie Atomique et aux Energies Alternatives
ANSTO	Australian Nuclear Science and Technology Organisation
NIST	National Institute of Standards and Technology
MURR	University of Missouri Research Reactor Center
HFIR	High Flux Isotope Reactor
SMARTS	Spectrometer for Materials Research at Temperature and Stress
SNS	Spallation neutron source
ORNL	Oak Ridge National Laboratory
USA	United States of America
POLDI	Pulse overlap diffractometer